Charles University in Prague
Faculty of Mathematics and Physics

DOCTORAL THESIS

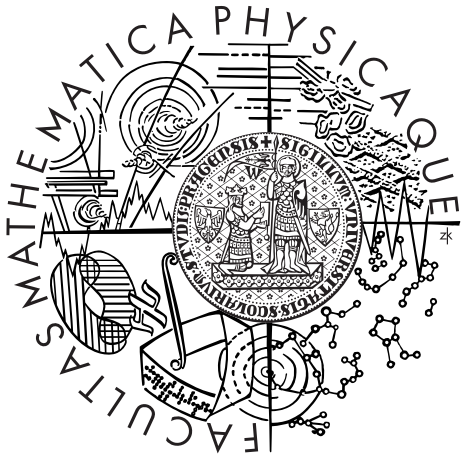

Michal Hejduk

Reactions of Hydrogen Molecules with Ions and Recombination of H_3^+ Ions with Electrons at Cryogenic Temperatures

Department of Surface and Plasma Science

Supervisor of the doctoral thesis:	prof. RNDr. Juraj Glosík, DrSc.
Study programme:	Physics
Specialisation:	4F2 Physics of Plasma and Ionized Media

Prague 2013

I would like to thank my supervisor for mentoring me. His advises, not only on our experimental results, helped us to finish the tasks when we seemed to have lost our way. None of the experiments in flowing and stationary afterglows could have been carried out without assistance of my colleagues Petr Dohnal, Jozef Varju and Peter Rubovič. Measurements using a radio-frequency trap would be impossible without the help from colleagues Illia Zymak, Dmytro Mulin, Pavol Jusko and Štěpán Roučka. The special thanks also go to RNDr. Radek Plašil and Dr. Dieter Gerlich for consultation and material support.

The special acknowledgement should be directed to alma mater: not only for educating me and financing our research but also for supporting attendance to conferences abroad. Meetings with researchers from other countries allowed me to see what is happening outside our small Bohemian pond and probably made me wiser.

I would not be able to reach this stage of issuing the thesis if I did not feel a strong support from my parents, and my wife – she filled up a part of my life that had not been occupied by my studies. With her at my side, no obstacles in the research and in studies were impossible to combat.

I declare that I carried out this doctoral thesis independently, and only with the cited sources, literature and other professional sources.

I understand that my work relates to the rights and obligations under the Act No. 121/2000 Coll., the Copyright Act, as amended, in particular the fact that the Charles University in Prague has the right to conclude a license agreement on the use of this work as a school work pursuant to Section 60 paragraph 1 of the Copyright Act.

In Prague 14th June 2013 Michal Hejduk

Název práce: Reakce iontů s molekulami H_2 a rekombinace iontů H_3^+ s elektrony při kryogenních teplotách

Autor: Michal Hejduk

Katedra: Katedra fyziky povrchů a plazmatu

Vedoucí disertační práce: prof. RNDr. Juraj Glosík, DrSc., Katedra fyziky povrchů a plazmatu

Abstrakt: Vliv rozdělení jaderně-spinových stavů iontů H_3^+ a molekul H_2 (zvaných para a ortho) na rychlostní koeficienty disociativní rekombinace iontu H_3^+ s elektrony a reakcí H_2 s H^+ a N^+ byl zkoumán v závislosti na kinetické a vnitřní teplotě reaktantů. Experimenty byly provedeny v prostředí dohasínajícího plazmatu či v souboru iontů zachycených v pasti. Byly použity diagnostické metody Langmuirovy sondy, laserové absorpční spektroskopie a hmotnostní spektroskopie. Distribuce jaderně spinových stavů byla měněna použitím speciálně zkonstruovaného konvertoru spinových stavů H_2. Byly změřeny rychlostní koeficienty ternární a binární rekombinace H_3^+ s elektrony v plně termalizovaném plazmatu pro jednotlivé jaderně-spinové stavy. Reakce N^+ + para/ortho-H_2 byla zkoumána s ohledem na rozdělení stavů jemné struktury N^+. Byla změřena teplotní závislost rychlostních koeficientů radiativního a ternárního kanálu reakce $H^+ + H_2$ pro jednotlivé jaderně spinové stavy H_2.

Klíčová slova: disociativní rekombinace, reakce iontů s molekulami, plazma, jaderný spin, iontová past

Title: Reactions of Hydrogen Molecules with Ions and Recombination of H_3^+ Ions with Electrons at Cryogenic Temperatures

Author: Michal Hejduk

Department: Department of Surface and Plasma Science

Supervisor: prof. RNDr. Juraj Glosík, DrSc., Department of Surface and Plasma Science

Abstract: We studied how distribution of nuclear-spin states of H_3^+ ions or H_2 molecules influence rate coefficients of H_3^+-electron recombination or reactions of H_2 with N^+ or H^+, with regard to kinetic and internal temperatures of the reactants. Experiments were carried out in plasma environment or in an ensemble of ions in an ion trap. Main diagnostic methods were the Langmuir probe diagnostics, laser absorption- and mass spectroscopy. The distribution of nuclear spin states (para and ortho) was varied using a specially constructed para-hydrogen generator. We performed pioneer measurements of the rate coefficients for the nuclear-spin-state-selective binary and ternary H_3^+-electron recombination in thermalised plasma. We performed studies of N^+ + para/ortho-H_2 reaction with high accuracy and interpreted the results as dependent on fine structure states of N^+ ions. We measured a temperature dependence of the rate coefficients for radiative and ternary channels of H^+ + para/ortho-H_2 association.

Keywords: dissociative recombination, ion-molecule reaction, plasma, nuclear spin, ion trap

Contents

Preface: Importance of being H_3^+

The space between the stars is filled with interstellar matter (ISM), which is an ensemble of neutral particles, positive and negative ions and electrons in the gas phase, together with a small solid component in the form of dust grains. The ISM is highly inhomogeneous in density as well as temperature. In the centre of denser parts ("molecular clouds"), the density of particles can reach values of $n \sim 10^6$ cm^{-3}, while the temperature T of the gas can be as low as 10 K [Ferrière, 2001]. In these cold dark clouds new stars and planets are being born through run-away collapse of local inhomogenities. For this process the existence of molecules is key, since only cascades of transitions between rovibrational energy levels in molecules provide sufficient cooling to avoid a pressure build-up that can stall the collapse.

More than 160 different molecules have been detected in the interstellar space so far (see table 1), among them important species like water, interstellar sugars and alcohol. In recent years a lot of effort was invested to unravel the molecular composition of the Universe. It is believed that we have to understand the formation of biologically relevant interstellar molecules to understand the origin of life on our own planet. Therefore, new telescopes like Herschel and ALMA – two of the most expensive astronomical facilities worldwide – focus on molecular lines exclusively. In particular, a large fraction of Herschel's observation time was dedicated to the WISH program (*W*ater *I*n *S*tar forming regions with *H*erschel [van Dishoeck et al., 2011]) that aims at a widespread search for water in space.

Besides its importance for terrestrial life, the H_2O molecule is also a particularly efficient cooling agent in interstellar space because of its dense emission spectrum and abundance: it is a compound of the first and the third most abundant elements in the Universe [Vasyunin et al., 2008], hydrogen and oxygen. Moreover, it is a unique diagnostic of the warmer gas and of the energetic processes that take place close to forming stars (in pre-stellar cores) because of its thermodynamic properties [Emprechtinger et al., 2010]. Its presence as an ice may have helped the coagulation process of dust grains that ultimately produced planets like ours [Caselli et al., 2012]. Water, which remained at the outer area of our planetary system after the ignition of the Sun was brought back to the Earth by water-containing asteroids and comets [Dauphas et al., 2000]. And this water later enabled the emergence of life as we know it.

A substantial amount of water in the pre-stellar cores is believed to be formed on the surface of dust grains [Whittet et al., 2011]. However H_2O synthesis before the creation of such cores and at UV-transparent parts of the pre-stellar cores is driven by gas-phase chemical networks [Hollenbach et al., 2009], where ion-neutral reactions and electron-ion recombination processes dominate because of the long range electric potential of the ions.

H_2O molecules are produced in the following chain of reactions [Dalgarno, 1994]:
cosmic ray ionisation

$$\mathrm{H_2} + \text{cosmic ray} \rightarrow \mathrm{H_2^+} + \mathrm{e^-} + \text{cosmic ray}\,, \tag{0.1}$$

H_2	PO	N_2O	CH_4	C_4H_2	H_2C_6
CH	SO	SO_2	SiH_4	H_2C_4	C_6H_2
CH^+	SO^+	SiCN	H_2COH^+	HC_2CHO	C_7H
NH	FeO	SiNC	CH_2NH	c-C_3H_2O	
OH		AlNC	H_2C_3	HC_3NH^+	CH_3CHCH_2
SH	H_3^+	MgCN	c-C_3H_2	C_5N	CH_3OCH_3
C_2	CH_2	MgNC	CH_2CN	HC_4N	CH_3CONH_2
CN	NH_2		NH_2CN		CH_3C_4H
CO	H_2O	CH_3	CH_2CO		C_8H
CO^+	H_2S	NH_3	HCOOH	CH_3CHO	C_8H^-
CF^+	CCH	H_3O^+	C_4H	CH_3NH_2	HC_7N
CP	HCN	H_2CO	C_4H^-	CH_3CCH	
CS	HNC	HCCH	HC_3N	C_2H_3OH	C_2H_5CHO
HF	HCO^+	H_2CN	HC_2NC	c-CH_2OCH_2	CH_3COCH_3
NO	HOC^+	$HCNH^+$	HNCCC	C_2H_3CN	$HOCH_2CH_2OH$
PN	HCO	H_2CS	C_5	HC_5N	CH_3C_5N
NS	HN_2^+	C_3H	C_4Si	C_6H	
AlF	HCP	c-C_3H		C_6H^-	CH_3C_6H
AlCl	HNO	HCCN			HC_9N
NaCl	HCS^+	HNCO	C_2H_4	C_2H_6	
KCl	C_3	$HOCO^+$	CH_3OH	$HCOOCH_3$	C_6H_6
SiC	C_2O	HNCS	CH_3SH	CH_3COOH	
SiN	C_2S	C_3N	CH_3CN	$HOCH_2CHO$	$HC_{11}N$
SiO	c-C_2Si	C_3O	CH_3NC	C_2H_3CHO	
SiS	CO_2	C_3S	CH_2CNH	CH_3C_3N	
N_2?	OCS	c-SiC_3	NH_2CHO	CH_2CCHCN	

Notes: "c" stands for cyclic species; "?" stands for ambiguous detections; isotopologues excluded.

Table 1: Gas phase interstellar and circumstellar molecules. Adopted from Herbst and Millar [2008].

followed by the well-known H_3^+ production by proton transfer

$$H_2^+ + H_2 \rightarrow H_3^+ + H\,,\ \Delta E = 1.8\,\mathrm{eV} \tag{0.2}$$

and the chain of ion-neutral reactions beginning with

$$H_3^+ + O \rightarrow \begin{cases} OH^+ + H_2, & \Delta E = 0.7\,\mathrm{eV}, \\ H_2O^+ + H, & \Delta E = 1.7\,\mathrm{eV}, \end{cases} \tag{0.3}$$

where ΔE is the kinetic energy release for production of ground-state products [Hunter and Lias, 1998; Willock, 2009] (for zero collision energy and reactants in the ground states). The chain further continues with reactions

$$OH^+ + H_2 \rightarrow H_2O^+ + H\,, \tag{0.4}$$

$$H_2O^+ + H_2 \rightarrow H_3O^+ + H\,, \tag{0.5}$$

Eventually H_3O^+ ions are neutralised by the dissociative recombination with free electrons

$$H_3O^+ + e^- \rightarrow \text{neutral products}\,. \tag{0.6}$$

From the reactions above we can see how crucial is the role H_3^+ ions are playing in ISM: they stand in the beginning of the chain leading to the water formation. Other illustration of the importance of H_3^+ is the figure 1 depicting a spreading tree of a chemical network. It is important to understand how they are formed and destroyed. The method of formation (0.2) is the fastest known

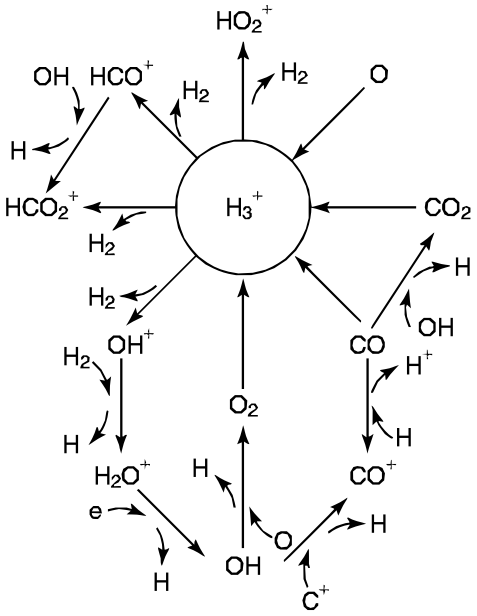

Figure 1: Interstellar chemical network. H_3^+ ions play a central role. Adopted from [Tennyson, 2003a].

so far (in the hydrogen-rich ISM) – because of its exothermicity, astrochemical databases like UDfA (UMIST database for astrochemistry, UMIST [2013]) take its rate coefficient as constant over wide range of temperatures 10–40000 K. The formation via radiative association

$$H^+ + H_2 \rightarrow H_3^+ + h\nu \tag{0.7}$$

has principally a low rate coefficient, but the question how much was not answered until 2011 [Zymak et al., 2011]. The ternary variation of this process

$$H^+ + H_2 + H_2 \rightarrow H_3^+ + H_2 \tag{0.8}$$

was not studied with H_2 molecules with rotational distribution corresponding to astrophysical temperatures of ~ 10 K until we did in 2013 (see chapter 11 and Attachment A.2).

No less interesting is the problem of H_3^+ destruction. One of the ways is the dissociative recombination

$$H_3^+ + e^- \rightarrow \begin{cases} H_2 + H \\ 3H\,. \end{cases} \tag{0.9}$$

This is the dominant mechanism in UV transparent regions with a high degree of ionisation, $> 10\%$ or $> 1\%$. (Otherwise proton transfer reactions like $H_3^+ + C \rightarrow CH^+ + H_2$ can play a more important role). The ambivalence in the value of the ionisation degree here is given by the fact, that the rate coefficient of reaction (0.9) strongly depends on internal temperatures of the ion. The question on which temperatures and how much was answered by other works of mine and my coworkers (chapter 12 and Attachments B and C).

During studies of aforementioned processes in laboratories, special care must be taken to have reactants in known internal states. In case of H_3^+

ions and H_2 molecules, nuclear spin states are coupled with specific rotational states. Since a spontaneous conversion of the nuclear spin states are forbidden, there is always a fraction of molecules or ions that is not able to radiate the excessive internal energy to settle themselves to the ground state. This kind of energy offset implied by the configuration of the nuclear spins can cause that some reactions appear to be dependent on the nuclear spin states: for example the thermoneutral reaction

$$N^+ + H_2(j) \rightarrow NH^+ + H \tag{0.10}$$

has the rate coefficient, which is three orders of magnitude larger for the rotational states $j = 1$ (with total nuclear spin $S = 1$) than for $j = 0$ ($S = 0$) at the kinetic temperature 11 K (chapter 9.2 and Attachment A.1). In ISM, the reaction (0.10) is followed by chain of hydrogen atom abstractions terminated by the dissociative recombination of NH_4^+ resulting in the formation of ammonia.

Another example of the influence of the internal energy of H_2 on a chemical composition in ISM is a chain of deuteration reactions:

$$H_3^+ + HD \leftrightarrow H_2D^+ + H_2 \tag{0.11}$$
$$H_2D^+ + HD \leftrightarrow D_2H^+ + H_2 \tag{0.12}$$
$$D_2H^+ + HD \leftrightarrow D_3^+ + H_2\,. \tag{0.13}$$

The reverse flow of the reactions (0.13)→(0.11) is hindered by energetic barriers of about 200 K, so if H_2 molecules are in the ground ($j = 0$) state, the process of deuteration is very rapid Pagani et al. [2009]). The situation changes dramatically if H_2 in the $j = 1$ state with internal energy equivalent to 170 K is introduced to this reaction system: the population of H_3^+ is enhanced at the expense of H_2D^+, as we have observed during the studies of reactions (0.7) and (0.8) (see chapter 11).

One of the ways how H_3^+ and H_2 ions can convert the nuclear spin states (labelled as S) in the gas phase is

$$H_3^+(S) + H_2(\tilde{S}) \leftrightarrow H_3^+(S') + H_2(\tilde{S}'). \tag{0.14}$$

The rate coefficient of this process depends on the combination S–$\tilde{S}$ and on the temperature, in which this reaction was studied (section 12.2.2 and Attachment B.1).

Organisation of contents

The content of the thesis is organised as follows: The text is divided to three parts. The first one (**Part I**) summarises the theoretical knowledge needed to understand the topic of the research.

The **Part II** gathers the minimum of information about employed experimental techniques plus specific topics I was concerned. This part also includes a thorough description of the para-hydrogen generator (chapter 5) I co-designed[1] and constructed.

[1]Special acknowledgement to colleague Mojmír Jílek.

The **Part III** deals with results of our experiments. Readers who are interested in detailed description may refer to the articles in the Attachments, others can have a short tour prepared in sections 10–12.4. This part also includes a description of determination of abundance of para-H_2 in a para-states-enriched hydrogen gas produced by the para-hydrogen generator (chapter 9).

This thesis could not contain everything I have done during my studies. Measurements of the recombination of D_3^+ ions with electrons are only mentioned at several places. The main reason is that it was not possible to determine the state-specific rate coefficients, which was the topic of my primary interest in the last several years. The other untouched topics are modification of the SA-CRDS apparatus for temperatures < 77 K or creation of own software for modelling of chemical kinetics. Despite these cuts in a number of topics, the text in your hand is rich in content. I wish you pleasant reading.

Goals of the thesis

This thesis deals with temperature-dependence studies of following reactions:

$$\begin{aligned} H^+ + H_2 &\rightarrow H_3^+ + h\nu\,, \\ H^+ + 2H_2 &\rightarrow H_3^+ + H_2\,, \\ N^+ + H_2 &\rightarrow NH^+ + H\,, \\ H_3^+ + e^- &\rightarrow \text{neutral products}, \\ H_3^+ + e^- + He &\rightarrow \text{neutral products} + He \end{aligned}$$

in gas (or plasma) phase. We study dependence of rate coefficients of these reactions on population of nuclear spin states of H_2 or H_3^+, or on population of fine structure states of N^+ ions.

The association of H^+ with H_2 is studied by an ion-trapping technique at temperatures 11–50 K. The reaction of N^+ with H_2 is scrutinised using the ion-trap at temperatures 11–100 K.

The H_3^+-e^- recombination is examined in the afterglow plasma. Main diagnostic methods are the Langmuir probe diagnostics and the Cavity Ring-Down Spectroscopy (CRDS). The kinetic temperatures of the reactants are set in the range 55–300 K. Special attention is payed to a rotational temperature of H_3^+ ions.

Part I

Theoretical background

1. Quantum structure of H_2 and H_3^+

1.1 Para/normal-hydrogen

The wave function of H_2 molecule associated with the total angular momentum can be written as a product of wave functions associated with the nuclear spin (Ψ_S) and with the rotation molecular angular momentum (Ψ_J):

$$\Psi = \Psi_J \Psi_S \,. \tag{1.1}$$

This can be done because of weak spin-rotation interactions.

Ψ must be antisymmetric to the permutation operation $\mathcal{P}$ because protons are fermions and they obey the Fermi-Dirac statistics. Since the rotation wave function Ψ_J can be either symmetric or antisymmetric, Ψ_S is antisymmetric if Ψ_J is symmetric, and symmetric if Ψ_J is antisymmetric. The symmetric state Ψ_S (ortho) has a spin degeneracy of three and corresponding nuclear spin wave functions are $|\uparrow\uparrow\rangle$, $1/\sqrt{2}(|\uparrow\downarrow\rangle + |\downarrow\uparrow\rangle)$ and $|\downarrow\downarrow\rangle$. The antisymmetric state (para) is the singlet state with the corresponding wave function $-1/\sqrt{2}(|\uparrow\downarrow\rangle - |\downarrow\uparrow\rangle)$.

As a consequence of these symmetry restrictions the following coupling of the total nuclear spin (S) and the total rotation angular momentum (J) exists:

para-states $S = 0,\ J = 0, 2, 4, \ldots,$

ortho-states $S = 1,\ J = 1, 3, 5, \ldots$

Then the degeneracy of energetic levels is

$$g(L) = (2S+1)(2J+1) = \begin{cases} 2J+1 & J = 0, 2, \ldots, \\ 3(2J+1) & J = 1, 3 \ldots \end{cases} \tag{1.2}$$

and the partition function for the spin isomer is, under the rigid rotor approximation and TDE (thermodynamic equilibrium) at temperature T,

$$Q_{\text{para, ortho}} = \sum_J g(J) \exp\left(-\frac{E_J}{k_\text{B} T}\right) = \sum_J g(J) \exp\left(-\frac{J(J+1)\hbar^2}{2 I k_\text{B} T}\right), \tag{1.3}$$

where J is even for para-hydrogen, odd for ortho-hydrogen, I is the moment of inertia.

Such separation into two ensembles distinguished by the nuclear spin state is possible because the conversion para↔ortho nuclear spin states is forbidden. At high temperatures when all rotational levels are equally populated $Q_\text{para} : Q_\text{ortho} = 1 : 3$, if TDE is established. It means that at the room temperature, population of ortho states ${}^\text{o}f_2 = 0.75$ and population of para states ${}^\text{p}f_2 = 0.25$ – such hydrogen gas is called normal-H_2 (marked as ${}^\text{n}H_2$ here). In this work, any hydrogen gas with population of ortho states $< 75\%$ is called para-states-enriched H_2 (${}^\text{e}H_2$). Para-H_2 (${}^\text{p}H_2$) is H_2 gas with ${}^\text{p}f_2 = 1$. Dependence of ${}^\text{p}f_2$ and ${}^\text{o}f_2$ on the temperature at TDE is plotted in figure 1.1.

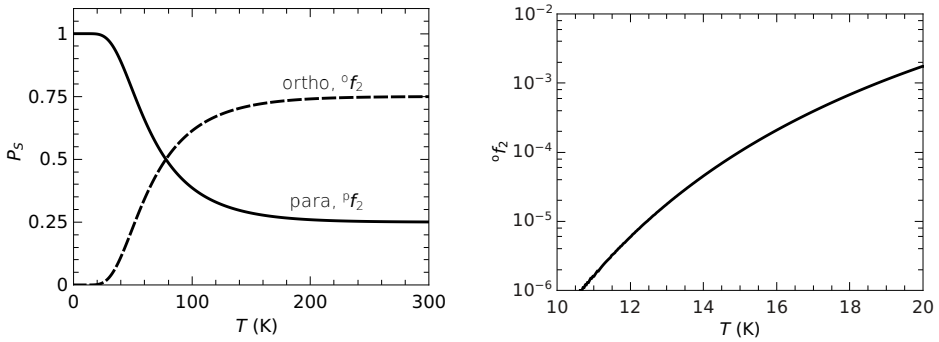

(a) $^{p}f_2$ and $^{o}f_2$ (b) $^{o}f_2$

Figure 1.1: Dependence of thermal population of para- and ortho- states of H_2 ($^{p}f_2$ and $^{o}f_2$, respectively) on temperature

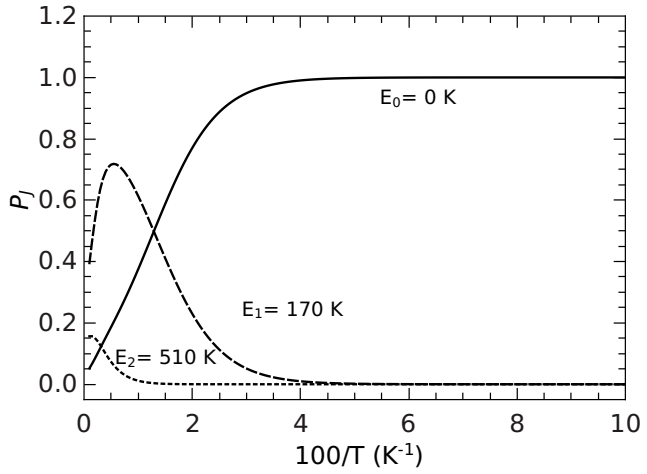

Figure 1.2: Dependence of thermal distribution of the three lowest rotational states of H_2 on temperature. E_J is the energy level corresponding to the state J (the value above the ground level).

The energy difference between the two lowest rotational states ($J = 0$, 1) of the ground vibronic state, each corresponding to the different nuclear spin state, is

$$\frac{E_{J=1} - E_{J=0}}{k_{\mathrm{B}}} \approx 170\,\mathrm{K}\,. \tag{1.4}$$

A dependence of distribution of the three lowest rotational levels on temperature for H_2 with thermal distribution of nuclear spin states is in figure 1.2.

1.2 para/ortho-H_3^+

Like in the case of H_2, the total wave function of H_3^+ ion Ψ can be considered as the product of separate electronic (Ψ_{e}), rotation-vibration (Ψ_{rv}), and nuclear spin (Ψ_S) wave functions

$$\Psi = \Psi_{\mathrm{e}}\Psi_{\mathrm{rv}}\Psi_S \tag{1.5}$$

because of weak spin-rotation and spin-spin interactions within the ion.

S_3	E	3(12)	2(123)
A_1	1	1	1
A_2	1	−1	1
E	2	0	−1

$\underbrace{\qquad\qquad}_{\mathcal{A}}$

$\otimes$

E^*	E	E^*
A'	1	1
A''	1	−1

$=$

S_3^*	E	3(12)	2(123)	E^*	$3(12)^*$	$2(123)^*$
A_1'						
A_2'		$\mathcal{A}$			$\mathcal{A}$	
E'						
A_1''						
A_2''		$\mathcal{A}$			$-\mathcal{A}$	
E''						

Table 1.1: Character tables of $S_3^* = S_3 \otimes E^*$ [McCall, 2001]. The permutation group S_3 is formed by 6 symmetry operations: identity operation, three permutations of two protons (12), two cyclic permutations of three protons. $\mathcal{A}$ is the interpretation of the table as the matrix.

H_3^+ has both permutation and inversion symmetries so its wave functions must be described by the permutation-inversion group $S_3^* = S_3 \otimes E^*$. The character tables of these groups are written in table 1.1 [McCall, 2001]. The representation Γ of the total wave function is the direct product of representations of the partial wave functions from equation (1.5): $\Gamma = \Gamma_\mathrm{e} \otimes \Gamma_\mathrm{rv} \otimes \Gamma_S$. Γ must be A_2' or A_2'' because of Pauli principle (protons are fermions).

It can be shown that if H_3^+ is in the ground electronic state, $\Gamma_\mathrm{e} = A_1'$ [see references in McCall, 2001]. This implies that

$$\Gamma_\mathrm{rv} \otimes \Gamma_S \subset A_2' \text{ or } A_2'' \,. \tag{1.6}$$

There are 2^3 combinations of $|\uparrow\rangle$ and $|\downarrow\rangle$ wave functions forming the total nuclear spin wave function Ψ_S. These wave functions form the basis of the reducible representation $4A_1' \oplus 2E'$ of the S_3^* group (use the operations from table 1.1 to derive). The A_1' representation corresponds to the ortho spin configuration (with all three spins aligned), and E' corresponds to the para configuration (with one spin antiparallel to the other two). Since $\Gamma_\mathrm{rv} \otimes \Gamma_S \subset A_2'$ or A_2'', if $\Gamma_S = A_1'$ (ortho), the rovibrational symmetry must be $\Gamma_\mathrm{rv} \in \{A_2', A_2''\}$. If $\Gamma_S = E'$ (para), $\Gamma_\mathrm{rv} \in \{E', E''\}$. Like in case of H_2 (in section 1.1), here we have unique coupling of nuclear spin states with rovibrational states.

Now we must find, which rovibrational states are represented by wave functions with aforementioned symmetries.

1.2.1 "Motional" quantum numbers of H_3^+ ions

In the following text, I will not derive Ψ_rv but just simply conclude the approach leading to the derivation and its results. More about the topic can be found in the work by McCall [2001].

For any molecule, the only truly rigorous quantum numbers are the total angular momentum (F) and the parity ($\pm$), which arise from isotropy and inversion symmetry of space, not from the properties of the molecule. Because of same arguments as used in definition of total wave function (1.1), the total angular momentum F can be decomposed to the nuclear spin angular momentum S and the "motional" angular momentum J. S, J and $\pm$ are the only good quantum numbers for H_3^+ at arbitrarily high energies.

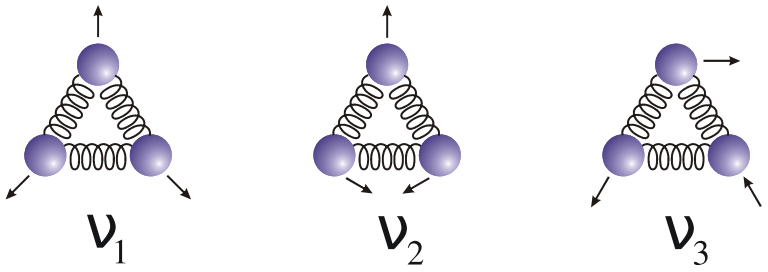

Figure 1.3: Schematic representation of the vibrational modes of H_3^+. The symmetric "breathing" mode ν_1. The ν_2 mode is doubly degenerated and has a bending mode ν_{2x} a symmetric stretch ν_{2y} mode. Adopted from Varju [2011, p. 17].

H_3^+ ions in its ground state has the form of an equilateral triangle with an average bond length of 0.85 Å [Carney and Porter, 1974]. Its symmetry can be described by the point group C_{3v} [see Bishop, 1973, p. 282 for the point group]. Such ion has several vibrational modes depicted in figure 1.3. The symmetric breathing mode is infrared inactive because it does not generate any dipole moment. The degenerate mode ν_2 (labeled as $v_2\nu_2^l$) possesses vibrational angular momentum l. For v_2 quanta of ν_2, l can have values $-v_2, -v_2 + 2, \ldots v_2 - 2, v_2$. If we define the quantum number k to express a projection of J to the molecular axis, we obtain a quantum number $G = |k - l|$ used often for H_3^+ ion. $G = k$ for the vibrational ground state.

For our purpose, now we have enough quantum numbers, which allow us to formulate Ψ_{rv} of the ground vibrational level as $|J, G\rangle$. Among them, the wave functions with $G = 3n$ correspond to rovibrational symmetry A_2, and $G = 3n \pm 1$ corresponds to E (n is a natural number). Hence, we have the following correspondence between nuclear spin and the G quantum number:

ortho $\Leftrightarrow G = 3n$,

para $\Leftrightarrow G = 3n \pm 1$.

$|J = 0, G = 0\rangle$ corresponds to the rovibrational symmetry A_1, which does not satisfy the condition given by (1.6). Some energy levels of these states are plotted in figure 1.4.

The spontaneous nuclear spin transition is forbidden like in the case of H_2, i.e. $\Delta S = 0$. This corresponds with the another selection rule $\Delta g = k - l = 3n$ (only transitions in one nuclear spin manifold are allowed). The other selection rules can be found in Lindsay and McCall [2001]; McNab [2007]; Ramanlal [2005]; Watson [1984]

In this work the H_3^+ quantum states and transitions are labeled according to the scheme proposed by McCall [2001]. Energy levels are written in the form

$$(J, G)\{u|l\}v_1\nu_1 + v_2\nu_2^{|l|}\,. \tag{1.7}$$

For the states that have the same G but different k and l (i.e. they form an l resonance pair), the symbols u and l are used to distinguish if the level is the upper or lower of this l resonance pair, respectively. Transitions are written in the form

$$^{[n|t]}\{\mathrm{P}|\mathrm{Q}|\mathrm{R}\}(J, G)^{[u|l]}_{[u|l]}v_1\nu_1 + v_2\nu_2^{|l|} \leftarrow 0\,, \tag{1.8}$$

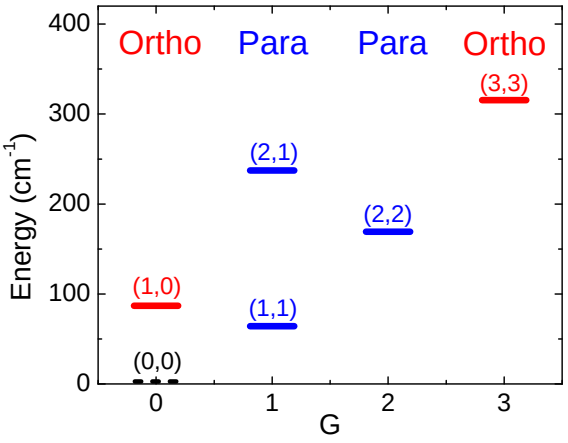

Figure 1.4: The lowest rotational energy levels (J, G) of the ground vibrational state of H_3^+. (0,0) state is forbidden. Copied from Hejduk et al. [2012a].

where PQR is the common $\Delta J = \{-1|0|1\}$ notation, respectively. The $[n|t]$ superscript indicates, whether $\Delta g = -3$ or 3, respectively. (J, G) belongs to the lower state here. The u and l superscript and subscript designate the position of the upper and lower level in the l resonance pair, respectively.

1.2.2 Nuclear spin conversion of H_3^+

The nuclear spin conversion of H_3^+ can proceed in collision with H_2 via formation of intermediate $(H_5^+)^*$ complex:

$$H_3^+(S) + H_2(\tilde{S}) \rightarrow (H_5^+)^* \rightarrow H_3^+(S') + H_2(\tilde{S}'). \tag{1.9}$$

The nuclear spin selection rules imposed by the symmetries of the reactants and the products apply here. These were formulated by Quack [1977], who used permutation-inversion groups (same as in the section 1.2.1). This approach was later replaced with more straightforward angular momentum algebra, the approach using the rotation group representation of the nuclear spin angular momenta, described by Oka [2004]. A simple application of these group algebras assumes full scrambling of the nuclear spins in the $(H_5^+)^*$ intermediate complex. In such case, no energy restrictions are considered, therefore we call this statistical interpretation "the high temperature model". Both algebras provide same nuclear spin statistical weights for the products written in table 1.2.

It was questioned by experiments [Cordonnier et al., 2000; Gerlich, 1993] whether the proton scrambling is generally complete. We can define three statistical reaction pathways to formulate how the incomplete scrambling may work:

$$\begin{aligned} \tilde{H}_3^+ + H_2 &\rightarrow \tilde{H}_3^+ + H_2\,, && (1.10)\\ &\rightarrow H_2\tilde{H}^+ + \tilde{H}_2\,, && (1.11)\\ &\rightarrow H\tilde{H}_2^+ + H\tilde{H}\,, && (1.12) \end{aligned}$$

(H_3^+,H_2)	Weight	(o,o)	(o,p)	(p,o)	(p,p)
(o,o)	12	37/5	1	14/5	4/5
(o,p)	4	1	1	2	0
(p,o)	12	14/5	2	28/5	8/5
(p,p)	4	4/5	0	8/5	8/5

Table 1.2: The nuclear spin statistical weights for the $H_3^+ + H_2$ reaction. The table rows correspond to the nuclear spin configuration of reactant (H_3^+,H_2) pairs (written in terms para/p/ and ortho/o/), and the table columns correspond to the product pairs.

where (1.10), (1.11), (1.12) are the identity, proton hop and hydrogen exchange pathways, respectively. There is no experimental measurement of the probabilities of these pathways. Crabtree et al. [2011a,b] have performed absorption spectroscopy measurements in H_2 discharge, but they did not obtain useful results because [H_2] was high ($\sim 10^{17}$ cm^{-3}) and they had to consider one more scrambling mechanism via $(H_5^+ + H_2)^*$ complex. Their comparison with results from microcanonical statistical calculations for low temperatures [Park and Light, 2007] did not confirm correctness of these calculations.

The nuclear spin statistic weights were calculated also by Eaker and Schatz [1986]; Gerlich et al. [2006]. Hugo et al. [2009] have approached to the theoretical description in the similar way as Park and Light [2007]. They applied their calculations to interpretation of their measurements of H_3^+/H_2D^+ fractionation in a terrestrial H_2/HD mixture at temperatures approximately 10–300 K , but they did not study the processes (1.11) and (1.12) in-situ. Later the group Grussie et al. [2012] performed measurements of steady state distribution of H_3^+ ions' nuclear spin states in thermal mixtures of $^pH_2$ and $^oH_2$ at temperatures 46–93 K using radiofrequency linear multipole trap: the obtained distribution was thermal. They estimate that H_3^+ undergoes 60 collisions prior to the measurement of the distribution by the laser induced reaction

$$H_3^+(v_1 + v_2 > 1) + Ar \rightarrow ArH^+ + H \tag{1.13}$$

in their experiment.

2. Formation of ${}^{\mathrm{p}}H_3^+$ and ${}^{\mathrm{o}}H_3^+$

In the gas phase or in the plasma, H_3^+ ions are effectively formed by the exothermic reaction (0.2)

$$ {}^{\mathrm{p,o}}H_2{}^+ + {}^{\mathrm{p,o}}H_2 \rightarrow {}^{\mathrm{p,o}}H_3^+ + H\,. \tag{2.1} $$

where superscript p (o) denote the para (ortho) nuclear spin state. Again, using the symmetry group algebra, one can obtain nuclear spin statistic weight written in table 2.1. Due to the exothermicity of the reaction, this description is used even for low temperature in this work.

Using the statistics from table 2.1, one can define a so called nascent fraction of ${}^{\mathrm{p}}H_3^+$

$$ {}^{\mathrm{p}}f_3 = \frac{2}{3}\,{}^{\mathrm{p}}f_2 + \frac{1}{3} \tag{2.2} $$

resulting from reaction (2.1). Note that ${}^{\mathrm{p}}f_3 = 0.5$ if ${}^{\mathrm{p}}f_2 = 0.25$, which are the values corresponding to TDE at the room temperature.

In this work one more exothermic reaction is used to produce H_3^+:

$$ ArH^+ + {}^{\mathrm{p,o}}H_2 \rightarrow {}^{\mathrm{p,o}}H_3^+ + Ar\,. \tag{2.3} $$

The nuclear spin statistic weights can be calculated using angular momentum algebra: the reaction can be rewritten as

$$ \mathcal{D}_{1/2} \otimes (\mathcal{D}_1 \oplus \mathcal{D}_0) \rightarrow \mathcal{D}_{3/2} \oplus 2\mathcal{D}_{1/2}\,, \tag{2.4} $$

where subscripts indicate the nuclear spin. The spin relation for the reaction

$$ ArH^+ + {}^{\mathrm{o}}H_2 \tag{2.5} $$

can be rewritten as

$$ \mathcal{D}_{1/2} \otimes \mathcal{D}_1 \rightarrow 4(\mathcal{D}_{3/2}/4) \oplus 2(\mathcal{D}_{1/2}/2)\,, \tag{2.6} $$

where the formula for the direct product

$$ \mathcal{D}_{I_1} \otimes \mathcal{D}_{I_2} = \mathcal{D}_{I_1+I_2} \oplus \mathcal{D}_{I_1+I_2-1} \oplus \cdots \oplus \mathcal{D}_{|I_1-I_2|} \tag{2.7} $$

$(H_2{}^+, H_2)$	Weight	o	p
(o,o)	9	6	3
(o,p)	3	1	2
(p,o)	3	1	2
(p,p)	1	0	1

Table 2.1: The nuclear spin statistical weights for the reaction $H_2{}^+ + H_2 \rightarrow H_3^+ + H$. The table rows correspond to the nuclear spin configuration of reactant ($H_2{}^+$,H_2) pairs (written in terms para/p/ and ortho/o/), and the table columns correspond to the product H_3^+. [Cordonnier et al., 2000; Oka, 2004].

(H_2)	Weight	o	p
o	6	4	2
p	2	0	2

Table 2.2: The nuclear spin statistical weights for the reaction $ArH^+ + H_2 \rightarrow H_3^+ + Ar$. The table rows correspond to the nuclear spin configuration of H_2 (written in terms para/p/ and ortho/o/), and the table columns correspond to the product H_3^+.

is used [Oka, 2004]. The terms in the right hand side of (2.6) are normalised to the statistical weight of the nuclear spin state $(2S + 1)$ [Widicus Weaver et al., 2009]. Hence we will get the branching ratio ${}^{o}H_3^+$:${}^{p}H_3^+$ of 4:2 for reaction (2.5).

The reaction $ArH^+ + {}^{p}H_2$ yields only ${}^{p}H_3^+$ according to the relation

$$\mathcal{D}_{1/2} \otimes \mathcal{D}_0 \rightarrow 2(\mathcal{D}_{1/2}/2)\,. \tag{2.8}$$

The results are concluded in table 2.2. We can also formulate the dependence of ${}^{p}f_3$ resulting from the reaction (2.3) on ${}^{p}f_2$:

$${}^{p}f_3{}' = \frac{2}{3}\,{}^{p}f_2 + \frac{1}{3}\,, \tag{2.9}$$

which is same as (2.2). This expression can be interpreted also in the way that "${}^{p}f_3{}'$ fraction of ArH^+ ions forms ${}^{p}H_3^+$ and $(1 - {}^{p}f_3{}')$ fraction forms ${}^{o}H_3^+$" [Grussie et al., 2012].

2.1 $H^+ + H_2$ association

According to Gerlich and Horning [1992], the overall association reaction

$$H^+ + H_2 \xrightarrow{k^*} H_3^+ \tag{2.10}$$

is usually described by an apparent second order rate coefficient k^*. This process is often considered to proceed in two independent stages: metastable complex formation (with the rate coefficient k_c)

$$H^+ + H_2 \xrightarrow{k_c} (H_3^+)^* \tag{2.11}$$

and stabilisation, either via emission of a photon

$$(H_3^+)^* \xrightarrow{\tau_r} H_3^+ + h\nu \tag{2.12}$$

or by stabilising collisions with neutral molecule, for example H_2,

$$(H_3^+)^* + H_2 \xrightarrow{k_{H_2}} H_3^+ + H_2\,. \tag{2.13}$$

However, more often the complex redissociates

$$(H_3^+)^* \xrightarrow{\tau_{dis}} H^+ + H_2\,. \tag{2.14}$$

The collisional stabilisation rate with a third body H_2 is written as

$$\frac{1}{\tau_{H_2}} = k_{H_2}[H_2]\,, \tag{2.15}$$

where k_{H_2} is the rate coefficient for stabilising $(H_3^+)^*$ by collision with H_2 related to the Langevin rate coefficient k_L:

$$k_{H_2} = k_L f_{H_2} \tag{2.16}$$

where f_{H_2} is the stabilisation efficiency factor. Then the coefficient k^* can be approximated as

$$k^* = k_c \frac{1/\tau_{H_2} + 1/\tau_r}{1/\tau_{dis} + 1/\tau_{H_2} + 1/\tau_r}. \tag{2.17}$$

At low densities of H_2 and if $\tau_{dis} \ll \tau_r$ the preceding formula is transformed to

$$k^* = k_c(\tau_{dis} k_{H_2}[H_2] + \frac{\tau_{dis}}{\tau_r}) = \underbrace{k_c \tau_{dis} k_{H_2}}_{k_3}[H_2] + \underbrace{k_c \tau_{dis}/\tau_r}_{k_r}\,. \tag{2.18}$$

The coefficient k_r is the rate coefficient for the radiative channel (2.12), k_3 is the rate coefficient for the ternary channel (2.14).

Until 2013, no experimental study of the process (2.10) was performed at kinetic temperatures < 80 K with thermal distribution of nuclear spin states (see table 1 in Attachment A.2). From the theoretical point of view, only separate calculations of k_c, τ_{dis} and τ_r were available for long time Gerlich and Horning [1992] and just recently quantum mechanical numerical calculations of $H^+ + H_2$ collision system were performed [Honvault et al., 2011a,b, 2012]. The cross sections calculated for ortho-para transitions at millielectronvolt translational energies show a resonance structure [see figure 1 in Honvault et al., 2011a]. Depending on experimental conditions, $(H_3^+)^*$ ions from (2.11) may be produced in highly excited states with energies up to 3000 cm^{-1} above the dissociation limit [Carrington et al., 1993] and with microsecond lifetimes – such long-lived resonances can be expected to be responsible for the radiative association (2.12).

As far as the ternary association channel is concerned, in most statistical model calculations, the lifetime of a $(H_3^+)^*$ complex

$$\tau_{dis} \propto T^{l/2+\delta} \tag{2.19}$$

where l is the number of active rotational degrees of freedom in the separated reactants and δ is used to account for the temperature dependence of the stabilisation efficiency f_{H_2} [Gerlich and Horning, 1992]. However, at temperatures ~ 10 K, only few resonances are populated and not every can contribute to the ternary association, therefore the adequateness of the statistical approach is questionable (see more details in the Discussion of Attachment A.2 and section 11.1).

2.1

3. Destruction of H_3^+

3.1 Reactions of H_3^+ with molecules

3.1.1 H_5^+ formation

H_5^+ ions are formed at high [H_2] and [He] via

$$H_3^+ + H_2 \quad +H_2 \quad \underset{k_B}{\overset{k_F}{\rightleftharpoons}} H_5^+ + H_2\,, \tag{3.1}$$

$$+He \quad \underset{k_B}{\overset{k_F}{\rightleftharpoons}} H_5^+ + He\,. \tag{3.2}$$

The mechanism of the process (3.1) was studied at kinetic temperature $T_{Kin} = 10$ K in detail by Paul et al. [1995] and at temperatures above 135 K by Johnsen et al. [1976] and Hiraoka and Kebarle [1975]. The knowledge about process (3.2) is little bit sparse but the reaction has been observed by our group [see Glosík et al., 2003; Plašil et al., 2002, and references therein]. The rate coefficients k_F for both processes are of the order $\sim 10^{-29}$ cm^6 s^{-1} at 300 K and in the case of (3.1), k_F rises up to $\sim 10^{-28}$ cm^6 s^{-1} as temperature decreases down to 10 K Paul et al. [1995]. The rate coefficients for collision induced dissociation k_B were shown to decrease with decreasing temperature in aforementioned works ($k_B \sim 10^{-16}$ cm^{3}s^{-1} at 10 K). Formation of H_5^+ ions becomes a dominant H_3^+-loss process for example if $n_e/[H_2] \lesssim 10^{-4}$ and [He] $\sim 10^{17}$ cm^{-3} (typical He number density in afterglow experiments in chapter 12) at low temperatures.

A strong nuclear-spin dependence was observed for reaction (3.1) at 10 K [Paul et al., 1995]. At this temperature, the coefficient k_F is four times higher in $^pH_2$ than in $^nH_2$ (and the reverse reaction does not almost proceed: $k_B \sim 10^{-16}$ cm^{3}s^{-1}). This effect is explained to be caused by availability of the internal rotational energy from equation (1.4) that destabilises produced hydrogen clusters in the case of the $^oH_2$ reactant. If this is true, it means that proton scrambling is efficient in intermediate clusters

$$(H_3^+ + H_2 + H_2) \leftrightarrow (H_7^+)^*$$

and their re-dissociation obeys nuclear spin selection rules [Crabtree et al., 2011b].

3.1.2 Hydrogen-deuterium exchange

H_3^+ cation in ISM acts as a vector dragging the deuterium from its reservoir and spreading it further, directly or indirectly, to other species [Hugo et al., 2009]:

$$H_3^+ + HD \quad \leftrightarrow \quad H_2D^+ + H_2 + 232\,\text{K} \tag{3.3}$$

$$H_2D^+ + HD \quad \leftrightarrow \quad D_2H^+ + H_2 + 187\,\text{K} \tag{3.4}$$

$$D_2H^+ + HD \quad \leftrightarrow \quad D_3^+ + H_2 + 234\,\text{K}. \tag{3.5}$$

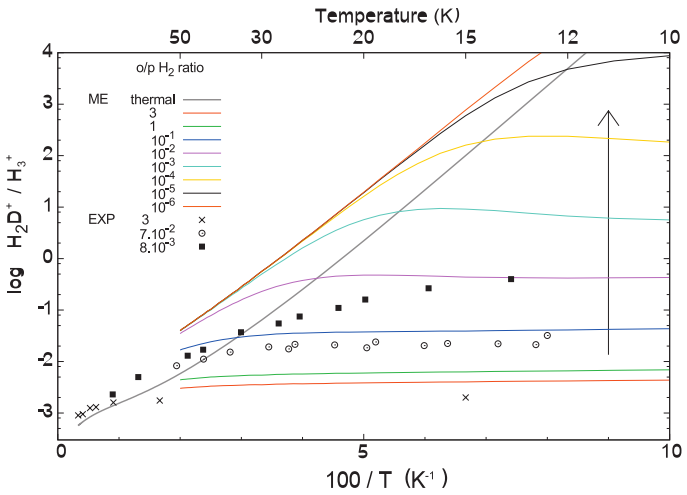

Figure 3.1: Steady-state H_2D^+/H_3^+ isotopic fractionation in a H_2 environment with terrestrial hydrogen deuteride abundance $HD/H_2 = 3.2 \times 10^{-4}$. The solid lines are results of the theoretical calculations. The arrow indicates a decreasing o/p ratio of H_2. The points are experimental results EXP of ${}^{o}f_2$:${}^{p}f_2$ ratios 3, 7×10^{-2}, and 8×10^{-3}. Copied from Hugo et al. [2009]

As can be seen here, the backward reaction are endothermic with written energy barriers (when considering only the ground level for each species) [Pagani et al., 2009]. The reactions above are promoted by differences between zero-point vibrational energies of the species on both sides of the reactions. The backward and forward rate coefficients vary with the nuclear spin states of H_2D^+, H_3^+ and H_2 (see table 8 of Hugo et al. [2009]).

The energy barrier of 232 K in the reaction (3.3) is close to (1.4). Therefore ratio $H_2D^+ : H_3^+$ can act as a meter of ${}^{p}H_2$ population (${}^{p}f_2$) as it is illustrated in figure 3.1.

3.2 Recombination with electrons

This work deals with studies of the recombination of H_3^+ ions with electrons in plasma. Generally, if H_3^+ ions are dominant, i.e. $[H_3^+] \approx n_e$, and if there is no ionisation process taking place (for example if a discharge generating the plasma is switched off) the number density of electrons n_e decreases in time due to loss processes according to

$$\frac{\mathrm{d}n_e}{\mathrm{d}t} = -\alpha_{\mathrm{eff}} n_e^2 - \frac{n_e}{\tau}\,, \tag{3.6}$$

where α_{eff} is the recombination rate coefficient and τ is the characteristic time of diffusion-like processes. The analytic solution of this is

$$n_e(t) = \frac{n_0}{\alpha_{\mathrm{eff}} \tau n_0 (\exp(t/\tau) - 1) + \exp(t/\tau)}\,, \tag{3.7}$$

where n_0 is an initial electron number density at $t = 0$.

The value of effective recombination rate coefficient α_{eff} consists of contributions from the binary recombination process and several different ternary

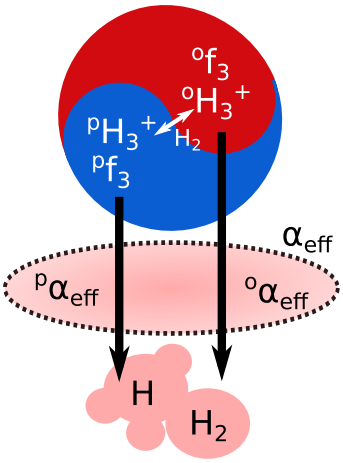

Figure 3.2: Scheme of recombination of nuclear spin manifolds. See the text for a commentary.

processes, which can be added together in the first approximation:

$$\alpha_{\mathrm{eff}} = \alpha_{\mathrm{bin}} + \sum_{\mathrm{X}} K_{\mathrm{X}}[\mathrm{X}], . \tag{3.8}$$

The coefficient α_{bin} corresponds to purely binary H_3^+-e^- recombination. K_{X} corresponds to the ternary recombination process assisted or enhanced by a particle X, which may be e^-, He, H_2 or other neutral. This prescription does not indicate that all ternary processes are of the same nature. The linear addition of binary and ternary recombination rate coefficients implied here is valid only when the two recombination mechanisms occur in parallel, but not when binary and ternary recombination share the same "finite resource", for instance, an intermediate excited state that is formed by electron capture [Johnsen et al., 2013].

If the rate of para↔ortho conversion of H_3^+ ions in collision with H_2 (with the rate coefficient k_{po}, see section 1.2.2) is larger than the rate of recombination (i.e. $k_{\mathrm{po}}[H_2] \gg \alpha_{\mathrm{eff}} n_{\mathrm{e}}$), the population of $^{\mathrm{p}}H_3^+$ ions does not vary in time ($^{\mathrm{p}}f_3 = \mathrm{const.}$) and therefore we can separate α_{eff} to nuclear-spin-state-specific parts

$$\alpha_{\mathrm{eff}} = {}^{\mathrm{p}}f_3\,{}^{\mathrm{p}}\alpha_{\mathrm{eff}} + {}^{\mathrm{o}}f_3\,{}^{\mathrm{o}}\alpha_{\mathrm{eff}}\,, \tag{3.9}$$

where $^{\mathrm{p}}\alpha_{\mathrm{eff}}$ and $^{\mathrm{o}}\alpha_{\mathrm{eff}}$ can be described by formula (3.8) for each of them separately (see the illustrated explanation in figure 3.2).

In following sections, I describe processes corresponding to the terms in right hand side of (3.8).

3.2.1 Binary recombination

Until the end of the previous millennium, a number of mutually inconsistent experiments regarding dissociative recombination (DR)

$$H_3^+ + e^- \xrightarrow{\alpha_{\mathrm{bin}}} \begin{cases} H_2 + H \\ 3\,H \end{cases} \tag{3.10}$$

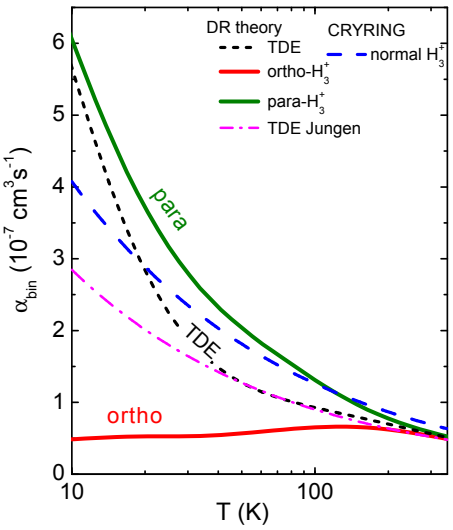

Figure 3.3: Dependence of binary recombination rate coefficient on temperature predicted by theory [Floresca dos Santos et al., 2007]. The values marked as "TDE Jungen" are thermal values computed from the energy dependent recombination rate coefficients published by Pratt and Jungen [2011]. Values for $^{n}H_2$ from CRYRING measurements [McCall et al., 2004] are also included.

was carried out Adams et al. [1984]; Amano [1990]; Johnsen [2005]; Larsson and Orel [2008]; Laubé et al. [1998]; Leu et al. [1973]; Oka [2000]; Plašil et al. [2002]; Smith and Španěl [1993] and no unifying theoretical explanation was present. This has changed recently when cross sections obtained at a storage ring Kreckel et al. [2005]; McCall et al. [2003]; Petrignani et al. [2009]; Tom et al. [2009b] and theoretical values (calculated by going beyond the Born-Oppenheimer approximation and accounting for Jahn-Teller coupling Floresca dos Santos et al. [2007]; Kokoouline and Greene [2003]; Kokoouline et al. [2001]; Pagani et al. [2009]) started approaching each other.

The theory [Floresca dos Santos et al., 2007] predicts different values of α_{bin} for different nuclear spin states of H_3^+ at temperatures < 200 K ($^{p}\alpha_{\mathrm{bin}}$ for $^{p}H_3^+$, $^{o}\alpha_{\mathrm{bin}}$ for $^{o}H_3^+$, see figure 3.3). The qualitative reason is that, at small collisional energies, there are more Rydberg resonances of the neutral para-H_3 that can be populated during the electron-ion collisions. It is because there are more low energy rotational states of the ground vibrational states of $^{p}H_3^+$, for example (2,2) and (2,1) (corresponding to energy of ≈ 151 and 249 K). For $^{o}H_3^+$, the lowest rotational states of the ground vibrational state have relatively higher energies [for example, (3,0) corresponds to ≈ 650 K]. More Rydberg resonances in $^{p}H_3^+$ enhances DR cross sections in $^{p}H_3^+$ more than in $^{o}H_3^+$ at low temperatures (< 200 K).

The aforementioned storage ring experiments, however, succeeded to confirm different recombination cross sections for para and ortho nuclear spin states of the ion only qualitatively. Quantitative difference between the theory and the experiments appeared later to be caused by the fact that rotational temperatures were much higher Petrignani et al. [2011] than those previously stated. Any further study about the recombination of H_3^+ has to show how well the internal temperature (population of internal states) is determined first, as it is done in this work (section 12.2.2 and Attachment B.1).

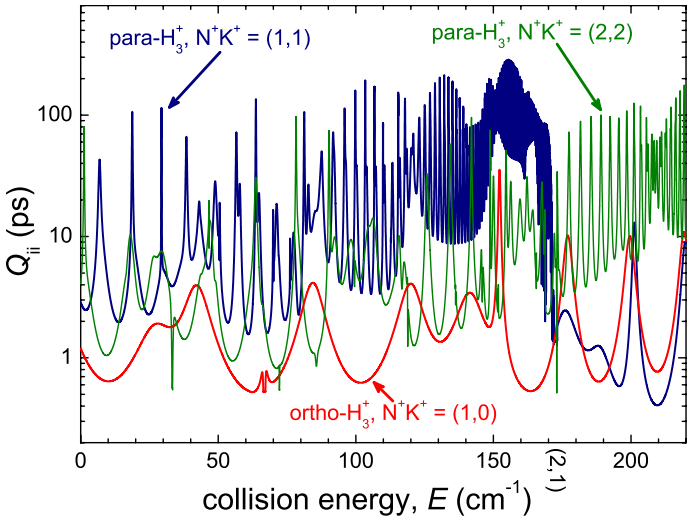

Figure 3.4: Diagonal elements of a so called lifetime matrix [Glosík et al., 2009] for three lowest incident channels – (1,1), (1,0) and (2,2) – for the $e^- + H_3^+$ collisions. The lifetime of a resonance is given by the value at the peak divided by 4, if only one channel is open. Note the difference between the values for ${}^pH_3^+$ and for ${}^oH_3^+$. Reprinted from [Glosík et al., 2009].

3.2.2 Ternary He-assisted recombination

While the theories [Floresca dos Santos et al., 2007; Pratt and Jungen, 2011] succeeded to interpret storage ring measurements to certain extent, there was no interpretation of haphazard ensemble of rate coefficients from the plasmatic experiments that would put data measured in plasma and storage rings into connection.

Our group has recently shown that, besides the two body electron-ion recombination process, the ternary recombination process (He assisted, if helium buffer gas is used)

$$H_3^+ + e^- + He \xrightarrow{K_{He}} \left\{ \begin{matrix} H_2 + H \\ H + H + H \end{matrix} \right\} + He \tag{3.11}$$

plays a significant role in a laboratory afterglow plasma dominated by H_3^+ and could possibly explain discrepancies between many plasmatic measurements Glosík et al. [2008, 2009].

This process is theoretically treated as a two step process. H_3^+ ion captures the electron into the $l = 1$ partial wave and forms neutral unstable molecule H_3^* in autoionising resonance. Almost always, this resonance decays back to H_3^+-e^-pair. However, in certain circumstances, the lifetime of these resonances can be long, as shown in figure 3.4. If it happens so, H_3^* can change the electronic or rotational state to a stable one in a collision with He atom. Then the molecule dissociates. The ternary recombination rate coefficient is determined by the rate coefficients of H_3^* formation, l-changing collisions and the lifetime of H_3^*. Its theoretical temperature dependence is in figure 3.5.

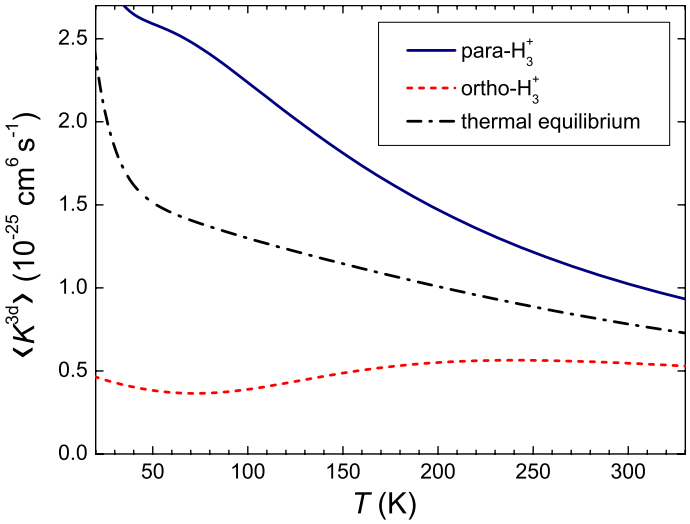

Figure 3.5: Calculated thermally-averaged three body rate coefficient $\langle K^{3d} \rangle$ (the different notation is used to distinguish between theoretical and experimental (K_{He}) coefficients). Note the difference between the values for $^pH_3^+$ and for $^oH_3^+$. Reprinted from [Glosík et al., 2009].

3.2.3 Collisional radiative recombination

In the collisional radiative recombination (CRR) the electron collides with the target ion and the excess energy released by the recombining electron is carried away by a third particle – electron:

$$H_3^+ + e^- + e^- \xrightarrow{K_{CRR} \equiv K_{e^-}} \left\{ \begin{matrix} H_2 + H \\ H + H + H \end{matrix} \right\} + e^- , \qquad (3.12)$$

The amount of the energy can be estimated to $\Delta E \approx 0.13$ eV in the case of H_3^+, which corresponds to the ionisation potential of the lowest Rydberg state de-excited predominantly by collisions rather than radiative transitions [Byron et al., 1962; Stevefelt et al., 1975].

Results of numerical calculations of CRR by Stevefelt et al. [1975] based on a semi-classical theory can be expressed by the following formula for an effective binary rate coefficient at kinetic temperature of electrons T_e:

$$\alpha_{CRR} = 3.8 \times 10^{-9} T_e^{-4.5} n_e + 1.55 \times T_e^{-0.63} + 6 \times 10^{-9} T_e^{-2.18} n_e^{0.37} \, cm^3 s^{-1} \qquad (3.13)$$

and for a corresponding ternary rate coefficient at low temperature (neglecting the second and third terms):

$$K_{CRR} \approx \alpha_{CRR}(T_e)/n_e = 3.8 \times 10^{-9} T_e^{-4.5} \, cm^6 \, s^{-1} . \qquad (3.14)$$

Experimental data on CRR were previously measured at temperatures above 300 K and only very recently the temperature range was extended down to 50 K for Ar^+ ions [see Kotrík et al., 2011a,b].

3.2.4 Influence of H_5^+ formation: [H_2]-dependent term

If the conversion (3.1), (3.2) between H_3^+ and H_5^+ proceeds with a faster rate than the recombination of H_5^+ (recombination rate coefficient $\alpha_5 \sim 10^{-6} cm^3 s^{-1}$

[Glosík et al., 2003; Hiraoka, 1987]), the ratio

$$R = \frac{[H_5^+]}{[H_3^+]} = \frac{k_F[H_2]}{k_B} = K_C[H_2] \tag{3.15}$$

is constant. K_C is a constant given by an entropy and an enthalpy change in the reaction and is generally different for (3.1) and (3.2) and depends on the temperature and on the nuclear spin states of H_3^+, H_5^+ and H_2 [Atkins and de Paula, 2006; Glosík et al., 1998; Hiraoka and Kebarle, 1975; Johnsen et al., 1976; Paul et al., 1995].

In such situation the effective rate coefficient is modified in the following manner:

$$\alpha_{\text{eff}} = (\alpha_{\text{eff}}{}' + \alpha_5 K_C[H_2])\frac{1}{1 + K_C[H_2]} = \alpha_{\text{eff}}{}'(1-\xi) + \alpha_5\xi\,, \tag{3.16}$$

where

$$\xi \equiv \frac{[H_5^+]}{[H_5^+] + [H_3^+]} = \frac{[H_5^+]}{n_e} \tag{3.17}$$

and

$$\frac{[H_3^+]}{n_e} = 1 - \xi\,. \tag{3.18}$$

The first term in (3.16) corresponds to the recombination of H_3^+, the second to the recombination of H_5^+. For medium value of $[H_2] \sim 10^{12}$–$10^{13}\ \text{cm}^{-3}$, we obtain

$$K_{H_2} = \alpha_5 K_C \tag{3.19}$$

for the effective $[H_2]$-dependent ternary coefficient from (3.8). Since this notation evokes "H_2-assisted" recombination similar to the He-assisted one (section 3.2.2) we rather mark it as K_5, i.e.

$$K_5 \equiv K_{H_2}\,.$$

Problems occur if one wants to obtain α_{eff} in the situation when such equilibrium is not established yet (like in figure 3.6). If $[He] \sim 10^{18}\ \text{cm}^{-3}$, $[H_2] \sim 10^{14}\ \text{cm}^{-3}$, $k_F \sim 10^{-28}\ \text{cm}^6\ \text{s}^{-1}$ at $T_{\text{Kin}} = 80$ K [Paul et al., 1995], $k_B \sim 10^{-14}\ \text{cm}^3\text{s}^{-1}$ [Johnsen et al., 1976] the characteristic time for H_5^+ ion formation by reaction (3.2) is

$$\tau' = \frac{1}{k_F[He]\,[H_2]} \sim 0.01\ \text{ms}\,, \tag{3.20}$$

but if $n_e \sim 10^9\ \text{cm}^{-3}$, for example,

$$\tau'' = \frac{1}{\alpha_5 n_e} \sim 0.01\ \text{ms}\,. \tag{3.21}$$

It means that $[H_5^+]$ culminates around the time $t = 0.01$ ms and then slowly decreases like in figure 3.6, i.e. $\text{d}[H_5^+]/\text{d}t \approx 0\ \text{cm}^{-3}\,\text{s}^{-1}$ in comparison with

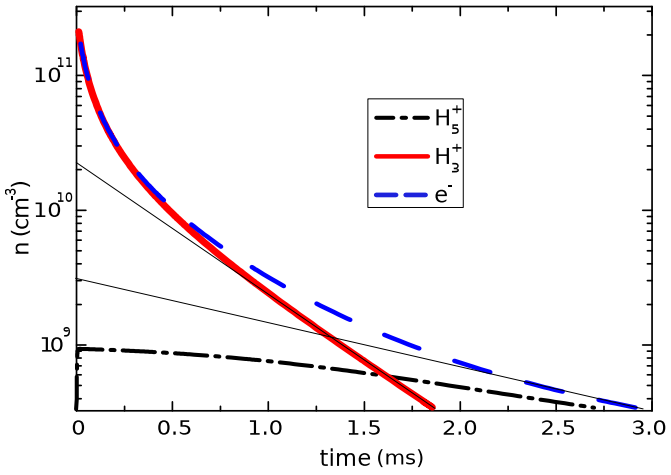

Figure 3.6: Advocatus diaboli: Kinetic model of the afterglow. $P = 2000$ Pa, $[\mathrm{He}] = 1.9 \times 10^{18}\ \mathrm{cm}^{-3}$ $[^{\mathrm{n}}\mathrm{H}_2] = 10^{14}\ \mathrm{cm}^{-3}$, $T_{\mathrm{Kin}} = 77$ K. The full black lines indicate possible fits of the diffusion part of the formula (3.6).

$\mathrm{d}[\mathrm{H}_3^+]/\mathrm{d}t$. In such situation, the chemical kinetics of the e^--H_3^+-H_5^+ system is described by a set of differential equations

$$\frac{\mathrm{d}[\mathrm{H}_3^+]}{\mathrm{d}t} = -\alpha_{\mathrm{eff}}'(1-\xi)n_{\mathrm{e}}^2 - k_{\mathrm{F}}(1-\xi)n_{\mathrm{e}}[\mathrm{H}_2][\mathrm{He}] + k_{\mathrm{B}}\xi n_{\mathrm{e}}[\mathrm{He}] \tag{3.22}$$

$$\frac{\mathrm{d}[\mathrm{H}_5^+]}{\mathrm{d}t} = -\alpha_5\xi n_{\mathrm{e}}^2 + k_{\mathrm{F}}(1-\xi)n_{\mathrm{e}}[\mathrm{H}_2][\mathrm{He}] - k_{\mathrm{B}}\xi n_{\mathrm{e}}[\mathrm{He}]\,. \tag{3.23}$$

Since $\mathrm{d}[\mathrm{H}_5^+]/\mathrm{d}t \approx 0\ \mathrm{cm}^{-3}\,\mathrm{s}^{-1}$,

$$\alpha_5\xi = k_{\mathrm{F}}\frac{1-\xi}{n_{\mathrm{e}}}[\mathrm{H}_2][\mathrm{He}] - k_{\mathrm{B}}\frac{\xi}{n_{\mathrm{e}}}[\mathrm{He}]\,. \tag{3.24}$$

Hence

$$K_5 \propto [\mathrm{He}]\,, \tag{3.25}$$

which is different than (3.19). If only $[\mathrm{H}_3^+]$ is monitored in time, one measures the diffusion time from equation (3.6) as

$$\frac{1}{\tau} = \frac{1}{\tau_{\mathrm{D}}} + \frac{1}{\tau_{\mathrm{R}}} = \frac{1}{\tau_{\mathrm{D}}} + \alpha_5[\mathrm{H}_5^+]\,. \tag{3.26}$$

where τ_{D} is the real diffusion time and τ_{R} is the contribution from reaction (3.2). The effect is shown by straight full black lines in figure 3.6.

As shown above, H_5^+ formation can influence measured H_3^+-e^- recombination rate coefficients in a great excess. Therefore the experimental conditions, namely $[\mathrm{H}_2]$, must be chosen with caution. The comparison of the characteristic times from equations (3.20) and (3.21) seems to be a good guide.

4. N^+ + para/normal-H_2

In ISM, the reaction

$$N^+(^3P_{j_a}) + H_2(J) \rightarrow NH^+ + H \tag{4.1}$$

stands in the beginning of a chain of hydrogen abstraction reactions leading to formation of NH_4^+. This ion then recombines with an electron and forms ammonia [Le Bourlot, 1991].

Low temperature studies of the process (4.1) by Gerlich [1989, 1993]; Marquette et al. [1988] with H_2 in $J = 0$ states (with $^eH_2$) showed that the reaction, known from earlier to be endoergic for H_2 in $J = 1$ state (see references in the cited works), is promoted by the rotational energy E_J of $^oH_2$ [see equation (1.4)]. It means that the rate coefficients for $^pH_2$ and $^oH_2$ (^pk and ^ok) obey the relation

$$^{p,o}k = {}^{p,o}k_0 \exp\left(\frac{-\Delta H + E}{T}\right), \tag{4.2}$$

where ΔH is the apparent endothermicity (in Kelvins) and E the energy brought to the N^+-H_2 system (in Kelvins). In the mixture of $^pH_2$ and $^oH_2$ (with populations $^pf_2$ and $^of_2$, respectively), the effective rate coefficient

$$k = {}^ok\,{}^of_2 + {}^pk\,{}^pf_2 \;\; = {}^of_2\,{}^ok + (1 - {}^of_2)\,{}^pk = ({}^ok - {}^pk)\,{}^of_2 + {}^pk\,. \tag{4.3}$$

Earlier fits of $^of_2\,^ok$ and ^pk to are indicated by dashed lines in the figure 4.1.

There have been doubts about the nature of ΔH and E in equation (4.2). Depending on the fact whether the fine-structure (FS) energy of N^+ (E_{j_a} = 6.1 meV and 16.2 meV for $j_a = 1$, 2, respectively, relatively to $^3P_0$) is available to promote the reaction or not, $E = E_J$, or $E = E_J + E_{j_a}$ [Marquette et al.,

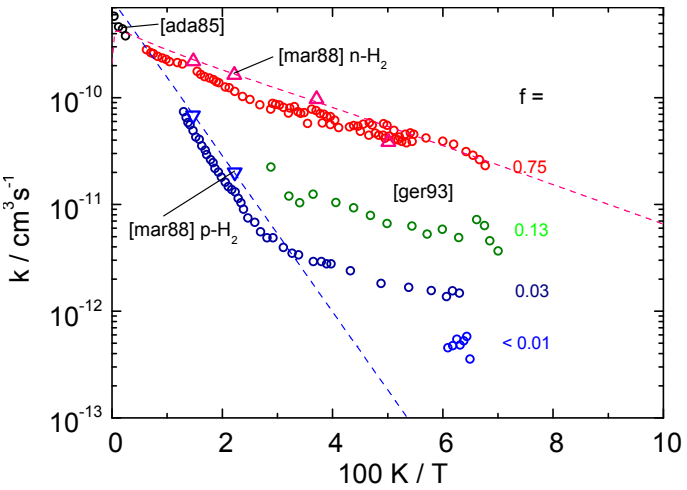

Figure 4.1: Arrhenius plot of rate coefficients k for reaction (4.1) measured by Adams and Smith [1985] [ada85], Marquette et al. [1988] [mar88] and Gerlich [1993] [ger93]. Data of Marquette et al. [1988] are fitted with function (4.2) ($\Delta H \approx 19$ meV and $E = E_J + E_{j_a}$). The constant f stands for $^of_2$. Reprinted from Zymak et al. [2013].

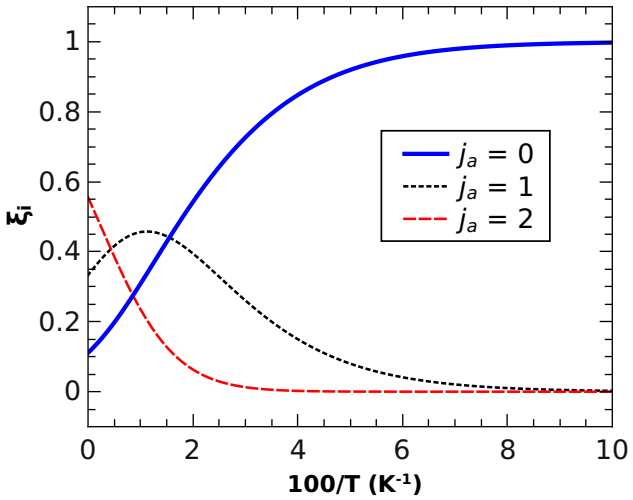

Figure 4.2: Dependence of distribution of FS states $^3\mathrm{P}_{j_\mathrm{a}}$ on temperature.

1988]. Hence the ambiguity concerning the endothermicity ΔH (or a reaction barrier) results: the theoretical value varies in the range 11–33 meV [Gerlich, 2008; Wilhelmsson et al., 1992].

The uncertainty about the endothermicity is connected with the question what the distribution of $^3\mathrm{P}_{j_\mathrm{a}}$ states in experiments of Gerlich [1993]; Marquette et al. [1988] was. If one assumes, like Marquette et al. [1988], that the distribution of FS states is effectively thermalised in collisions with neutral molecules, the $^3\mathrm{P}_{j_\mathrm{a}}$ states are populated in the way as it is plotted in figure 4.2. This enables to interpret measured effective rate coefficients ${}^{\mathrm{p}}k$, ${}^{\mathrm{o}}k$ in a following manner:

$$T > 50\,\mathrm{K} \Rightarrow {}^{\mathrm{o}}k \sim {}^{\mathrm{p}}k \Rightarrow \lim_{{}^{\mathrm{o}}f_2 \to 0} k = {}^{\mathrm{p}}k \tag{4.4}$$

and

$$T \approx 10\,\mathrm{K} \Rightarrow {}^{\mathrm{o}}k \gg {}^{\mathrm{p}}k \Rightarrow k \simeq {}^{\mathrm{o}}f_2\,{}^{\mathrm{o}}k \text{ for } \mathrm{N}^+(^3\mathrm{P}_0)\,. \tag{4.5}$$

Marquette et al. [1988] assumed that ${}^{\mathrm{p}}k_0$ and ${}^{\mathrm{o}}k_0$ [from equation (4.2)] are same for all FS states and calculated the endothermicities for ${}^{\mathrm{o}}\mathrm{H}_2$ and ${}^{\mathrm{p}}\mathrm{H}_2$ using the populations of FS states (ξ_{j_a}) from figure 4.2. They obtained same $\Delta H \approx 19$ meV for ${}^{\mathrm{n}}\mathrm{H}_2$ and ${}^{\mathrm{p}}\mathrm{H}_2$ if they took $E = E_J + E_{j_\mathrm{a}}$ (see table IV. in their work and figure 4.1). It should be noted, however, that their conclusions are based only on 5 experimental points.

The assumption of the spin-orbit relaxation is in contradiction with adiabatic model by Russel and Manolopoulos [1999], which supposes that only 3 of 9 spin-orbit coupled potential energy surfaces (PES) lead to the product channel. Tosi et al. [1994] and Gerlich [1993] compared their experimental data with FS-state-specific reaction rate coefficients calculated statistically by [Gerlich, 1989] and concluded that if the FS relaxation takes place, it must be "unrealistically" fast because otherwise they would observe double-exponential decay of N^+ number in a 22-pole trap [Gerlich, 1993]. They offer the hypothesis that FS-energy is not available for the reaction and that the rate coefficient is one and same for all FS states. However, it is important to note, that the slowness of spin-orbit quenching is not a general rule and its rate coefficient

can be even larger than the reaction rate in specific cases – see experimental work by Hamdan et al. [1984] or theoretical calculations of Abrahamsson et al. [2007]; Mielke et al. [1996]. To conclude, one must suppose the non-adiabatic behaviour to explain the relaxation of FS states, but such interpretation contradicts the starting point of the existing theoretical descriptions.

Part II

Experimental methods

5. Para-hydrogen generator

$^{e}H_2$ is produced by catalytic conversion of $^{n}H_2$ on a surface of paramagnetic material cooled down to temperatures 11–18 K. A specialised device – *the para-hydrogen generator* was constructed for this purpose. The device consists of following functional systems:

- vacuum system;
- cooling system;
- computer controlled heating system;
- ortho-to-para hydrogen catalyst and its container;
- electronic backup security system.

In the text below each of them is thoroughly described.

5.1 Vacuum system

The vacuum system can be divided to two subsystems: isolation vacuum subsystem and hydrogen pipelines. The overall view at the vacuum system is in figure 5.1. A cold head (CH in the picture) serves as a cooler for the catalyst and also as a cryo-pump for the isolation vacuum.

The isolation vacuum subsystem keeps the pressure around CH sufficiently low to minimise heat transfer from walls of an outer chamber (C1) to CH and a catalyst container (CC). This pressure is always kept to $P_{C1} < 10^{-3}$ mbar by a turbo-molecular pump. Fore-vacuum is maintained by a rotary pump.

The hydrogen pipelines, drawn by blue lines in figure 5.1, lead H_2 gas through CC situated on CH to another experimental apparatus. The water impurities in $^{n}H_2$ are adsorbed on tube walls in liquid nitrogen freezer before entering C1 and CC. CC kept at temperatures < 20 K serves not only to convert $^{n}H_2$ to $^{e}H_2$ but also to purify the gas from nitrogen and other impurities. $^{e}H_2$ is leaked to another experimental apparatus by the sapphire leak valve. The redundant $^{e}H_2$ that does not flow through the leak valve is pumped away by the turbo-molecular pump through a by-pass (indicated in figure 5.1).

5.2 Cooling and heating system

CC is cooled down to $T_{CC} = 10$–18 K by a helium closed circle refrigerator that consists of the cold head CH (Leybold RGD 210, figure 5.2) and helium compressor that is cooled by flowing water (figure 5.3).

5.2.1 Cooling system

CH has the bottom (1st) and the upper (2nd) stage. The cooling power of the bottom one is $W = 12$ W at 80 K and it is able to get cooled down to

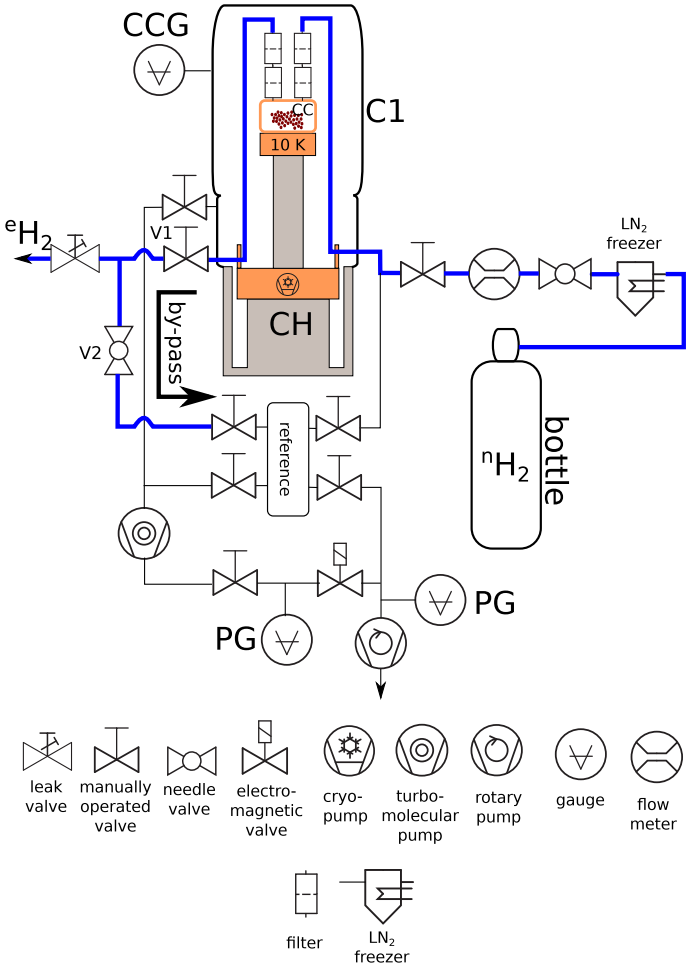

Figure 5.1: Scheme of the para-hydrogen generator's vacuum system

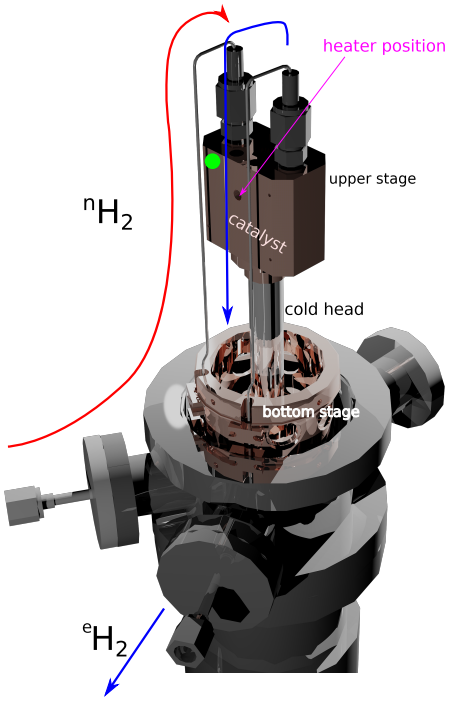

Figure 5.2: Artist's view at catalyst container and the cold head. A position of a temperature sensor (a silicon diode) is indicated by light green spot.

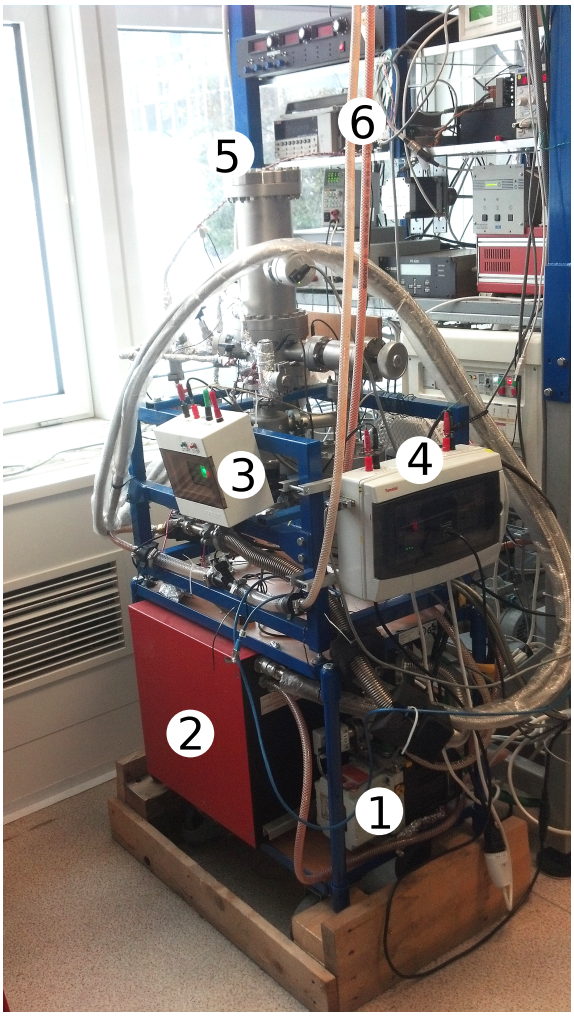

Figure 5.3: Overall view at para-hydrogen generator. 1: the rotary pump; 2: the compressor; 3: heating security; 4: backup security system; 5: the isolation vacuum chamber C1; 6: water hoses.

35 K. The upper stage has the cooling power $W = 2$ W at 20 K and the lowest achievable temperature 10 K.

On the upper stage, CC is situated (see figure 5.2). Inside the isolation vacuum chamber C1, $^{n}H_2$ is fed to CC through thin (0.5 mm inner diameter) stainless steel tubes. Such thickness reduces the heat flow from C1 to CC and increases the velocity of $^{n}H_2$ so it does not get frozen in the tubes and does not plug them up. In order to minimise the heat transfer further, tubes are touching the copper collar (visible in figure 5.2) at the bottom stage of CH and being pre-cooled.

As already mentioned in the section 5.1, the gas in the space around CH and CC is pumped to reduce the heat transfer from the outer chamber C1 by ambient gas molecules. At the temperature of the cold head 11 K and $P_{C1} \approx 10^{-5}$ mbar, such heat transfer is already efficient enough to rise the temperature of CC to 16 K. If the ambient gas pressure is low enough, the transfer of heat by radiation from the walls dominates. To suppress these losses, CC is shielded by a stainless steel cylinder that is cooled by the bottom stage of CH.

Despite all these measures, the cooling process takes 5 hours. Therefore the time-scheduled switch-on system (of the compressor and CH) was implemented (see section 5.4).

5.2.2 Computer controlled heating system

During the experiments, it is needed to maintain the vapour pressure of $^{e}H_2$ above the catalyst in CC stable to obtain constant flow of $^{e}H_2$ from CC. The vapour pressure is set by the temperature of CC (T_{CC}) which is varied by a special cartridge heater (produced by Cryo-con, part n. 3039-001) that is powered by a voltage source controlled by a computer. A software for the voltage control is based on an algorithm of proportional integral-derivative controller that takes temperatures measured by a silicon diode (attached to Lakeshore 218 temperature monitor) and returns the signal for the voltage source containing the needed voltage value. In this way, we can keep the constant T_{CC} over several hours. A temperature fluctuation in a shorter timescale is shown in figure 5.4. In the figure, a deviation of T_{CC} over 60 minutes is indicated ($\sigma_{T_{CC}} = \pm 0.02$ K).

The heating system is backed-up by a dedicated security system (3 in figure 5.3). The input is connected with a relay of the Lakeshore temperature monitor that switches off when a temperature threshold is exceeded. If it happens so, the relay of the security system interrupts the cold head's heating circuit (the position of the heating elements is indicated in figure 5.2).

5.3 Catalyst

As the catalyst we used either Fe_2O_3 (CAS number 1309-37-1) or $HFeO_2$ (CAS number 20344-49-4). Fe_2O_3 was used in the form of 0.5 cm sized flakes, $HFeO_2$ had the form of a powder. $HFeO_2$ is recommended by makers to undergo so called "reactivation": the catalyst is heated to 470 K in a dry hydrogen atmosphere. Since the catalyst must not be in contact with the air after this

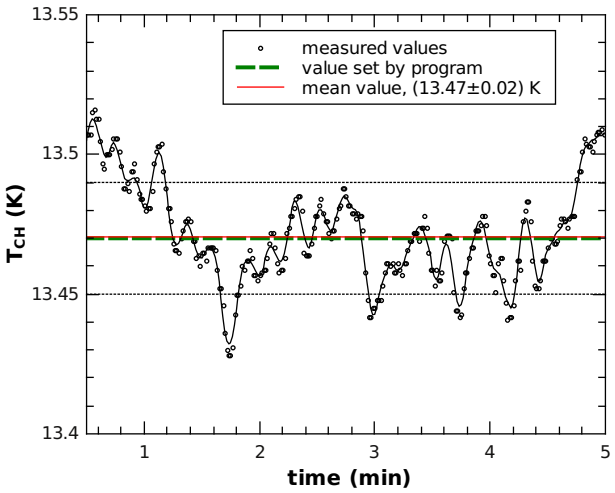

Figure 5.4: Demonstration of temperature-maintaining capability of computer controlled heating system. The mean value and the deviation from it are calculated for the period 60 min.

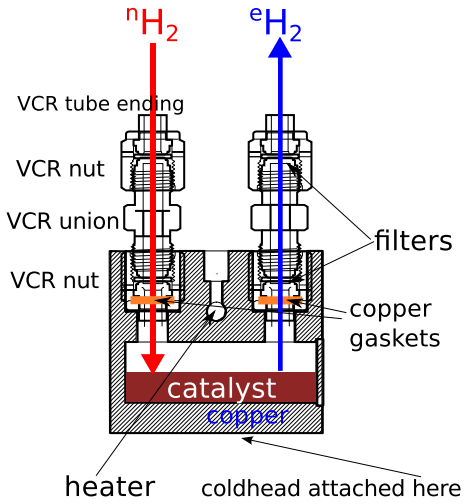

Figure 5.5: Cross-section of catalyst container with VCR connections indicated.

process, the reactivation was carried out in CC detached from CH by stainless-steel screws while CH was switched on.

5.3.1 Catalyst container

CC is made of copper which has good thermal conductivity ($\approx 0.35\,\mathrm{Wcm^{-1}K^{-1}}$ at 20 K [Mendelssohn and Rosenberg, 1952]). The stainless steel tubes (mentioned in section 5.2.1) have VCR tube endings (from Swagelok) with female nuts installed. CC has two same female nuts silver-soldered into the body. Both nuts are connected with VCR male unions. Between the union and the tube ending, the particle filter gasket (with 5 μm mesh) is situated. Similarly, between the VCR nut in CC body and the VCR union the copper gasket, VCR tube ending and particle filter gasket is installed (in the direction from bottom to top). Whole installation of the tubes to CC is depicted in figure 5.5.

5.3.2 Filling procedure

The common mode of operation of the para-hydrogen generator for all experiments in this work is following: hydrogen is liquefied in CC and the vapours of $^{e}H_2$ are collected. There are several things one should concern when filling CC with $^{n}H_2$ gas:

- $^{o}H_2$ molecules should undergo many collisions with a surface of the catalyst to convert effectively to $^{p}H_2$: it means that $^{n}H_2$ should not get frozen on the surface of the catalyst and make a layer obstructing collisions of other molecules with the catalyst. Therefore the catalyst should have $T_{CC} > 15$ K (14.01 K is the melting point of H_2) for at least 30 min after filling is finished.

- $^{n}H_2$ should not get frozen in the pipes, so the pipes should have the temperature higher than 20.28 K (the boiling point of H_2) in the majority of its length. This is achieved by setting $T_{CC} = 18$ K while filling.

- The amount of $^{n}H_2$ in CC should be big enough not to be forced later to use the last (the lowest) layer of H_2 frozen on the surface of the catalyst since $^{o}H_2$ is preferentially adsorbed on the surface. In the other words, using the last remaining adsorbed H_2 could lower $^{p}f_2$ of $^{e}H_2$. We normally adsorb 50 scc, which was proved to be enough for 8 hours of flow $f \approx 0.1$ sccm in average.

- The catalyst should be situated only in CC. Therefore inlet and outlet tubes are separated from CC by two pairs of particle filters (as described in 5.3.1). It is however wise not to shoot atmospheres of $^{n}H_2$ with flow of hundreds of sccm through CC so that the catalyst would pass through the filters. The inlet tube of the para-hydrogen generator is equipped with a flow meter and a needle valve (see figure 5.1) in order to keep the flow $f < 20$ sccm. It is recommended to rise the flow gradually.

5.3.3 Output procedure

In the experiments with the FALP and CRDS apparatuses (see section 12), a constant flow of $^{e}H_2$ (f) ranging from 0.01 sccm to 1 sccm is required. However usage of a flow controller is better to be avoided because of its heated parts, which may convert $^{p}H_2$ to $^{o}H_2$. Air and water impurities in the outlet tubes can also cause such back-conversion, so excessive usage of leak valves and needle valves which results in storage of $^{e}H_2$ gas in the stainless steel tubes at the room temperature is not favourable. The material of some leak valves based on chromium- or aluminium-oxides can act as a catalyst having the room temperature so here we have another reason not to use such flow-limiting instruments. The outlet tube (connected to the experimental apparatus) is shortened as much as possible and if the flow of $^{e}H_2$ over a long distance is required, the tube with an inner diameter 1.5 mm is used to maximise the gas speed.

Due to the absence of the flow meter, the flow of $^{e}H_2$ to SA-CRDS of Cryo-FALP II apparatuses must be calibrated. At $T_{CC} = 18$ K, a specific value of

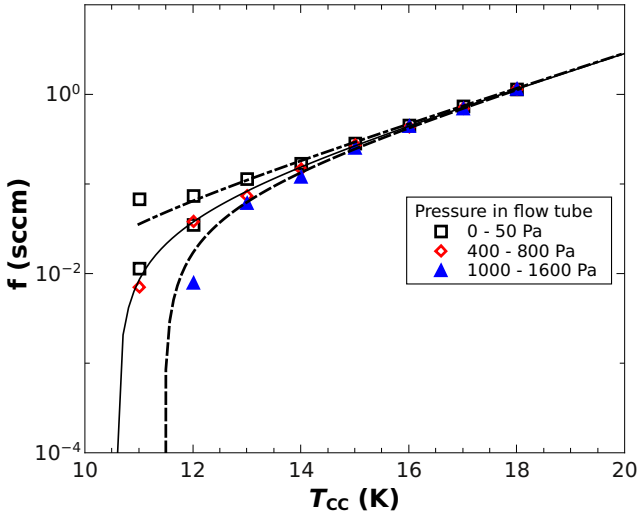

Figure 5.6: Dependence of flow on T_{CC} for different pressures at outlet

a pressure above a pump (usually turbomolecular), so called "reference point", is set opening the valve V1. Then the outlet to the pump is closed and the gas is expanded to a chamber with a known volume (V) equipped with a gauge. We record an increase of the pressure p in time and evaluate the flow f from a derivative

$$\frac{\mathrm{d}p}{\mathrm{d}t} = \frac{f}{V}\,. \tag{5.1}$$

This is done for several values of T_{CC} and we get the calibration curve f vs T_{CC} like in figure 5.6. The flow depends on the pressure in the chamber at very low pressures above the catalyst, i.e. at very low flows of $^{\mathrm{e}}\mathrm{H}_2$, therefore the derivative must be measured at several values of p. The relative uncertainty of f at $T_{\mathrm{CC}} < 12$ K is more than 100% for $p > 50$ Pa. The results in the figure are fitted with empirical formula

$$f = -0.09 + 0.075 \times \exp\left(-\frac{p}{965\,\mathrm{Pa}}\right) + 3.7 \times 10^{-4} \times \exp\left(\frac{T_{\mathrm{CC}}}{2.23\,\mathrm{K}}\right)\,. \tag{5.2}$$

Note that f is in sccm. The fit in the figure was performed for measurements with Cryo FALP II and the similar one was carried out also before experiments with the SA-CRDS apparatus. Once we have this prescription, it is enough to set only the "reference point" before each experimental session.

5.4 Electronic backup security system

serves to monitor pressures in the isolation vacuum chamber and above the rotary pump and to open the electromagnetic valve, switch the compressor (2 in figure 5.3), its water supply (6) valve or the turbine accordingly (see figure 5.1 for the pumps and gauges). It can be also used to switch on the whole apparatus (except the rotary pump) in a specified time to start the long cooling procedure when no experiments are carried out.

The electromagnetic valve above the rotary pump, the turbine, the compressor's power supply and the valve of the water cooling system are switched

by relays connected to Fatek FBs-10MA programmable logical circuit (PLC). This electronic part has built-in relays switched by a loaded program that takes the pressures in C1 and above the rotary pump, the flow of water, the error signal from the turbine as input parameters. Decision of the program according to these signals can be overridden by sending a signal from a hardware button. The ladder diagram of this program is in Attachment D.1. The switch-on timer values are modified by a special program from a computer that is occasionally connected to the PLC through a network interface.

5.4

6. 22-pole radio-frequency trap

22PT apparatus is a combination of a 22-pole radio-frequency trap and an storage ion source (SIS). It is a sophisticated tool for studies of ion-molecule reactions. The basics of storing ions in RF fields have been described thoroughly in Gerlich [1992, 1995] and Hejduk [2009, translation to Czech language]. Therefore here I will give only a basic introduction to technical aspect of the present apparatus.

6.1 Overview

The operational scheme of the 22PT apparatus is in figure 6.1. Ions are produced by electron bombardment in SIS. A mass of the ions is filtered by a quadrupole mass filter. Then the ions are directed to the trap through an electrostatic quadrupole bender (QB). The reaction area, the trap, is filled with He buffer gas and the reactant gas, H_2 in this work. Ions are confined in the potential well created by alternate radio-frequency (RF) electric potential at a set of 22 rods with 1 mm diameter. Ring electrodes (RE) at static potential prevent the ions from escaping in the axial direction. During the filling period, the electrostatic barrier at the entrance RE is slightly negative relatively to the potential of the trap. After various storage times, the trap exit (another RE) is opened and the ions move through the quadrupole (QP) mass spectrometer and are converted into a fast negative pulse using an MCP (Micro-Channel Plate) detector (Hamamatsu F4655-12) followed by a discriminator. The standard measuring procedure is based on filling the trap at a fixed frequency with a well-defined number of primary ions (typically a few thousand) and analysing the content after different storage times.

The trap is surrounded by a copper box that is mounted onto the cold head of a closed cycle helium refrigerator. Stationary temperatures between 10 K and 100 K are set by simultaneously cooling and heating. The temperature is measured by silicon diodes.

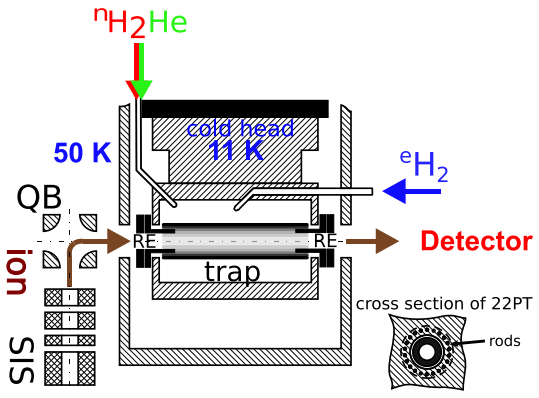

Figure 6.1: Scheme of 22PT apparatus

6.1.1 Vacuum system

Hydrogen gas can be introduced into the trap via two leak valves, allowing us to produce any mixture from almost pure $^{p}H_2$ to $^{n}H_2$. A few collisions of the neutral gas with the walls are sufficient to cool down the kinetic temperature T_{Kin} of the neutrals to the temperature of the cold head. The gas density inside the trap is determined using a spinning rotor gauge or a calibrated ionisation gauge [Asvany, 2003]. Since the trap is continuously pumped by turbomolecular pumps, a temperature dependence of the number density of the neutral molecules ($n_{22\mathrm{PT}}$) in the trap does not follow the inverse reciprocity given by the ideal gas law exactly – the calculation is rather based on a principle of preservation of particle flows: the particle flow to the trap j_2 and from the trap (j_1) are equal, i.e.

$$j_1 = \frac{1}{4} n_{22\mathrm{PT}} \langle v_{22\mathrm{PT}} \rangle = \frac{1}{4} n \langle v \rangle = j_2;\; n = \frac{p}{k_{\mathrm{B}} T}\,, \tag{6.1}$$

where the subscript 22PT indicates the number density n or particle velocity v in the trap. T is the temperature of the chamber walls, typically the room temperature. The pressure in the chamber measured by a gauge is labelled as p. Since

$$\langle v \rangle = \sqrt{\frac{8 k_{\mathrm{B}} T}{\pi m}}\,, \tag{6.2}$$

where m is the mass of the neutral,

$$n_{22\mathrm{PT}} = \frac{p}{k_{\mathrm{B}} T} \sqrt{\frac{T}{T_{22\mathrm{PT}}}}\,. \tag{6.3}$$

A simplified view at the vacuum system is available in figure 6.2. The apparatus consists of three main chambers connected with standard CF flanges (CF 100 between the detection chamber and the trap chamber, CF 40 between the storage ion source chamber and the trap chamber) that are pumped differentially by turbo-molecular pumps pre-pumped by turbo-molecular drag pumps (TDP). N_2 gas is injected to the space below TDP of the trap chamber to increase a pumping speed of the hydrogen gas. All turbines are backed up by an electronic system which takes the pressure measured in the trap chamber (by ionisation gauge) as an input.

The background pressure of the main chamber is lower than 10^{-7} Pa. With the exception of HD, most gas impurities are frozen out below 77 K. The operational (experimental) pressures are 10^{-7}–10^{-3} Pa.

Further description of the apparatus can be found in Zymak [2013].

6.2 Calculation of rate coefficients

A simple model of elastic collisions of trapped ions with buffer gas molecules leads us to conclusion that the kinetic temperature of the ions T_{Kin} converges to the temperature of the buffer gas within ≈ 10 collisions if the initial $T_{\mathrm{Kin}} \approx$ 300 K (the temperature of the storage ion source) and the temperature of the gas is 11 K (the lowest value, at which the experiments are carried out). If

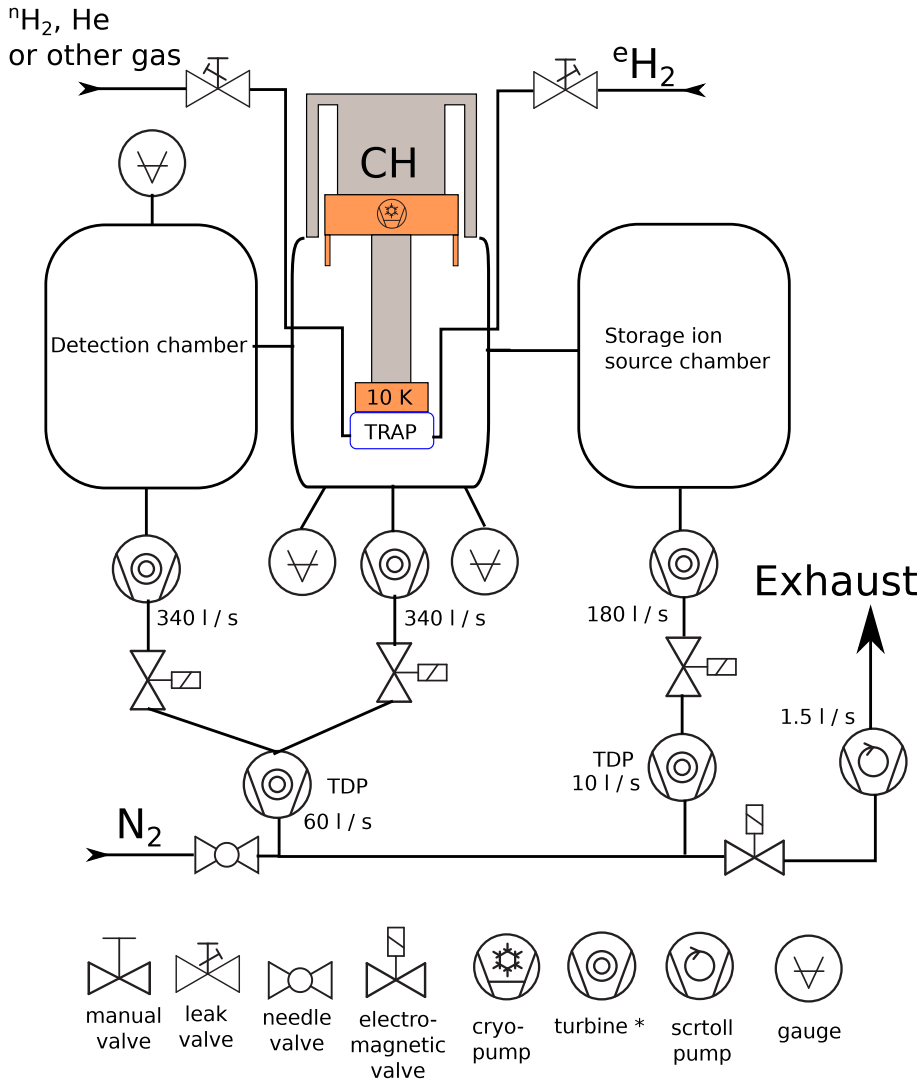

Figure 6.2: Simplified scheme of vacuum system of 22PT apparatus used in this work. Pumping speeds of the pumps for N_2 are written beside their symbols. TDP: turbo-molecular drag pump.

$[H_2] \sim 10^{12}\,\mathrm{cm}^{-3}$ and a rate coefficient for the collisions of the same order as typical Langevin value is considered, H^+ or N^+ ions are kinetically thermalised in ≈ 10 ms. During the experiment, thermalisation of the ions is observable as a gradual increase of counts of detected ions in the first milliseconds of the trapping period, as is visible in figure 3 of Attachment A.1. This is caused by the fact that the transmission of the ions through QP mass analyser at the exit rises with decreasing initial energy of extracted particles. Sources of kinetic heating of the ions in the trap like the influence of a RF field amplitude are discussed in Gerlich [1992].

When the primary ions are thermalised, they react with the neutral target gas molecules, H_2 in the case of this work, and number of trapped ions N decreases with trapping time t:

6.2

$$\frac{\mathrm{d}N}{\mathrm{d}t} = -kN[H_2]\,, \tag{6.4}$$

where k is the reaction rate coefficient. The solution of this gives the rate coefficient

$$k = \frac{1}{(t_{\mathrm{fin}} - t_0)[H_2]} \log \frac{N(t_0)}{N(t_{\mathrm{fin}})} = \frac{\log\{N(t_0)\} - \log\{N(t_{\mathrm{fin}})\}}{\Delta t[H_2]}\,, \tag{6.5}$$

where t_0 is the time when the decay begins (after thermalisation) and t_{fin} corresponds to the end of the measured decay. We can see that the rate coefficient can be evaluated from measurements of N at two distinct times. This can be done repetitively to minimise the noise of N. The noise can be also suppressed by measuring the decay with the period Δt long enough so that $N(t_{\mathrm{fin}})/N(t_0) < {}^1/_{10}$.

At any time t of the decay (the trapping time), the total number of charged particles must be constant, it means that

$$N(t_0) = N(t) + N'(t)\,, \tag{6.6}$$

where N' is a sum of all products of the ion-neutral reaction. Then equation (6.5) can be modified to

$$k = \frac{1}{\Delta t[H_2]} \log \frac{N(t) + N'(t)}{N(t)}\,. \tag{6.7}$$

This measurement method is advantageous if the condition $N(t_{\mathrm{fin}})/N(t_0) < {}^1/_{10}$ cannot be achieved within a sensible time because of too low k. Note that t can be set to any moment when N' is measurable with low error. A disadvantage is that the detection efficiency can be different for product ions, therefore a calibration factor for N' must be obtained before every experiment. Another problem is that if a chain of reactions follows the studied reaction, the products from this chain must be also counted into N'.

7. Cavity Ring-Down Spectroscopy

7.1 Absorption spectroscopy basics

When monochromatic light of frequency ν with intensity I passes through a homogeneous absorbing medium, its intensity decreases according to the Lambert-Beer law

$$\frac{\mathrm{d}I(x,\nu)}{\mathrm{d}x} = -\alpha(\nu)I(x,\nu)\,, \tag{7.1}$$

where $\alpha(\nu)$ is the absorption coefficient, x the distance the light travels through the absorbing medium. The solution of this differential equation is simply

$$I(x,\nu) = I_0 \exp\{-\alpha(\nu)x\}\,, \tag{7.2}$$

where I_0 is the initial density.

A spectral line is characterised by its cross section of photo-absorption $\sigma(\nu)$, which is related to the absorption coefficient α and number density of absorbing particles N in the following manner:

$$\alpha(\nu) = N(x)\sigma(\nu)\,, \tag{7.3}$$

The cross section σ is related to the line-shape function $g(\nu)$ and the integral absorption coefficient (spectral line intensity) S:

$$\sigma(\nu) = Sg(\nu). \tag{7.4}$$

The normalisation condition

$$\int_0^\infty g(\nu)\mathrm{d}\nu = 1 \tag{7.5}$$

applies to the line-shape function.

Absorbance A is defined here as

$$A = -\log\left(\frac{I}{I_0}\right)\,. \tag{7.6}$$

Considering (7.2), we can write

$$A(\nu) = \alpha(\nu)L \tag{7.7}$$

for homogeneous medium where L is the total travel distance.

7.1.1 Population of energy levels and determination of number density

TDE population P of energy level E_m is given by the relation

$$P(E_m) = \frac{g_m}{Q(T)} \exp\left(-\frac{E_m}{k_\mathrm{B}T}\right)\,, \tag{7.8}$$

	H_3^+ (in TDE)	$^pH_3^+$	$^oH_3^+$
offset (cm^{-1})	0	64.123	86.9591
a_0	−35.2007	1.6702	0.5579
a_1	73.1854	−4.3613	2.8498
a_2	−68.1800	8.2473	−6.1672
a_3	37.2205	−7.6655	6.7433
a_4	−12.3723	3.6618	−3.9144
a_5	2.3413	−0.8479	1.1366
a_6	−0.1923	0.0764	−0.1275

Table 7.1: Coefficients of the partition function expression (7.10) for H_3^+(in TDE), $^pH_3^+$ and $^oH_3^+$calculated by Hlavenka [2007].

7.1

where $Q(T)$ is the partition function and g_m is a degeneracy factor like in equation (1.2). The value of partition function

$$Q(T) = \sum_m g_m \exp\left(-\frac{E_m}{k_B T}\right) \tag{7.9}$$

at temperature T is possible to calculate from its fit by a logarithmic formula

$$\log_{10} Q(T) = \sum_{i=0}^{n} a_i (\log_{10} T)^i \,, \tag{7.10}$$

where a_i are coefficients originating from numerical calculations. It is often useful to notice that a few energy levels are populated at low temperatures, therefore there is no need to sum (7.9) over m running to infinity. Similarly, only an expansion of (7.10) to finite series, i.e. to finite n, is needed. Aforementioned information for rotational levels of H_3^+ ion can be found in Hlavenka [2007]; Neale et al. [1996]; Tennyson [2003b]. The a_i parameters are written in table 7.1.

The derivation of formula for number density is written in Rothman et al. [1998]; Varju [2011]. Here I give only the final formulas valid for H_3^+ ions in rotational states J_n of the ground vibrational state. Under an assumption of Maxwell-Boltzmann distribution, the integral absorption coefficient is calculated by formula

$$S = \frac{C g_n}{\nu_{nm}^2 Q(T)} \exp\left(-\frac{E_m}{k_B T}\right) \left\{1 - \exp\left(-\frac{E_n - E_m}{k_B T}\right)\right\} A_{nm} \,. \tag{7.11}$$

The variables and constants used in this equation are explained in table 7.2.

If the absorbance A is measured, the number density N of the ions in J_n state is

$$N = \frac{A\sqrt{2\pi}\sigma_D(T)}{S(T)L} \,, \tag{7.12}$$

where σ_D is a width of the spectral line (originating mainly from Doppler broadening in this work, see below).

	Description	Units
S	integral absorption coefficient	$\mathrm{cm}^{-1}/(\mathrm{molecule} \times \mathrm{cm}^{-2})$
C	$1/(8\pi c) = 1.3266 \times 10^{-12}\,\mathrm{cm}^{-1}\mathrm{s}$	$\mathrm{cm}^{-1}\mathrm{s}$
g_n	degeneracy factor for upper level of the transition $g_n = (2S_n + 1)(2J_n + 1)$	–
S_n	total nuclear spin for upper level	–
J_n	total angular momentum for upper level	–
E_m	Energy of the lower rotational state	J
E_n	Energy of the upper rotational state	J
A_{mn}	Einstein coefficient of spontaneous emission	s^{-1}
ν_{mn}	transition frequency	cm^{-1}

Table 7.2: Variables in equation (7.11).

7.1.2 Internal temperatures

So far, we considered T as a temperature describing the ensemble of particles in TDE. In a reactive environment, all internal degrees of freedom are not thermalised, generally. Therefore we can talk about electronic (T_{Es}), vibrational (T_{Vib}) or rotational (T_{Rot}) temperatures of the particles, namely H_3^+ ions, depending on the fact which energy levels we consider. Under TDE, all these temperatures are equal to the kinetic temperature, i.e.

$$T = T_{\mathrm{Kin}} = T_{\mathrm{Es}} = T_{\mathrm{Vib}} = T_{\mathrm{Rot}} = \cdots \tag{7.13}$$

Kinetic temperature T_{Kin}

T_{Kin} is evaluated from Doppler broadening of a monitored spectral line with frequency ν_0. Its shape can be described by a Gaussian function of the frequency ν

$$g(\nu) = \frac{1}{\sqrt{2\pi}\sigma_{\mathrm{D}}} \exp\left\{-\frac{(\nu-\nu_0)^2}{2\sigma_{\mathrm{D}}^2}\right\}, \tag{7.14}$$

where $\nu_0 \equiv \nu_{mn}$ and

$$\sigma_{\mathrm{D}} = \nu_0\sqrt{\frac{k_{\mathrm{B}}T_{\mathrm{Kin}}}{Mc^2}} \tag{7.15}$$

M is the particle mass. (The commonly used full width at half maximum (FWHM) can be obtained by multiplying σ_{D} with the factor $2\sqrt{2\log 2}$.) Hence

$$T_{\mathrm{Kin}} = \frac{\sigma_{\mathrm{D}}^2 Mc^2}{\nu_0^2 k_{\mathrm{B}}}. \tag{7.16}$$

The Doppler effect is not the only one source of broadening of spectral line, of course, but under experimental conditions of this work, it is the dominant broadening effect. For example, the collisional broadening of H_3^+ spectral lines in He buffer gas at 10 mbar and $T = 77$ K is 36.1 MHz. This is much less than broadening of 786 MHz caused by the Doppler effect at the same pressure and temperature.

Nuclear spin temperature T_{NS}

In the case of H_3^+ ion at very low temperatures, when only the two lowest rotational levels $[(J,G) = (1,1)$ and $(1,0)]$ are populated, it is meaningful to introduce a nuclear spin temperature:

$$\frac{{}^{\mathrm{o}}f_3}{{}^{\mathrm{p}}f_3} = \frac{g_{\mathrm{o}}}{g_{\mathrm{p}}} \exp\left(-\frac{\Delta E}{k_{\mathrm{B}} T_{\mathrm{NS}}}\right) = 2\exp\left(-\frac{32.9\,\mathrm{K}}{T_{\mathrm{NS}}}\right) \tag{7.17}$$

(note $g_{\mathrm{o,p}} = 2S+1$) and hence

$$T_{\mathrm{NS}} = \frac{32.9\,\mathrm{K}}{\log\left(\frac{2\,{}^{\mathrm{p}}f_3}{{}^{\mathrm{o}}f_3}\right)}\,. \tag{7.18}$$

7.2

In TDE, $T = T_{\mathrm{NS}}$.

Rotational temperature T_{Rot}

If we cannot assume the validity of (7.13), T in (7.8) refers to T_{Rot}. T_{Rot} can be calculated from ratio between populations of two rotational states J_m and $J_{m'}$:

$$\frac{P(E_m)}{P(E_{m'})} = \frac{g_m}{g_{m'}} \exp\left\{-\frac{(E_m - E_{m'})}{k_{\mathrm{B}} T_{\mathrm{Rot}}}\right\} \tag{7.19}$$

The similar rule holds for the vibrational temperature. Since the vibrational states are effectively thermalised by collisions with the buffer gas molecules and by reaction (1.13) (see a discussion in Attachment B.1), I will skip further discussion here.

7.2 SA-CRDS apparatus

The technology of Stationary Afterglow in Cavity Ring-Down Spectrometer apparatus (SA-CRDS) is based on the well-known principles of continuous-wave Cavity Ring-Down Spectroscopy (cw-CRDS) [Romanini et al., 1997]. Implementation described here is rare because the data-acquisition is synchronised with switch-on/off of a discharge. During the discharge-afterglow cycle, the ring-down events occur accidentally, but eventually, after several hundreds of thousands of the cycle repetitions, the time evolution of the monitored states is recorded with microsecond resolution. A thorough description of the SA-CRDS was given for example in the work of Varju [2011]. Here I give only a basic description.

A laser beam is coupled to an optical cavity whose highly reflective mirrors (reflectivity over 99.98%) are periodically swept until an optical resonator is formed (see figure 7.1). When the resonator is set up, the power of the laser radiation in the cavity rises and the incoming laser beam is interrupted by an acousto-optic modulator (see figure 7.2) as soon as the intensity measured by PIN or avalanche diode behind one of the mirrors exceeds a threshold. After the laser beam is intercepted, the trapped light intensity I decreases in

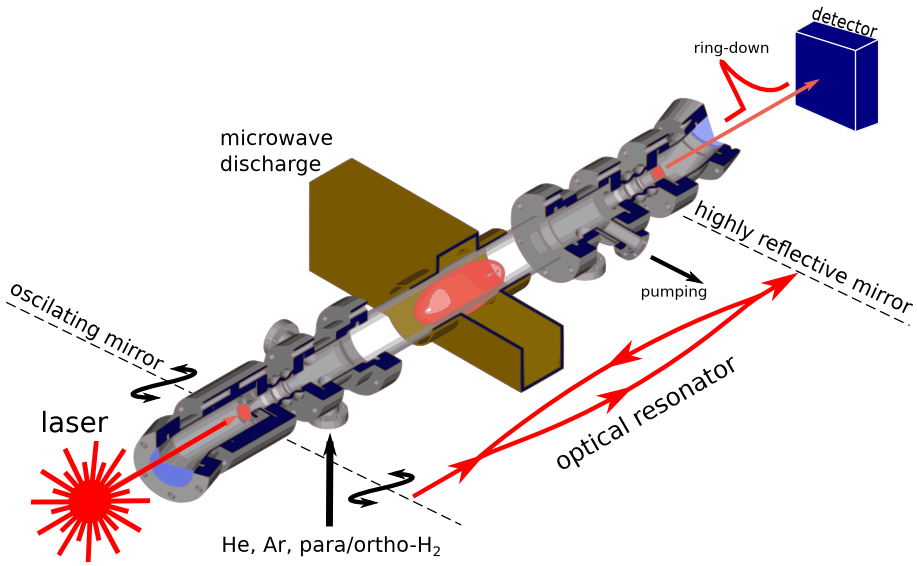

Figure 7.1: Scheme of SA-CRDS apparatus. The discharge in a gas mixture is ignited in the optical resonator consisting of two highly reflective mirrors. The oscillating mirror helps to establish the resonance, i.e. to inject the laser light, in the cavity in random times. When it happens so, the laser light is switched off and the light travels several km in the cavity being gradually absorbed by the plasma. This gradual decrease of the optical signal recorded by the detector is called ring-down. Shorter the ring-down event is, more absorbing is the medium – higher is the concentration of monitored ions.

time t because of the losses at the mirrors and the absorption by the medium in the cavity [according to equation (7.1)]:

$$I(t,\nu) = I_0 \exp\left(-\frac{t}{\tau(\nu)}\right) . \tag{7.20}$$

This is called a "ring-down signal". The characteristic time of the decrease of the intensity τ is a function of the light frequency and is inversely proportional to the concentration of absorbing molecules in the medium:

$$\frac{1}{\tau(\nu)} = \frac{1}{\tau_0} + \frac{c}{d}A(\nu) , \tag{7.21}$$

where d is a distance between mirrors and A is the absorbance from (7.7). The constant τ_0 is the time constant of light decay in an empty cavity, so called baseline. Hence, we can write

$$A(\nu) = \frac{d}{c}\left\{\frac{1}{\tau(\nu)} - \frac{1}{\tau_0}\right\} . \tag{7.22}$$

Practically, when we track the concentration of the ions, $\tau(\nu)$ is obtained from ring-down signals during the discharge period and τ_0 from the ring-down signals at late afterglow times when there are almost no ions in the cavity. Frequency of ring-down events is ~ 100 Hz.

As the light source, a fibre-coupled distributed feedback (DFB) laser diode was used. Central wavelength of the laser is 1381.55 nm in case of H_3^+-e^-

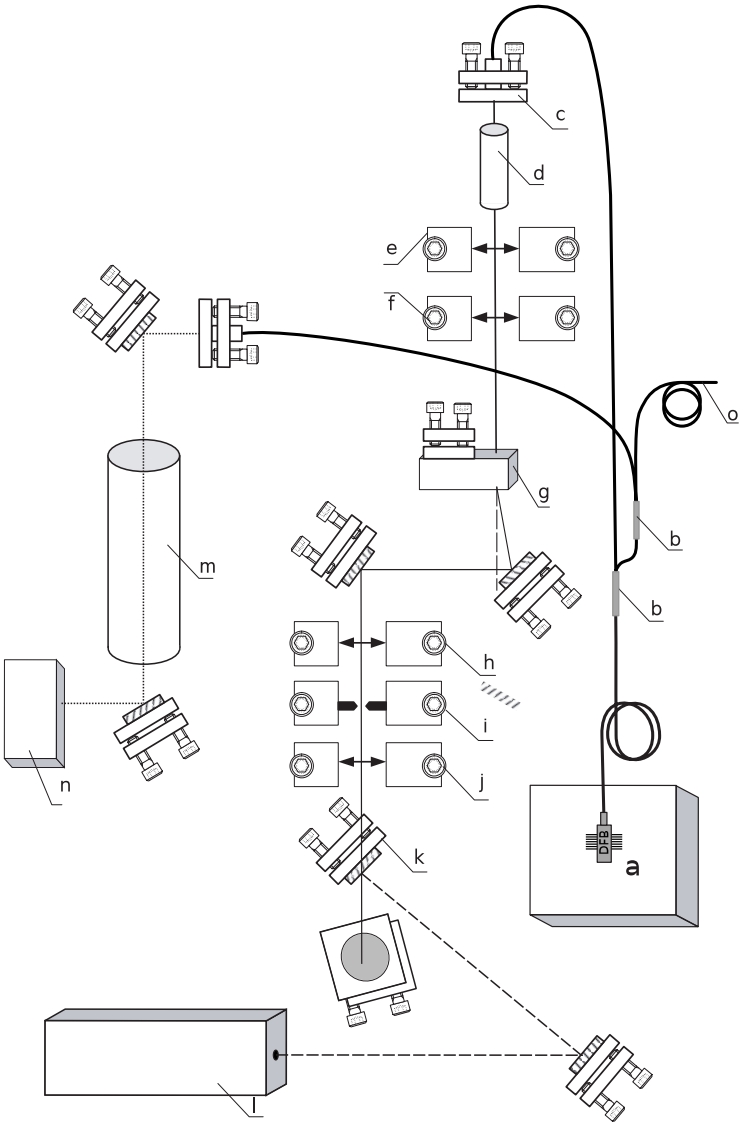

Figure 7.2: Top view of the placement of optical components. Copied from Varju [2011]. Optical fibre from the DFB laser (a) is connected to two 95:5 fibre beam splitters (b). The main fraction of the laser exits the fibre via the collimator (c). The optical isolator (d) follows. The beam shrinking telescope from lenses (e) and (f) focuses the beam on the active region of the acousto-optical modulator (g). The beam is focused on the pinhole (i) by the lens (h) and mode matched with lens (j). The HeNe guiding laser (l) and Fabry-Pérot (m) resonator are also placed on the optical breadboard.

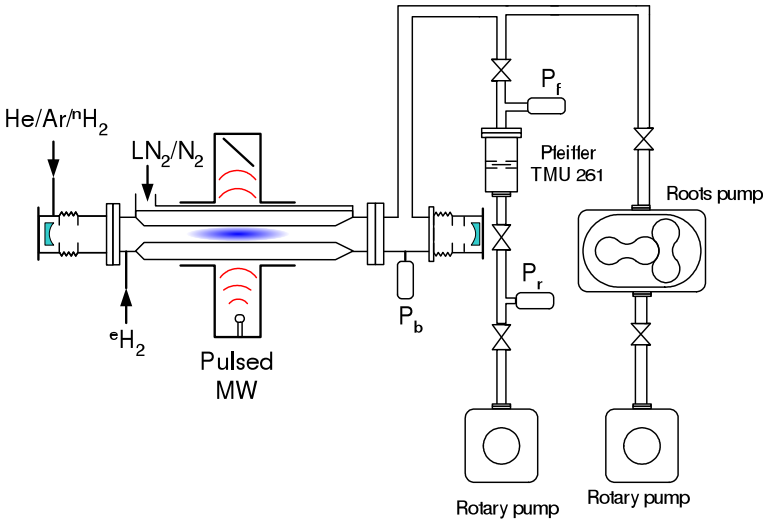

Figure 7.3: Vacuum system of SA-CRDS apparatus. P_r: Pirani gauge, P_b: capacitance gauge, P_f: full range gauge. Reprinted from Varju [2011].

recombination studies. The line-width of the laser is < 2 MHz at 1 second timescales. Maximum output optical power is 20 mW. The beam from the laser undergoes spatial filtering to form Gaussian profile matching to the optical resonator. Set wavelength is measured absolutely using a Michelson interferometer and relatively by Fabry-Pérot etalon.

Figure 7.3 shows the vacuum system of the SA-CRDS apparatus schematically. Gas handling system is common with Cryo-FALP II apparatus (see figure 8.2). The He buffer gas is provided from a pressure vessel containing the gas of 5.0 grade purity and cleaned further in zeolite molecular sieve cooled by liquid nitrogen. Flows of He buffer gas, Ar and $^{n}H_2$ reactant gases are measured by flow meters. This cannot be done in the case of $^{e}H_2$ since we want to avoid para-to-ortho back conversion on heated parts of the flow meters. Also we do not want to store $^{e}H_2$ in a tube at the room temperature and leak it through a needle valve to the discharge cavity. Therefore the flow of $^{e}H_2$ is controlled by a temperature of the para-hydrogen generator's cold head and calibrated by pressure above the pump TMU 261 in figure 7.3 measured by gauge P_f (see chapter 5.3.3 for a description of the calibration procedure).

The discharge tube is cooled by a liquid nitrogen or its vapours. The vapours are produced by heating the liquid nitrogen in a dewar using a resistant coil, and guided by an insulated copper tube into the space between the microwave resonator and the discharge tube (made of fused silica).

7.2.1 Mode matching

The optical resonator of SA-CRDS apparatus consists of two spherical mirrors with radius $R_a = R_b = 1$ m and mutual distance $d = 0.75$ m. This configuration satisfies a stability criterion [Yariv, 1997, p. 136]

$$0 \leq \left(1 - \frac{d}{R_a}\right)\left(1 - \frac{d}{R_b}\right) \leq 1\,. \tag{7.23}$$

The transversal modes of resonators composed of spherical mirrors are labelled with l and m and commonly referred to as TEM_{lm}. The resonant frequency for TEM_{lm} and longitudinal mode index q is [Yariv, 1997, p. 143]

$$\nu_{q,l,m} = \frac{c}{2nd}\left[q + (l+m+1)\frac{\cos^{-1}\left\{\pm\sqrt{\left(1-\frac{d}{R_\mathrm{a}}\right)\left(1-\frac{d}{R_\mathrm{b}}\right)}\right\}}{\pi}\right], \quad (7.24)$$

where n is a refractive index of the medium. The frequency ν (or the wave number) is set by the laser diode temperature controller to desired values (the ones for the H_3^+-e^- recombination study described in this work are in table 12.2). The value of d is varied by changing the position of one of the mirrors situated on a piezoelectric element (see figure 7.1).

7.2

The intensity of the laser light transmitted through the cavity in the resonance can be described in the same manner as in case of Fabry-Pérot resonator

$$I = I_0\frac{(1-R)^2}{(1-R)^2 + 4R\sin^2\frac{2\pi d}{\lambda}}, \quad (7.25)$$

where R is the reflectivity of the mirrors and λ is the wavelength of the light. This is valid only for a stationary case, where the resonator is in resonance with the incident light for infinite time. The transmission is the highest for the TEM_{00} mode, which undergoes the lowest diffraction loss per reflection [see figure 4-13 in Yariv, 1997]. For higher transverse mode indices l, m the energy extends further in the resonator and some of it will not be intercepted by the mirrors and will therefore be lost. This also results in a shorter ring-down time τ for higher modes.

Because of reasons mentioned above, mode-matching of incident beam to TEM_{00} mode is favourable. The mode-matching is carried out by injecting the light through a system lens-pin hole-lens (h, i, j in figure 7.2). The first lens (h) serves to direct the light from the acousto-optic modulator AOM (g) to the pin hole (i). The pin hole with diameter of aperture 50μm is situated nearly to the focal length distance from the first lens to cut off higher spatial frequencies. Then the beam behind the pin hole has a Gaussian profile (which corresponds qualitatively to TEM_{00} mode). The last lens (j) serves to modify parameters of this Gaussian beam (a curvature of the phase front and a spot size) to match the TEM_{00}, i.e. to match the beam quantitatively.

The whole procedure can be described using a matrix formalism. The Gaussian beam can be described by the complex beam parameter q that is parameterised by the phase front curvature R and the spot size ω in the following way:

$$\frac{1}{q} = \frac{1}{R(z)} - i\frac{\lambda}{\pi\omega^2(z)}, \quad (7.26)$$

where z is the spatial coordinate along the axis. The parameters R and ω depend on spatial coordinate as follows:

$$R(z) = z\left[1 + \left(\frac{z_\mathrm{R}}{z}\right)^2\right], \quad (7.27)$$

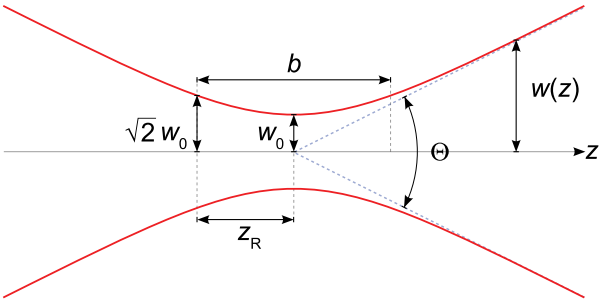

Figure 7.4: Gaussian beam width $\omega(z)$ as a function of the axial distance z. ω_0: beam waist; b: depth of focus; z_R: Rayleigh range; Θ: total angular spread. Taken from Wikipedia [2013].

$$\omega(z) = \omega_0 \sqrt{1 + \left(\frac{z_\mathrm{R}}{z}\right)^2}\,. \tag{7.28}$$

The parameter z_R is called the Rayleigh range and depends on a beam waist ω_0 in (7.28):

$$z_\mathrm{R} = \frac{\pi\omega_0^2}{\lambda}\,. \tag{7.29}$$

If $z \gg z_\mathrm{R}$ the divergence of the beam

$$\theta \simeq \frac{\lambda}{\pi\omega_0} \tag{7.30}$$

and the total angular spread is defined as

$$\Theta \equiv 2\theta\,. \tag{7.31}$$

The relations between the parameters described above is illustrated in figure 7.4.

The practical way of obtaining $R(z)$ and $\omega(z)$ is as following. At long distance $z \gg z_\mathrm{R}$, behind AOM (in the direction to the optical cavity), a series of spot-sizes $\omega(z)$ is measured by a knife-edge method – note that the spot size is the parameter of the Gaussian intensity profile written in the form

$$I \propto \exp\left(-2\frac{r^2}{\omega^2}\right)\,, \tag{7.32}$$

i.e. it is the $1/\mathrm{e}^2$ half-width. The slope of this linear $\omega(z)$ dependence is interpreted as θ. The beam waist ω_0 is calculated according to (7.30). Eventually, the Rayleigh range is calculated using formula (7.29). The position of the point $z = 0$ in the real space is found by extrapolation of $z(\omega)$ dependence to the value $\omega = 0$. Typically, the point $z = 0$ is found several cm in front of AOM.

The complex beam parameter of the beam at the space of entrance to the mode-matching system is calculated using space transformations (7.27) and (7.28). One must use correct spatial coordinate system with the correct origin measured in the way as it was described above. When passing through an

i	Description	M_i
1	Lens h	$\begin{bmatrix} 1 & 0 \\ -\frac{1}{f_1} & 1 \end{bmatrix}$
2	Propagation over distance l_1	$\begin{bmatrix} 1 & l_1 \\ 0 & 1 \end{bmatrix}$
3	Lens j	$\begin{bmatrix} 1 & 0 \\ -\frac{1}{f_2} & 1 \end{bmatrix}$
4	Propagation over distance l_2	$\begin{bmatrix} 1 & l_2 \\ 0 & 1 \end{bmatrix}$
5	Entrance to the mirror	$\begin{bmatrix} 1 & 0 \\ 0 & \frac{1}{n} \end{bmatrix}$
6	Propagation in the mirror	$\begin{bmatrix} 1 & d_\mathrm{m} \\ 0 & 1 \end{bmatrix}$
7	Exiting the mirror	$\begin{bmatrix} 1 & 0 \\ \frac{(n-1)}{R} & n \end{bmatrix}$

Table 7.3: Ray matrices M_i used to calculate positions of lens of mode-matching. 5: planar dielectric interface; 7: spherical dielectric interface. n: a refractive index of the glass the mirrors in the cavity are made from; d_m: thickness of the mirror (4 mm); l_1: distance between lenses; l_2: distance from the last lens to the optical cavity.

optical component, the complex beam parameter is transformed according to the ABCD law

$$q' = \frac{Aq + B}{Cq + D} \tag{7.33}$$

when the ray matrices

$$M_i = \begin{bmatrix} A & B \\ C & D \end{bmatrix} \tag{7.34}$$

are used. The beam undergoes transformations by optical components, whose ray matrices are written in table 7.3. The beam at the moment of exiting the first mirror of the resonator is a modification of the original beam by the product of these ray matrices

$$M = \prod_{i=1}^{7} M_i \tag{7.35}$$

The complex beam parameter calculated according to (7.33) is labelled as q' from now.

The stability criteria of the optical resonator demands the complex beam parameter with the absolute value given by the prescription [see Yariv, 1997, p. 134]

$$q_\mathrm{res} = -\frac{1}{R} - i\sqrt{\frac{1}{dR}\left(2 - \frac{d}{R}\right)}\,. \tag{7.36}$$

It means that condition

$$q' = q_{\mathrm{res}} \tag{7.37}$$

must be fulfilled. The freely variable parameters are l_1 and l_2, the separation of both lenses of the mode matching system and the distance from the last mirror to the optical resonator, respectively. One can obtain them from the solutions of two equations with two variable (l_1 and l_2)

$$\mathrm{Im}(q') = \mathrm{Im}(q_{\mathrm{res}}) \tag{7.38}$$

and

$$\mathrm{Re}(q') = \mathrm{Re}(q_{\mathrm{res}})\,. \tag{7.39}$$

Their solution can be calculated well using a computer algebra system like Maxima (`http://maxima.sourceforge.net`).

7.3 Evaluation of recombination rate coefficients

The effective recombination rate coefficient is evaluated by fitting the formula (3.7) to the measured evolution of the number density of monitored ion specie after the discharge is switched off. The number density of the ions in specific states are calculated according to (7.12). The overall number density of the ions is calculated according to (7.8). At low temperatures only several states are populated. If we can monitor them, the sum of their number densities is taken as the overall number density.

7.3

8. Flowing Afterglow with Langmuir Probe – Cryo-FALP II

Cryo-FALP II apparatus is a modification of a standard FALP (Flowing Afterglow with Langmuir Probe) device. The details of the FALP technique are in Larsson and Orel [2008] and Smith et al. [1975]. The current experimental setup is described in Kotrík et al. [2011b] and very thoroughly in Kotrík [2013], therefore I will give only a basic description here.

8.1 Overview

A scheme of principle of the apparatus is drawn in figure 8.1. A helium buffer gas is ionised in a microwave discharge in the upstream glass section of the flow tube, enters the stainless steel flow tube, and is pumped out by a Roots pump located at the other end of the flow tube. Argon is added a few centimetres down stream from the discharge (section I. in the figure) to remove metastable helium atoms and to form an Ar^+ dominated plasma. Further down stream (section II. in the figure), H_2 (or D_2) is added to form H_3^+ (or D_3^+) dominated plasma. The sequence of ion–molecule reactions leading to the formation of H_3^+ (D_3^+) dominated plasma is discussed for example in Novotný et al. [2006]; Plašil et al. [2002]. The crucial reactions are written in table 8.1. The decrease of the electron number density n_e along the flow tube is measured by means of axially movable Langmuir probe.

The region I. in figure 8.1 is pre-cooled by a liquid nitrogen to ≈ 100 K. The region II. is cooled by a cold head of helium closed-cycle refrigerator Sumitomo CH 110. The desired temperature is achieved by simultaneous cooling of the cold head and heating of the elements connecting thermally the cold head with the flow tube. The cold head is positioned in a vacuum vessel and thermally isolated in this way. The temperature is monitored by silicon diodes and transistors installed along the flow tube and on the cold head at several places. Since the buffer gas has the velocity of several meters

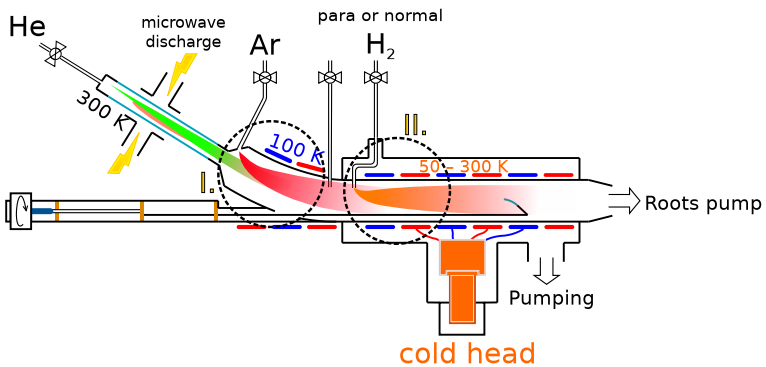

Figure 8.1: Scheme of principle of Cryo-FALP II apparatus and its mode of operation. I. and II. indicate two different reaction- and temperature regions. The inner diameter of the flow tube $d = 5$ cm.

region	reaction			rate coefficient (cm^3s^{-1})	reference
I.	$He^M + Ar$	$\rightarrow$	$Ar^+ + He + e$	7(−11)	Ikezoe et al. [1987]
	$He_2^+ + Ar$	$\rightarrow$	$Ar^+ + 2\ He$	0.2(-9)	Anicich [2003]
II.	$Ar^+ + H_2$	$\rightarrow$	$ArH^+ + H$	0.8(-9)	Dotan and Lindinger [1982]
		($\rightarrow$	$H_2^+ + Ar$)	negligible	and Anicich [2003]
	$H_2^+ + Ar$	$\rightarrow$	$ArH^+ + H$	2.3(-9)	Glosík [1994]
	$H_2^+ + H_2$	$\rightarrow$	$H_3^+ + H$	2(-9)	Cordonnier et al. [2000]
	$ArH^+ + H_2$	$\rightarrow$	$H_3^+ + Ar$	1.5(-9)	Villinger et al. [1982]

Table 8.1: The most important reactions leading to H_3^+ formation in Cryo-FALP II, the room temperature values. He^M stands for helium atom in a metastable state (2^3S, Plašil et al. [2002]). The last two reactions are mentioned in chapter 2 because of their branching ratios to different nuclear spin states of H_3^+ ions. The rate coefficients of reactions for region II. have not-fully-understood temperature dependence at low temperatures [Ervin and Armentrout, 1985; Hawley and Smith, 1992; Hu et al., 2013].

per second, its temperature T_{He} does not correspond to the temperature of the flow tube T_{FT}. Typical axial distance l, at which $T_{He} = T_{FT}$ has the magnitude of order of the diameter of the flow tube. Lower the temperature is and faster the gas velocity is, longer is this "relaxation length". This must be considered during evaluation of measured n_e decay curves. For the computer simulation of buffer gas cooling, see Kotrík [2013].

The gases flow through a purification cold trap – reservoir filled with liquid nitrogen or pre-cooled ethanol ($\approx$ 170 K), depending on the boiling point of the gas used. The He gas, as a main source of impurities due to large flows used, is purified also in two zeolite molecular traps cooled by liquid nitrogen. Flows of He, Ar and $^nH_2$ gases are measured by flow meters and controlled by flow controllers or needle valves. The flow of $^eH_2$ is set by temperature of the para-hydrogen generator's cold head. Since there is no flow meter on the way of $^eH_2$ to avoid a back conversion on a surface of the meter's heated parts, the conductivity of the valve V1 from figure 5.1 (para-hydrogen generator's vacuum scheme) must be calibrated before each measurement. This is done by setting the pressure above turbine TMH 260 (measured by Pn3 Penning gauge) and a specific flow at flow meter FM1 shown in figure 8.2.

8.2 Data analysis

In Cryo-FALP II, n_e along the flow tube is measured by the movable Langmuir probe. Since the gas and the plasma are flowing, the position of the probe l in the flow tube can be interpreted as the time position t in the physicochemical processes if we use an appropriate transformation $t = f(l)$. This function is obtained by a calibration measurements when the power of the microwave discharge is modulated and the time delay of n_e modulation at various positions l is measured [see Kotrík, 2013]. The Langmuir probe is calibrated by measurements of a well-known reaction rate-coefficient, typically of O_2^+-e^- recombination.

To obtain the effective recombination rate coefficient α_{eff}, measured n_e(t)

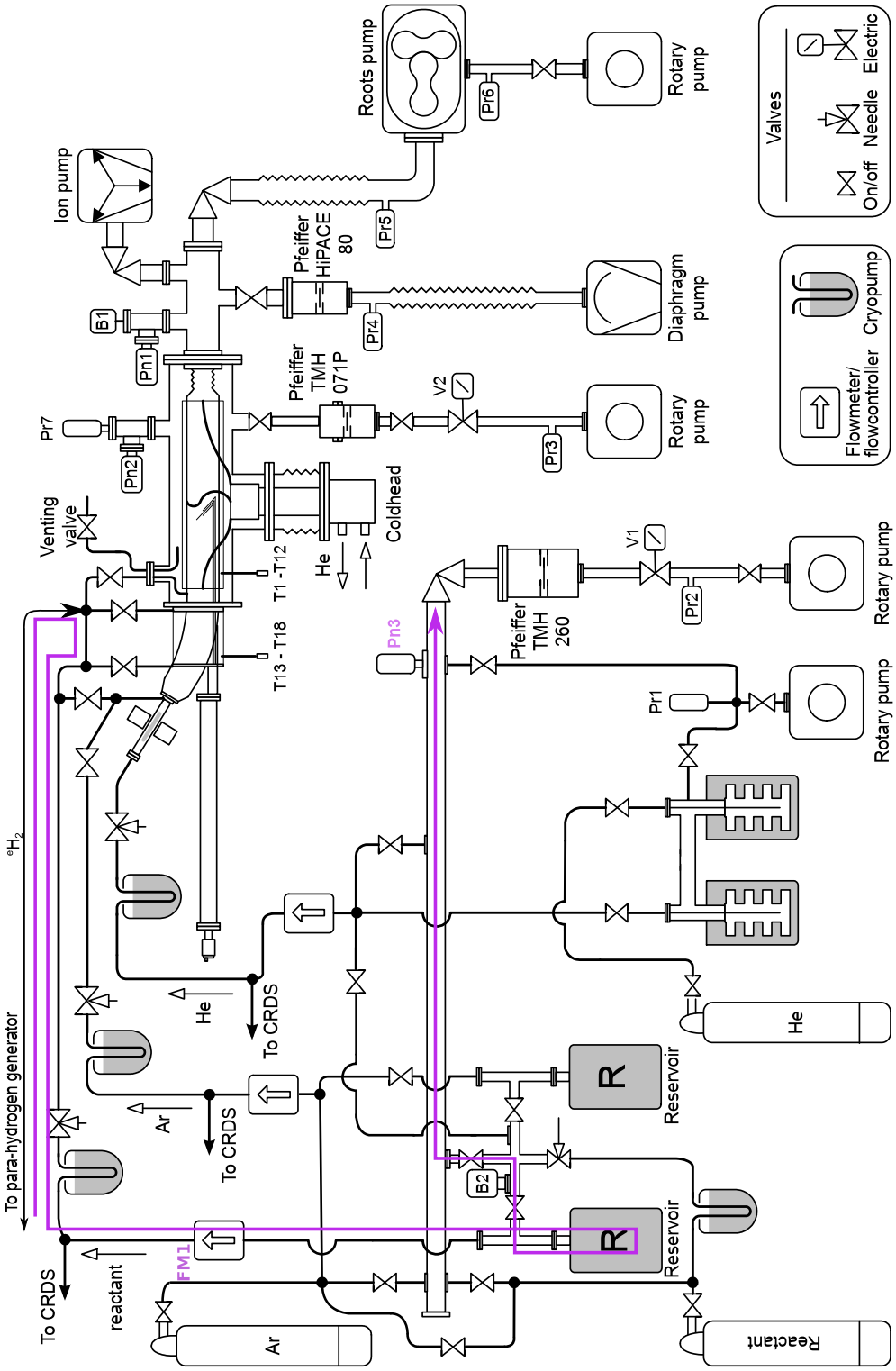

Figure 8.2: Vacuum scheme of Cryo-FALP II apparatus. A path of $^{e}H_2$ gas during calibration is highlighted by a purple line. Modified picture from Kotrík [2013].

can be fitted by function (3.7). The problem is that this method is partly based on a subjective choice of the beginning of the decay time period $t = 0$ in the flowtube (note the time-space transformation): one often cannot distinguish when the ion-formation (consisting of reactions from table 8.1) is complete and when only the recombination and the diffusion prevail. The ideal decay curve described by function (3.7) can be also perturbed by inhomogeneous temperature in the beginning of the flowtube in reality. Another problem is that function (3.7) is non-linear in its parameters, so the usage of the simple least-square fitting method is not favourable [Press, 2007].

To overcome the aforementioned disadvantages, a so called "advanced integral analysis method" [Korolov et al., 2008] was used to filter out the effect of diffusion and ion formation from the recombination curve. This is based on a formula obtained from integration of equation (3.6)

8.2

$$\log\left[\frac{n_\mathrm{e}(t_1)}{n_\mathrm{e}(t_0)}\right] + \frac{t_1 - t_0}{\tau} = -\alpha_\mathrm{eff} \int_{t_0}^{t_1} \xi(t) n_\mathrm{e}(t) \mathrm{d}t \tag{8.1}$$

where $\xi = [\mathrm{A}^+]/n_\mathrm{e}$ (A^+ is a studied dominant ion) and t_0 and t_1 are integration limits. If we define

$$x = \int_{t_0}^{t_1} n_\mathrm{e}\,\mathrm{d}t \tag{8.2}$$

and

$$y = \log\left[\frac{n_\mathrm{e}(t_1)}{n_\mathrm{e}(t_0)}\right] + \frac{t_1 - t_0}{\tau}\,, \tag{8.3}$$

then if $\xi = 1$ (the studied ion is dominant),

$$y(x) = -\alpha_\mathrm{eff} x\,. \tag{8.4}$$

When we analyse measured data, the integration limit t_0 is chosen so that the resulting $y(x)$ has the form of the relation (8.4) [1]. The constant α_eff is obtained as a slope of $y(x)$. In this way we avoid the region in the flow tube, in which the chemical kinetics can not be simply described by the recombination and the diffusion.

A similar method can be used to obtain the rate coefficient for the collisional radiative recombination K_CRR, if we substitute α_eff to K_CRR and $\xi(t)$ to $\zeta(t)n_\mathrm{e}$ ($\zeta = [\mathrm{A}^+]/n_\mathrm{e}$).

[1] This holds only when proper τ is used. The diffusion time τ is regarded as a variable parameter obtained by minimising the χ^2 of the linear fit.

Part III

Experimental Results

9. Determining population of H_2 molecule's nuclear spin states

9.1 Nuclear magnetic resonance

$^{p}H_2$ has been used to enhance a sensitivity of nuclear magnetic resonance (NMR) experiments for more than 30 years [Canet et al., 2006]. In so called PASADENA or ALTA-DENA experiments, $^{p}H_2$ molecule is inserted in a molecule at two non-equivalent positions by an appropriate chemical reaction. The resultant product exhibits 10^4–10^5 times greater "hyperpolarised signals" in proton NMR spectra [see Canet et al., 2006, and references therein]. In case of evaluation of $^{p}f_2$ in $^{e}H_2$ gas, one can simply take advantage of the fact that $^{p}H_2$ is not visible in NMR spectrum because of its zero magnetic moment, and compare the $^{o}H_2$ signals from $^{e}H_2$ and $^{n}H_2$, which has known $^{p}f_2 = 0.25$.

9.1.1 Methodology

NMR spectrum was obtained using Bruker DRX 500 NMR Spectrometer operating at magnetic field 11.7 T (^{1}H resonance frequency 500 MHz)[1]. The samples were prepared in a following manner. 50×10^5 Pa cm^3 of $^{n}H_2$ was liquefied in para-hydrogen generator containing untreated Fe_2O_3 catalyst at $T_{CC} = 11$ K. After 30 minutes, the catalyst was heated to $T_{CC} = 18$ K to obtain $^{e}H_2$ gas with vapour pressure $\approx 10^5$ Pa. Since this gas was going to be the one with a maximum value of $^{p}f_2$ we distinguish it by labelling it as $^{e}_{m}H_2$ in this work. The outlet of the $^{e}_{m}H_2$ (from CC) was opened to an evacuated NMR cuvette immersed into the liquid nitrogen in order to obtain a higher room-temperature pressure of the sample. The $^{n}H_2$ was simply put to the $^{n}H_2$ cuvette from a bottle and the gas pressure was set by a reduction valve to $\approx 2 \times 10^5$ Pa. As soon as the samples were prepared, the NMR measurements at temperature 77 K were performed.

The exact amount of the gas in the cuvettes was not measured until the NMR experiments were finished to avoid ortho-para back-conversion on unknown surfaces of a gauge. Eventually, the amount of H_2 gas in the cuvettes was measured as a pressure in a chamber with known volume, to which the gas was expanded.

9.1.2 Results and discussion

The results from measurements of NMR spectra of $^{e}_{m}H_2$ and $^{n}H_2$ samples are shown in figure 9.1. The value of $^{p}f_2$ for $^{e}_{m}H_2$ was evaluated from the integrated signal intensities and it was found to be (0.87 ± 0.01) (the uncertainty results from an error of the fit).

Since this value was lower than expected, 41 ^{1}H spectra of $^{o}H_2$ were acquired during the period of 20 hours at 298 K. The integrated signal intensities

[1] Special acknowledgement to RNDr. Jan Lang, Ph.D. from the Department of Low Temperature Physics.

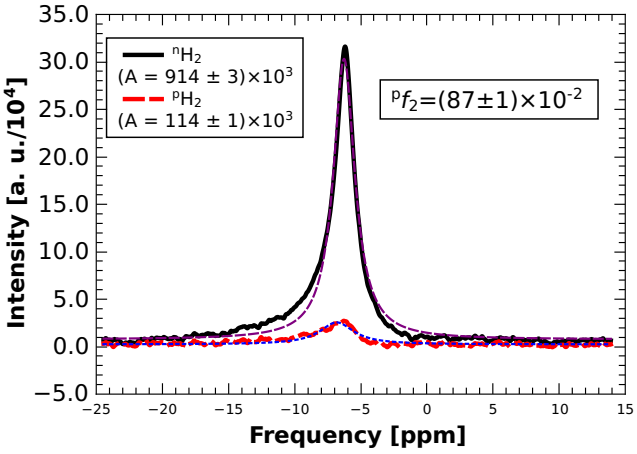

Figure 9.1: NMR spectrum of $^{\mathrm{p}}\mathrm{H}_2$ and $^{\mathrm{o}}\mathrm{H}_2$ in cuvette

were subject to exponential fit. The back conversion rate was calculated to be $\tau = (97 \pm 4)$ hours, which means 0.9% in the first hour. This agrees with the observation by Tom et al. [2009a] (0.8% hour^{-1} for NMR tube). Such a high back-conversion rate is most probably caused by presence of O_2 impurities, which may have been caused by a bad seal of the cuvette and by difficulty of evacuation of such glass container (see section 9.1.1 and work by Tom et al. [2009a]).

9.2

The high initial value of $^{\mathrm{o}}f_2$ could have several reasons: the impurity in the NMR cuvette; a high temperature of the outlet tube, which may have contained a catalysing dust; Fe_2O_3 catalyst was not treated by heat in hydrogen atmosphere (see section 5.3); the ortho-to-para conversion period of 30 minutes could have been not enough. However, the most probable is the variant that $^{\mathrm{e}}_{\mathrm{m}}\mathrm{H}_2$ was leaking from the NMR cuvette and the pressure inside measured after the NMR experiment was lower than during the NMR measurement. This had the effect that the $^{\mathrm{o}}\mathrm{H}_2$ signal was assigned to lower $[\mathrm{H}_2]$ than it was in reality.

Because of big amount of possible systematic errors, NMR measurement of $^{\mathrm{p}}f_2$ is perceived as a rough estimation. Since the precise knowledge of $^{\mathrm{p}}f_2$ is of no importance for H_3^+-recombination studies the final statement that

$$^{\mathrm{p}}f_2 = 0.87^{+0.13}_{-0.01}$$

(for $^{\mathrm{e}}_{\mathrm{m}}\mathrm{H}_2$) was satisfactory.

9.2 $\mathrm{N}^+ + \mathrm{H}_2$ reaction

We measured dependence of the reaction rate coefficient k from (4.3) on kinetic temperature of H_2 and He buffer gases at various ratios $[^{\mathrm{e}}_{\mathrm{m}}\mathrm{H}_2]$:$[^{\mathrm{n}}\mathrm{H}_2]$. Heat-activated $HFeO_2$ (see section 5.3) was used as the catalyst and typically 50 scc of $^{\mathrm{n}}\mathrm{H}_2$ was adsorbed on it at $T_{\mathrm{CC}} = 11$ K for more than 1 hour.

The results of the measurements of k are plotted in figure 9.3. The dashed lines indicate the fits of $^{\mathrm{o}}k$ and $^{\mathrm{p}}k$ by the Arrhenius-type formula

$$k = k_{\mathrm{A}} \exp(-T_{\mathrm{A}}/T) \tag{9.1}$$

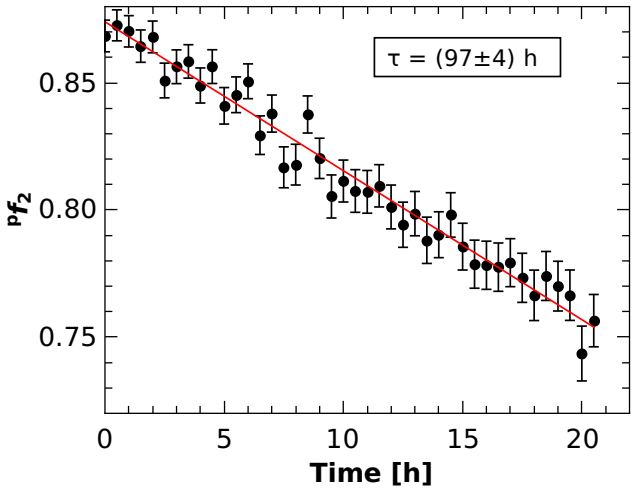

Figure 9.2: Decrease of ${}^{\mathrm{p}}f_2$ in cuvette in time

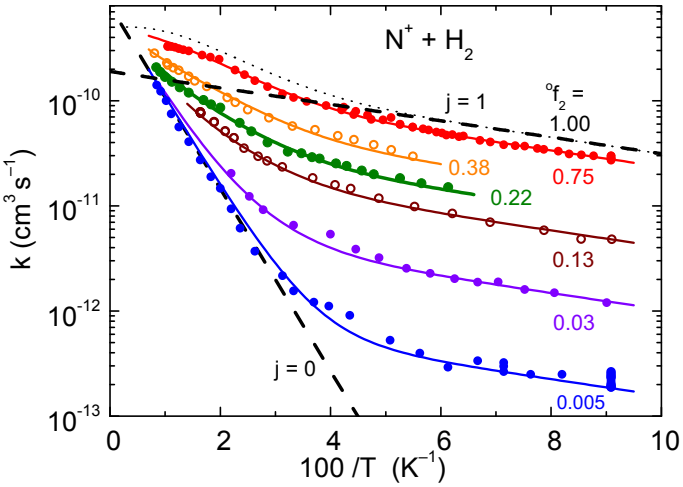

Figure 9.3: Arrhenius plot of the reaction rate coefficient k for various values of ${}^{\mathrm{o}}f_2$. Dashed lines: fits of ${}^{\mathrm{e}}\mathrm{H}_2$ and ${}^{\mathrm{o}}\mathrm{H}_2$ data by formula (9.1). ${}^{\mathrm{o}}\mathrm{H}_2$: $k_{\mathrm{A}} = 1.9 \times 10^{-10}\,\mathrm{cm^3 s^{-1}}$, $T_{\mathrm{A}} = 18$ K. ${}^{\mathrm{p}}\mathrm{H}_2$: $k_{\mathrm{A}} = 14 \times 10^{-10}\,\mathrm{cm^3 s^{-1}}$, $T_{\mathrm{A}} = 230$ K.

in the temperature ranges mentioned in relations (4.4) and (4.5). The lowest obtainable ${}^{\mathrm{o}}f_2$ was found to be 0.5%. Figure 9.4 depicts a calibration line for evaluating ${}^{\mathrm{o}}f_2$ from the value of k measured at the temperature of the trap 11 K.

9.2.1 Investigation of influence of vacuum system's settings on ${}^{\mathrm{p}}f_2$

This chapter is an extension and explanation of the article by Hejduk et al. [2012b].

The lowest accessible ${}^{\mathrm{o}}f_2$ is affected by the duration of ${}^{\mathrm{e}}_{\mathrm{m}}\mathrm{H}_2$ gas' stay in the pipe leading from the para-hydrogen generator to the trap, probably because of the para-to-ortho back-conversion on unknown catalytic surface, for example walls of the pipe. Most probably, the following holds for final ${}^{\mathrm{p}}f_2$ of the gas

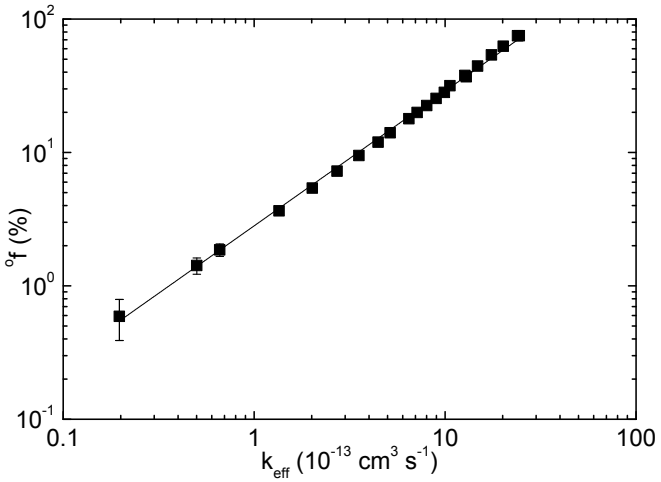

Figure 9.4: Dependence of $^{\mathrm{o}}f_2$ on k at temperature of the trap 11 K – " $^{\mathrm{o}}f_2$-meter". Obtained at $T_{\mathrm{CC}} = 11$ K. The value of $^{\mathrm{o}}f_2$ was varied by adding $^{\mathrm{e}}\mathrm{H}_2$ to $^{\mathrm{n}}\mathrm{H}_2$. The line (if drawn in linear scales) is a degree 1 polynomial, which has the value $^{\mathrm{o}}f_2 = 0$ at $k = 0\,\mathrm{cm^3 s^{-1}}$. $[\mathrm{H}_2] = 5.5 \times 10^{11}\,\mathrm{cm^{-3}}$ – $5.0 \times 10^{12}\,\mathrm{cm^{-3}}$, He not present.

9.2

injected to the trap:

$$^{\mathrm{p}}f_2 = {}^{\mathrm{p}}f_{20} \exp\left(-\nu\tau\right), \tag{9.2}$$

where $^{\mathrm{p}}f_{20}$ is the initial value of $^{\mathrm{p}}f_2$ of the $^{\mathrm{e}}_{\mathrm{m}}\mathrm{H}_2$ gas above the catalyst, ν is a para-to-ortho back-conversion rate (in $\mathrm{s^{-1}}$) and τ is the time $^{\mathrm{e}}\mathrm{H}_2$ gas has spent in the pipe. This time τ can be shortened by side-pumping of $^{\mathrm{e}}\mathrm{H}_2$ gas that has not flown into the trap through a by pass depicted in figure 5.1. In an approximation,

$$\tau = \frac{P_{\mathrm{x}} M l}{q} = \frac{P_{\mathrm{x}} M l}{PS}, \tag{9.3}$$

where P_{x} is the pressure inside the connection pipe, M and l are a cross section and a length of the pipe, respectively, and q is the flow through the turbine, which is equal to the product of the pressure above the turbine P and its pumping speed S.

Since majority of the $^{\mathrm{e}}\mathrm{H}_2$ gas is pumped by turbine

$$(P_{\mathrm{C}} - P_{\mathrm{x}})C_1 = PS \Rightarrow P_{\mathrm{x}} = P_{\mathrm{C}} - \frac{PS}{C_1}, \tag{9.4}$$

where P_{C} is the pressure above the catalyst and C_1 is the conductance of valve V1 (see figure 5.1). P_{C} can be expressed by a simplified Antoine equation

$$P_{\mathrm{C}} = A \exp\left(-\frac{B}{T_{\mathrm{CC}}}\right) \tag{9.5}$$

with free parameters A and B.

If we put all the relations together, we obtain

$$\log {}^{\mathrm{p}}f_2 = \log {}^{\mathrm{p}}f_{20} - \left\{A \exp\left(-\frac{B}{T_{\mathrm{CC}}}\right) - \frac{PS}{C_1}\right\} \frac{Ml\nu}{PS}, \tag{9.6}$$

Variable	Meaning	Units
${}^{\mathrm{p}}f_{20}$	initial ${}^{\mathrm{p}}f_2$	–
A	vapour pressure dependence parameter	Pa
B	vapour pressure dependence parameter	K
T_{CC}	catalyst temperature	K
P	pressure above the turbomolecular pump	Pa
S	pumping speed of the turbomolecular pump	$\mathrm{cm}^3\ \mathrm{s}^{-1}$
C_1	conductance of the valve V1	$\mathrm{cm}^3\ \mathrm{s}^{-1}$
M	cross section of the pipe	cm^2
l	length of the pipe	cm
ν	rate of para-to-ortho back-conversion	s^{-1}

Table 9.1: Variables in equation (9.6). The dependence of the vapour pressure on the catalyst temperature is a simplified Antoine equation.

for the final ${}^{\mathrm{p}}f_2$ (used variables are summarised in table 9.1). The expression can be simplified further to

$$\log {}^{\mathrm{p}}f_2 = X + Y \exp\left(-\frac{Z}{T}\right) \tag{9.7}$$

to contain only three unknown parameters X, Y and Z.

If we keep P and C_1 constant and vary T_{CC}, we can obtain the rate of back-conversion ν. Results of the measurement carried out for this purpose are in figure 9.5. The experimental data are fitted using the simplified equation (9.7). The resulting parameters are the following: $X = (2 \pm 9)\,10^{-3}$, $Y = -(8 \pm 30)$, $Z = (93 \pm 6)$ K. From Y we can estimate $\nu < 5 \times 10^{-2}\mathrm{s}^{-1}$ if we take the value for A from van Itterbeek et al. [1964] (as an estimation because of different temperature range in the work), however with huge (one order of magnitude) error.

As a complementary measurement, a dependence of ${}^{\mathrm{p}}f_2$ on P with the catalyst at a temperature $T_{\mathrm{CC}} = 11$ K was measured. This is equivalent to measuring the dependence of ${}^{\mathrm{p}}f_2$ on side-pumping speed. P was set by the needle valve V2. Equation (9.6) can be modified to the form

$$\log {}^{\mathrm{p}}f_2 = X - \frac{Y}{P}\,. \tag{9.8}$$

By fitting this to experimental data for two different C_1, we obtain $X = -(6.5 \pm 0.5)\,10^{-3}$ and $Y = (3.8 \pm 0.7)\,10^{-6}$ Pa for the first case, $X = -(6.0 \pm 0.5)\,10^{-3}$ and $Y = (9 \pm 4)\,10^{-7}$ Pa for the second case. If we put (9.7) and (9.8) to one equation and take the vapour pressure above solid hydrogen at the temperature 11 K from Bates [2002], we can estimate $\nu > 5 \times 10^{-4}\,\mathrm{s}^{-1}$. Moreover, we can derive backwards, that the valve V1 was open more in the first case than in the second case, which is in perfect agreement with our intuition: if we open the valve V1 more, we need to close the valve V2 more to keep the same P and therefore P_{x} rises and the back-conversion speeds up.

The measurements described above have shown that the back-conversion rate $\nu \in \langle 10^{-4}, 10^{-2} \rangle\ \mathrm{s}^{-1}$. The uncertainty is caused by the unknown pressure

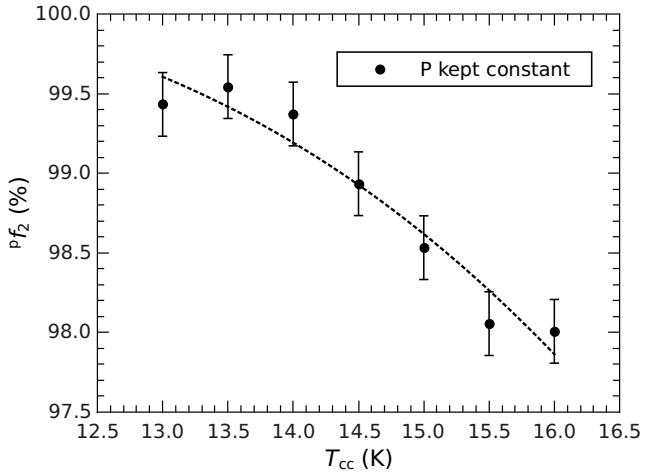

Figure 9.5: The dependence of $^{p}f_2$ on the catalyst temperature at fixed P. The formula from equation (9.7) is fitted to experimental data (dashed line). $X = (2\pm9)\,10^{-3}$, $Y = -(8\pm30)$, $Z = (93\pm6)$ K. $P = 5\times10^{-2}$ Pa, temperature of the trap 11 K.

9.2

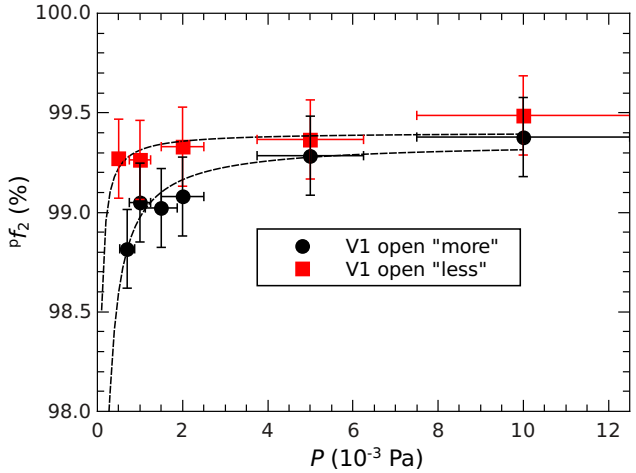

Figure 9.6: The dependence of $^{p}f_2$ on the pressure above the turbomolecular pump. (0.8) is fitted to the results (dashed line). Dots: $X = -(6.5\pm0.5)\,10^{-3}$, $Y = (3.8\pm0.7)\,10^{-6}$ Pa, squares: $X = -(6.0\pm0.5)\,10^{-3}$, $Y = (9\pm4)\,10^{-7}$ Pa, and hence C_1 for dots data is lower than for squares data.

behind the valve V1 (above the catalyst) P_C. Since the spontaneous para-to-ortho back conversion is forbidden, the calculated rate is relatively fast. This can be caused by the presence of a catalytic material on the way of $^eH_2$ gas to the trap. One of the candidates for such material is the material of the leak valve, for example, whose seal is made of Sapphire or Ruby which are both oxides of Al or Cr.

9.2.2 Conclusion

We are able to calculate the abundance of $^oH_2$ in $^eH_2$ produced by the para-hydrogen generator from measured rate coefficient of the reaction (4.1) (see figure 9.4). The lowest obtainable fraction of the ortho-states is

$$^of_2 = (0.5 \pm 0.2)\% \,.$$

This limit was tried to be lowered further by examining the influence of by-pass pumping of the abundant H_2 gas (H_2 gas which does not flow to the trap immediately). Even though the influence of the fraction on the pressure in the outlet tube was observed, it is not possible to reach higher abundance of the para-states by any setting of the para-generator's vacuum system. The para-to-ortho back-conversion rate was estimated to lie in the interval $\nu \in \langle 10^{-4},\, 10^{-2} \rangle\, s^{-1}$. The role of the pipe's and valves' material composition in the para-to-ortho back-conversion is disputable. In any case, the level of ortho-H_2 impurity in our para-states-enriched H_2 in the trap is the lowest in-situ value ever documented in detail at similar ion-trapping experiments [Gerlich and Kaefer, 1989; Gerlich et al., 2002; Hugo et al., 2009].

9.2

10. $N^+ + H_2 \rightarrow NH^+ + H$

This chapter is an explanation and a summary of Attachment A.1.

The title reaction was studied using 22PT apparatus. See Attachment A.1 for the results of these studies and section 6 for a description of the measurement procedure. The experiments were performed with N^+ primary ions produced via dissociative ionisation of N_2 in SIS using energetic electrons (60 eV). Under such conditions, population of $^3P_0/^3P_1/^3P_2$ states is 1:3:5 (see figure 4.2). The target molecules H_2 were present in the form of gas filling up the chamber with the trap.

A typical set of raw data, recorded at a 22-pole temperature of 52 K and with buffer and reactant gas in the trap ([He] = 5.2×10^{11} cm^{-3}, [$^nH_2$] = 1.6×10^{11} cm^{-3}), is shown in figure 3 of Attachment A.1. In the first 10 ms, the sum of all detected ions Σ is increasing due to phase-space compression of the injected ion cloud via collisions with the cold buffer gas. This leads to an increase of the detection efficiency (mainly acceptance and transmission of the quadrupole).

Figure 10.1 shows a linear decay of the number density of N^+ over 4 orders of magnitude. The decay is obviously single-exponential with one rate coefficient written in the figure. No deviation from this behaviour was observed in the temperature range 11–100 K and concentration ranges [H_2] $\sim 10^{11}$–10^{13} cm^{-3} and [He] $\sim 10^{12}$–10^{13} cm^{-3}. The rate coefficient of the reaction k was evaluated predominantly using the formula (6.5). The figure 3 of Attachment A.1, illustrates that t_0 had to be set to later than 10 ms because of the thermalisation (see section 6.2). The thermalisation concerns the kinetic temperature but also the FS states. The relaxation of the latter contradicts theoretical descriptions of the reaction, as it was mentioned in section 4. The period $\Delta t = (t_{\text{fin}} - t_0)$ was always set long enough to let the counts of N^+ decrease at least 6 times, i.e.

$$\Delta t > \frac{\log 6}{k[H_2]}\,. \tag{10.1}$$

The figure 9.3 shows the dependence of the rate coefficients on the buffer gas temperature for several values of $^o f_2$. A deviation of the Arrhenius-type dependence from a single-exponential at higher gas temperatures (> 33 K) for $^o f_2 = 0.75$ is obvious at first glance (see also figure 4 of Attachment A.1).

10.1 FS state-specific reaction rate coefficients, method of gradual fitting

Non-single-exponential characteristic of the Arrhenius-type dependence in figure 9.3 cannot be reproduced by the model when all three FS states have same reaction rate coefficients with the single-exponential temperature dependence like (4.2) and the distribution of FS states is independent on the temperature

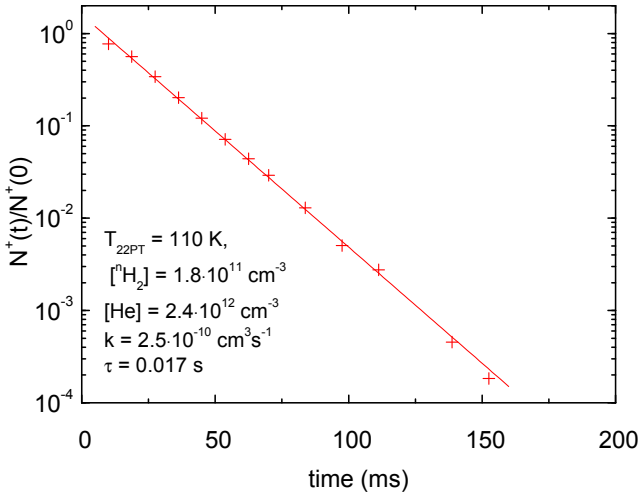

Figure 10.1: Decay of number of N^+ ions in over long period (150 ms).

(1:3:5 for $j_a = 0$, 1, 2, for example). Therefore we suggest that

$$k = {}^{o}f_2 \underbrace{(\xi_0 k_{1,0} + \xi_1 k_{1,1} + \xi_2 k_{1,2})}_{k_{1,x}} + (1 - {}^{o}f_2) \underbrace{(\xi_0 k_{0,0} + \xi_1 k_{0,1}) + \xi_2 k_{0,2}}_{{}^{p}k}, \quad (10.2)$$

10.1

where ξ_{j_a} is a thermal population of FS state $^3P_{j_a}$, $k_{j,j_a}(T)$ is a state specific rate coefficient for H_2 in the rotational state with angular momentum quantum number j and N^+ ion in the $^3P_{j_a}$ state.[1] To keep things simple, we offer following prescription of k_{j,j_a}:

$$k_{j,j_a} = k_A \exp(-T_A/T), \quad (10.3)$$

where the Arrhenius parameters k_A (the "frequency factor") and T_A (the activation energy) are different for each combination of j, j_a.

Results of measurements of a dependence of k on ${}^{o}f_2$ are plotted in figure 5 of Attachment A.1 for 5 different temperatures (11, 33, 47, 57, 100 K). We can see from the figure that, as far as ${}^{o}f_2$ dependence of k is concerned, the relation (10.2) is valid.

We can extract the first term of the formula (10.2) ($k_{1,x}$) by following operation on measured data from figure 9.3:

$$k_{1,x} = \frac{k - {}^{p}f_2 {}^{p}k}{{}^{o}f_2}. \quad (10.4)$$

The coefficient ${}^{p}k$ was obtained from the data for ${}^{o}f_2 = 0.005$ (see figure 9.3). The result is plotted in figure 10.2. Now the coefficient $k_{1,0}$ can be obtained by fitting the data in $^3P_0$-dominant region (see table 10.1).

Similarly, $k_{1,1}$ can be obtained by operation

$$k_{1,1} = \frac{k_{1,x} - k_{0,0}\xi_0}{\xi_1} \quad (10.5)$$

and the result is plotted in figure 10.3.

[1] Here I refer to the angular momentum quantum number as j unlike in chapter 1 to keep track with Attachment A.1.

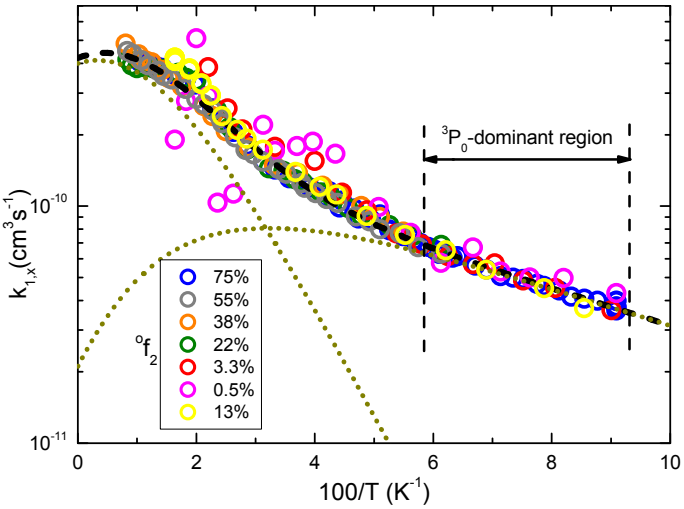

Figure 10.2: Dependence of $k_{1,x}$ from equation (10.4) on temperature. Dotted lines: $k_{1,0}$ and $k_{1,1}$ calculated using the Arrhenius parameters from table 10.1. Dashed line: $k_{1,0} + k_{1,1}$. Data obtained at various fractions (written in a box) are distinguished by colours.

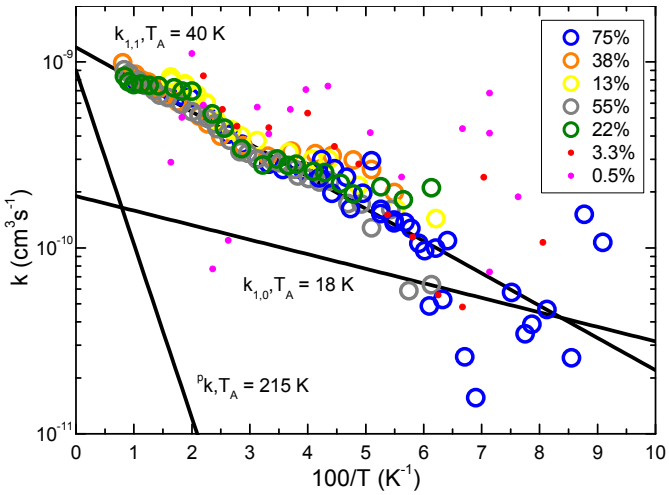

Figure 10.3: Dependence of $k_{1,1}$ form (10.5) on temperature. $k_{1,0}$ and ^pk are also drawn. See also table 10.1

	k_A (10^{-10} cm^{3}s^{-1})	T_A (K)
${}^pk$	9.0	215
$k_{1,0}$	1.9	18
$k_{1,1}$	12	40

Table 10.1: Parameters of (10.3) evaluated by the method of gradual fitting

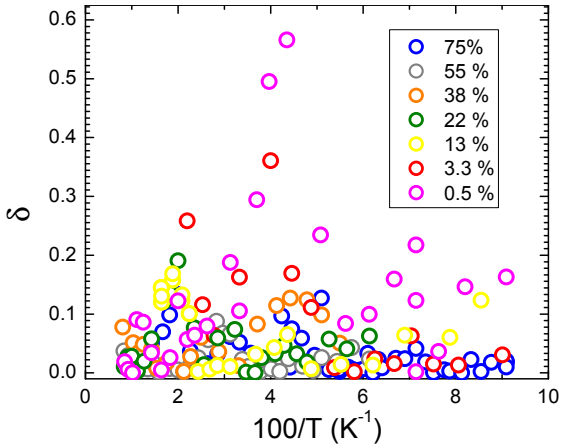

Figure 10.4: Dependence of δ (relative error) on temperature. Note that values for ${}^o f_2 = 0.5\%$ and 3.3% are mainly affected by single-exponential fit of ${}^pk$.

10.2

The coefficient $k_{1,2}$ was not evaluated because of high error originating from the procedure described above. The coefficient ${}^pk$ has also ξ_{j_a} dependent parts, but since the described method leads to high errors of $k_{0,0}$ and $k_{0,1}$, ${}^pk$ was set to be equal for all FS states. The characteristics of the Arrhenius-type dependences for ${}^o f_2 < 3.3\%$ are affected by impurities in helium buffer gas – in case of typical concentration 5×10^{12} cm^{-3}, impurities contribute to k evaluated by the formula (6.5) with $\Delta k \approx 5 \times 10^{-12}$ cm^{3}s^{-1} at $T > 50$ K and with $\Delta k \approx 3 \times 10^{-13}$ cm^{3}s^{-1} at $T < 50$ K according to our measurements. The coefficients k_A and T_A evaluated here are summarised in table 10.1.

The error of our model can be expressed as

$$\delta = \sqrt{\frac{(k - k_{\text{fit}})^2}{k_{\text{fit}}^2}}\,, \tag{10.6}$$

where k is the measured rate coefficient and

$$k_{\text{fit}} = {}^o f_2(k_{1,0}\xi_0 + k_{1,1}\xi_1) + (1 - {}^o f_2){}^pk\,. \tag{10.7}$$

The error δ is plotted in figure 10.4. We can see that the relative error is $\approx$ 10 % for data for ${}^o f_2 > 3.3\%$. This is much better than δ originating from comparison of our data with a single-exponential relation proposed by Marquette et al. [1988] that rises up to 100% at low temperatures. The effort to minimise δ even for data for ${}^o f_2 \leq 3.3\%$ lead to fitting results written in table 1 in Attachment A.1.[2]

[2]Special acknowledgement to prof. Dieter Gerlich.

10.2 Relaxation of FS states, model of chemical kinetics

Here I speculate on the relaxation of FS states that may take place in our experiment. I constructed a model of chemical kinetics including the association reactions and the conversion between FS states. The main purpose was to test sensitivity of our physical model from section 10.1 to introduction of finite relaxation rate coefficients. In following piece of text, I try to answer questions

1. how fast the relaxation must be to observe a single exponential decay like in figure 10.1 if coefficients from table 10.1 are supposed to be real;

2. How fast the relaxation must be to observe the Arrhenius-type dependence from figure 9.3 to keep the results from table 10.1 valid.

If we consider that N^+ ions are produced with high temperature distribution 1:3:5 for states $^3P_0$,$^3P_1$,$^3P_2$, it appears at first glance that the rate coefficient of relaxation

$$N^+(^3P_{j_a}) + H_2(j) \xrightarrow{k_{\text{relax}}} N^+(^3P_{j_a\prime}) + H_2(j') \tag{10.8}$$

must be several orders of magnitude larger than the reaction rate coefficient. Here I do not consider a case when spin-orbit energy promotes the rotational energy of H_2 because such process has a low probability from energetic point of view. Let us consider that k_{j,j_a} has the Arrhenius-type dependence (10.3). Then we can construct a model of chemical kinetics with the reaction rate coefficients with parameters from table 10.1 and with the rate coefficient of relaxation

$$k_{\text{relax}} = m \times \{^{\text{o}}f_2(k_{1,0}\xi_0 + k_{1,1}\xi_1) + (1 - {}^{\text{o}}f_2)^{\text{p}}k\}\,, \tag{10.9}$$

where m is a parameter connected with the probability that the relaxation process takes place before the reaction. The rate coefficient k_{relax} follows the same type of temperature dependence as k. This is inspired by works by Mielke et al. [1996] and Abrahamsson et al. [2007] on Cl + H_2 reaction, in which theoretical relaxation rate coefficients have a same type of temperature dependence as reaction rate coefficients. Moreover, the relaxation rate coefficient is several orders of magnitude higher than the reaction rate coefficient in these works ($k_{\text{relax}} \sim 10^{-12}$ cm^{3}s^{-1} vs. $k \sim 10^{-15}$ cm^{3}s^{-1}). I am aware of differences between ion-neutral and neutral-neutral collisions, but these were only the works about the spin-orbit relaxation (within one degenerate electronic state) for a reactive couple known to me. Siska [2001] deals with the spin-orbit relaxation in He + Ne^+ collisions, but these two particles do not form a stable product by a radiative association or other ternary process at our experimental temperatures, as far as I know.

The backward rate coefficient (corresponding to excitation) can be calculated according to a principle of micro-reversibility

$${}^{(-1)}k_{\text{relax}} = \frac{\xi_{j_a\prime,\,\text{TDE}}}{\xi_{j_a,\,\text{TDE}}} k_{\text{relax}}\,, \tag{10.10}$$

where $\xi_{j_\mathrm{a},\,\mathrm{TDE}}$ is the TDE value of ξ_{j_a} for a considered temperature (see figure 4.2). Only FS state change $\Delta j_\mathrm{a} = \pm 1$ is considered. Changes $\Delta j_\mathrm{a} = \pm 2$ are considered as improbable.

We did not evaluate $k_{1,2}$ in section 10.1 because of high error, but now we need some estimation of its value for our model. Figure 3 in Gerlich [1989] suggests that $k_{1,2} = {}^\mathrm{p}k$ because mainly $^3\mathrm{P}_2$ state is populated at high temperatures. Adiabatic model by Russel and Manolopoulos [1999] assumes that the ions in $^3\mathrm{P}_2$ state do not react at all but here I reject this opinion not to be biased by the theory.

10.2.1 Model of decay, answer to question 1

Figure 10.5 shows a simulated evolution of number of $\mathrm{N}^+(^3\mathrm{P}_{j_\mathrm{a}})$ ions and population of FS states (ξ_{j_a}) in time. The initial FS state distribution was set to

$$\xi_{j_\mathrm{a}} = \xi_{j_\mathrm{a},\,\mathrm{TDE}}(400\,\mathrm{K}). \tag{10.11}$$

In all following simulations. Here the multiplication factor is $m = 0.05$ and temperature $T = 50$ K – the temperature, at which the Arrhenius-type dependence for ${}^\mathrm{n}\mathrm{H}_2$ deviates from the single-exponential. In the top panel, a deviation of curve for all N^+ ions from single-exponential is obvious. The bottom panel shows the evolution of ξ_{j_a} in time in comparison with $\xi_{j_\mathrm{a},\,\mathrm{TDE}}$. The arrow (if present) points at the "relaxation time"

$$t_\mathrm{relax} = 3 \times \tau_\mathrm{relax} = 3/(k_\mathrm{relax}[\mathrm{H}_2])\,. \tag{10.12}$$

The distribution of FS states does undergo major changes after this time, typically.

Figure 10.6 depicts the evolution of number of N^+ ions if $m = 0.5$. We can see the linear slope in the top panel (within experimental errors) but the bottom panel shows that TDE distribution of FS states is not established. Apparently, the single exponential slope is achievable even without thermalisation of FS states. The resulting effective rate coefficient of the reaction is apparently low because of non-reacting $\mathrm{N}^+(^3\mathrm{P}_2)$ ions (compare with the experimental decay line N_exp).

To make the image complete, figure 10.7 shows the results of the same model with $m = 1.5$. TDE distribution of FS states is almost established. Higher the value of m is, sooner is the steady state distribution established and more it resembles the TDE distribution.

If we abandon constraints of our physical model given by the parameters in table 10.1, the single-exponential decay can be fitted to measured data in various combination of the reaction and relaxation rate coefficients like in figure 7 in Attachment A.1.[3]

10.2.2 Simulation of measurements of Arrhenius-type temperature dependence, answer to question 2

The following figures 10.8 and 10.9 are de facto results of computer simulation of our measurements of Arrhenius-type dependence with ${}^\mathrm{n}\mathrm{H}_2$ (${}^\mathrm{o}f_2 = 0.75$).

[3]Special acknowledgements to prof. Dieter Gerlich.

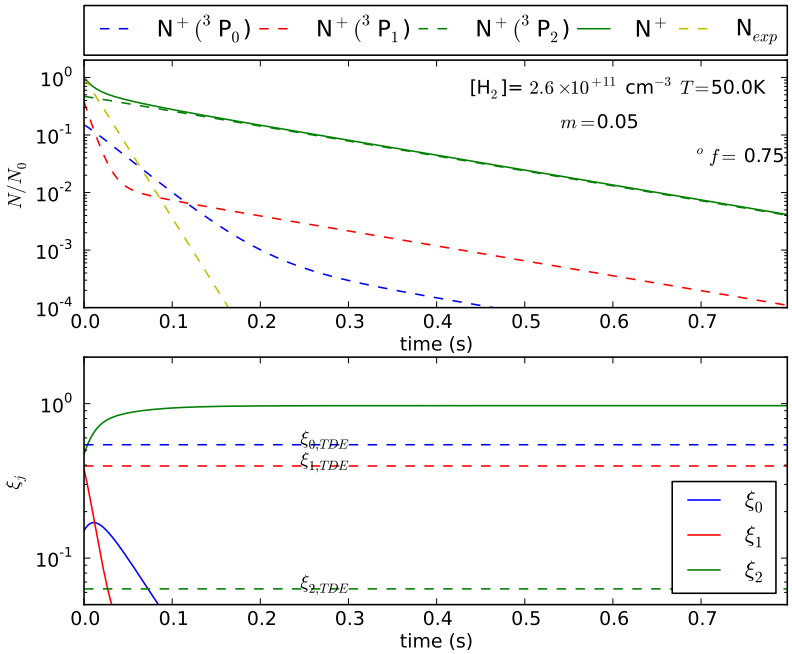

Figure 10.5: Model of spin-orbit relaxation with relaxation factor $m = 0.05$. N_{exp}: measured N^+ decay curve. The arrow pointing at the relaxation time t_{relax} is not present because it lies out of the x-scale range of the graph.

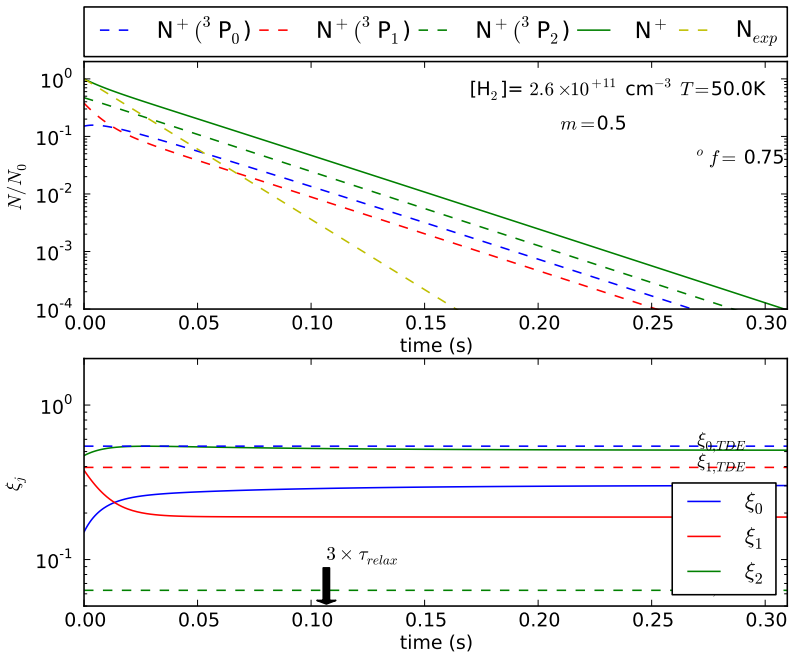

Figure 10.6: Model of spin-orbit relaxation with $m = 0.5$. The top panel: evolution of number of N^+ ions in $^3P_{0,1,2}$ states and of overall number of trapped N^+ ions. These decay curves are compared with the experimental one (yellow dashed line). The bottom panel: evolution of population of the FS states, compared with TDE values (dashed lines). See the discussion in the text.

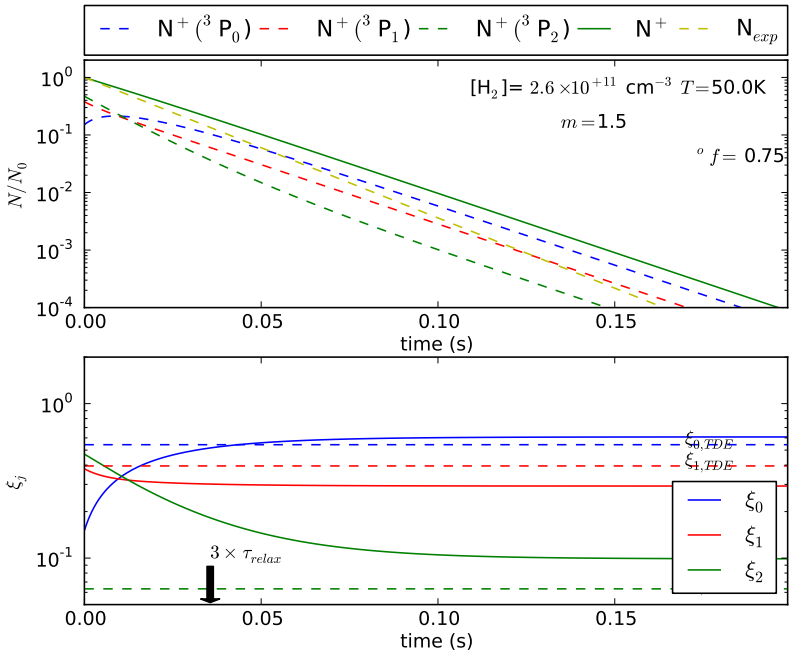

Figure 10.7: Model of spin-orbit relaxation with $m = 1.5$. The top panel: the decay curve for all N^+ ions is single-exponential and difficult to distinguish from the experimental one (yellow dashed line). The bottom panel: the modelled distribution of the FS states reached the state indistinguishable from the TDE distribution. See the discussion in the text.

10.2

A set of decays was calculated in a temperature range 100–10 K and the rate coefficient k was calculated from N^+-curve (see figures 10.5 – 10.7) using the relation (6.5). The value of t_0 was set to 10 ms and t_{fin} was set either to 200 ms or the value from (10.1), whichever was longer.

Figure 10.8 shows such simulation when $m = 0.5$, i.e. $k_{\text{relax}} < k$. In such case, TDE distribution is not established at all. At low temperatures $N^+(^3P_2)$ ions do not react and remain in the trap. The effective value of k is lowered over the whole temperature range more than 1.5 times.

Figure 10.9 depicts the dependence of k on temperature if $m = 1.5$. The deviation from the real experimental value $\delta \approx 67\%$. The population of $^3P_0$ state is close to TDE value in the whole temperature range. Deviation of the population of other states at low temperatures is given by the choice of t_0 and t_{fin} from equation (6.5): the steady state for ξ_{j_a} is not established in the period between these times.

If m is raised to even higher values, δ decreases further and the characteristics of the measured temperature dependence, including the stair between $T = 20$–30 K is reproduced.

10.2.3 Conclusion

It was shown in section 10.2.1 that the single-exponential decay is reproducible even if the spin-orbit relaxation and the FS-state-dependent rate coefficients are considered.

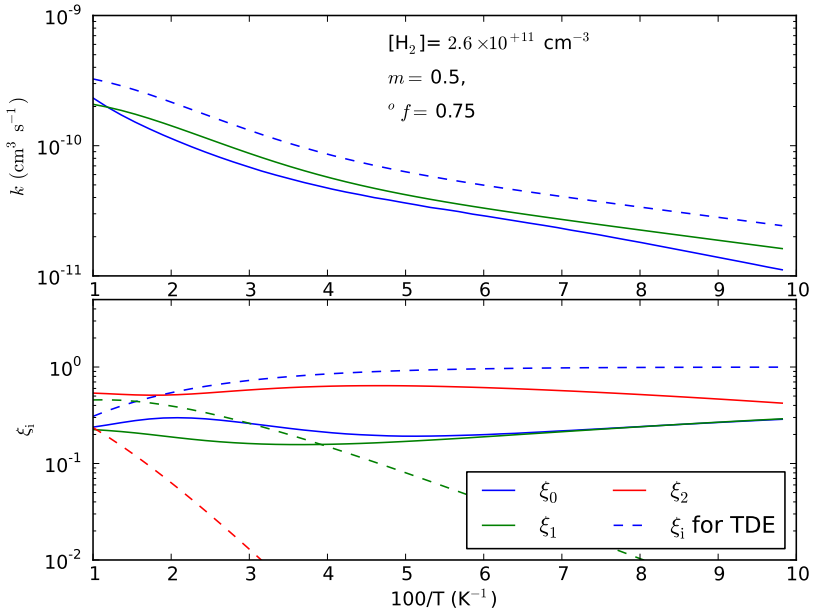

Figure 10.8: Temperature dependence of k resulting from model with $m = 0.5$. The top panel: dashed line: k_{relax}, green line: fit of experimental data, blue line: modelled curve. The bottom panel: Temperature dependence of modelled (full lines) and thermal (dashed lines) populations of the FS states. The modelled population does not reach the TDE population at any temperature.

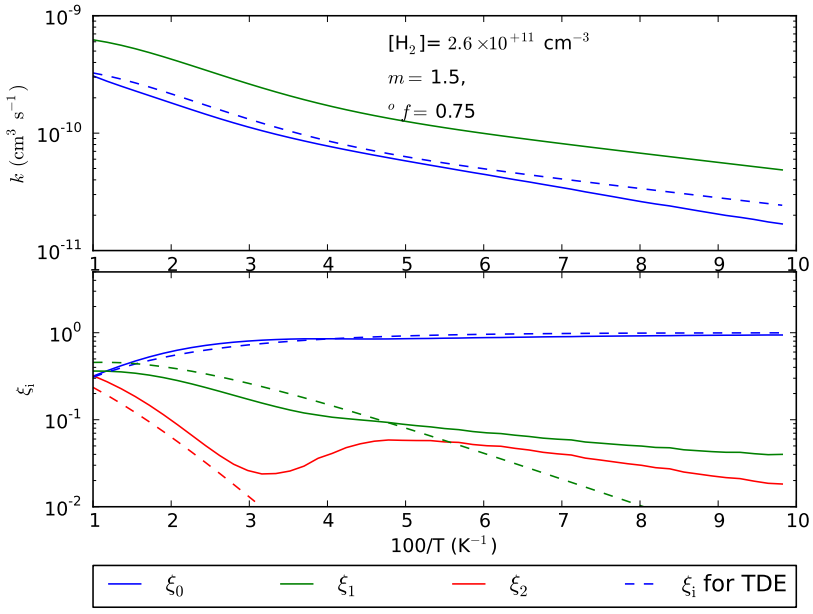

Figure 10.9: Temperature dependence of k resulting from model with $m = 1.5$. The top panel: dashed line: k_{relax}, green line: fit of experimental data, blue line: modelled curve. The bottom panel: the distribution of modelled FS states (full lines) reaches a satisfactory agreement with the thermal distribution (dashed lines).

The results from section 10.2.2 have shown that our physical model suffers from inaccuracy only if $k_{\mathrm{relax}} \leq 1.5 \times k$, where k is the reaction rate coefficient.

Attachment A.1 is based on the discussion here. The Arrhenius-type dependence for $^{\mathrm{p}}\mathrm{H}_2$ was fitted with FS dependent terms and the possibility of achieving single-exponential decay curve by any combination of $k_{j,j_{\mathrm{a}}}$ and k_{relax} was illustrated.

10.2

11. Association of H^+ with H_2

This chapter is an explanation and a summary of Attachment A.2.

We studied reactions

$$H^+ + {}^{p,o}H_2 \rightarrow H_3^+ + h\nu\,, \tag{11.1}$$

$$H^+ + {}^{p,o}H_2 + {}^{p,o}H_2 \rightarrow H_3^+ + H_2 \tag{11.2}$$

using the 22PT apparatus. We measured dependence of their rate coefficients on the ${}^{p}H_2$ population (${}^{p}f_2$) and on the temperature. Results were published in Gerlich et al. [2013] (Attachment A.2). Here I give a short comment on published results.

The rate coefficients were calculated by formulas (6.5) or (6.7), i.e. from the decay of H^+ ions' number or from the number of product ions in a specified time. The typical decay curve of number of stored H^+ ions is illustrated in figure 1 of Attachment A.2. The evolution of numbers of all detectable ions in the trap cooled to 11 K from experiments with ${}^{n}H_2$ or ${}^{e}_{m}H_2$ are plotted in figures 11.1 and 11.2, respectively.

The thermalisation of H^+ ions was checked in the same way as in the case of N^+ ions (see section 10). The decay of the ion counts can be measured only under the condition that the rate of the reaction of H^+ with H_2 is faster than with other molecules present in the trap. The influence of impurities of the background gas was checked by measurement of H^+ ions' number decay when H_2 is not present. The presence of impurities in H_2 gas was checked by mass scan of charged particles in the trap and by measurements of the evolution of their numbers (figures 11.1 and 11.2). In the case of measurement with ${}^{e}H_2$ (figure 11.2), deuterated ionic species are present ($[H_3^+] \sim 10 \times [H_2D^+]$ in the whole time scale). This could be interpreted as a result of the reaction of H^+ with HD. However, since the abundance of HD in ${}^{e}H_2$ gas is probably same as in ${}^{n}H_2$ (or even lower because HD freezes in the para-hydrogen generator) and we cannot see such effect in figure 11.1, higher abundance of H_2D^+ and D_3^+ is caused by a chain of hydrogen-deuterium exchange reactions (3.3), (3.4), (3.5). The value of ${}^{p}f_2$ evaluated from $[H_2D^+]$:$[H_3^+]$ ratio's temperature dependence in figure 3.1 for the measurement in figure 11.2 equals to 0.01, approximately, which is in correspondence with the value obtained from the study of $N^+ + H_2$ reaction.

The figure 1 of Attachment A.2 shows a significant dependence of the H^+ decay rate ("apparent binary association rate coefficient k^*") on the nuclear spin state of H_2 at 11 K. The radiative and ternary association terms k_r and k_3 [equation (2.18)] are separated from k^* by measuring dependence of k^* on $[H_2]$. Such measured dependence is plotted in figure 2 (for temperatures 11, 22 and 33 K) and in figure 5 (for temperature of the trap 11 K), both in Attachment A.2.

In figure 3, Attachment A.2, we plot temperature dependence of k_r and k_3 measured in ${}^{n}H_2$ and in ${}^{e}_{m}H_2$. It is apparent that k_3 for ${}^{n}H_2$ is lower than for ${}^{e}_{m}H_2$ in the whole temperature range and that the dependence is positive ($\partial k_3/\partial T_{22PT} > 0$). On the other hand, it is obvious that $\partial k_r/\partial T_{22PT} < 0$.

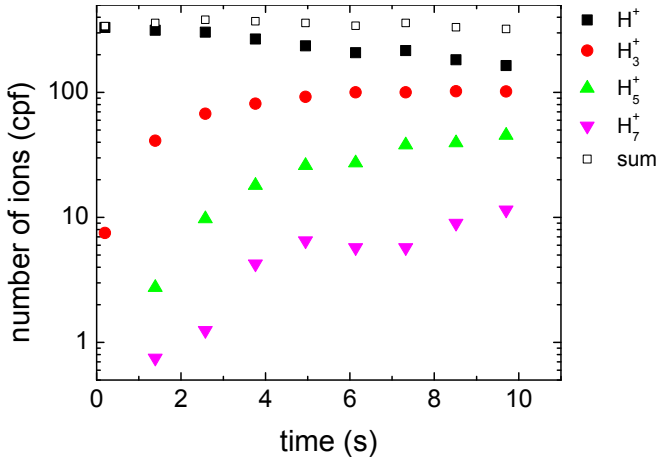

Figure 11.1: Time evolution of number of H^+ and product ions from the reaction $H^+ + {}^{n}H_2$ in 22PT. $[H_2] = 4 \times 10^{11}$ cm^{-3}, $T_{22PT} = 11$ K.

11.0

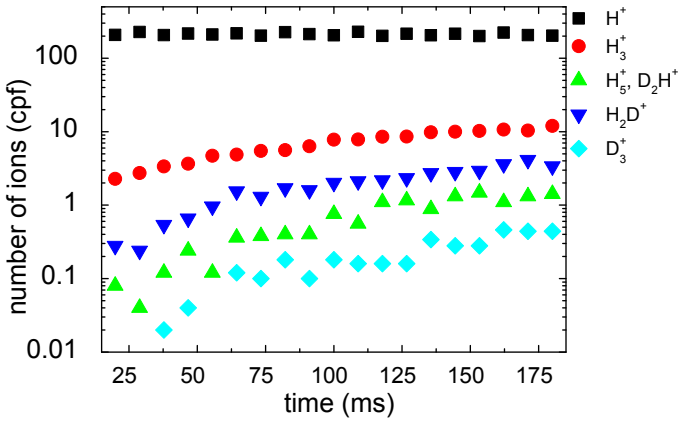

Figure 11.2: Time evolution of number of H^+ and product ions from the reaction $H^+ + {}^{e}_{m}H_2$ in 22PT ($^{o}f_2 < 0.01$). $[H_2] = 6.9 \times 10^{13}$cm^{-3}, $T_{22PT} = 11$ K. Note the ratio between the numbers of H_3^+ and H_2D^+ ions.

	$^{e}H_2$	$^{n}H_2$(1)	$^{p}H_2$	$^{o}H_2$
$k_3(10^{-29}\,\mathrm{cm}^6\,\mathrm{s}^{-1})$	4.4 (0.4)	1.4 (0.1)	4.4 (0.4)	0.4 (0.0)
$k_r(10^{-16}\,\mathrm{cm}^3\mathrm{s}^{-1})$	1.0 (-0.01)	2.3 (-0.07)	1.0 (-0.009)	2.7 (-0.09)

Table 11.1: Measured binary and ternary reaction rate coefficients and calculated nuclear-spin-state-specific values. The notation a (b) means $(a + b \times T_{22PT}/\mathrm{K})$. It is assumed in the calculation of ortho/para specific values that $^{p}f_2 = 0.99$. Note (1): Data taken from Plašil et al. [2012].

Parameters of formulas for fitted curves are summarised in table 11.1. The values for $^{o}H_2$ and $^{p}H_2$ serve for orientation: $^{o}H_2$ does not almost react via ternary association in comparison with $^{p}H_2$, the radiative channel is important mainly for $^{o}H_2$. These values were calculated under the assumption that the contribution from $^{p}H_2$ and from $^{o}H_2$ are linearly added, i.e.

$$k^*(^{p}f_2) = (1 - {}^{o}f_2)\,{}^{p}k^* + {}^{o}f_2\,{}^{o}k^*\,, \tag{11.3}$$

which was systematically tested by measuring dependence of k_3 on $^{o}f_2$ – see figure 4 of Attachment A.2 (k_r was not studied this way because of high experimental error of such measurements). The formula seems to be valid in the first approximation.

11.1 Discussion and Conclusion

For a detailed discussion, see a relevant part in Attachment A.2 and references therein.

In the review on earlier experiments by Gerlich and Horning [1992] mentioned in section 2.1, one can find that the temperature dependence of the dissociation life time τ_{dis} (section 2.1) was calculated to obey the temperature dependence $\tau_{dis} \propto T^{-1.9}$, and at 80 K the calculated value was $\sim 10^{-11}$ s. This finding may agree with two data points of k_r obtained in $^{n}H_2$, but poorly with the values measured in $^{e}H_2$, if no special temperature dependence is expected for the $(H_3^+)^*$ intermediate complex formation rate coefficient k_c (see equation (2.18)).

In former experiments [see Gerlich and Horning, 1992], it has been also found that the rate of radiative emission from excited H_3^+ complex (2.12) τ_r lies in a millisecond range, i.e.

$$\tau_r \sim 10^{-3}\,\mathrm{s}. \tag{11.4}$$

From the formula (2.18) in section 2.1 we can see that

$$k_c \tau_{dis} = k_r \tau_r = \frac{k_3}{k_{H_2}}\,. \tag{11.5}$$

Hence we get the rate coefficient for a collision-induced re-dissociation of the $(H_3^+)^*$ intermediate complex

$$k_{H_2} = \frac{k_3}{k_r}\,\frac{1}{\tau_r}\,. \tag{11.6}$$

If we substitute formulas described in table 11.1 for k_3 and k_r in equation (11.6), we get that k_{H_2} has a positive temperature dependence both for $^oH_2$ and $^pH_2$.[1] This agrees with a common opinion that the intermediate complex is more stable at lower temperatures, i.e. the complexes re-dissociate with a lower rate. The explanation of differences between $^pH_2$ and $^oH_2$ is beyond the possibilities of the simple physical model described in section 2.1.

If we assume that the dependence $\tau_{dis} \propto T^{-1.9}$ is valid, the processes of the $(H_3^+)^*$ intermediate complex formation [the process (2.11)] and re-dissociation [the processes (2.12) and (2.13)] are strongly dependent on nuclear spin states and have non-trivial temperature dependence as it would appear from prescriptions for k_r and k_3 in equation (2.18). However, neither the temperature dependence of τ_{dis} is properly known for a low temperature region and different nuclear spin states as it was calculated only for total reaction energies > 0.1 eV [Schlier and Vix, 1985]. Further studies on lifetimes of highly excited H_3^+ ions (and probably also H_5^+ ions) are needed to explain our experimental data.

11.1

[1] Until the critical temperatures ≈ 30 K and 100 K (for $^oH_2$ and $^pH_2$ respectively) when $k_{H_2}(T)$ diverges. These critical temperatures are given by our simplified fits (linear approximations) of the experimental data (calculated from the parameters in table 11.1) so no importance should be assigned to them.

12. Recombination of H_3^+ with electrons

The recombination processes (3.10), (3.11) and (3.12) were studied using two apparatuses: SA-CRDS (described in chapter 7) and Cryo-FALP II (chapter 8). The results of these studies are written in works Dohnal et al. [2012a,b,c]; Glosík et al. [2010]; Johnsen et al. [2013]; Rubovič et al. [2013]; Varju et al. [2011]. Except Glosík et al. [2010], all articles are in attachment. The work by Hejduk et al. [2012a] (in Attachment B.1) deals with internal temperatures of H_3^+ ions in the experiments using SA-CRDS apparatus: the knowledge about the possible excitation of H_3^+ ions was crucial for a correct interpretation of measured recombination rate coefficients.

12.1 Experimental conditions

Approaches of both apparatuses (SA-CRDS and Cryo-FALP II) to solution of H_3^+-e^- state-selective recombination problem are compared in table 12.1.

The SA-CRDS apparatus is described in chapter 7. The microwave power used to ignite the discharge was 4–12 W. Fe_2O_3 catalyst was used in para-hydrogen generator. At the time of the experiments, only the value of ${}^{\mathrm{p}}f_2$ obtained from NMR measurement was available, therefore the uncertainty of ${}^{\mathrm{p}}f_2$ was high. Despite this, enhanced population of ${}^{\mathrm{p}}H_3^+$ was achieved, which was the main purpose of using ${}^{\mathrm{e}}_{\mathrm{m}}H_2$.

Cryo-FALP II is briefly described in chapter 8. Activated $HFeO_2$ was used as a catalyst in para-hydrogen generator. The maximum ${}^{\mathrm{p}}f_2$ was known from studies of $N^+ + H_2$ reaction, and the value was assumed to be valid also in the flow tube.

Following chapters comment results from measurements at both apparatuses described in attached articles.

Parameter	SA-CRDS	Cryo-FALP II
Gas temperature	77–300 K	55–300 K
Diagnostics	Spectroscopy	Langmuir probe
What is measured	Populations of three low-lying rotational states of H_3^+, T_{Kin} and T_{Rot} of H_3^+	Electron number density n_{e}
Generation of H_3^+ ions	discharge in in $He/Ar/H_2$ mixture, $ArH^+ + H_2$, $H_2^+ + H_2$	discharge in He, subsequent ionisation of Ar, $ArH^+ + H_2$
[He]	$\sim 10^{17}$ cm^{-3}	$\sim 10^{16}$ – 10^{17} cm^{-3}
[Ar]	$\sim 10^{14}$ – 10^{15} cm^{-3}	$\sim 10^{14}$ cm^{-3}
[H_2]	$\sim 10^{13}$ – 10^{14} cm^{-3}	$\sim 10^{12}$ – 10^{13} cm^{-3}
$1/(\alpha_{\mathrm{eff}} n_{\mathrm{e}})$	~ 0.1 ms	~ 10 ms
measurement timescale	~ 1 ms	~ 10 ms
maximum ${}^{\mathrm{p}}f_2$	$0.87^{+0.13}_{-0.01}$	0.995 ± 0.005
catalyst	Fe_2O_3	activated $HFeO_2$

Table 12.1: Comparison of SA-CRDS and Cryo-FALP II experiments

transition	wave-number (cm^{-1})	nuclear spin state
$3\nu_2^1(2,1) \leftarrow 0\nu_2^0(1,1)$	7237.285	para
$3\nu_2^1(2,0) \leftarrow 0\nu_2^0(1,0)$	7241.245	ortho
$3\nu_2^1(4,3) \leftarrow 0\nu_2^0(3,3)$	7234.957	ortho

Table 12.2: Transitions used in studies of H_3^+-e^- recombination

12.2 Measurements by SA-CRDS

Attachments B.1, B.2, B.3 and B.4 deal solely with measurements using SA-CRDS apparatus. Attachments C.1, C.2 also contain results from these articles. Attachment B.5 deals with D_3^+-e^- recombination studies performed using the same technology as in the case of H_3^+ ions.

During the studies of H_3^+-e^-recombination we monitored three of the lowest rotational states of the ground vibrational state of H_3^+: $(J,G) = (1,1)$, $(1,0)$ and $(3,3)$ corresponding to para and two ortho states (respectively, see figure 1.4). Specific transitions and their wavelengths are written in table 12.2.

12.2.1 The first in-situ determination of nuclear spin state specific recombination of H_3^+

This section is an explanation and a summary of Attachment B.4

The Attachment B.4 deals with the measurements of recombination rate coefficients for ${}^{p}H_3^+$ and ${}^{o}H_3^+$ at temperature of the buffer gas $T_{He} = 77$ K. The kinetic temperature of the ions was found to be equal to T_{He} (evaluation method in section 7.1.2). It was the first time in the history of nuclear spin-state-specific recombination studies the population of para-state was determined in-situ, using the transitions corresponding to (1,1) and (1,0) states (corresponding to para and ortho nuclear spin states, respectively; the transition for 3,3 state was not measured at that time yet). The nuclear spin dependent recombination rate coefficients α_{eff} had to be extracted from two measurements with two different population of ${}^{p}H_3^+$ (${}^{p}f_3$), i.e. by solution of

$$\alpha_{eff}{}' \equiv {}^{n}\alpha_{eff} = {}^{p}\alpha_{eff}\,{}^{p}f_3' + {}^{o}\alpha_{eff}(1 - {}^{p}f_3') \tag{12.1}$$

$$\alpha_{eff} \equiv {}^{e}\alpha_{eff} = {}^{p}\alpha_{eff}\,{}^{p}f_3 + {}^{o}\alpha_{eff}(1 - {}^{p}f_3)\,, \tag{12.2}$$

with respect to ${}^{p}\alpha_{eff}$ and ${}^{o}\alpha_{eff}$. The accented variables were obtained in ${}^{n}H_2$, and α_{eff} and ${}^{p}f_3$ were measured in ${}^{e}_{m}H_2$. State specific coefficients ${}^{p}\alpha_{eff}$ and ${}^{o}\alpha_{eff}$ were separated to state-specific binary and [He]-dependent parts – see equation (3.8). For the results of these manipulations, see figure 2 of Attachment B.4. This method of evaluation assumes that the conversion between para-ortho nuclear spin states (1.9) has higher rate than the recombination. This was proven by recording the evolution of ${}^{p}f_3$ in time: ${}^{p}f_3$ does not change in the discharge and neither in the afterglow, as it is shown in figure 1 of Attachment B.4. As a final result, binary recombination rate coefficient α_{bin} for ${}^{p}H_3^+$ was found to be almost 10 times higher than for ${}^{o}H_3^+$ (figure 3, Attachment B.4).

12.2.2 Study of rotational temperatures in discharge and para/ortho-H_3^+ conversion

This section is an explanation and a summary of Attachment B.1

The rotational temperature T_{Rot} was supposed to be equal to T_{He} in Attachment B.4. Later, the preceding storage ring studies of H_3^+-e^- recombination were questioned because of high T_{Rot} [Petrignani et al., 2011]. To prove that our measurements are carried out in the ensemble of H_3^+ ions where the distribution of rotational states is thermalised, the transition corresponding to the state (3,3) was found and monitored in the discharge and in the early afterglow. This allowed us to study the rotational temperature T_{Rot} corresponding to ortho nuclear spin manifold ($T_{\mathrm{Rot\text{-}ortho}}$). Note that fast para-ortho conversion allows us to perceive ${}^{\mathrm{p}}H_3^+$ and ${}^{\mathrm{o}}H_3^+$ ions as separate entities (see sections 1.2.2, 3.2).

The Attachment B.1 deals with the topic mentioned above, i.e. with the internal temperature of H_3^+ ions in the discharge, mainly. Since there is no input of power in the afterglow, if the internal degrees of freedom are thermalised in the discharge, the same must be true in the afterglow. We observed evolution of T_{Kin} in time and showed that the kinetic temperature of the ions is equal to the helium buffer gas temperature T_{He} that is supposed to have the same temperature as the one of the discharge tube measured by a thermocouple, $T_{\mathrm{He}} = T_{\mathrm{Kin}}$ (figure 4[1]). Figure 6 compares $T_{\mathrm{Rot\text{-}ortho}}$ with T_{Kin} and indicates that $T_{\mathrm{Rot\text{-}ortho}} = T_{\mathrm{Kin}}$. In ${}^{\mathrm{n}}H_2$ ${}^{\mathrm{p}}f_3$ was found to correspond to the value in TDE for given experimental temperatures 77–200 K (figure 8). This also means that the distribution of the rotational states of H_3^+ is thermal in case of discharge in ${}^{\mathrm{n}}H_2$.

The nuclear spin temperature (7.18) is equal to T_{Rot} at 77 K in ${}^{\mathrm{n}}H_2$ when the population of (3,3) state is negligible. This can be seen in figure 7 and also in figure 10 of the attachment or figure 12.1 here: compare the experimental data obtained at $T_{\mathrm{Kin}} = 80\ K$ for ${}^{\mathrm{p}}f_2 = 0.25$ with the full line corresponding to TDE values of ${}^{\mathrm{p}}f_2$ and ${}^{\mathrm{p}}f_3$. The dependences of ${}^{\mathrm{p}}f_3$ on ${}^{\mathrm{p}}f_2$ in figure 10 of the attachment or in figure 12.1 in this section (left panel) are linear as assumed by the high temperature model 2. However, lower the temperature is, slighter is the slope. The dependence does not follow formulas (2.2) or (2.9) (the nascent line in the figure). Since no [Ar] dependence was observed at $T_{\mathrm{Kin}} = 80$ K, we conclude that the slope (derivative) is given by temperature dependence of reaction (1.9). We have shown that

$$T = T_{\mathrm{He}} = T_{\mathrm{Kin}} = T_{\mathrm{Rot\text{-}ortho}} \tag{12.3}$$

and that

$${}^{\mathrm{p}}f_3 = {}^{\mathrm{p}}f_3({}^{\mathrm{p}}f_2, T)\,, \tag{12.4}$$

in the discharge plasma. We supposed that these hold for the afterglow as well because of absence of external electromagnetic field that would accelerate or excite the particles – these statements were further verified in the work by Dohnal et al. [2012b] (Attachment B.2, figures 4 and 6).

[1] In this section, I refer to figures included in Attachment B.1 (if not stated otherwise), therefore their origin from this attachment is not mentioned further.

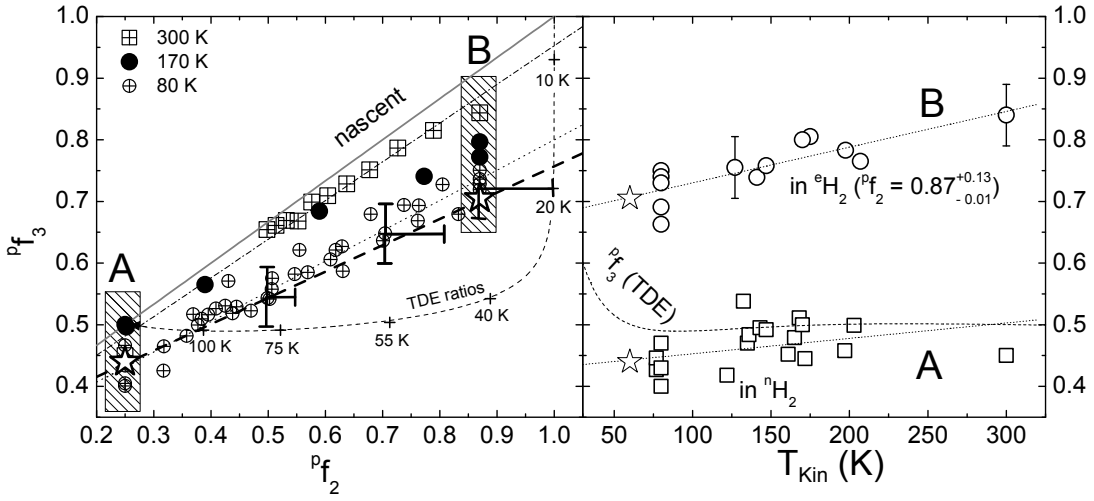

Figure 12.1: Dependence of $^{p}f_3$ on $^{p}f_2$ and on temperature. Left panel: Dependence of $^{p}f_3$ on $^{p}f_2$. See section 9.1 for x-axis error bars. Dashed line with '+' signs in the left panel: $^{p}f_3$ and $^{p}f_2$ for TDE at indicated temperatures. Right panel: Dependence of $^{p}f_3$ on temperature for $^{n}H_2$ and $^{e}H_2$. The experimental data are fitted by linear polynomials. The $^{p}f_3$ curve for TDE is drawn in the right panel as well. The fitted curves are extrapolated to lower temperatures. The star symbols indicate the values for 60 K. All plotted points originate from measurements in the discharge (see the text in section 12.2.2).

12.2

12.2.3 Temperature dependence of α_{bin} and K_{He}, collisional radiative recombination

This section is an explanation and a summary of Attachments B.2 and B.3.

We performed measurements of α_{eff} in temperature range 80 – 200 K and evaluated nuclear spin state specific α_{bin} and K_{He} at these temperatures. The results are drawn in figures 12 and 13 in Attachment B.2. The experimental values for TDE (i.e. for $^{n}H_2$, as it was discussed above) were shown to lie on theoretical curves predicted by Floresca dos Santos et al. [2007] for α_{bin} and by Kokoouline for K_{He} [Glosík et al., 2010]. Measured state-specific α_{bin} are following the trend predicted by the theory, but the descent of $^{o}\alpha_{\mathrm{bin}}$ for $^{o}H_3^+$ towards low temperature is steeper than predicted. The state-specific values of K_{He} seem not to follow the theoretical curve, but the accordance within the order is important to note.

We did not observe the collisional radiative recombination (section 3.2.3) at all in the whole temperature range. In the attachment of the paper by Dohnal et al. [2012b] (Attachment B.2), the numerical fit of the solution of

$$\frac{\mathrm{d}n_{\mathrm{e}}}{\mathrm{d}t} = -K_{\mathrm{CRR}}(T_{\mathrm{e}})n_{\mathrm{e}}^3 - \alpha_{\mathrm{eff}} - \frac{n_{\mathrm{e}}}{\tau_{\mathrm{D}}} \tag{12.5}$$

to ($[^{o}H_3^+] + [^{p}H_3^+]$) decay curve for $T_{\mathrm{Kin}} = 77$ K was performed but the best agreement with experimental results was achieved when K_{CRR} was negligible (figure 14 of the attachment). Since, according to a theory, the electrons are

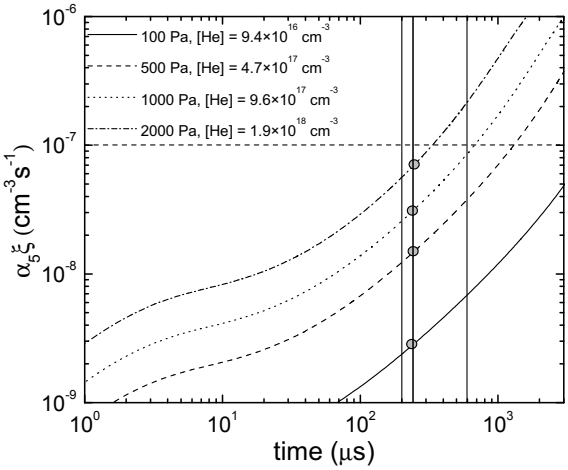

Figure 12.2: Dependence of $\alpha_5\xi$ on time for several [He] at $[H_2] = 10^{14}\text{cm}^{-3}$ and $T = 77$ K calculated from a model of chemical kinetics using experimental α_{eff}, $\alpha_5 = 2 \times 10^{-6}\,\text{cm}^3\text{s}^{-1}$ and the rate coefficient for reaction (3.2) $10^{-29}\,\text{cm}^6\,\text{s}^{-1}$. The grey circles indicate values from 250 μs that were fitted by a linear function and plotted in figure 12.3 in a modified form.

heated in the CRR process from $T_e = 77$ K only to 100 K, which makes CRR still observable, the electron heating is not on blame. CRR was observed neither in D_3^+ plasma (Attachment B.5). Why CRR is not observable in case of studied molecular ions is still an open question.

12.2.4 Influence of H_5^+ formation on measured α_{eff}

Here I deal with the influence of (3.1) on measured α_{eff}. If we look at equation (3.16), $(1-\xi)\alpha_{\text{eff}}{}'$ is the rate coefficient that is possible to evaluate from a decay curve for H_3^+ ions. The systematic error of not taking process (3.2) into account is equal to $\alpha_5\xi$ computed by a model of chemical kinetics and plotted in figure 12.2 for several [He] at $[H_2] = 10^{14}\,\text{cm}^{-3}$.

As discussed in Attachments B.4 and B.5, α_{eff} is evaluated from data in the time range $\langle 200, 600\rangle$ μs (after the discharge is switched off). The lower limit is set to exclude H_3^+ ion formation period. The upper limit is given by the decrease of the signal below a noise level. Since the fitting algorithm puts bigger weight to data that are less scattered, the "mean moment" of evaluation α_{eff} can be typically set to the time 250 μs. If I do so, I can draw a figure 12.3 depicting the uncertainty area of measured dependence of α_{eff} on [He]. The area is lying within the scatter of experimental data. Since $\alpha_5\xi$ forms a part of diffusion term in equation (3.26), $\alpha_5\xi$ is interpreted as a systematic scatter of data, not the offset.

12.2

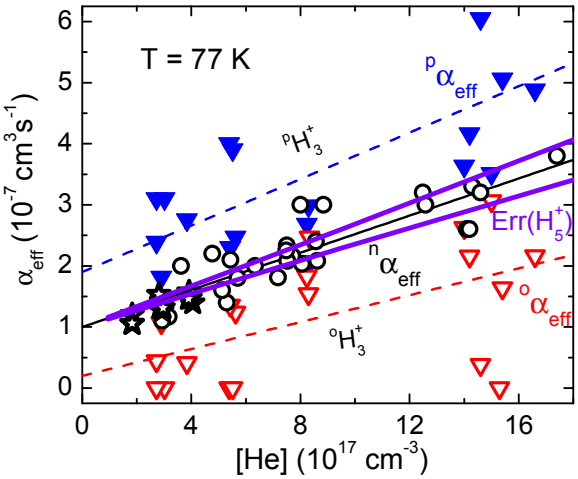

Figure 12.3: Modification of $^{n}\alpha_{\text{eff}}$ by α_5. The purple lines Err(H_5^+) outline the uncertainty area of experimental data imposed by H_5^+ formation.

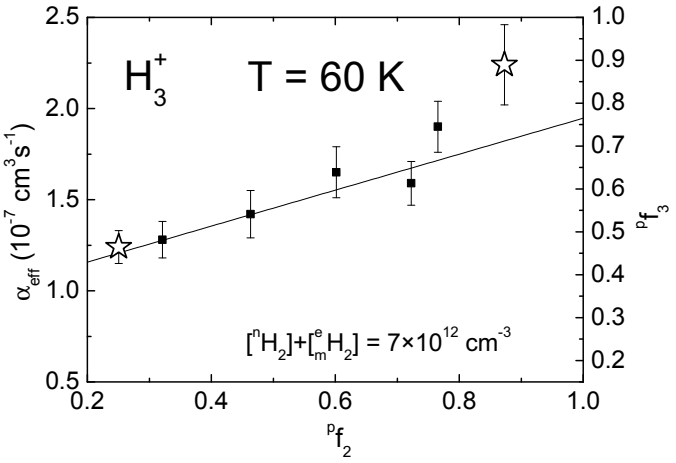

Figure 12.4: Dependence of α_{eff} on ${}^{\text{p}}f_2$ and ${}^{\text{p}}f_3$ derived from ${}^{\text{p}}f_2$ using figure 12.1 (right panel). The star values correspond to star-labelled ${}^{\text{p}}f_2$ in figure 12.1. The error of the value for ${}^{\text{p}}f_2 = 0.87$ is high because of high uncertainty of ${}^{\text{p}}f_2$.

12.3 Measurements by Cryo-FALP II

We performed series of measurements of α_{eff} at various [He], [H_2], temperatures of the flow tube and ${}^{\text{p}}f_2$. The typical sets of data are illustrated in figures 12.4, 12.5 and 12.6. *The measurements with* ${}^{\text{n}}H_2$ *are summarised in Attachments C.*

Figure 12.4 illustrates a measured dependence of α_{eff} on ${}^{\text{p}}f_2$. The linear dependence (12.2) is preserved approximately. The values are assigned to corresponding ${}^{\text{p}}H_3^+$ populations ${}^{\text{p}}f_3$ (right axis) using the dependence of ${}^{\text{p}}f_3$ on ${}^{\text{p}}f_2$ from figure 12.1 measured in SA-CRDS.

Dependences of α_{eff} on $[{}^{\text{e}}_{\text{m}}H_2]$ for four different values of [He] are plotted in figure 12.5. We can see a linear dependence (3.16). The lines intersect y-axis at the points indicated as α_{extrap} in figure 12.6 (for ${}^{\text{e}}_{\text{m}}H_2$):

$$\alpha_{\text{eff}} = \alpha_{\text{extrap}} + K_5[H_2]\,. \tag{12.6}$$

Figures 12.5 and 12.6 are cross sections of each other. The intersection of α_{extrap} with y-axis in figure 12.6 (open red triangles) is the value of

$$\alpha_{\text{bin}} = {}^{\text{p}}f_3{}^{\text{p}}\alpha_{\text{bin}} + (1 - {}^{\text{p}}f_3)^{\text{o}}\alpha_{\text{bin}}\,.$$

The slope of α_{extrap} is equal to

$$K_{\text{He}} = {}^{\text{p}}f_3{}^{\text{p}}K_{\text{He}} + (1 - {}^{\text{p}}f_3)^{\text{o}}K_{\text{He}}\,.$$

In the following text, leading superscripts "e" and "n" relate α_{eff} and K_{He} to used type of H_2 gas: either ${}^{\text{e}}_{\text{m}}H_2$ or ${}^{\text{n}}H_2$, respectively. The values of ${}^{\text{p}}\alpha_{\text{eff}}$, ${}^{\text{p}}\alpha_{\text{bin}}$, ${}^{\text{p}}K_{\text{He}}$ and their ortho-counterparts are calculated from ${}^{\text{e}}\alpha_{\text{eff}}$, ${}^{\text{n}}\alpha_{\text{eff}}$ or ${}^{\text{e}}K_{\text{He}}$, ${}^{\text{n}}K_{\text{He}}$ in the same manner as it was done in spectroscopic studies [section 12.2.1, equation s (12.1) and (12.2)]. See Attachments B.2, B.3, B.4 for details on the method of evaluation of the state-specific recombination rate coefficients.

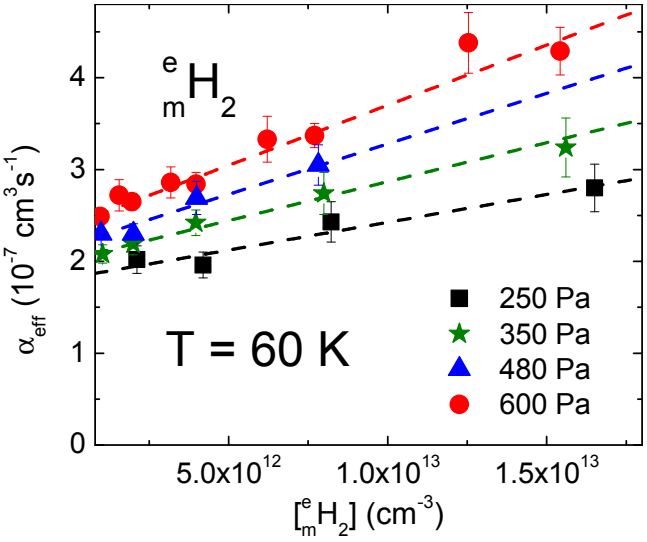

Figure 12.5: Dependence of α_{eff} on $[^{\text{e}}_{\text{m}}\text{H}_2]$ at temperature of the flow tube $T_{\text{FT}} = 60$ K for four different buffer gas (He) pressures. The extrapolated values at $[\text{H}_2] = 0$ are called α_{extrap} and plotted in figure 12.6.

12.3

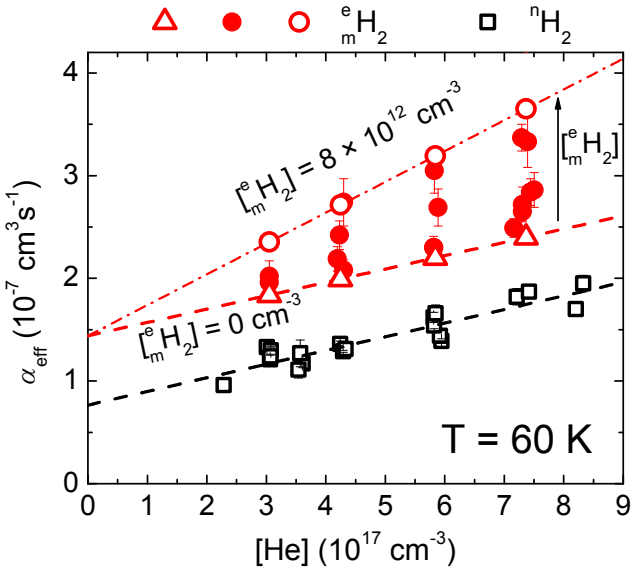

Figure 12.6: Dependence of α_{eff} on [He] at temperature of the flow tube $T_{\text{FT}} = 60$ K for various values of $[\text{H}_2]$. Full red circles: measured in $^{\text{e}}_{\text{m}}\text{H}_2$; open black rectangles: measured in $^{\text{n}}\text{H}_2$. The values for $^{\text{e}}\text{H}_2$ show much stronger dependence on $[\text{H}_2]$ than for $^{\text{n}}\text{H}_2$. Open red triangles and circles indicate recombination rate coefficients for the limit values for $[^{\text{e}}_{\text{m}}\text{H}_2] = 0\,\text{cm}^{-3}$ and $8 \times 10^{12}\,\text{cm}^{-3}$, respectively (calculated from the fits of experimental data in figure 12.5). They are fitted by linear polynomials – the dashed line and the dash-dot line. The arrow shows a direction of growing $[^{\text{e}}_{\text{m}}\text{H}_2]$. Open red triangles correspond to α_{extrap} from equation (12.6).

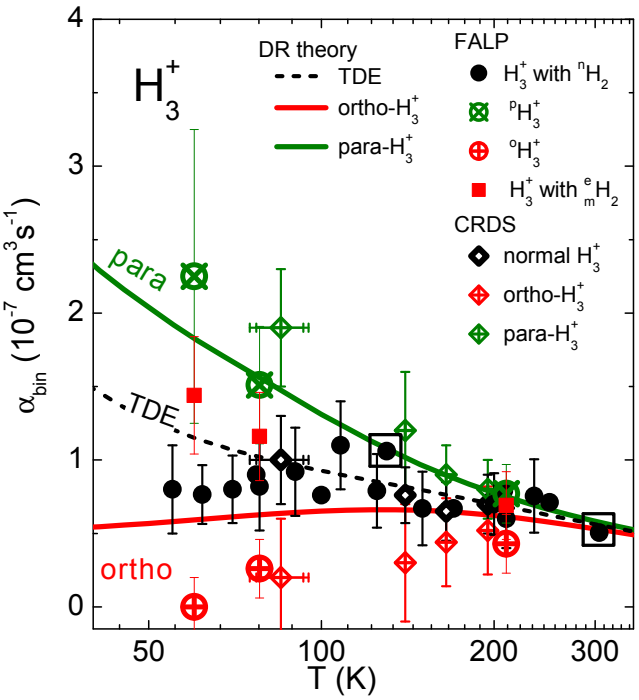

Figure 12.7: Measured temperature dependence of ${}^{\mathrm{n}}\alpha_{\mathrm{bin}}$, ${}^{\mathrm{o}}\alpha_{\mathrm{bin}}$, ${}^{\mathrm{p}}\alpha_{\mathrm{bin}}$. "Normal-$H_3^+$" refers to data measured in experiments with ${}^{\mathrm{n}}H_2$. FALP data measured with ${}^{\mathrm{n}}H_2$ (${}^{\mathrm{e}}_{\mathrm{m}}H_2$) are indicated by filled circles (filled squares). Values for ${}^{\mathrm{p}}H_3^+$ and ${}^{\mathrm{o}}H_3^+$ are calculated using ${}^{\mathrm{p}}f_3$ from figure 12.1 (right panel). Combined SA-CRDS/FALP data at 100 K and 305 K are indicated by a filled circle in a square. The lines indicate the theoretical coefficients for ${}^{\mathrm{p}}H_3^+$, ${}^{\mathrm{o}}H_3^+$ and for H_3^+ ions in TDE.

Results of the data-analysis described above are plotted in figures 12.7 and 12.8. The values for ${}^{\mathrm{p}}f_3$ in were obtained from figure 12.1. The nuclear-spin-state dependent rate coefficients were calculated by the same method as in section 12.2.1.

12.3.1 Binary recombination

Figure 12.7 summarises values of ${}^{\mathrm{n}}\alpha_{\mathrm{bin}}$ and ${}^{\mathrm{e}}\alpha_{\mathrm{bin}}$ measured by Cryo-FALP II and SA-CRDS in ${}^{\mathrm{n}}H_2$ or ${}^{\mathrm{e}}H_2$, respectively, and ${}^{\mathrm{p}}\alpha_{\mathrm{bin}}$ and ${}^{\mathrm{o}}\alpha_{\mathrm{bin}}$ calculated from measured data. The values of ${}^{\mathrm{n}}\alpha_{\mathrm{bin}}$, ${}^{\mathrm{o}}\alpha_{\mathrm{bin}}$ and ${}^{\mathrm{p}}\alpha_{\mathrm{bin}}$ for temperatures 200 K and 80 K obtained by both apparatuses are equal within errors. We successfully confirmed measurements at SA-CRDS by experiments using Cryo-FALP II. In this work, we added values of ${}^{\mathrm{p}}\alpha_{\mathrm{bin}}$, ${}^{\mathrm{o}}\alpha_{\mathrm{bin}}$, ${}^{\mathrm{n}}\alpha_{\mathrm{bin}}$ and ${}^{\mathrm{e}}\alpha_{\mathrm{bin}}$ at 60 K. The relative uncertainty of ${}^{\mathrm{p}}\alpha_{\mathrm{bin}}$ and ${}^{\mathrm{o}}\alpha_{\mathrm{bin}}$ is high because of uncertainty of ${}^{\mathrm{p}}f_3$, which we cannot measure directly in Cryo-FALP II.[2] These values agree well with theoretical prediction by Floresca dos Santos et al. [2007]. The values of ${}^{\mathrm{n}}\alpha_{\mathrm{bin}}$ are decreasing below the theoretical curve for TDE at low temperatures.

[2]Nevertheless, the values in the graph are the first nuclear-spin-state-specific recombination rate coefficients for H_3^+ ions with thermal distribution of rotational states at temperatures 60–300 K.

This is probably because H_3^+ ensemble in $^{n}H_2$ has enhanced population of ortho-states if compared with the TDE value of $^{p}f_3$ in figure 12.1. Interesting is the fact, that observed $^{o}\alpha_{bin}$ decreases below the reliably calculable level at 60 K.

12.3.2 Ternary recombination

Figure 12.8 summarises values of $^{p}K_{He}$, $^{o}K_{He}$ and $^{n}K_{He}$ (the raw values from measurements in $^{n}H_2$) measured by Cryo-FALP II and SA-CRDS. The values of $^{n}K_{He}$, $^{o}K_{He}$ and $^{p}K_{He}$ for temperatures 80–200 K obtained by both apparatuses are equal within errors with exception of the values at $\approx$ 170 K. Temperature dependences of $^{p}K_{He}$, $^{o}K_{He}$ and $^{n}K_{He}$ differ from theoretical predictions [Glosík et al., 2010] but the values are of the same order. Figure 2 of Attachment C.2 compares the data measured in $^{n}H_2$ with the He-assisted ternary recombination rate coefficient of Ar^+. No similarity is found. However, in case of D_3^+-e^- recombination (which was studied in Cryo-FALP II as well, figure 3 in the same attachment) the values of K_{He} follow the theoretical curve for Ar^+ [Bates and Khare, 1965]. By the way, this equality is strange, because the value of K_{He} should be scaled with the reduced mass of colliding partners (Ar-He vs. D_3^+-He). Such inclination to the theoretical curve (drawn by a full line in figure 12.8) is not visible in the case of the para-state-specific coefficient $^{p}K_{He}$ and in the case of $^{o}K_{He}$ the similarity cannot be deduced just from three measured values reliably.

The values for 60 K have big error because they are evaluated using $^{p}f_3$ from figure 12.4.

12.3

12.3.3 Measurements below 60 K

Attempts to replicate results for 60 K and for $^{e}H_2$ described above also for the temperature of the flow tube 50 K were unsuccessful. The fits (described in section 8.2) of α_{eff} to measured decays varied with the initial time position t_0 during the decay. If CRR was taking place, α_{eff} would decrease with time because of decreasing n_e. However, in this case, α_{eff} was increasing with the time as it is shown in figure 12.9. This may correspond to slow formation of H_3^+ ions and rapid creation of H_5^+ ions in $^{e}H_2$. The difference between cases with $^{e}H_2$ and with $^{n}H_2$ is also visible in dependences of K_5 on the buffer gas pressure 12.10 and 12.11: while they are same for $^{e}H_2$ and $^{n}H_2$ at $\approx$ 77 K, their slope differ significantly at lower temperatures.

There are several possible explanations of the slow formation of H_3^+ in $^{e}H_2$. One is that the chemical kinetics leading to H_3^+ ions is different for $^{e}H_2$ and $^{n}H_2$ significantly at low temperatures. The dominant formation process in Cryo-FALP II is reaction (2.3). ArH^+ is created in reaction $Ar^+ + H_2$ – there are still uncertainties about behaviour of this reaction at low temperatures. Some groups of experimentalists made conclusions in past that this reaction's pathway is hindered by a potential barrier of the height $\approx$ 50 K [Ervin and Armentrout, 1985; Hawley and Smith, 1992]. A reliable experimental confirmation of this hypothesis does not however exist so far. The second hypothesis explaining our measurements is that the recombination dynamics is much more

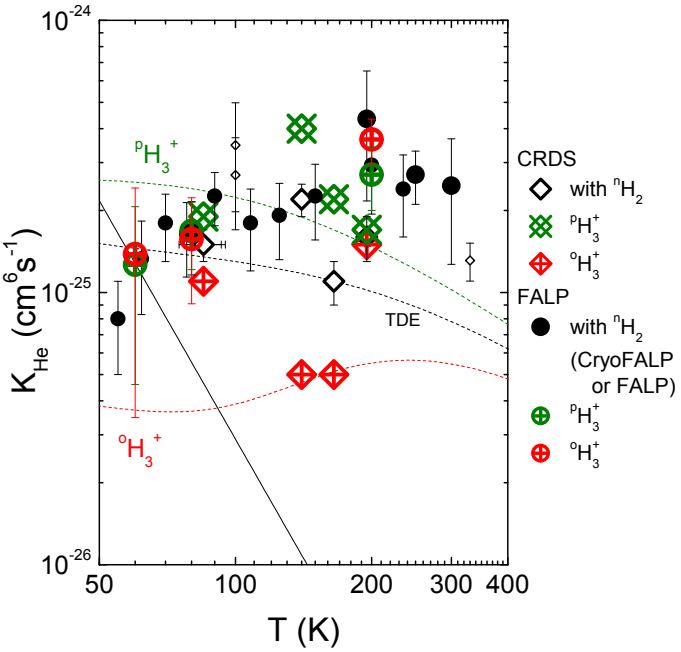

Figure 12.8: Measured temperature dependence of ${}^{\mathrm{n}}K_{\mathrm{He}}$, ${}^{\mathrm{o}}K_{\mathrm{He}}$, ${}^{\mathrm{p}}K_{\mathrm{He}}$. FALP data measured with ${}^{\mathrm{n}}\mathrm{H}_2$ are indicated by filled circles. The lines indicate the theoretical coefficients for ${}^{\mathrm{p}}\mathrm{H}_3^+$, ${}^{\mathrm{o}}\mathrm{H}_3^+$ and for H_3^+ ions in TDE. The full line is a theoretical curve for Ar^+ [Bates and Khare, 1965].

different in ${}^{\mathrm{e}}\mathrm{H}_2$ than in ${}^{\mathrm{n}}\mathrm{H}_2$ and the competition between $[\mathrm{H}_2]$-enhanced and He-assisted recombination exists. This is reflected to our measurements in the form of different K_5 for ${}^{\mathrm{e}}\mathrm{H}_2$ and for ${}^{\mathrm{n}}\mathrm{H}_2$ like in figure 12.11.

Lowering of $[\mathrm{H}_2]$ to suppress H_5^+ formation may not help, because the para-ortho conversion rate will decrease below the recombination rate, which would result in faster recombination of ${}^{\mathrm{p}}\mathrm{H}_3^+$ in the beginning and re-establishment of a para:ortho steady state in later decay times. Such effect would make the reliable fit of α_{eff} to the n_{e} decay curve impossible.

12.4 Conclusion

Our achievements in measurements of H_3^+-e^- state specific binary and ternary recombination rate coefficients are summarised in figures 12.7 and 12.8. We obtained them in the temperature range 60–300 K using two different apparatuses and two different diagnostic methods. Measurements from both experimental setups are in accordance with each other.

We have shown that the difference between the binary recombination rate coefficients for ${}^{\mathrm{p}}\mathrm{H}_3^+$ and ${}^{\mathrm{o}}\mathrm{H}_3^+$ increases significantly with the decreasing kinetic temperature. This is in accordance with the theory of Floresca dos Santos et al. [2007]. ${}^{\mathrm{o}}\mathrm{H}_3^+$ recombines with one order of magnitude lower rate coefficient than ${}^{\mathrm{p}}\mathrm{H}_3^+$ at temperatures < 77 K. Our results are obtained in a thermalised afterglow plasma where the rotational temperature of the ${}^{\mathrm{p}}\mathrm{H}_3^+$ and ${}^{\mathrm{o}}\mathrm{H}_3^+$ ensembles are equal to the kinetic temperature of the ions. Even though there are several uncertainties concerning the electron temperature, the mechanism

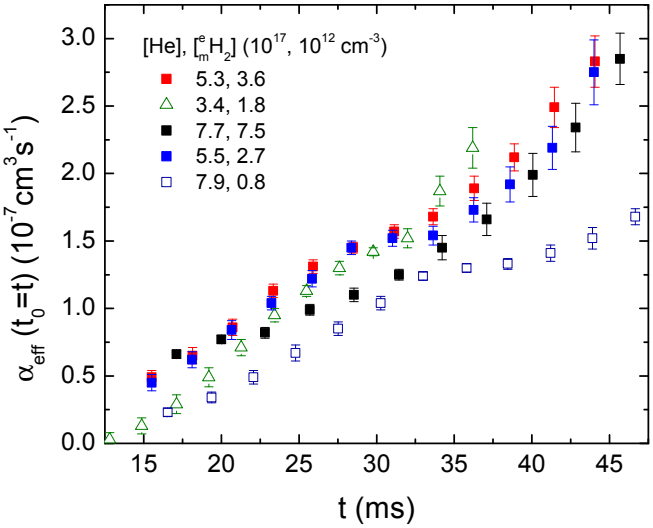

Figure 12.9: Dependence of α_{eff} on initial fitting time t_0 from equation (8.1) if $^{e}_{m}H_2$ is used. Measurements were carried out at $T_{\text{FT}} = 55$ K. Values of [He] and [$^{e}_{m}H_2$] are written in a legend.

12.4

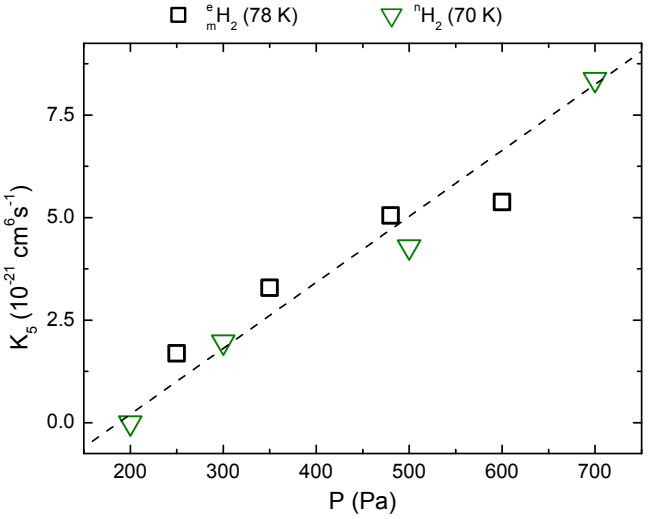

Figure 12.10: Dependence of K_5 on buffer gas pressure at temperature of the flow tube $T_{\text{FT}} \approx 77$ K. Values for $^{n}H_2$ and $^{e}_{m}H_2$ are fitted by one linear polynomial (dashed line).

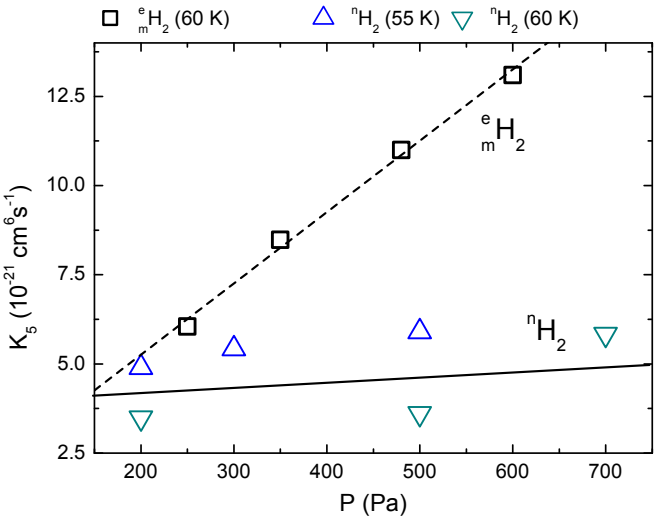

Figure 12.11: Dependence of K_5 on buffer gas pressure at temperature of the flow tube $T_{\mathrm{FT}} \approx 60$ K. The values for ${}^{\mathrm{n}}H_2$ and ${}^{\mathrm{e}}_{\mathrm{m}}H_2$ are fitted by linear polynomials (dashed line in the case of ${}^{\mathrm{e}}_{\mathrm{m}}H_2$, full line in the case of ${}^{\mathrm{n}}H_2$).

of electron heating in CRR cannot explain observed decay curves (see section 12.2.3).

The ternary H_3^+-e^- recombination rate coefficient K_{He} shows a strong dependence on the nuclear spin states. Data obtained in Cryo-FALP II suffer from big error because the population of para and ortho states of the ions is not determined in-situ.

The convergence of the temperature dependence of the ternary recombination rate coefficient to the theoretical curve of Bates and Khare [1965] observed with D_3^+ ions was not apparent in the case of H_3^+ ions. Further decrease of experimental temperature could explain more but such practical step demands better understanding of the chemical kinetics and the dynamics of key H_3^+-producing reactions in cryogenic plasma.

Epilogue

I studied temperature dependence of following reactions:
reaction of N^+ with H_2

$$N^+ + \left\{ \begin{matrix} {}^{p}H_2 \\ {}^{o}H_2 \end{matrix} \right\} \rightarrow NH^+ + H\,, \tag{12.7}$$

Attachment A.1

radiative and ternary association of protons with H_2

$$H^+ + \left\{ \begin{matrix} {}^{p}H_2 \\ {}^{o}H_2 \end{matrix} \right\} \rightarrow H_3^+ + h\nu\,, \tag{12.8a}$$

Attachment A.2

$$H^+ + \left\{ \begin{matrix} {}^{p}H_2 \\ {}^{o}H_2 \end{matrix} \right\} + \left\{ \begin{matrix} {}^{p}H_2 \\ {}^{o}H_2 \end{matrix} \right\} \rightarrow H_3^+ + H_2\,, \tag{12.8b}$$

and recombination of H_3^+ ions with electrons

$$\left. \begin{matrix} {}^{p}H_3^+ \\ {}^{o}H_3^+ \end{matrix} \right\} + e^- \rightarrow \text{neutrals products}\,, \tag{12.9a}$$

Attachments B.2, B.3, B.4 and section 12.3 (using ${}^{e}H_2$ and ${}^{n}H_2$), Attachments C (using ${}^{n}H_2$)

$$\left. \begin{matrix} {}^{p}H_3^+ \\ {}^{o}H_3^+ \end{matrix} \right\} + e^- + He \rightarrow \text{neutral products} + He\,, \tag{12.9b}$$

We obtained nuclear-spin-state-specific reaction rate coefficients of these processes. In the case of reaction (12.7) we also discussed the influence of distribution of N^+ ions' FS energy states.

The effect of nuclear spin conversion reaction

$$^{p,o}H_3^+ + {}^{p,o}H_2 \rightarrow {}^{p,o}H_3^+ + {}^{p,o}H_2 \tag{12.10}$$

Attachment B.1

was observed in the discharge plasma by means of the Cavity Ring-Down Spectroscopy. We have also shown spectroscopically that the studies of H_3^+-e^- recombination were performed with ensembles of ${}^{p}H_3^+$ and ${}^{o}H_3^+$ ions with thermal distribution of their rotational states.

Attachments B.1 and B.2

Reactions (12.8a), (12.8b) and (12.7) were studied in the ion trap (chapter 6) and the recombination was studied using Cryo-FALP II and SA-CRDS apparatuses (chapters 7 and 8). In all experiments, ${}^{n}H_2$ gas and specially prepared ${}^{e}H_2$ gas were used either as a reactant or as a source gas for formation of H_3^+ ions with specific population of its nuclear spin states.

Attachments, publications in journals, are organised according to the experimental apparatuses.

Bib

Bibliography

E. Abrahamsson, G. C. Groenenboom, and R. V. Krems. Spin-orbit relaxation of Cl($^2P_{1/2}$) and F($^2P_{1/2}$) in a gas of H_2. *The Journal of Chemical Physics*, 126(18):184303, 2007. doi:10.1063/1.2732751.

N. G. Adams and D. Smith. A study of the nearly thermoneutral reactions of N^+ with H_2, HD and D_2. *Chemical Physics Letters*, 117:67–70, 1985. doi:10.1016/0009-2614(85)80407-3.

N. G. Adams, D. Smith, and E. Alge. Measurements of dissociative recombination coefficients of H_3^+, HCO^+, N_2H^+, and CH_5^+ at 95 and 300 K using the FALP apparatus. *The Journal of Chemical Physics*, 81(4):1778–1784, 1984. doi:10.1063/1.447849.

T. Amano. The dissociative recombination rate coefficients of H_3^+, HN_2^+, and HCO^+. *The Journal of Chemical Physics*, 92(11):6492–6501, 1990. doi:10.1063/1.458594.

V. G. Anicich. *An Index of the Literature for Bimolecular Gas Phase Cation-Molecule Reaction Kinetics*. NASA JPL, Pasadena, California, 2003.

O. Asvany. *Experiments with ions and clusters in a variable temperature 22-pole ion trap*. PhD thesis, Technische Universität Chemnitz, 2003.

P. Atkins and J. de Paula. *Atkins' Physical Chemistry*. Oxford University Press, Oxford, UK, 8th edition, 2006. ISBN 9780198700722.

D. R. Bates and S. P. Khare. Recombination of positive ions and electrons in a dense neutral gas. *Proceedings of the Physical Society*, 85(2):231, 1965. doi:10.1088/0370-1328/85/2/305.

S. C. Bates. Compilation of the engineering properties of solid hydrogen. Technical report, Thoughtventions Unlimited LLC, Glastonbury, CT 06033, 2002.

D. M. Bishop. *Group theory and chemistry*. Dover Books on Chemistry Series. Dover Pubn Incorporated, 1973. ISBN 9780486673554.

S. Byron, R. C. Stabler, and P. I. Bortz. Electron-ion recombination by collisional and radiative processes. *Physical Review Letters*, 8:376–379, 1962. doi:10.1103/PhysRevLett.8.376.

D. Canet, C. Aroulanda, P. Mutzenhardt, et al. Para-hydrogen enrichment and hyperpolarization. *Concepts in Magnetic Resonance Part A*, 28A(5): 321–330, 2006. doi:10.1002/cmr.a.20065.

G. D. Carney and R. N. Porter. H_3^+: Geometry dependence of electronic properties. *The Journal of Chemical Physics*, 60(11):4251–4264, 1974. doi:10.1063/1.1680896.

A. Carrington, I. R. McNab, and Y. D. West. Infrared predissociation spectrum of the H_3^+ ion. II. *The Journal of Chemical Physics*, 98(2):1073–1092, 1993. doi:10.1063/1.464331.

P. Caselli, E. Keto, E. A. Bergin, et al. First detection of water vapor in a pre-stellar core. *The Astrophysical Journal Letters*, 759:L37, 2012. doi:10.1088/2041-8205/759/2/L37.

M. Cordonnier, D. Uy, R. M. Dickson, et al. Selection rules for nuclear spin modifications in ion-neutral reactions involving H_3^+. *The Journal of Chemical Physics*, 113(8):3181–3193, 2000. doi:10.1063/1.1285852.

K. N. Crabtree, C. A. Kauffman, B. A. Tom, et al. Nuclear spin dependence of the reaction of H_3^+ with H_2. II. Experimental measurements. *The Journal of Chemical Physics*, 134(19):194311, 2011a. doi:10.1063/1.3587246.

K. N. Crabtree, B. A. Tom, and B. J. McCall. Nuclear spin dependence of the reaction of H_3^+ with H_2. I. Kinetics and modeling. *The Journal of Chemical Physics*, 134(19):194310, 2011b. doi:10.1063/1.3587245.

A. Dalgarno. Terrestrial and extraterrestrial H_3^+. volume 32 of *Advances In Atomic, Molecular, and Optical Physics*, pages 57 – 68. Academic Press, 1994. doi:10.1016/S1049-250X(08)60010-5.

N. Dauphas, F. Robert, and B. Marty. The late asteroidal and cometary bombardment of Earth as recorded in water deuterium to protium ratio. *Icarus*, 148(2):508 – 512, 2000. doi:10.1006/icar.2000.6489.

P. Dohnal, M. Hejduk, P. Rubovič, et al. Binary and ternary recombination of D_3^+ ions at 80–130 k: Application of laser absorption spectroscopy. *Journal of Chemical Physics*, 137(19):194320, 2012a. doi:10.1063/1.4767396.

P. Dohnal, M. Hejduk, J. Varju, et al. Binary and ternary recombination of para-H_3^+ and ortho-H_3^+ with electrons: State selective study at 77–200 k. *Journal of Chemical Physics*, 136(24):244304, 2012b. doi:10.1063/1.4730162.

P. Dohnal, M. Hejduk, J. Varju, et al. Binary recombination of para- and ortho-H_3^+ with electrons at low temperatures. *Philosophical Transactions of the Royal Society A – Mathematical Physical and Engineering Sciences*, 370 (1978):5101–5108, 2012c. doi:10.1098/rsta.2012.0097.

I. Dotan and W. Lindinger. Energy dependencies of the reactions of Ar^+ with H_2, N_2, CO, O_2, CO_2, N_2O, and COS. *The Journal of Chemical Physics*, 76(10):4972–4977, 1982. doi:10.1063/1.442843.

C. W. Eaker and G. C. Schatz. A surface hopping quasiclassical trajectory study of the $H_2^+ + H_2$ and $(H_2 + D_2)^+$ systems. *Chemical Physics Letters*, 127(4):343–346, 1986. doi:10.1016/0009-2614(86)80293-7.

M. Emprechtinger, D. C. Lis, T. Bell, et al. The distribution of water in the high-mass star-forming region NGC 6334 I. *Astronomy and Astrophysics*, 521:L28, 2010. doi:10.1051/0004-6361/201015086.

K. M. Ervin and P. B. Armentrout. Translational energy dependence of $Ar^+ + XY \rightarrow ArX^+ + Y$ (XY=H_2,D_2,HD) from thermal to 30 eV c.m. *The Journal of Chemical Physics*, 83(1):166–189, 1985. doi:10.1063/1.449799.

K. M. Ferrière. The interstellar environment of our galaxy. *Reviews of Modern Physics*, 73:1031–1066, 2001. doi:10.1103/RevModPhys.73.1031.

S. Floresca dos Santos, V. Kokoouline, and C. H. Greene. Dissociative recombination of H_3^+ in the ground and excited vibrational states. *The Journal of Chemical Physics*, 127(12):124309, 2007. doi:10.1063/1.2784275.

D. Gerlich. Reactive scattering of $N^+ + H_2$ and deuterated analogs: Statistical calculation of cross sections and rate coefficients. *The Journal of Chemical Physics*, 90(7):3574–3581, 1989. doi:10.1063/1.455816.

D. Gerlich. Inhomogeneous RF fields: A versatile tool for the study of processes with slow ions. In C.-Y. Ng and M. Baer, editors, *State-Selected and State-to-State Ion-Molecule Reaction Dynamics. Part 1: Experiment*, volume LXXXII of *Advances in Chemical Physics*. John Wiley & Sons, Inc., 1992.

D. Gerlich. Experimental investigations of ion-molecule reactions relevent to interstellar chemistry. *Journal of the Chemical Society, Faraday Transactions*, 89(13):2199–2208, 1993. doi:10.1039/FT9938902199.

D. Gerlich. Ion-neutral collisions in a 22-pole trap at very low energies. *Physica Scripta*, 1995(T59):256, 1995. doi:10.1088/0031-8949/1995/T59/035.

D. Gerlich. The study of cold collisions using ion guides and traps. In I. W. M. Smith, editor, *Low Temperatures and Cold Molecules*, chapter 3., pages 121–174. World Scientific Publishing, 1st edition, 2008.

D. Gerlich and S. Horning. Experimental investigation of radiative association processes as related to interstellar chemistry. *Chemical Reviews*, 92(7):1509–1539, 1992. doi:10.1021/cr00015a003.

D. Gerlich and G. Kaefer. Ion trap studies of association processes in collisions of CH_3^+ and CD_3^+ with n-H_2, p-H_2, D_2, and He at 80 K. *The Astrophysical Journal*, 347:849–854, 1989. doi:10.1086/168174.

D. Gerlich, E. Herbst, and E. Roueff. $H_3^+ + HD \leftrightarrow H_2D^+ + H_2$: low-temperature laboratory measurements and interstellar implications. *Planetary and Space Science*, 50(12–13):1275 – 1285, 2002. doi:10.1016/S0032-0633(02)00094-6. Special issue on Deuterium in the Universe.

D. Gerlich, F. Windisch, P. Hlavenka, et al. Dynamical constraints and nuclear spin caused restrictions in $H_mD_n^+$ collision systems. *Philosofical Transactions of The Royal Society A*, 2006. doi:10.1098/rsta.2006.1685.

D. Gerlich, R. Plašil, I. Zymak, M. Hejduk, et al. State specific stabilization of $H^+ + H_2(j)$ collision complexes. *The Journal of Physical Chemistry A*, 2013. accepted for publication.

J. Glosík. Measurement of the reaction rate coefficients of reactions of H_2^+ with Ne, Ar, Kr, Xe, H_2, D_2, N_2 and CH_4 at thermal energy. *International Journal of Mass Spectrometry and Ion Processes*, 139(1):15–23, 1994. doi:10.1016/0168-1176(94)90004-3.

J. Glosík, G. Bano, E. E. Ferguson, and W. Lindinger. Selected ion flow drift tube study of the formation and dissociation of $CO^+.N_2$ ions in nitrogen buffer gas: the $CO^+.N_2$ bond energy. *International Journal of Mass Spectrometry*, 176(3):177–188, 1998. doi:10.1016/S1387-3806(98)14019-8.

J. Glosík, O. Novotný, A. Pysanenko, et al. The recombination of H_3^+ and H_5^+ ions with electrons in hydrogen plasma: dependence on temperature and on pressure of H_2. *Plasma Sources Science and Technology*, 12(4):S117–S122, 2003. doi:10.1088/0963-0252/12/4/027.

J. Glosík, I. Korolov, R. Plašil, et al. Recombination of H_3^+ ions in the afterglow of a He–Ar–H_2 plasma. *Journal of Physics B: Atomic, Molecular and Optical Physics*, 41(19):191001, 2008. doi:10.1088/0953-4075/41/19/191001.

J. Glosík, R. Plašil, I. Korolov, et al. Temperature dependence of binary and ternary recombination of H_3^+ ions with electrons. *Physical Review A*, 79(5): 052707, 2009. doi:10.1103/PhysRevA.79.052707.

J. Glosík, R. Plašil, T. Kotrík, et al. Binary and ternary recombination of H_3^+ and D_3^+ ions with electrons in low temperature plasma. *Molecular Physics*, 108:2253–2264, 2010. doi:10.1080/00268976.2010.507555.

F. Grussie, M. H. Berg, K. N. Crabtree, et al. The low-temperature nuclear spin equilibrium of H_3^+ in collisions with H_2. *The Astrophysical Journal*, 759 (1):21, 2012. doi:10.1088/0004-637X/759/1/21.

M. Hamdan, K. Birkinshaw, and N. Twiddy. The reactions of $Ar(^2P_{3/2})$ and $Ar^+(^2P_{1/2})$ with H_2 over the collision energy range 0.04–0.2 eV. *International Journal of Mass Spectrometry and Ion Processes*, 62(3):297–302, 1984. doi:10.1016/0168-1176(84)87116-5.

M. Hawley and M. A. Smith. The low translational energy dependence of the reaction $Ar^+(^2P3/2, 1/2)$ + H_2 (D_2). *The Journal of Chemical Physics*, 96 (10):7440–7444, 1992. doi:10.1063/1.462394.

M. Hejduk. Iontová past. Master's thesis, Charles University in Prague, 2009.

M. Hejduk, P. Dohnal, J. Varju, et al. Nuclear spin state-resolved cavity ring-down spectroscopy diagnostics of a low-temperature H_3^+ -dominated plasma. *Plasma Sources Science and Technology*, 21(2):024002, 2012a. doi:10.1088/0963-0252/21/2/024002.

M. Hejduk, I. Zymak, D. Mulin, R. Plašil, D. Gerlich, J. Glosík, and S. Gärtner. In-situ determination of the population of nuclear spin states of H_2 injected to the 22-pole trap. In J. Šafránková and J. Pavlů, editors, *WDS'12 Proceedings of Contributed Papers: Part II - Physics of Plasmas and Ionized Media*, pages 31–37, Praha, Czech Republic, 2012b. Matfyzpress. ISBN 978-80-7378-225-2.

E. Herbst and T. J. Millar. The chemistry of cold interstellar cloud cores. In I. W. M. Smith, editor, *Low Temperatures and Cold Molecules*, chapter 1. Imperial College Press, London, 2008.

K. Hiraoka. A determination of the stabilities of $H_3^+(H_2)_n$ with n = 1–9 from measurements of the gas-phase ion equilibria $H_3^+(H_2)_{n-1}$ + H_2=$H_3^+(H_2)_n$. *The Journal of Chemical Physics*, 87(7):4048–4055, 1987. doi:10.1063/1.452909.

K. Hiraoka and P. Kebarle. A determination of the stabilities of H_5^+, H_7^+, H_9^+, and H_11^+ from measurement of the gas phase ion equilibria H_n^+ + H_2= H_{n+2}^+ (n= 3, 5, 7, 9). *The Journal of Chemical Physics*, 62(6):2267–2270, 1975. doi:10.1063/1.430751.

P. Hlavenka. *The spectroscopic study of cold ions in plasma and ion trap*. PhD thesis, Charles University in Prague, 2007.

D. Hollenbach, M. J. Kaufman, E. A. Bergin, et al. Water, O_2, and ice in molecular clouds. *The Astrophysical Journal*, 690(2):1497, 2009. doi:10.1088/0004-637X/690/2/1497.

P. Honvault, M. Jorfi, T. González-Lezana, et al. Ortho-para H_2 conversion by proton exchange at low temperature: An accurate quantum mechanical study. *Physical Reviwe Letters*, 107:023201, 2011a. doi:10.1103/PhysRevLett.107.023201.

P. Honvault, M. Jorfi, T. González-Lezana, et al. Quantum mechanical study of the proton exchange in the ortho-para H_2 conversion reaction at low temperature. *Physical Chemistry Chemical Physics*, 13:19089–19100, 2011b. doi:10.1039/C1CP21232J.

P. Honvault, M. Jorfi, T. González-Lezana, et al. Erratum: Otho-para H_2 conversion by proton exchange at low temperature: An accurate quantum mechanical study [phys. rev. lett. 107, 023201 (2011)]. *Physical Review Letters*, 108:109903, 2012. doi:10.1103/PhysRevLett.108.109903.

M. Hu, W. Xu, X. Liu, et al. Time-dependent quantum wave packet study of the Ar + $H_2^+ \rightarrow ArH^+$ + H reaction on a new ab initio potential energy surface for the ground electronic state ($1^2A'$). *The Journal of Chemical Physics*, 138(17):174305, 2013. doi:10.1063/1.4803116.

E. Hugo, O. Asvany, and S. Schlemmer. H_3^+ + H_2 isotopic system at low temperatures: Microcanonical model and experimental study. *The Journal of Chemical Physics*, 130(16):164302, 2009. doi:10.1063/1.3089422.

E. P. L. Hunter and S. G. Lias. Evaluated gas phase basicities and proton affinities of molecules: An update. *Journal of Physical and Chemical Reference Data*, 27(3):413–656, 1998. doi:10.1063/1.556018.

Y. Ikezoe, S. Matsuoka, M. Takebe, and A. Viggiano. *Gas Phase Ion-Molecule Reaction Rate Constants*. The Mass Spectroscopy Society of Japan, Tokyo, 1987.

R. Johnsen. A critical review of H_3^+ recombination studies. *Journal of Physics: Conference Series*, 4(1):83, 2005. doi:10.1088/1742-6596/4/1/011.

R. Johnsen, C.-M. Huang, and M. A. Biondi. Three-body association reactions of H^+ and H_3^+ ions in hydrogen from 135 to 300 k. *The Journal of Chemical Physics*, 65(4):1539–1541, 1976. doi:10.1063/1.433209.

R. Johnsen, P. Rubovič, P. Dohnal, M. Hejduk, R. Plašil, and J. Glosík. Ternary recombination of H_3^+ and D_3^+ with electrons in He-H_2 (D_2) plasmas at temperatures from 50 to 300 K. *The Journal of Physical Chemistry A*, 0 (0):null, 2013. doi:10.1021/jp311978n.

V. Kokoouline and C. H. Greene. Unified theoretical treatment of dissociative recombination of D_{3h} triatomic ions: Application to H_3^+ and D_3^+. *Physical Review A*, 68:012703, 2003. doi:10.1103/PhysRevA.68.012703.

V. Kokoouline, C. H. Greene, and B. D. Esry. Mechanism for the destruction of H_3^+ ions by electron impact. *Nature*, 412:891, 2001. doi:10.1038/35091025.

I. Korolov, T. Kotrík, R. Plašil, et al. Application of langmuir probe in recombination dominated afterglow plasma. *Contributions to Plasma Physics*, 48 (5-7):521–526, 2008. doi:10.1002/ctpp.200810084.

T. Kotrík. *Electron-Ion Recombination at Temperatures below 300 K*. PhD thesis, Charles University, Praha, 2013.

T. Kotrík, P. Dohnal, S. Roučka, et al. Collisional-radiative recombination $Ar^+ + e + e$: Experimental study at 77–180 k. *Physical Review A*, 83(3): 032720, 2011a. doi:10.1103/PhysRevA.83.032720.

T. Kotrík, P. Dohnal, P. Rubovič, et al. Cryo-falp study of collisional-radiative recombination of Ar^+ ions at 40–200 k. *European Physical Journal – Applied Physics*, 56(2):24011, 2011b. doi:10.1051/epjap/2011110158.

H. Kreckel, M. Motsch, J. Mikosch, et al. High-resolution dissociative recombination of cold H_3^+ and first evidence for nuclear spin effects. *Physical Review Letters*, 95(26):263201, 2005. doi:10.1103/PhysRevLett.95.263201.

M. Larsson and A. Orel. *Dissociative Recombination of Molecular Ions*. Cambridge University Press, Cambridge, 2008.

S. Laubé, A. Le Padellec, O. Sidko, et al. New FALP-MS measurements of H_3^+, D_3^+ and HCO^+ dissociative recombination. *Journal of Physics B: Atomic, Molecular and Optical Physics*, 31:2111, 1998. doi:10.1088/0953-4075/31/9/023.

J. Le Bourlot. Ammonia formation and the ortho-to-para ratio of H_2 in dark clouds. *Astronomy and Astrophysics*, 242:235–240, 1991. URL `http://adsabs.harvard.edu/abs/1991A%26A...242..235L`.

M. T. Leu, M. A. Biondi, and R. Johnsen. Measurements of recombination of electrons with H_3^+ and H_5^+ ions. *Physical Review A*, 8:413, 1973. doi:10.1103/PhysRevA.8.413.

C. M. Lindsay and B. J. McCall. Comprehensive evaluation and compilation of H_3^+ spectroscopy. *Journal of Molecular Spectroscopy*, 210:60–83, 2001. doi:10.1006/jmsp.2001.8444.

J. B. Marquette, C. Rebrion, and B. R. Rowe. Reactions of $N^+(^3P)$ ions normal, para and deuterated hydrogens at low temperatures. *The Journal of Chemical Physics*, 89(2041), 1988. doi:10.1063/1.455101.

B. J. McCall. *Spectroscopy of H_3^+ in Laboratory and Astrophysical Plasmas*. PhD thesis, University of Chicago, USA, 2001.

B. J. McCall, A. J. Huneycutt, R. J. Saykally, et al. An enhanced cosmic-ray flux towards zeta persei inferred from a laboratory study of the H_3^+-e^- recombination rate. *Nature*, 422:500, 2003. doi:10.1038/nature01498.

B. J. McCall, A. J. Huneycutt, R. J. Saykally, et al. Dissociative recombination of rotationally cold H_3^+. *Physical Review A*, 70:052716, 2004. doi:10.1103/PhysRevA.70.052716.

I. R. McNab. *The Spectroscopy of H_3^+*, pages 1–87. John Wiley & Sons, Inc., 2007. doi:10.1002/9780470141489.ch1.

K. Mendelssohn and H. M. Rosenberg. The thermal conductivity of metals at low temperatures I: The elements of group 1, 2 and 3. *The Proceedings of The Physical Society*, 65(6):390A, 1952. doi:10.1088/0370-1298/65/6/301.

S. L. Mielke, T. C. Allison, D. G. Truhlar, and D. W. Schwenke. Quantum mechanical rate coefficients for the Cl + H_2 reaction. *The Journal of Physical Chemistry*, 100(32):13588–13593, 1996. doi:10.1021/jp960782b.

L. Neale, S. Miller, and J. Tennyson. Spectroscopic Properties of the H_3^+ Molecule: A New Calculated Line List. *The Astrophysical Journal*, 464:516, 1996. doi:10.1086/177341.

O. Novotný, R. Plašil, A. Pysanenko, I. Korolov, and J. Glosík. The recombination of D_3^++ and D_5^++ ions with electrons in deuterium containing plasma. *Journal of Physics B – Atomic Molecular and Optical Physics*, 39(11):2561–2569, 2006. doi:10.1088/0953-4075/39/11/019.

T. Oka. Introductory remarks. *Philosofical Transactions of the Royal Society A*, 358(1774):2363–2369, 2000. doi:10.1098/rsta.2000.0653.

T. Oka. Nuclear spin selection rules in chemical reactions by angular momentum algebra. *Journal of Molecular Spectroscopy*, 228(2):635–639, 2004. doi:10.1016/j.jms.2004.08.015.

L. Pagani, C. Vastel, E. Hugo, et al. Chemical modeling of L183 (= L134N) : an estimate of the ortho/para H_2 ratio. *Astronomy and Astrophysics*, 494: 623, 2009. doi:10.1051/0004-6361:200810587.

K. Park and J. C. Light. Microcanonical statistical study of ortho-para conversion in the reaction $H_3^+ + H_2 \rightarrow (H_5^+)^* \rightarrow H_3^+ + H_2$ at very low energies. *The Journal of Chemical Physics*, 126(4):044305, 2007. doi:10.1063/1.2430711.

W. Paul, B. Lücke, S. Schlemmer, and D. Gerlich. On the dynamics of the reaction of positive hydrogen cluster ions (H_5^+ to H_{23}^+) with para and normal hydrogen at 10 K. *International Journal of Mass Spectrometry and Ion Processes*, 149:373–387, 1995. doi:10.1016/0168-1176(95)04269-Q.

A. Petrignani, H. Kreckel, M. H. Berg, et al. Spectroscopy and dissociative recombination of the lowest rotational states of H_3^+. *Journal of Physics: Conference Series*, 192(1):012022, 2009. doi:doi: 10.1088/1742-6596/192/1/012022.

A. Petrignani, S. Altevogt, M. H. Berg, et al. Resonant structure of low-energy H_3^+ dissociative recombination. *Physical Review A*, 83(3):032711, 2011. doi:10.1103/PhysRevA.83.032711.

R. Plašil, J. Glosík, V. Poterya, et al. Advanced integrated stationary afterglow method for experimental study of recombination of processes of H_3^+ and D_3^+ ions with electrons. *International Journal of Mass Spectrometry*, 218(2):105 – 130, 2002. doi:10.1016/S1387-3806(02)00714-5.

R. Plašil, I. Zymak, P. Jusko, D. Mulin, D. Gerlich, and J. Glosík. Stabilization of $H^+ + H_2$ collision complexes between 11 and 28 K. *Philosofical Transactions of The Royal Society A*, 370:5066–5073, 2012.

S. T. Pratt and C. Jungen. Dissociative recombination of small polyatomic molecules. *Journal of Physics: Conference Series*, 300(1):012019, 2011. doi:10.1088/1742-6596/300/1/012019.

W. H. Press. *Numerical Recipes 3rd Edition: The Art of Scientific Computing*. Cambridge University Press, 2007. ISBN 9780521880688.

M. Quack. Detailed symmetry selection rules for reactive collisions. *Molecular Physics*, 34:477–504, 1977. doi:10.1080/00268977700101861.

J. Ramanlal. *Low Energy to Dissociation*. PhD thesis, University College London, 2005.

D. Romanini, A. A. Kachanov, and F. Stoeckel. Diode laser cavity ring down spectroscopy. *Chemical Physics Letters*, 270(5-6):538–545, 1997. doi:10.1016/S0009-2614(97)00406-5.

L. Rothman, C. Rinsland, A. Goldman, et al. The HITRAN molecular spectroscopic database and HAWKS (HITRAN atmospheric workstation): 1996 edition. *Journal of Quantitative Spectroscopy and Radiative Transfer*, 60(5): 665–710, 1998. doi:10.1016/S0022-4073(98)00078-8.

P. Rubovič, P. Dohnal, M. Hejduk, et al. Binary recombination of H_3^+ and D_3^+ ions with electrons in plasma at 50 – 230 K. *The Journal of Physical Chemistry A*, 2013. doi:10.1021/jp3123192. Article ASAP.

C. L. Russel and D. E. Manolopoulos. Time-dependent wave packet study of $N^+ + H_2$ reaction. *The Journal of Chemical Physics*, 110(117), 1999. doi:10.1063/1.478093.

C. Schlier and U. Vix. Lifetimes of triatomic collision complexes. *Chemical Physics*, 95(3):401 – 409, 1985. doi:10.1016/0301-0104(85)80163-4.

P. E. Siska. Cold and ultracold ion-neutral inelastic collisions: Spin–orbit relaxation in He + Ne^+. *The Journal of Chemical Physics*, 115(10):4527–4533, 2001. doi:10.1063/1.1394938.

D. Smith and P. Španěl. Dissociative recombination of H_3^+ and some other interstellar ions: a controversy resolved. *International Journal of Mass Spectrometry and Ion Processes*, 129:163 – 182, 1993. doi:10.1016/0168-1176(93)87040-Y.

D. Smith, N. G. Adams, A. G. Dean, and M. J. Church. The application of Langmuir probes to the study of flowing afterglow plasmas. *Journal of Physics D: Applied Physics*, 8(2):141, 1975. doi:10.1088/0022-3727/8/2/007.

J. Stevefelt, J. Boulmer, and J. F. Delpech. Collisional-radiative recombination in cold plasmas. *Physical Review A*, 12:1246–1251, 1975. doi:10.1103/PhysRevA.12.1246.

J. Tennyson. *Handbook of Molecular Physics and Quantum Chemistry*, volume 3, chapter Molecules in Space, page 356. John Wiley & Sons, Ltd, Chichester, UK, 2003a.

J. Tennyson. Astrodata. `http://www.tampa.phys.ucl.ac.uk/ftp/astrodata/h3+/`, 2003b.

B. A. Tom, S. Bhasker, Y. Miyamoto, et al. Producing and quantifying enriched para-h_2. *Review of Scientific Instruments*, 80(1):016108, 2009a. doi:10.1063/1.3072881.

B. A. Tom, V. Zhaunerchyk, M. B. Wiczer, et al. Dissociative recombination of highly enriched para-H_3^+. *The Journal of Chemical Physics*, 130(3):031101, 2009b. doi:10.1063/1.3065970.

P. Tosi, O. Dmitriev, D. Bassi, O. Wick, and D. Gerlich. Experimental observation of the energy threshold in the ion–molecule reaction $N^+ + D_2 \rightarrow ND^+ + D$. *The Journal of Chemical Physics*, 100(6):4300–4307, 1994. doi:10.1063/1.466311.

UMIST. The UMIST database for astrochemistry. `http://www.udfa.net`, 2013. [Online; accessed 7-June-2013].

E. F. van Dishoeck, L. E. Kristensen, A. O. Benz, et al. Water in Star-forming Regions with the Herschel Space Observatory (WISH). I. Overview of Key Program and First Results. *Publications of the Astronomical Society of the Pacific*, 123:138–170, 2011. doi:10.1086/658676.

A. van Itterbeek, O. Verbeke, F. Theewes, K. Staes, and J. de Boelpaep. The difference in vapour pressure between normal and equilibrium hydrogen. Vapour pressure of normal hydrogen between 20 K and 32 K. *Physica (Amsterdam)*, 30:1238–1244, 1964. doi:10.1016/0031-8914(64)90114-4.

J. Varju. *Study of H_3^+ recombination in selected quantum states*. PhD thesis, Charles University in Prague, 2011.

J. Varju, M. Hejduk, P. Dohnal, et al. Nuclear spin effect on recombination of H_3^+ ions with electrons at 77 K. *Physical Review Letters*, 106(20):203201, 2011. doi:10.1103/PhysRevLett.106.203201.

A. I. Vasyunin, D. Semenov, T. Henning, et al. Chemistry in protoplanetary disks: A sensitivity analysis. *The Astrophysical Journal*, 672(1):629, 2008. doi:10.1086/523887.

H. Villinger, J. Futrell, F. Howorka, et al. The proton transfer from ArH^+ to various neutrals. *The Journal of Chemical Physics*, 76(7):3529–3534, 1982. doi:10.1063/1.443454.

J. K. Watson. Higher-order vibration-rotation energies of the X_3 molecule. *Journal of Molecular Spectroscopy*, 103:350–363, 1984. doi:10.1016/0022-2852(84)90062-6.

D. C. B. Whittet, A. M. Cook, E. Herbst, et al. Observational constraints on methanol production in interstellar and preplanetary ices. *The Astrophysical Journal*, 742(1):28, 2011. doi:10.1088/0004-637X/742/1/28.

S. L. Widicus Weaver, D. E. Woon, B. Ruscic, and B. J. McCall. Is HO_2^+ a detectable interstellar molecule? *The Astrophysical Journal*, 697(1):601, 2009. doi:10.1088/0004-637X/697/1/601.

Wikipedia. Gaussian beam — Wikipedia, the free encyclopedia, 2013. URL `http://en.wikipedia.org/wiki/Gaussian_beam`. [Online; accessed 7-June-2013].

U. Wilhelmsson, P. E. M. Siegbahn, and R. Schinke. A three-dimensional potential energy surface for the reaction $N^+(^3P)+H_2(^1\Sigma_g^+)$ = NH^+ ($X\ ^2\Pi$)+$H(^2S)$. *The Journal of Chemical Physics*, 96(11):8202–8211, 1992. doi:10.1063/1.462325.

D. J. Willock. *Molecular Symmetry*, chapter Symmetry in Chemical Bonding, page 227. John Wiley & Sons, Ltd, Chichester, UK, 2009.

A. Yariv. *Optical Electronics in Modern Communications*. Oxford University Press, New York, USA, 5th edition, 1997.

I. Zymak. *Study of State Specific Interactions of Ions with Molecular Hydrogen at Temperatures Relevant to Astrochemistry*. PhD thesis, Charles University in Prague, 2013. to be defended.

I. Zymak, P. Jusko, Š. Roučka, et al. Ternary association of H^+ ion with H_2 at 11 K, experimental study. *European Physical Journal – Applied Physics*, 56(2):24010, 2011. doi:10.1051/epjap/2011110172.

I. Zymak, M. Hejduk, D. Mulin, et al. Low temperature ion trap studies of $N^+(^3P_{ja}) + H_2(j) \rightarrow NH^+ + H$. *The Astrophysical Journal*, 768(1):86, 2013. doi:10.1088/0004-637X/768/1/86.

Complete list of publications of Michal Hejduk

Articles in impacted journals

P. Dohnal, P. Rubovič, T. Kotrík, **M. Hejduk**, R. Plašil, R. Johnsen, and J. Glosík. Collisional radiative recombination of Ar^+ ions with electrons in ambient helium at temperatures from 50 K to 100 K. *Physical Review A*, 87 (5):052716, 2013. ISSN 1094-1622. doi:10.1103/PhysRevA.87.052716.

P. Dohnal, **M. Hejduk**, P. Rubovič, J. Varju, v. Roučka, R. Plašil, and J. Glosík. Binary and ternary recombination of D_3^+ ions at 80–130 K: Application of laser absorption spectroscopy. *The Journal of Chemical Physics*, 137(19), 2012a. ISSN 0021-9606. doi:10.1063/1.4767396.

P. Dohnal, **M. Hejduk**, J. Varju, P. Rubovič, S. Roučka, T. Kotrík, R. Plašil, R. Johnsen, and J. Glosík. Binary recombination of para- and ortho-H_3^+ with electrons at low temperatures. *Philosophical Transactions of the Royal Society A – Mathematical Physical and Engineering Sciences*, 370(1978):5101–5108, 2012b. ISSN 1364-503X. doi:10.1098/rsta.2012.0097.

P. Dohnal, **M. Hejduk**, J. Varju, P. Rubovič, v. Roučka, T. Kotrík, R. Plašil, J. Glosík, and R. Johnsen. Binary and ternary recombination of para-H_3^+ and ortho-H_3^+ with electrons: State selective study at 77-200 K. *The Journal of Chemical Physics*, 136(24), 2012c. ISSN 0021-9606. doi:10.1063/1.4730162.

D. Gerlich, R. Plašil, I. Zymak, **M. Hejduk**, P. Jusko, D. Mulin, and J. Glosík. State specific stabilization of $H^+ + H_2(j)$ collision complexes. *The Journal of Physical Chemistry A*, 0(0):null, 0, 2013. doi:10.1021/jp400917v.

J. Glosík, R. Plašil, T. Kotrík, P. Dohnal, J. Varju, **M. Hejduk**, I. Korolov, S. Roučka, and V. Kokoouline. Binary and ternary recombination of H_3^+ and D_3^+ ions with electrons in low temperature plasma. *Molecular Physics*, 108(17, SI):2253–2264, 2010. ISSN 0026-8976. doi:10.1080/00268976.2010.507555.

M. Hejduk, P. Dohnal, J. Varju, P. Rubovič, R. Plašil, and J. Glosík. Nuclear spin state-resolved cavity ring-down spectroscopy diagnostics of a low-temperature H_3^+-dominated plasma. *Plasma Sources Science & Technology*, 21(2), 2012. ISSN 0963-0252. doi:10.1088/0963-0252/21/2/024002.

R. Johnsen, P. Rubovič, P. Dohnal, **M. Hejduk**, R. Plašil, and J. Glosík. Ternary recombination of H_3^+ and D_3^+ with electrons in He-H_2 (D_2) plasmas at temperatures from 50 to 300 K. *The Journal of Physical Chemistry A*, 0 (0):null, 0, 2013. doi:10.1021/jp311978n.

I. Korolov, T. Kotrík, R. Plašil, **M. Hejduk**, and J. Glosík. Application of Langmuir probe in recombination dominated afterglow plasma. *Contributions to Plasma Physics*, 48(5-7):521–526, 2008. ISSN 0863-1042. doi:10.1002/ctpp.200810084. 7th International Workshop on Electrical

Probes in Magnetized Plasmas (IWEP 2007), Prague, Czech Republic, Jul 22-25, 2007.

P. Rubovič, P. Dohnal, **M. Hejduk**, R. Plašil, and J. Glosík. Binary recombination of H_3^+ and D_3^+ ions with electrons in plasma at 50–230 K. *The Journal of Physical Chemistry A*, 0(0):null, 0, 2013. doi:10.1021/jp3123192.

J. Varju, **M. Hejduk**, P. Dohnal, M. Jilek, T. Kotrík, R. Plašil, D. Gerlich, and J. Glosík. Nuclear Spin Effect on Recombination of H_3^+ Ions with Electrons at 77 K. *Physical Review Letters*, 106(20), 2011. ISSN 0031-9007. doi:10.1103/PhysRevLett.106.203201.

I. Zymak, **M. Hejduk**, D. Mulin, R. Plasil, J. Glosik, and D. Gerlich. Low-temperature ion trap studies of $N^+(^3P_{j_a}) + H_2(j) \rightarrow NH^+ + H$. *Astrophysical Journal*, 768(1):86, 2013. ISSN 0004-637X. doi:10.1088/0004-637X/768/1/86.

Articles in other peer-reviewed journals

M. Hejduk, P. Dohnal, P. Rubovič, J. Varju, S. Opanasiuk, R. Plašil, and J. Glosík. Equilibrium in low temperature H_3^+-dominated plasma, application of Cavity Ring-Down Spectroscopy. *Acta Universitatis Carolinae – Mathematica et Physica*, 53(1):51–59, 2012b.

Articles in conference proceedings

P. Dohnal, **M. Hejduk**, J. Varju, P. Rubovič, R. Plašil, and J. Glosík. Recombination of para- and ortho-H_3^+ with electrons in low temperature afterglow plasma. In J. Šafránková and J. Pavlů, editors, *WDS'11 Proceedings of Contributed Papers: Part II - Physics of Plasmas and Ionized Media*, pages 169–174, Praha, Czech Republic, 2011a. Matfyzpress. ISBN 978-80-7378-185-9.

P. Dohnal, J. Varju, **M. Hejduk**, T. Kotrík, P. Rubovič, R. Plašil, and J. Glosík. State selective recombination of para- and ortho-H_3^+ at 140 K. In J. Országh, P. Papp, and Š Matejčík, editors, *Book of Contributed Papers: 18th Symposium on Application of Plasma Processes and Workshop on Plasmas as a Planetary Atmospheres Mimics*, pages 166–170, Bratislava, Slovakia, 2011b. Department of Experimental Physics, Faculty of Mathematics, Physics and Informatics, Comenius University in Bratislava (Slovakia); Society for Plasma Research and Applications in cooperation with Library and Publishing Centre CU, Bratislava, Slovakia. ISBN 978-80-89186-77-8.

J. Glosík, R. Plašil, T. Kotrík, P. Dohnal, **M. Hejduk**, P. Jusko, Š Roučka, and P. Rubovič. Recombination in low temperature plasma. In J. Országh, P. Papp, and Š Matejčík, editors, *Book of Contributed Papers: 18th Symposium on Application of Plasma Processes and Workshop on Plasmas as a Planetary Atmospheres Mimics*, pages 179–184, Bratislava, Slovakia, 2011. Department of Experimental Physics, Faculty of Mathematics, Physics and Informatics, Comenius University in Bratislava (Slovakia); Society for Plasma

Research and Applications in cooperation with Library and Publishing Centre CU, Bratislava, Slovakia. ISBN 978-80-89186-77-8.

M. Hejduk, J. Varju, P. Dohnal, M. Jílek, R. Plašil, Š. Roučka, J. Glosík, and J. Lang. Formation and destruction of para and ortho H_3^+ in discharge and afterglow. Experiments with para-hydrogen. In J. Šafránková and J. Pavlů, editors, *WDS'10 Proceedings of Contributed Papers: Part II - Physics of Plasmas and Ionized Media*, pages 54–59, Praha, Czech Republic, 2010. Matfyzpress. ISBN 978-80-7378-140-8.

M. Hejduk, P. Dohnal, P. Rubovič, S. Opanasiuk, R. Plašil, and J. Glosík. Cavity ring-down spectroscopy of D_3^+-dominated low-temperature plasma. In S. Ratynskaya, L. Blomberg, and A. Fasoli, editors, *Europhysics Conference Abstracts*, volume 36F, page P2.143, Stockholm, Sweden, 2012a. European Physical Society. ISBN 2-914771-79-7. 39th EPS Conference on Plasma Physics and 16th International Congress on Plasma Physics 2–6 July 2012, 4 pp.

M. Hejduk, I. Zymak, D. Mulin, R. Plašil, D. Gerlich, J. Glosík, and S. Gärtner. In-situ determination of the population of nuclear spin states of H_2 injected to the 22-pole trap. In J. Šafránková and J. Pavlů, editors, *WDS'12 Proceedings of Contributed Papers: Part II - Physics of Plasmas and Ionized Media*, pages 31–37, Praha, Czech Republic, 2012c. Matfyzpress. ISBN 978-80-7378-225-2.

M. Hejduk, P. Dohnal, P. Rubovič, J. Varju, A. Kálosi, R. Plašil, and J. Glosík. Experimental studies of state specific processes in hydrogen plasma. In J. Országh, P. Papp, Š Matejčík, and M. Danko, editors, *Book of Contributed Papers: 19th Symposium on Application of Plasma Processes and Workshop on Ion Mobility Spectrometry*, pages 160–165, Bratislava, Slovakia, 2013. Department of Experimental Physics, Faculty of Mathematics, Physics and Informatics, Comenius University in Bratislava (Slovakia); Society for Plasma Research and Applications in cooperation with Library and Publishing Centre CU, Bratislava, Slovakia.

I. Korolov, T. Kotrík, R. Plašil, **M. Hejduk**, J. Varju, P. Dohnal, and J. Glosík. Recombination of KrD^+ and KrH^+ ions in afterglow plasma. In W. J. van der Zande, editor, *Seventh International Conference on Dissociative Recombination: Theory, Experiments and Applications (DR2007)*, volume 192 of *Journal of Physics Conference Series*, Bristol, UK, 2009. IOP Publishing Ltd. doi:10.1088/1742-6596/192/1/012018. 7th International Conference on Dissociative Recombination: Theory, Experiments and Applications, Radboud Univ Nijmegen, Ameland, Netherlands, Jul 18–23, 2007, 4 pp.

T. Kotrík, P. Dohnal, P. Rubovič, **M. Hejduk**, S. Opanasiuk, R. Plašil, and J. Glosík. Collisional radiative recombination of Ar^+ ions, experimental study at 40–300K. In I. D. Williams, H. W. Van der Hart, J. F. McCann, and D. S. F. Crothers, editors, *XXVII International Conference on Photonic, Electronic and Atomic Collisions (ICPEAC 2011), PTS 1-15*, volume 388 of *Journal of Physics Conference Series*, Bristol, UK, 2012. IOP Publishing

Ltd. doi:10.1088/1742-6596/388/6/062033. 27th International Conference on Photonic, Electronic and Atomic Collisions (ICPEAC), Queens Univ Belfast, Belfast, North Ireland, Jul 27-Aug 02, 2011, 1 pp.

D. Mulin, I. Zymak, **M. Hejduk**, P. Dohnal, R. Plašil, D. Gerlich, and J. Glosík. Limits for the N^+ + p/o-H_2 reaction study using 22-pole ion trap apparatus. In J. Šafránková and J. Pavlů, editors, *WDS'11 Proceedings of Contributed Papers: Part II - Physics of Plasmas and Ionized Media*, pages 25–30, Praha, Czech Republic, 2012. Matfyzpress. ISBN 978-80-7378-225-2.

S. Opanasiuk, T. Kotrík, P. Dohnal, **M. Hejduk**, P. Rubovič, R. Plašil, and J. Glosík. Study of collisional-radiative recombination using CRYO-FALP. In J. Šafránková and J. Pavlů, editors, *WDS'11 Proceedings of Contributed Papers: Part II - Physics of Plasmas and Ionized Media*, pages 141–145, Praha, Czech Republic, 2011. Matfyzpress. ISBN 978-80-7378-185-9.

R. Plašil, J. Varju, **M. Hejduk**, P. Dohnal, T. Kotrík, and J. Glosík. Experimental study of para- and ortho-H_3^+ recombination. In S. L. Guberman and A. E. Orel, editors, *Eighth International Conference on Dissociative Recombination: Theory, Experiments and Applications (DR2010)*, volume 300 of *Journal of Physics Conference Series*, Bristol, UK, 2011. IOP Publishing Ltd. doi:10.1088/1742-6596/300/1/012023. 8th International Conference on Dissociative Recombination, Lake Tahoe, CA, Aug 16-20, 2010, 8 pp.

P. Rubovič, T. Kotrík, P. Dohnal, Š. Roučka, **M. Hejduk**, S. Opanasiuk, R. Plašil, and J. Glosík. Swarm experiments at 40–100 K, Cryo-FALP. In J. Šafránková and J. Pavlů, editors, *WDS'11 Proceedings of Contributed Papers: Part II - Physics of Plasmas and Ionized Media*, pages 146–151, Praha, Czech Republic, 2011. Matfyzpress. ISBN 978-80-7378-185-9.

J. Varju, **M. Hejduk**, P. Dohnal, T. Kotrík, M. J. R. Plašil, and J. Glos'ik. Recombination in plasmas with different populations of para and ortho H_3^+. In J. Šafránková and J. Pavlů, editors, *WDS'10 Proceedings of Contributed Papers: Part II - Physics of Plasmas and Ionized Media*, pages 60–65, Praha, Czech Republic, 2010. Matfyzpress. ISBN 978-80-7378-140-8.

List of Tables

Lst

List of Figures

List of Abbreviations and Symbols

Acronyms

22PT 22-Pole Trap

ALMA Atacama Large Millimeter/submillimeter Array, the largest astronomical project in existence financed by Europe, North America and East Asia in cooperation with the Republic of Chile

ALTA-DENA Adiabatic Longitudinal Transport After Dissociation Engenders Net Alignment

AOM Acousto-Optic Modulator

C1 Outer chamber for isolation vacuum of para-hydrogen generator

CC Catalyst container of para-hydrogen generator

CH Cold head of a closed cycle helium refrigerator

CRR Collisional radiative recombination

CRYRING Facility at the Manne Siegbahn Laboratory of the Stockholm University consisting of a small ion synchrotron and storage ring with electron cooling, an radiofrequency linear accelerator and two injectors for different types of ions.

DR Dissociative recombination

FS Fine structure, related to spin-orbit interaction in atom or molecule

ISM Interstellar matter

MCP Micro-Channel Plate

NMR Nuclear Magnetic Resonance

PASADENA Parahydrogen and Synthesis Allow Dramatically Enhanced Nuclear Alignment

PES Potential Energy Surface

PLC Programmable Logical Circuit

QP QuadruPole

RE Ring Electrode

RF Radio Frequency

RF Radio-Frequency

SIS Storage Ion Source

TDE ThermoDynamic Equilibrium

TDP Turbo-molecular Drug Pump

UDfA UMIST Database for Astrochemistry

UMIST University of Manchester Institute of Science and Technology

WISH Water In Star forming regions with Herschel, a program of searching for water spectra in the Universe using Hershel telescope

Physical constants

c Speed of light

const. Constant

h Planck constant

k_{B} Boltzmann constant, $k_{\mathrm{B}} \approx 1.38 \times 10^{-23}\,\mathrm{J\,K^{-1}}$

Atoms, molecules and other particles

$^{\mathrm{e}}\mathrm{H}_2$ Para-states-enriched H_2 gas with ${}^{\mathrm{p}}f_2 > 0.25$

$^{\mathrm{e}}_{\mathrm{m}}\mathrm{H}_2$ Para-states-enriched H_2 gas with maximal obtainable population of para-states. See chapter 9 for the value of ${}^{\mathrm{p}}f_2$.

e^- Electron

$^{\mathrm{n}}\mathrm{H}_2$ Normal H_2, H_2 gas with ${}^{\mathrm{p}}f_2$ and ${}^{\mathrm{o}}f_2$ corresponding to TDE at the room temperature, ${}^{\mathrm{p}}f_2 = 0.25$.

Lst

$^{\mathrm{o}}\mathrm{H}_3^+$ H_3^+ ion in ortho nuclear spin state

$^{\mathrm{p}}\mathrm{H}_3^+$ H_3^+ ion in para nuclear spin state

Symbols

$\approx$ Rounded to a significant digit. If the values is the best known, = sign is used instead.

$\langle a, b \rangle$ Closed interval

$[\mathbf{X}]$ Number density of particle X

$\oplus$ $\Gamma = \Gamma^1 \oplus \Gamma^2 \oplus \Gamma^3$ means: "The representation Γ can be reduced to $\Gamma^{1,2,3}$ through a similarity transformation." [see Bishop, 1973, p. 111]

$\otimes$ Direct product [see Bishop, 1973, p. 157]

$\{\ldots, \ldots\}$ Enumeration of elements in a set

$\equiv$ Equality by definition.

a–b From a to b

Im Imaginary part of complex number

$\in$ Expression $a \in B$ means that a is an element of B

$\lesssim$ Expression $a \lesssim b$ means that the order of magnitude of a is less or equal to the one of b.

log Natural logarithm

$\Leftrightarrow$ Logical equivalence

$\propto$ Expression $a \propto b$ means that variable a is proportional to expression or value b.

Re Real part of complex number

$\Rightarrow$ Logical implication

$\sim$ Equal within an order of magnitude

$\subset$ $A \subset B$ means that A is a subset of B

Units

Å Ångström, 1 Å $= 10^{-10}$ m.

cm^{-1} Wave number w. Serves to express the wavelength λ via relation $\lambda = 1/w$ (in cm) or energy E (in K) via $E = h\,c\,w \approx (1.4\,\mathrm{K\,cm})\,w$.

eV Electron-Volt, eV $\approx 11605\ k_\mathrm{B}$K

h Hour

K Kelvin, unit of temperature

min Minute (time unit)

sccm Standard cubic centimetre per minute, unit of flow. $1\,\mathrm{sccm} \approx 1.67 \times 10^{-3}$ Pa m^3 s^{-1}.

scc Standard cubic centimetre, $1\,\mathrm{scc} \equiv 0.1$ Pa m^3.

Variables

α_bin Binary recombination rate coefficient evaluated from α_eff

α_eff Effective recombination rate coefficient (evaluated from decays of charged particles' number density measured in experiments)

${}^\mathrm{e}\alpha_\mathrm{bin}$ Binary recombination rate coefficient for H_3^+ ensemble in ${}^\mathrm{e}\mathrm{H}_2$ evaluated from ${}^\mathrm{e}\alpha_\mathrm{eff}$

${}^\mathrm{e}\alpha_\mathrm{eff}$ Effective recombination rate coefficient for H_3^+ ensemble formed in ${}^\mathrm{e}\mathrm{H}_2$

${}^\mathrm{e}K_\mathrm{He}$ Ternary He-assisted recombination rate coefficient for H_3^+ ensemble in ${}^\mathrm{e}\mathrm{H}_2$ evaluated from ${}^\mathrm{e}\alpha_\mathrm{eff}$

J, j Angular momentum quantum number

K_{CRR} Ternary recombination rate coefficient for collisional radiative recombination

K_{He} Ternary He-assisted recombination rate coefficient evaluated from α_{eff}

K_5 Ternary recombination rate coefficient evaluated from $[H_2]$ dependence

${}^{\mathrm{n}}\alpha_{\mathrm{bin}}$ Binary recombination rate coefficient for H_3^+ ensemble in ${}^{\mathrm{n}}H_2$ evaluated from ${}^{\mathrm{n}}\alpha_{\mathrm{eff}}$

${}^{\mathrm{n}}\alpha_{\mathrm{eff}}$ Effective recombination rate coefficient for H_3^+ ensemble formed in ${}^{\mathrm{n}}H_2$

${}^{\mathrm{n}}K_{\mathrm{He}}$ Ternary He-assisted recombination rate coefficient for H_3^+ ensemble in ${}^{\mathrm{n}}H_2$ evaluated from ${}^{\mathrm{n}}\alpha_{\mathrm{eff}}$

ν Frequency of light

${}^{\mathrm{o}}\alpha_{\mathrm{bin}}$ Binary recombination rate coefficient for ${}^{\mathrm{o}}H_3^+$ evaluated from ${}^{\mathrm{o}}\alpha_{\mathrm{eff}}$

${}^{\mathrm{o}}\alpha_{\mathrm{eff}}$ Effective recombination rate coefficient for ${}^{\mathrm{o}}H_3^+$

${}^{\mathrm{o}}f_2$ Population of ortho states of H_2, ${}^{\mathrm{o}}f_2 = 1 - {}^{\mathrm{p}}f_2$ for H_2

${}^{\mathrm{o}}f_3$ Population of ortho states of H_3^+, ${}^{\mathrm{o}}f_3 = 1 - {}^{\mathrm{p}}f_3$

${}^{\mathrm{o}}K_{\mathrm{He}}$ Ternary He-assisted recombination rate coefficient for ${}^{\mathrm{o}}H_3^+$ evaluated from ${}^{\mathrm{o}}\alpha_{\mathrm{eff}}$

${}^{\mathrm{p}}\alpha_{\mathrm{bin}}$ Binary recombination rate coefficient for ${}^{\mathrm{p}}H_3^+$ evaluated from ${}^{\mathrm{p}}\alpha_{\mathrm{eff}}$

${}^{\mathrm{p}}\alpha_{\mathrm{eff}}$ Effective recombination rate coefficient for ${}^{\mathrm{p}}H_3^+$

P_{C} Pressure of ${}^{\mathrm{e}}_{\mathrm{m}}H_2$ above catalyst in para-hydrogen generator

Lst

P_{C1} Pressure of isolation vacuum of the para-hydrogen generator

${}^{\mathrm{p}}f_3$ Population of para states of H_3^+, ${}^{\mathrm{p}}f_3 = [{}^{\mathrm{p}}H_3^+]/[H_3^+]$

${}^{\mathrm{p}}K_{\mathrm{He}}$ Ternary He-assisted recombination rate coefficient for ${}^{\mathrm{p}}H_3^+$ evaluated from ${}^{\mathrm{p}}\alpha_{\mathrm{eff}}$

${}^{\mathrm{p}}f_2$ Population of para states of H_2, ${}^{\mathrm{p}}f_2 = [{}^{\mathrm{p}}H_2]/[H_2]$

S Total nuclear spin quantum number, pumping speed or integral absorption coefficient

T_{CC} Temperature of catalyst container

T_{e} Kinetic temperature of electrons

T_{FT} Temperature of flowtube

T_{He} He buffer gas temperature

T_{Kin} Kinetic temperature. Related to velocity distribution of particles.

$T_{\mathrm{Rot\text{-}ortho}}$ T_{Rot} evaluated from two ${}^{\mathrm{o}}H_3^+$ transition lines

Attachments

Lst

Lst

A. 22PT

A.1 Low-Temperature Ion Trap Studies of $N^+(^3P_{j_a}) + H_2(j) \rightarrow NH^+ + H$

I. Zymak, M. Hejduk, D. Mulin, R. Plašil, J. Glosík and D. Gerlich.
Astrophysical Journal, 768(1):86, 2013. doi:10.1088/0004-637X/768/1/86.

The Astrophysical Journal, 768:86 (8pp), 2013 May 1 doi:10.1088/0004-637X/768/1/86

LOW-TEMPERATURE ION TRAP STUDIES OF $N^+(^3P_{ja}) + H_2(j) \rightarrow NH^+ + H$

I. Zymak[1], M. Hejduk[1], D. Mulin[1], R. Plašil[1], J. Glosík[1], and D. Gerlich[1,2,3]
[1] Faculty of Mathematics and Physics, Charles University, Prague, Czech Republic
[2] Department of Physics, Technische Universität Chemnitz, D-09107 Chemnitz, Germany
Received 2012 December 30; accepted 2013 February 22; published 2013 April 17

ABSTRACT

Using a low-temperature 22-pole ion trap apparatus, detailed measurements for the title reaction have been performed between 10 K and 100 K in order to get some state specific information about this fundamental hydrogen abstraction process. The relative population of the two lowest H_2 rotational states, $j = 0$ and 1, has been varied systematically. NH^+ formation is nearly thermo-neutral; however, to date, the energetics are not known with the accuracy required for low-temperature astrochemistry. Additional complications arise from the fact that, so far, there is no reliable theoretical or experimental information on how the reactivity of the N^+ ion depends on its fine-structure (FS) state $^3P_{ja}$. Since in the present trapping experiment, thermalization of the initially hot FS population competes with hydrogen abstraction, the evaluation of the decay of N^+ ions over long storage times and at various He and H_2 gas densities provides information on these processes. First assuming strict adiabatic behavior, a set of state specific rate coefficients is derived from the measured thermal rate coefficients. In addition, by recording the disappearance of the N^+ ions over several orders of magnitude, information on nonadiabatic transitions is extracted including FS-changing collisions.

Key words: astrochemistry – ISM: abundances – molecular processes

Online-only material: color figures

1. INTRODUCTION

As discussed recently by Dislaire et al. (2012) atomic nitrogen and nitrogen-containing molecules are important tracers for understanding astrophysical objects. Due to the abundance of hydrogen, the nitrogen hydrides, NH, NH_2, and NH_3, and their ions are of central importance in astrochemistry. For example, subsequent hydrogen abstraction reactions, starting with N^+, finally lead to the formation of interstellar ammonia (Le Bourlot 1991). In order to obtain quantitative abundances in various environments, e.g., in dark clouds, the reaction

$$N^+(^3P_{ja}) + H_2(j) \rightarrow NH^+ + H \qquad (1)$$

A.1

and its dependence on the rotational ($j = 0, 1, \ldots$) and the FS ($j_a = 0$, 1, and 2) states plays a special role. In the 1980s and early 1990s, there were several experimental activities in which this reaction was studied at room temperature and below. Various techniques such as SIFDT (selected ion flow and drift tube; Adams & Smith 1985), CRESU (Cinétique de réactions en écoulement supersonique uniforme; Marquette et al. 1988), low-temperature penning ion trap (Barlow et al. 1986), and guided ion beams with scattering cells (Sunderlin & Armentrout 1994) provided detailed results. First applications of low-temperature radio frequency (RF) ion traps to the title reaction were mentioned in Gerlich (1989) and extended results have been given in Gerlich (1993). Probably the most sophisticated experiments have been based on crossing or merging a guided N^+ ion beam with a supersonic hydrogen beam (Tosi et al. 1994); however, the ambitious goal of determining state specific cross sections has not been reached so far. There have also been various theoretical studies (see Gerlich 1989; Nyman & Wilhelmsson 1992; Wilhelmsson & Nyman 1992; Russell & Manolopoulos 1999, and references therein), and interesting aspects have been discussed; however, concerning reactions at low temperature, they raise more questions than they answer.

A basic problem is that one does not yet know whether the formation of $NH^+ + H$ is really endothermic or whether somewhere a barrier hinders the reaction. As reviewed by Gerlich (2008a), the analysis of measured temperature dependencies of reaction (1) with a statistical theory leads to an endothermicity of 17 meV if one presupposes that FS and rotational states are in thermal equilibrium and that, in promoting the reaction, their energies are as equally efficient as translational energy. If FS energy is not available at all, the assumed endothermicity has to be lowered to 11 meV to match the experimental results. High-level ab initio computations are not yet sufficiently accurate to predict this value with the required accuracy, i.e., within a few meV. This is rather unexpected since one has to calculate only the binding energy of NH^+. Discussions of different high-level ab initio computations, calculated potentials, bond dissociation energies, and heat of formation for NH and NH^+ can be found in Tarroni et al. (1997), Jursic (1998), and Amero & Vazquez (2005). Also related to this subject are the quantum chemical calculations of the adiabatic ionization energy of the NH_2 radical (Willitsch et al. 2006), the accuracy of which has been estimated to be about 100 cm^{-1}.

In order to understand reaction dynamics, one needs more than just the asymptotic energies. In the present case, several potential energy surfaces are involved. The situation is illustrated in Figure 1 with a simplified electronic correlation diagram (Mahan & Ruska 1976; Russell & Manolopoulos 1999). Inspection reveals that, at kinetic energies below 1 eV, only the $NH^+(X^2\Pi)$ product can be formed, if the two reactants N^+ and H_2 are in their ground state. For C_s symmetry the reaction can proceed adiabatically via the more than 6 eV deep double-well structure, as indicated by the dashed lines avoiding the crossings. An analytical fit of this lowest adiabatic $^3A''$ potential energy surface has been published by Wilhelmsson et al. (1992). This surface has been used for low-energy quasi-classical trajectory

[3] Author to whom any correspondence should be addressed.

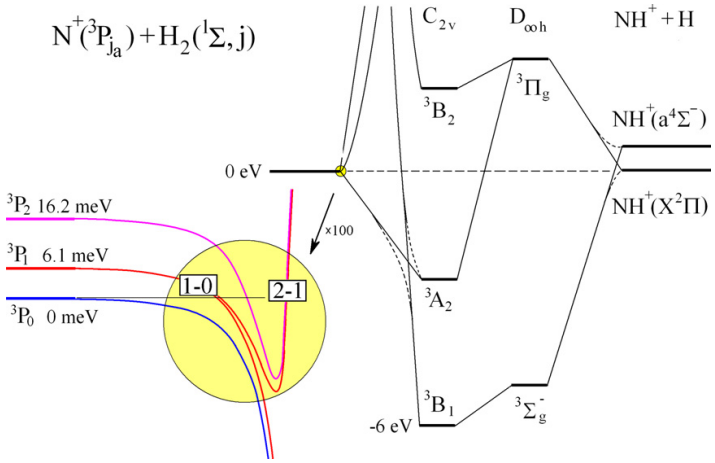

Figure 1. Schematic view of the electronic state correlation diagram for the NH_2^+ system (not to scale; for details see Mahan & Ruska 1976; González et al. 1986; Russell & Manolopoulos 1999). The horizontal dashed line indicates that reaction (1) is nearly thermoneutral. Typical experimental and theoretical values for the endothermicity (or barrier) range from 11 meV (Gerlich 2008a) to 33 meV (Wilhelmsson et al. 1992). The formation of a strongly bound NH_2^+ complex is possible via avoided intersections (C_s symmetry; dashed lines). Important for low-temperature collisions is the coupling between the nine near-degenerate spin–orbit potential-energy surfaces during the approach of the reactants. This can lead both to FS changes and reaction. The situation is illustrated in the lower left corner on a magnified scale in adiabatic approximation but also indicating schematically nonadiabatic transitions. The potential curves have been estimated in analogy to the N^+–He collision complex (Soldan & Hutson 2002).

(A color version of this figure is available in the online journal.)

calculations (Nyman & Wilhelmsson 1992; Wilhelmsson & Nyman 1992) as well as for time-dependent wave packet studies (Russell & Manolopoulos 1999). Problematic for the comparison of calculated reaction probabilities with low-temperature experimental data is that, on this surface, the reaction endothermicity is certainly too large with 33 meV.

Another shortcoming of the calculations mentioned above is that the role of FS splitting is included using only rather crude approximations. As can be seen from the electronic correlation diagram in Figure 1, only one of the three triplet surfaces that correlates with the entrance channel, allows direct access to the deep well, while the other two are repulsive. In statistical theories, this is accounted for by using suitable electronic degeneracy factors concerning the $N^+ + H_2$ system this is discussed in Gerlich (1989). A closer look at the initial splitting region (small circle in Figure 1) reveals that the open-shell structure of $N^+(^3P_{ja})$ results in at least nine spin–orbit coupled potential-energy surfaces. As plotted schematically in Figure 1 (large circle), they converge at large distances toward the three states $^3P_0$, $^3P_1$, and $^3P_2$. The question remains of how one can reach the product channel on these nine surfaces. Is there access to the deep well without any activation barrier? The assumption that only the three lowest spin–orbit surfaces lead to products, while reaction on the other six is not possible at low energies is very restrictive. This model, which is based on strict adiabatic behavior, was applied by Wilhelmsson & Nyman (1992) and Nyman & Wilhelmsson (1992). It has also been used by Russell & Manolopoulos (1999). Therefore, we also start the evaluation of our data on this basis. However, strict adiabatic behavior not only forbids reactions of ions in the $^3P_2$ state but also inhibits FS-changing collisions. As a consequence, N^+ ions in the highest fine structure would be completely insensitive to collisions with H_2. Since in our experiment, however, all N^+ ions are hydrogenated sooner or later, a more sophisticated kinetic model is required to account for the competition between reaction and thermalization of all three FS states.

Disregarding the details of any multi-surface model, a simpler question is how the different forms of energy, stored in the excited states of the reactants, can help to promote the reaction in the endothermic direction. Comparison of the thermal motion of the reactants (here up to 100 K, corresponding to $3/2\ k_B T = 12.9$ meV) with the electronic energy of N^+ ($^3P_1$ 6.1 meV, $^3P_2$ 16.2 meV) and rotational energy of H_2 (14.4 meV for $j = 1$) reveals that all these values are comparable to the endothermicity or barrier (11 or 17 meV, see above).

The equivalence of rotational and translational energy was first shown in the pioneering work from Marquette et al. (1988). In their low-temperature flow experiment, reaction (1) was studied using para hydrogen (p-H_2) as well as normal hydrogen (n-H_2). Note that p-H_2 has a total nuclear spin $I = 0$ and only even rotational states are allowed while ortho hydrogen has $I = 1$ and odd rotational states. Normal hydrogen is the 300 K statistical mixture consisting of 1/4 p-H_2 and 3/4 o-H_2. In what follows, other mixtures are characterized with the abbreviation f, indicating the fraction of o-H_2. The results from Marquette et al. (1988) were corroborated in a low-temperature trapping experiment (Gerlich 1993) and were extended using mixtures with $f = 0.13$, 0.03, and <0.01. More systematic studies of the f dependence are reported in this work.

In all experimental papers prior to 1994 it was postulated that the energy of the excited FS states is equivalent to translational and rotational energy. In addition it has been assumed that, in flow (Marquette et al. 1988) or trapping experiments (Gerlich 1993), thermal populations of the $^3P_{ja}$ states are reached rather quickly. There has never been any proof of this. In a guided ion beam experiment (Sunderlin & Armentrout 1994), FS energy was simply accounted for using the thermal mean value (9.5 meV at 300 K). As already mentioned, an analysis of all these experimental results, based on a detailed statistical model (Gerlich 1989), came to the conclusion that 17 meV is needed to promote the reaction. First doubts concerning the efficiency of the FS energy were formulated in

A.1

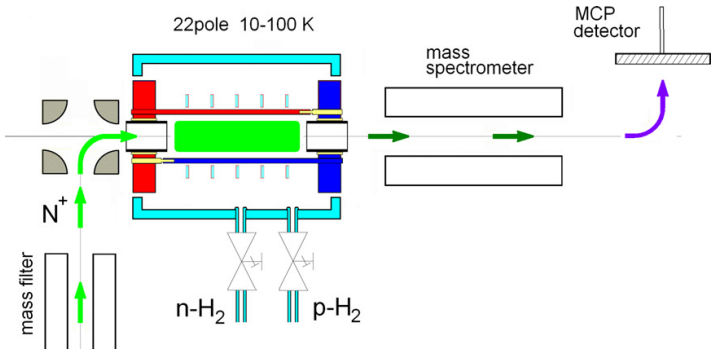

Figure 2. Schematic view of the 22 pole ion trap instrument used for studying reaction (1). The copper box surrounding the trap can be cooled down to 10 K. N^+ ions are produced from N_2 gas in a storage ion source (not shown), using electrons with a kinetic energy of 60 eV. After mass selection, they are transferred to the trap via an electrostatic quadrupole bender. In the radial direction the ions are confined by the RF field ($\Omega/2\pi = 19$ MHz, $V_0 = 20$ V). The potential inside the trap can be corrected locally with five ring electrodes. The entrance and exit electrode are used to open and close the trap with electrostatic barriers of some tens of meV. To the right, ions move through the quadrupole mass spectrometer toward the detector.

(A color version of this figure is available in the online journal.)

Tosi et al. (1994), especially in the context of Figure 4 of that publication.

This contribution reports new experimental results measured with a variable temperature RF ion trap. After a brief description of the instrument and typical measuring and calibration procedures, different sets of data are presented including the dependence of rate coefficients on the temperature and on the ortho fraction f and the time dependence of converting primary ions into products. The data are evaluated using first the adiabatic model resulting in state specific rate coefficients $k_{j,ja}(T)$ for $j = 0$, 1 and $j_a = 0$–2. In Section 4, additional information on the reactivity of $j_a = 2$ and the FS relaxation rate coefficient is presented. Some remarks concerning planned and possible extension of this work will conclude this paper.

2. EXPERIMENTAL

The instrument used in this study is the Chemnitz AB 22 pole trapping apparatus (Gerlich et al. 2011) which has been operated since 2009 at Charles University in Prague. It has been used recently in combination with an effusive beam of H atoms (Plasil et al. 2011; Gerlich et al. 2012). In the present study, the neutral target gas is leaked directly into the trap. The basics of storing ions in RF fields have been described thoroughly in Gerlich (1992, 1995). A summary of typical applications in low-temperature ion chemistry has been given in Gerlich (2008a, 2008b).

The central part of the instrument is shown schematically in Figure 2. The trap (22 rods with 1 mm diameter) is surrounded by a copper box which is mounted onto the cold head of a closed-cycle helium refrigerator. Stationary temperatures between 10 K and 100 K are set by simultaneously cooling and heating. Alternatively, temperature-dependent measurements are performed during the cooling down or warming up phases of the cold head. Hydrogen gas can be introduced into the trap via two leak valves, allowing us to produce any mixture from almost pure p-H_2 ($f < 0.01$) to n-H_2 ($f = 0.75$). A few collisions of the neutral gas with the walls are sufficient to get it into thermal equilibrium with the trap temperature, with the exception of the ortho/para ratio. The gas density inside the trap is determined using a spinning rotor gauge or a calibrated ionization gauge. The background pressure of the main chamber is lower than 10^{-7} Pa. With the exception of HD, most gas impurities are frozen out below 100 K; nonetheless, the small concentrations left can lead to errors as discussed below.

The primary N^+ ions are produced via dissociative ionization of N_2 in a storage ion source using energetic electrons (60 eV). Under such conditions it is safe to assume that the three fine-structure states $^3P_0$, $^3P_1$, and $^3P_2$ are populated according to their statistical weights, i.e., with 1, 3, and 5, respectively. Attempts to thermalize this population prior to reaction have been described in Gerlich (1993) and Tosi et al. (1994); however, no changes in the reactivity have been observed. After passing a mass filter and an electrostatic quadrupole bender, the primary ions are transferred into the trap. During the filling period, the electrostatic barrier at the entrance electrode is slightly negative relative to the potential of the trap. After various storage times, the trap exit is opened and the ions move through the quadrupole mass spectrometer and are converted into a fast negative pulse using an MCP detector followed by a discriminator. The standard measuring procedure is based on filling the trap at a fixed frequency with a well-defined number of primary ions (typically a few thousand) and analyzing the content after different storage times.

A typical set of raw data, recorded at a 22 pole temperature of 52 K and with buffer and reactant gas in the trap ([He] = 5.2×10^{11} cm^{-3}, [n-H_2] = 1.6×10^{11} cm^{-3}), is shown in Figure 3. The injected N^+ ions react with hydrogen and form NH^+. In subsequent collisions, these products react to form NH_2^+ and finally NH_3^+. As discussed by Gerlich (1993), NH_4^+ is also formed at length, however, very slowly, most probably via tunneling. In the first 10 ms, the sum of all detected ions (Σ) is increasing. This is due to phase-space compression of the injected ion cloud via collisions with the cold buffer gas leading to an increase of the detection efficiency (mainly acceptance and transmission of the quadrupole). Usually such time dependences are fitted with the solutions of a suitable rate equation system. In the present study, most information is derived simply from the decay of the primary ions. Quick information on the decay time constant is obtained by recording the number of N^+ ions at two or three suitable storage times. In order to get deeper insight into the kinetics, the disappearance of N^+ is followed in small time steps over several orders of magnitude (see below).

A.1

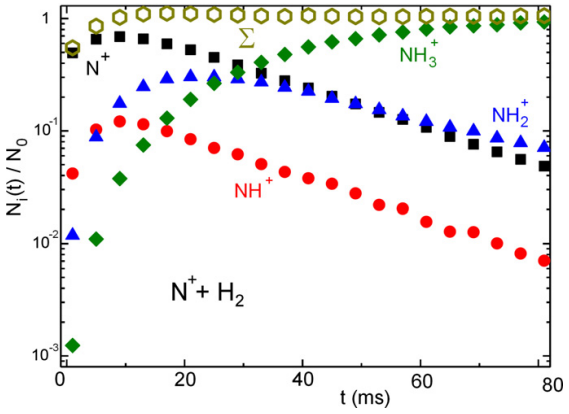

Figure 3. Sequential hydrogenation of trapped N^+ ions leading to NH_i^+ (i = 1–3) as a function of the storage time t. The measurements were performed at 52 K with helium buffer gas [He] = 5.2×10^{11} cm^{-3} and at a hydrogen number density of [n-H_2] = 1.6×10^{11} cm^{-3}. The sum of all ions (Σ) increases at the beginning (phase-space compression) and decays than very slowly. The 3.6% loss is most probably due to reactions with impurities. Evaluation of the decay of N^+ leads to a mean rate coefficient of 2.67×10^{10} cm^3 s^{-1}.

(A color version of this figure is available in the online journal.)

3. RESULTS AND FIRST EVALUATION

The upper part of Figure 4 shows a collection of rate coefficients, measured for the title reaction between 100 K and 10 K for different o-H_2 fractions f, ranging from 0.75 to 0.005. As explained in Section 2, most data have been taken during the cooling down phase of the cold head. In addition, some tests at selected temperatures have been made. Several sets of data, taken on different days, have confirmed the reproducibility.

One approach to evaluating such a manifold of experimental results is to use simple Arrhenius-type functions,

$$k = k_A \exp(-T_A/T), \quad (2)$$

where $T_A = E_A/k$ is the activation temperature, E_A is the activation energy, and k is the Boltzmann constant. In order to limit the number of free parameters, the restrictions imposed by the adiabatic model mentioned in Section 1 have been implemented. This means only the lowest three FS states can lead to products while the other six are so repulsive that there is no low-energy reaction path. In addition, it is postulated that the population of the FS states relaxes efficiently to the temperature of the trap. This assumption has also been made in the evaluation of all previous experimental data (Marquette et al. 1988; Gerlich 1993), although there has never been a direct proof. Under these boundary conditions, the measured rate coefficient k can be fitted using the ansatz

$$k = f(\xi_0 k_{1,0} + \xi_1 k_{1,1}) + (1 - f)(\xi_0 k_{0,0} + \xi_1 k_{0,1}). \quad (3)$$

In this equation, f is the selected ortho fraction, and the coefficients ξ_{ja} account for the thermal population of the two lowest FS states j_a. For the state specific rate coefficients, $k_{j,ja}(T)$ (with $j = 0$, 1 and $j_a = 0$ and 1), individual Arrhenius functions have been chosen. Contributions from $j = 2$ (3% in pure p-H_2 at 100 K) have been neglected. Inspection of the upper part of Figure 4 reveals that the lines follow the data points rather precisely, i.e., the restricted model fits all experimental data

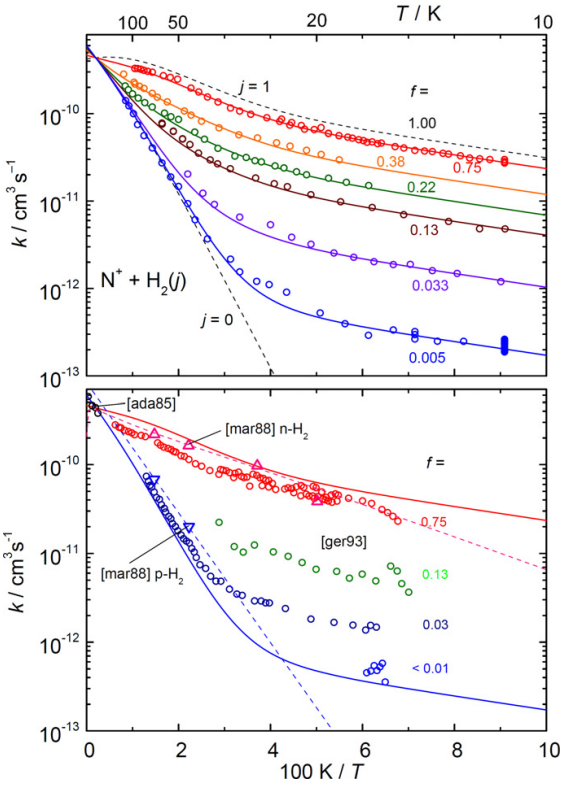

Figure 4. Arrhenius plot of experimental rate coefficients k for reaction (1), measured at different ortho-fractions f (upper panel). The data can be reproduced quite well with a thermally weighted superposition of state specific rate coefficients. The used function is given in Equation (3), the parameters in Table 1. The thin dashed lines are the analytical results for $f = 0$ (pure p-H_2) and $f = 1$ (pure o-H_2). In the lower panel, our data are compared to previous results. The triangles are CRESU results (Marquette et al. 1988), while the dots are ion trap results reported in (Gerlich 1993). The data at room temperature and above have been measured with an SIFDT instrument (Adams & Smith 1985). The dashed lines which go through the triangles indicate the functions used recently by Dislaire et al. (2012).

(A color version of this figure is available in the online journal.)

Table 1
State Specific Rate Coefficients for the Title Reaction, $k_{j,ja}$ (units 10^{-10} cm^3 s^{-1} and K), Derived from the $k(T)$

j, j_a	k_A	T_A
$k_{0,0}$	12	230
$k_{1,0}$	1.9	18
$k_{0,1}$	14	230
$k_{1,1}$	12	40

Notes. Results measured for various ortho fractions f (see Figures 4–6) and using Equation (2). $k_{0,2}$ and $k_{1,2}$ are set to zero (adiabatic approximation) and it is assumed that the ions are thermalized. For more information see the text.

quite well. The parameters obtained are presented in Table 1. More aspects of this analysis will be discussed below.

In the lower part of Figure 4, our data are compared to a variety of previously published measurements. For clarity and orientation, only our new analytical fits for $f = 0.75$ and 0.05 are included as solid lines. In addition, Table 2 presents numerical

A.1

Table 2
Previous Measured and Calculated Rate Coefficients for the Title Reaction (units 10^{-10} cm^3 s^{-1} and K)

k_A	T_A	n	Remarks	Reference
8.35	168.5	0	p-H_2	Marquette et al. (1988)
4.16	41.9	0	n-H_2	
15.3	177.5	0	p-H_2	Gerlich (1989)
4.06	42.5	0	n-H_2 (27–45 K)	
14.0	230	0	p-H_2	Gerlich (1993)
1.1	26	0	n-H_2 (10–40 K)	
4.2	44.5	−0.17	o-H_2	Dislaire et al. (2012)
9.0	220	0	p-H2	
1.5	180	−2.1	o-H2	This work
1.75	15	0		

Note. For comparison, the results from this work (last three lines) have also been parameterized using Equations (2) and (5).

values from other experiments and from a statistical theory. It can be seen that the previous ion trap results (Gerlich 1993) are slightly lower for n-H_2 ($f = 0.75$); however, they overlap within the combined uncertainties of absolute rate coefficients (typically 20%). The agreement of the steep decay of k between 100 K and 40 K for almost pure p-H_2, following the dotted line for $j = 0$ in the upper panel is gratifying. At temperatures below 25 K, the plots for the various mixtures run more or less parallel, indicating that k is mainly determined by the first half of Equation (3), i.e., the contributions from hydrogen in $j = 1$.

As explained in the context of Figure 2, the f values have been set absolutely by mixing n-H_2 and p-H_2. This method leads to very reliable values for $f > 0.2$. An analysis of possible errors indicates, that mixtures with less o-H_2 ($f < 0.2$) have an relative uncertainty of up to 10%. The ortho fractions given for "pure p-H_2" ($f < 0.01$) have been determined by fitting the experimental data using f as a free parameter. Note, however, that it is not yet clear whether the loss of N^+ in the low-temperature region is really just due to the reaction with the small o-H_2 admixtures or whether other processes, e.g., tunneling through a barrier, gas impurities such as HD or RF heating, are the reason for this.

In addition to the systematic variation of the temperature, the f dependence of the rate coefficients has also been recorded by increasing the ortho fraction in small steps from near zero to 0.75. The results, obtained at five different temperatures, are plotted in Figure 5. Comparison with the dashed lines reveals that all data follow a linear increase in good approximation. This is in accordance with Equation (3) predicting such an f dependence; however, it is only valid within the simple model used. Possible deviations could be expected due to more complex kinetics occurring in the trap, especially due to differences in FS relaxation for collisions of N^+ with $H_2(j = 0)$ or $H_2(j = 1)$. In this context, it is an interesting question whether the exothermic transfer of rotational energy into FS energy,

$$N^+\left(^3P_{ja}\right) + H_2(j = 1) \rightarrow N^+(^3P_{ja+1}) + H_2(j = 0), \quad (4)$$

can affect the FS population at very low temperatures. Most probably, this process is forbidden by nuclear spin restriction, i.e., the required ortho–para conversion is very unlikely.

4. DISCUSSIONS

As long as there are no directly measured state specific cross sections, assumptions have to be made about the role of the different energy forms in driving the reaction. In the evaluation above, the reactivity of ions in the highest excited FS state has been set to zero, based on the adiabatic model, leading to very good fits of the data. This agreement, however, cannot be taken as a proof of the validity of this model, since other analytical functions, also used in the analysis of chemical systems, are of fitting capable them.

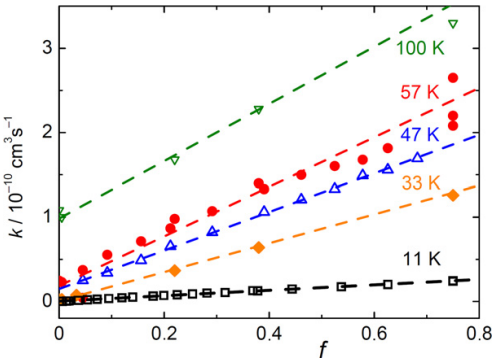

Figure 5. Rate coefficients for reaction (1) measured as a function of the ortho fraction for the indicated temperatures. As predicted from Equation (3) the data show a linear increase with increasing f. Nonetheless systematic deviations cannot be ruled out, especially at very low temperatures. It should be mentioned that the 11 K results extend over two orders of magnitude.

(A color version of this figure is available in the online journal.)

Deviations from the simple Arrhenius form (Equation (3)) are well known. They can be traced back to deviations of the threshold onset of an endothermic cross section from the functional form $\sim(E_t - E_o)^{1/2}/E_o$ (E_t is the translational energy; E_o is the threshold energy). In astrochemical data systems (see, for example, Equation (1) in Wakelam et al. 2012) it is common to account for this using a pre-exponential temperature-dependent factor with a free parameter n,

$$k = k_A(T/300\,\mathrm{K})^n \exp(-T_A/T). \quad (5)$$

This function, which is called the Arrhenius–Kooij formula, has been used recently by Dislaire et al. (2012) for reevaluating the $N^+ + H_2$ data of Marquette et al. (1988). Ignoring the role of FS energy, they obtained a new set of parameters for o-H_2 (see Table 2, Figures 4 and 6). For p-H_2 they used the unaltered results reported by Marquette et al. (1988).

In Figure 6, the results of two different fitting procedures can be compared with each other. In the upper part, the $f = 0.75$ results from Figure 4 are reproduced together with the fit based on Equation (3). The four thin lines show the individual contributions $k_{j,ja}$ weighted with the thermal population of the FS states (ξ_{ja}) and the ortho fraction f. Inspection of these contributions reveals that in this model the curvature of the measured data is mainly caused by the change of the thermal population of the FS states. Between 50 K and 100 K the state specific rate coefficient $k_{1,1}$, i.e., reaction of $N^+(^3P_1)$ with $H_2(j = 1)$, prevails while the contribution from FS ground-state ions dominates at low temperatures. It is obvious that the results obtained for $f = 0.75$ are not very sensitive to $k_{0,0}$ and $k_{0,1}$. For these state specific rate coefficients more information has been derived from measurements with p-H_2 as can be seen in Figure 4. In the lower panel, the three indicated functions (thin lines, based on Equations (2) and (5)) have been used. With the parameters given in the lower part of Table 2, very good agreement

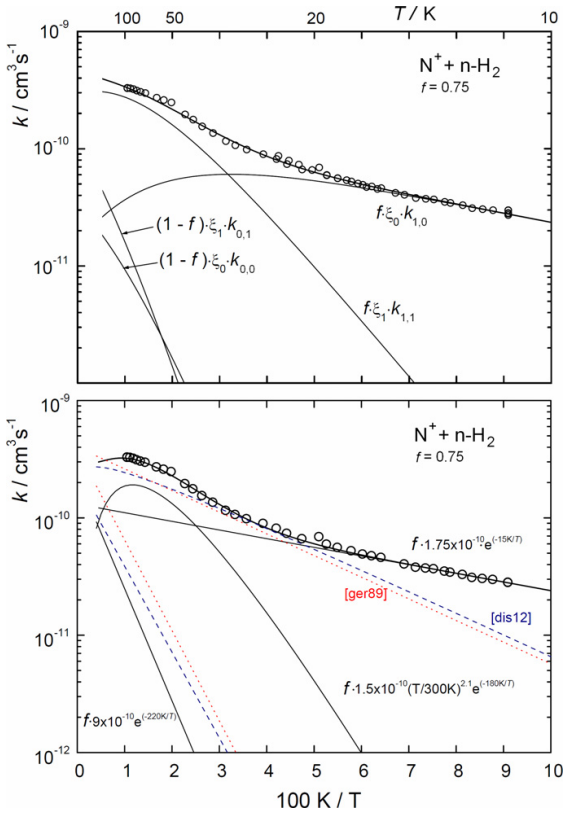

Figure 6. Two different fits of $k(T)$ measured with n-H_2. In the upper panel Equation (3) is used with the parameters given in Table 1. The four thin lines show the individual contributions $k_{j,ja}$, weighted with the thermal population of the FS states (ξ_{ja}) and the ortho fraction f. In the lower panel, the functions given in Equations (2) and (5) have been used directly. Three functions had to be used to get also a good fit. They are plotted as three thin lines together with the parameters used. In addition, this plot also shows the results from phase-space theory (short dashed line (Gerlich 1989) and the function used by Dislaire et al. (2012).

(A color version of this figure is available in the online journal.)

with the data points has also been reached. In this case, the curvature of the data is reproduced by the pre-exponential term. With the exception of the activation temperatures T_A, a scientific interpretation of these results is not obvious. Perhaps this can be taken as a hint that the $^3P_1$ state really plays a significant role at temperatures above 40 K.

The two examples shown in Figure 6 and discussed above illustrate that the analysis of the manifold of measured data is somehow arbitrary and that more experimental information is needed. Another problem, already mentioned in Section 1, is that our evaluation of the data is internally inconsistent since the $^3P_2$ state is excluded postulating adiabatic behavior on one side but it assumes efficient FS relaxation on the other side. In order to shed some more light on this conflict, additional experimental information is used, namely, the temporal changes of the ion composition in the trap as illustrated and discussed in Figure 3 and shown in Figure 7.

Since, due to the ionization process, the initially injected primary N^+ ions are in the $^3P_2$ state with a probability of 5/9 (3/9 in $^3P_1$, 1/9 in $^3P_0$) thermalization of the trapped ion ensemble and hydrogen abstraction reactions occur in

Table 3
Experimental Parameters Used in the Measurements Shown in Figure 7

	a	*b*	*c*	*d*
T (K)	110	98	11	11
[H_2] (cm^{-3})	1.8E12	2.6E11	2.0E12	2.8E13
f	0.75	0.0055	0.75	0.0093
[He] (cm^{-3})	2.4E12	2.3E12	1.2E12	2.4E12
$\langle k \rangle$	3.20E−10	1.00E−10	2.20E−11	2.20E−13

competition with each other. In order to model the kinetics, one needs the relevant rate coefficients. A first attempt, based on state specific reaction rate coefficients calculated with phase-space theory (Gerlich 1989) and assuming relaxation rate coefficients $kr_{ja\to ja-1} = 10^{-n}$ cm^3 s^{-1} with $n = 11$, 10, and also 9, was reported in Tosi et al. (1994). While all measured decay curves were mono-exponential (after thermalizing the kinetic energy; see also Figure 4 of Gerlich 1993) the simulation always predicted an initial fast decay of primary ions followed by a slower one (see Figure 4 of Tosi et al. 1994). This curved behavior is obviously due to the high reactivity of the excited N^+ ions as predicted by the phase-space theory. In Tosi et al. (1994), a trivial solution has been proposed: fine structure energy is just not available, i.e., all ions react with the same rate coefficient. Looking at the potential energy surface and Figure 1, there is no obvious reason for such an extreme behavior.

For testing various assumptions, additional measurements have been performed under different experimental conditions. The number density of H_2 has been varied over more than two orders of magnitude. In addition, He buffer gas has been added with a number density of some 10^{12} cm^{-3} so far without any significant changes. A selection of new results is plotted in Figure 7. The upper part shows the decay of the relative number of N^+ ions at about 100 K, the lower part of figure shows decay at 11 K. In the measurements on the left, n-H_2 was been used; on the right p-H_2 was used. All relevant experimental parameters are collected in Table 3. As can be seen from the thin lines, all four data sets can be fitted almost perfectly with a simple exponential decay function,

$$N_{N^+}(t) = N_0\, e^{-t/\tau}. \quad (6)$$

From the measured decay times τ and the hydrogen number densities [H_2], mean rate coefficients have been calculated

$$\langle k \rangle = (\tau\, [H_2])^{-1}. \quad (7)$$

The resulting parameters $\langle k \rangle$, which are an average over the time dependent FS population, are included in Table 3. In order to understand these observations in more detail, several additional facts need to be mentioned. (1) The decay rate of all N^+ ions is at all times the same. The slight deviations during the thermalization of the translational energy after ion injection can be ignored at the timescales used in Figure 7. (2) The monotonous decay can be followed until storage times where only 10^{-4} of the injected ions are left over. (3) Simulations with rate coefficients from phase-space theory always lead to a faster decay at the beginning (concave curvature). (4) Setting the rate coefficient for the $^3P_2$ state to zero (strict adiabatic model) but allowing for relaxation always leads to a convex curvature.

Guided by these facts we have developed a kinetic model that includes reaction of all three states of N^+ and also FS-changing

A.1

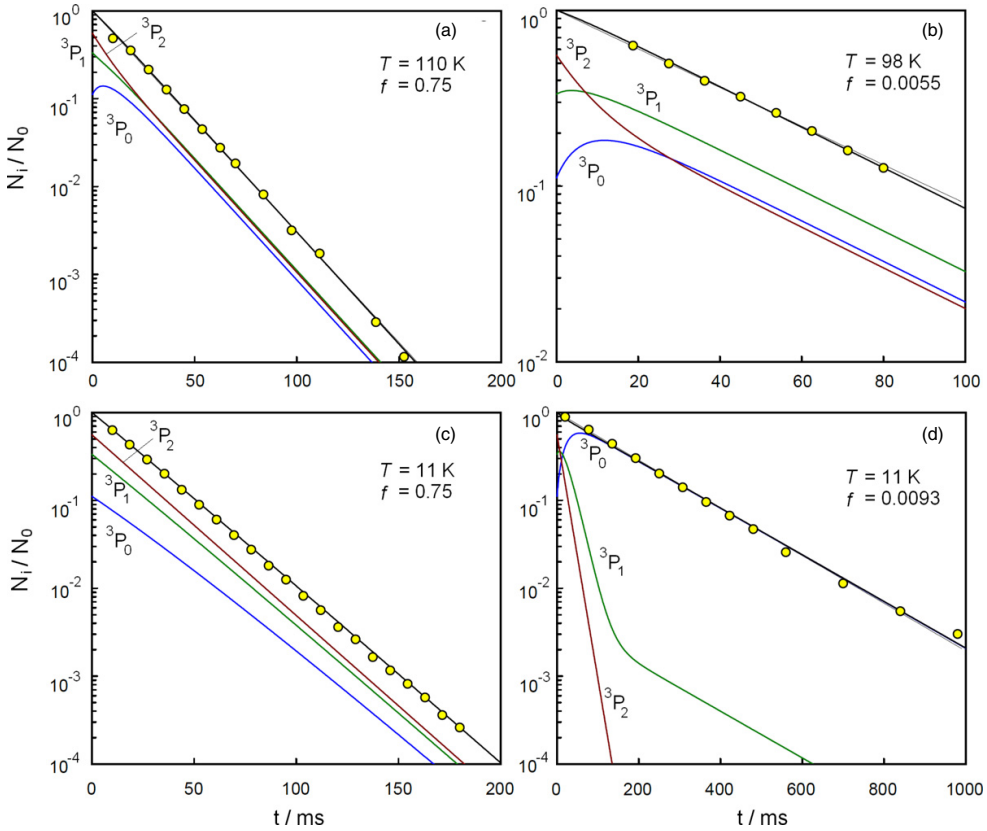

Figure 7. Decay of N^+ ions measured at the indicated temperatures and for n-H_2 (left, $f = 0.75$) and for p-H_2 with minor o-H_2 impurities (right, $f < 0.01$). Note the different scales. All relevant experimental parameters are collected in Table 3. The experimental data (circles) can be fitted well with a first-order exponential decay resulting in the mean rate coefficients $\langle k \rangle$ (also given in Table 3). In reality, the kinetics are more complicated due to the competition of FS-changing collisions and reactions with H_2. The three thin lines, marked with $^3P_{ja}$ ($j_a = 0, 1, 2$) show a special solution of the changes of the relative number of N^+ ions in specific FS states. In all cases, the high-temperature ratio 5:3:1 has been assumed for the initial population. The state specific rate coefficients for reaction and relaxation are given in Tables 1 and 4. Note that this result is not unique.

(A color version of this figure is available in the online journal.)

A.1

collisions. In order to restrict the number of free parameters of the simulation, we started with the state specific rate coefficients derived form our experiment, i.e., with the values given in Table 1. Then the rate coefficients $k_{0,2}$ and $k_{1,2}$, which have been set to zero in the adiabatic model, have been increased slowly. Motivated by the interaction shown schematically in Figure 1 only FS transitions from 2 to 1 and 1 to 0 have been accounted for with the relaxation rate coefficients $kr_{2\to1}$ and $kr_{1\to0}$. The reverse rate coefficients, $kr_{1\to2}$ and $kr_{0\to1}$, have been included in the calculation, making use of micro-reversibility. Direct transitions between 2 and 0 are assumed to be inefficient.

It has been rather easy to find parameters describing each individual data set. It also became evident that there are many specific solutions although there is a strong correlation between the competing processes imposed by the mono-exponential decay of the experimental data. The relaxation and reaction rate coefficients strongly depend on each other. To our surprise we finally found a very simple solution, taking the four unchanged rate coefficients given in Table 1 and also using simple Arrhenius-type rate coefficients for the highest FS state and for relaxation.

The resulting parameters fitting all our data sets are given in Table 4. The solutions for the temporal changes of the number of N^+ ions in specific $^3P_{ja}$ states and their sum are plotted in Figure 7. In all cases, the sum (solid line) follows nicely the mono-exponential decay of the measured data. A detailed inspection of (a) and (b) reveals that FS thermalization is achieved only after 30 ms since the relaxation rate coefficient is rather slow (4×10^{-11} cm^3 s^{-1}). In order to get the mono-exponential decay during this time the concave function describing the decay of ions in the $^3P_2$ state is compensated by the two convex functions. At 11 K relaxation is even slower

Table 4
State Specific Rate Coefficients for Reaction, $k_{j,ja}$, and Relaxation, $kr_{ja\to ja'}$, Derived from the Fits Shown in Figure 7 (units 10^{-10} cm^3 s^{-1} and K)

	k_A	T_A
$k_{0,2}$	0.51	53.4
$k_{1,2}$	1.44	18.4
$kr_{2\to1}$ $kr_{1\to0}$	0.58	37.0

Note. Rate coefficients needed in addition to those in Table 1 for fitting the exponential decay shown in Figures 7(a)–(d).

(2×10^{-12} cm^3 s^{-1}) and with n-H_2 (panel (c)) reaction is faster than relaxation. In order to get the mono-exponential time dependence, the three rate coefficients are similar. Impressive is the result (d), where the N^+ can only react with the traces of H_2 ($j = 1$). Since in this case the H_2 number density is more than 10 times higher than in (c), thermalization of the FS population is achieved in 200 ms. For further conclusions, more measurements and a detailed mathematical analysis of the coupled differential equations are needed.

In summary, the results of our model allow several conclusions. (1) FS-changing collisions are rather slow, especially at low temperatures indicating nearly adiabatic behavior. (2) In contradiction to the strict adiabatic model, the highest FS state contributes to the formation of NH^+ products, but much slower than predicted from statistical calculations. (3) Our experimental observations are qualitatively in accordance with the nonadiabatic couplings indicated in the oversimplified Figure 1. For a more quantitative understanding, one needs a detailed adiabatic or nonadiabatic formulation of the multi-surface problem. The first approach may be similar to the N^+–He system (Soldan & Hutson 2002); however, in addition to the spin–orbit coupling, one must include the correct long-range attraction (charge-induced dipole and charge–quadrupole) and the couplings induced by the anisotropy, and one has to account for the effects caused by the rotation of H_2. At very low energies hyperfine-interaction may also finally play a role. All this leads to a complex switch yard of crossings and needs help from theory to be sorted out!

5. CONCLUSIONS AND OUTLOOK

Based on an extensive set of new experimental rate coefficients $k(T; f)$ as well as on a careful analysis of the decay curves of trapped N^+ ions, for the first time state specific rate coefficients for the interaction of $N^+(^3P_{ja})$ with $H_2(j)$ have been extracted. There are still uncertainties concerning the role of the FS energy. Nonetheless it is rather clear that excitation of N^+ to the $^3P_2$ state reduces its reactivity, but not completely to zero as predicted from strict adiabatic assumptions (Wilhelmsson & Nyman 1992; Russell & Manolopoulos 1999).

As long as astrochemical models ignore the FS states of the N^+ ions, it is recommended that the rate coefficients for $j = 0$ and 1, presented in the lower part of Figure 6 and in Table 2, be used. However, it must be noted that the two N^+ lines ($^3P_2 \rightarrow {}^3P_1$) at 121.9 μm and ($^3P_1 \rightarrow {}^3P_0$) at 205.2 μm play an important role in certain astrophysical environments, e.g., in photo-dissociation regions, where matter is heated via penetrating far-ultraviolet photons and cooled via forbidden atomic fine-structure transitions. A detailed discussion of such cooling lines observed in the Orion Bar can be found in a recent publication by Bernard-Salas et al. (2012). It is obvious that one needs detailed rate coefficients for inelastic and reactive collisions with electrons, atoms, and molecules in order to model such observations.

The presented experimental results give some first information on the state specific rate coefficients $k_{j,ja}(T)$ for all combinations of $j_a = 0$–2 and $j = 0$–1. In order to check the results presented additional experiments must be performed. For example, using He number densities of several 10^{15} cm^{-3} and relaxation times of seconds or longer before hydrogen is leaked into the trap may finally lead to relaxation of the FS population prior to the reaction. An ultimate experiment would be the in situ state selected ionization of N-atoms via autoionizing resonances. Another striking idea is to maintain a stationary FS population of the trapped N^+ ions using an intense microwave wave field at the wavelengths mentioned above.

As established in Gerlich et al. (2011) the apparatus used in this work can also be operated with a neutral target beam. To fully understand the NH_2^+ collision system we plan to study the reverse reaction

$$NH^+ + H \rightarrow N^+ + H_2 \quad (8)$$

as a function of the temperature of the ion and the atomic beam source, similar to CH^+ + H (Plasil et al. 2011). This beam-trap arrangement can also be used with a high-temperature accommodator for producing rotationally and vibrationally excited H_2. Finally, it must be mentioned that the various deuterated variants of reactions (1) and (8) including the endothermic D–H exchange in ND^+ + H will provide deep insight into the role of zeropoint energies, barriers, and tunneling at low energies.

Since 2010, the AB 22PT instrument has been operated at the Faculty of Mathematics and Physics of Charles University in Prague. We thank the Technical University of Chemnitz and the DFG for lending us this instrument. This work is a part of research grant OC10046 financed by the Ministry of Education of the Czech Republic and was partly supported by GACR (P209/12/0233, 205/09/1183), by GAUK 388811, GAUK 406011, and by COST Action CM0805 (The Chemical Cosmos).

REFERENCES

Adams, N. G., & Smith, D. 1985, CPL, 117, 67
Amero, J. M., & Vazquez, G. J. 2005, IJQC, 101, 396
Barlow, S. E., Luine, J. A., & Dunn, G. H. 1986, IJMSI, 74, 97
Bernard-Salas, J., Habart, E., Arab, H., et al. 2012, A&A, 538, A37
Dislaire, V., Hily-Blant, P., Faure, A., et al. 2012, A&A, 537, A20
Gerlich, D. 1989, JChPh, 90, 3574
Gerlich, D. 1992, AdChP, 82, 1
Gerlich, D. 1993, J. Chem. Soc. Faraday Trans., 89, 2199
Gerlich, D. 1995, PhyS, T59, 256
Gerlich, D. 2008a, in Low Temperatures and Cold Molecules, ed. I. W. M. Smith (Singapore: Imperial College Press), 121
Gerlich, D. 2008b, in Low Temperatures and Cold Molecules, ed. I. W. M. Smith (Singapore: Imperial College Press), 295
Gerlich, D., Borodi, G., Luca, A., Mogo, C., & Smith, M. 2011, ZPC, 252, 475
Gerlich, D., Jusko, P., Roučka, Š., et al. 2012, ApJ, 749, 22
González, M., Aguilar, A., & Fernández, Y. 1986, CP, 104, 57
Jursic, B.S. 1998, AcTC, 99, 171
Le Bourlot, J. 1991, A&A, 242, 235
Mahan, B. H., & Ruska, W. E. W. 1976, JChPh, 65, 5044
Marquette, J. B., Rebrion, C., & Rowe, B. R. 1988, JChPh, 89, 2041
Nyman, G., & Wilhelmsson, U. 1992, JChPh, 96, 5198
Plasil, R., Mehner, T., Dohnal, P., et al. 2011, ApJ, 737, 60
Russell, C. L., & Manolopoulos, D. E. 1999, JChPh, 110, 177
Soldan, P., & Hutson, J. M. 2002, JChPh, 117, 3109
Sunderlin, L. S., & Armentrout, P. B. 1994, JChPh, 100, 5639
Tarroni, R., Palmieri, P., Mitrushenkov, A., Tosi, P., & Bassi, D. 1997, JChPh, 106, 10265
Tosi, P., Dmitriev, O., Bassi, D., Wick, O., & Gerlich, D. 1994, JChPh, 100, 4300
Wakelam, V., Herbst, E., Loison, J.-C., et al. 2012, ApJS, 199, 21
Wilhelmsson, U., & Nyman, G. 1992, JChPh, 96, 1886
Wilhelmsson, U., Siegbahn, P. E. M., & Schinke, R. 1992, JChPh, 96, 8202
Willitsch, S., Merkt, F., Kállay, M., & Gauss, J. 2006, MolPh, 104, 1457

A.1

A.2 State Specific Stabilization of $H^+ + H_2(j)$ Collision Complexes

D. Gerlich, R. Plašil, I. Zymak, M. Hejduk, P. Jusko, D. Mulin and J. Glosík,
The Journal of Physical Chemistry A, 0(0):null, 0, 2013. doi:10.1021/jp400917v.

THE JOURNAL OF PHYSICAL CHEMISTRY A

Article

pubs.acs.org/JPCA

State Specific Stabilization of $H^+ + H_2(j)$ Collision Complexes

D. Gerlich,*[,†,‡] R. Plašil,[†] I. Zymak,[†] M. Hejduk,[†] P. Jusko,[†] D. Mulin,[†] and J. Glosík[†]

[†]Faculty of Mathematics and Physics, Charles University, 121 16 Prague, Czech Republic

[‡]Department of Physics, University of Technology, 09107 Chemnitz, Germany

ABSTRACT: Stabilization of H_3^+ collision complexes has been studied at nominal temperatures between 11 and 33 K using a 22-pole radio frequency (rf) ion trap. Apparent binary rate coefficients, $k^* = k_r + k_3[H_2]$, have been measured for para- and normal-hydrogen at number densities between some 10^{11} and 10^{14} cm^{-3}. The state specific rate coefficients extracted for radiative stabilization, $k_r(T;j)$, are all below 2×10^{-16} cm^3 s^{-1}. There is a slight tendency to decrease with increasing temperature. In contrast to simple expectations, $k_r(11\ K;j)$ is for $j = 0$ a factor of 2 smaller than for $j = 1$. The ternary rate coefficients for p-H_2 show a rather steep T-dependence; however, they are increasing with temperature. The state specific ternary rate coefficients, $k_3(T;j)$, measured for $j = 0$ and derived for $j = 1$ from measurements with n-H_2, differ by an order of magnitude. Most of these surprising observations are in disagreement with predictions from standard association models, which are based on statistical assumptions and the separation of complex formation and competition between stabilization and decay. Most probably, the unexpected collision dynamics are due to the fact that, at the low translational energies of the present experiment, only a small number of partial waves participate. This should make exact quantum mechanical calculations of k_r feasible. More complex is three-body stabilization, because it occurs on the H_5^+ potential energy surface.

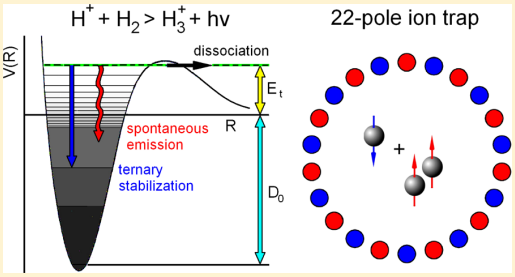

INTRODUCTION

In understanding the electronic structure of atoms and the formation of molecules, the hydrogen atom, the diatomic molecules H_2^+ and H_2, as well as the simplest polyatomic molecule H_3^+ play a fundamental role. Like H_2, the triatomic ion has only two electrons. But instead of one internuclear coordinate, already three are needed to describe the location or the motion of the three protons. Due to the importance of this special ion in fundamental science and in all kinds of hydrogen plasmas, including astrophysics, the last decades have seen many experimental and theoretical activities dealing with both bound and scattering states. In other word, H_3^+ is a benchmark system not only for understanding molecular structure but also for scattering dynamics.

Recently, Oka[1] has passed in review his personal engagement and involvement in searching for the IR spectrum of H_3^+ in the laboratory and in detecting this ion in space, finally in more and more astrophysical objects. It is a successful story, emphasizing the close interrelation between spectroscopy and astronomy. For identifying a molecule in space one must know its rotational−vibrational levels and the frequencies of photons that can be emitted or absorbed. Meanwhile, after more than 30 years, many transitions of H_3^+ and deuterated analogues have been measured and there is still space for filling more tables.[2,3] Present activities investigate the energy range where the three protons can leave their triangular structure and start to explore the configuration space toward linearity.[4] All these precisely measured lines are a challenge for rigorously testing ab initio theories. To determine the eigenstates and to predict transitions with spectroscopic accuracy, the quality of the ground state potential energy surface has been improved in many iterations. The most recent reports and references to previous publications can be found in refs 5 and 6. Despite all this, H_3^+ is far from being fully accessed experimentally or rigorously described by theory, especially if the total energy reaches the vicinity of the $H^+ + H_2$ continuum.

In the above-mentioned retrospective, Oka[1] also stated that the chemistry of H_3^+ is "extremely simple and allows one to interpret the observed abundances". Unfortunately, this is not true if one looks into the details of hydrogen chemistry leading to the formation or destruction of this central ion. Also inelastic collisions, just changing the vibrational−rotational state or inducing an ortho−para transition, are an unsolved experimental challenge, especially at low temperatures. Because H_3^+ is the most abundant polyatomic ion in the universe, it must be involved in many reactions with other atoms, molecules, anions, or electrons. Therefore, it certainly is a powerful sensor for probing specific astrophysical environments; however, more details on its role in chemistry are needed. One example is the still ongoing discussion on its recombination with electrons. The status of the $H_3^+ + e^-$ research was recently summarized

A.2

Special Issue: Oka Festschrift: Celebrating 45 Years of Astrochemistry

Received: January 27, 2013
Revised: March 14, 2013

   dx.doi.org/10.1021/jp400917v | J. Phys. Chem. A XXXX, XXX, XXX−XXX

with the statement "But this was not the end of the story, not even the beginning of the end; it marked only the end of the beginning."[7] Another basic but not yet solved question is the ortho–para conversion of H_3^+ in low temperature collisions with H_2.[8]

In this contribution, we concentrate on the $H^+ + H_2$ collision system, i.e., at H_3^+ ions having a total energy above the dissociation limit. To be of importance for dense interstellar clouds, the energy is restricted to a few millielectronvolts, relative to the asymptote. At higher collision energies, proton scrambling plays an important role in converting translational energy into internal excitation of the molecule followed by conversion into radiation. Most probably this energy transfer is more efficient in cooling primordial gas than the H_3^+ molecule with its infrared active modes.[9] Another important aspect of this rather simple collision system is the conversion of ortho-H_2 into para-H_2 or vice versa, catalyzed by the proton. Only recently has this process, which has been described in detail with statistical theories,[10,11] been treated with an exact quantum mechanical method.[12,13] The obtained thermal state-to-state rate coefficients (see erratum[14]) are smaller than the statistical predictions and, surprisingly, they fall with falling temperature. Is this an indication that statistical models are not any more applicable in the 10 K range? Also, other recent theoretical studies (see ref 15 and references therein) provide evidence that theoreticians are close to describing, with exact quantum mechanical methods, the interaction of a proton or deuteron with H_2 and D_2 at translational energies of a few millielectronvolts. It is obvious that, in this energy range, a very good potential energy surface with the correct long-range behavior is required. For this purpose, it seems to be still the best to include analytical approximations of the long-range electrostatic interaction into the ab initio potential.[16] It is an open question whether the improved potentials[5,6] and the methods to describe the vibrational–rotational motion of H_3^+ with spectroscopic accuracy are finally also suited to find the resonances determining the cross section for converting hydrogen in $j = 1$ into $j = 0$ in a low energy collision with protons, or to predict the probability to stabilize such a collision complex via emission of a photon.

A.2

Radiative stabilization of collision complexes is an important process in the growth of molecules in low-density interstellar clouds. From a fundamental point of view, formation of H_3^+ via radiative association,

$$H^+ + H_2 \xrightarrow{k_r} H_3^+ + h\nu \quad (1)$$

is a so-called "half-collision", an important subfield of collision dynamics. Most related experiments start with a stable molecule (e.g., photoinduced dissociation or detachment of an electron); here a molecule in a more or less long-lived scattering state is stabilized by losing the energy $h\nu$. Because these states are embedded in the energy continuum, one needs a barrier (for example caused by a rotational angular momentum, Feshbach-type resonances) to keep them bound for some time or other dynamical restrictions. It also should be mentioned that the total number of states in the energy interval of interest is an important criterion.

For long time, information on association of reactants has been extracted from experiments operating at rather high pressures. Under such conditions, H_3^+ is formed with the help of a third body, i.e., via

$$H^+ + 2H_2 \xrightarrow{k_3} H_3^+ + H_2 \quad (2)$$

Using a drift-tube mass spectrometer apparatus and operating at number densities close to 10^{16} cm^{-3}, Graham et al.[17] determined a ternary rate coefficient k_3 of 3×10^{-29} cm^6 s^{-1} at 300 K. Johnson et al.[18] extended the temperatures range from room temperature down to 135 K and observed a slight increase of k_3. The mentioned results are included in Table 1.

Table 1. Rate Coefficients for Radiative and Ternary Association of Protons with Hydrogen Molecules[a]

T	k_r	Δk_r	k_3	Δk_3	remarks	ref
300			0.30	0.15	drift tube	17
300			0.30	0.03	drift tube	18
135			0.43	0.04		
230	1.0	0.2	0.74	0.2	first TV rf trap	21
80	1.3	0.2	0.54	0.2	80 K RET	22
11	1.6	0.3	0.27	0.08	n-H_2 (Figure 5)	24
22	0.5	0.2	0.25	0.08		
11	0.9	0.2	0.88	0.04	p-H_2/$j = 0$ (Figure 2)	this work
22	0.4	0.2	1.31	0.01		
33	0.4	0.7	1.75	0.04		
11	1.8	0.4	0.06	0.09	$j = 1$	

[a]Units: T in K, k_r in 10^{-16} cm^3 s^{-1}, and k_3 in 10^{-28} cm^6 s^{-1}. In the upper part, values from the literature are collected, all measured with n-H_2. The lower part presents state specific results from this work. The errors Δk_r and Δk_3 include only the statistical uncertainties.

In such studies the ternary association rate coefficient is derived from the measured apparent binary rate coefficient, k^*, by dividing it through the number density $[H_2]$, $k_3 = k^*/[H_2]$. This is suitable for high pressure environments, in fact, k^* has two contributions,

$$k^* = k_r + k_3[H_2] \quad (3)$$

Inspection of this equation reveals that, to get a similar number of products from the first and second term, one has to operate at number densities in the range of $[H_2] = k_r/k_3$. In the present case it means below 10^{13} cm^{-3}. It also must be noted that at the densities in the range of 10^{16} cm^{-3}, higher order collisions and saturation effects may play a role.[19]

The eighties have seen the development of innovative trapping techniques extending gas phase chemistry toward both lower densities and temperatures. First results for radiative association, measured in a liquid helium cooled Penning ion trap, were published by the group of Dunn.[20] First results for reactions 1 and 2, determined with an early version of an rf ring electrode trap operating between 300 and 230 K, have been reported in a conference contribution.[21] A similar trap, directly cooled with liquid nitrogen, provided results at 80 K.[22] All mentioned ternary and radiative rate coefficients are collected in Table 1 and discussed in more detail in an early review on radiative association.[19]

Although rf ion traps have been further improved,[23] they never have been used to extend the mentioned early experiments toward lower temperatures. However, due to continuous improvements of computers and methods, the $H^+ + H_2$ collision system is now within the reach of exact quantum mechanical calculations (see refs 13 and 15 and references therein). Therefore, it is timely to get more experimental information, especially state specific rate coefficients at very low temperatures.

dx.doi.org/10.1021/jp400917v | J. Phys. Chem. A XXXX, XXX, XXX–XXX

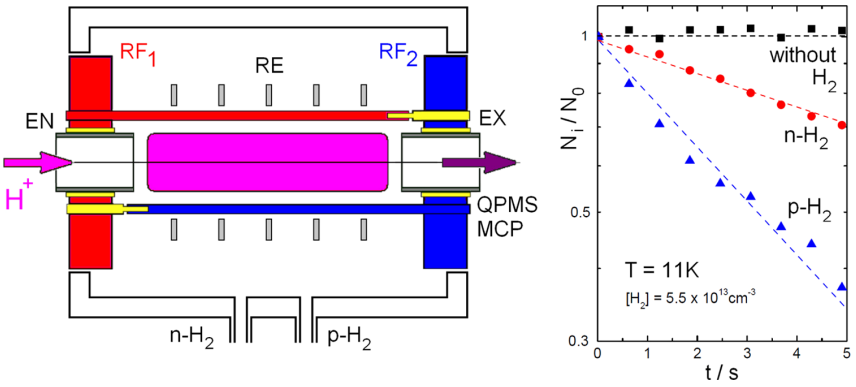

Figure 1. Left: 22-pole ion trap, the central part of the AB-22PT instrument.[36] Utilizing a cold head, wall temperatures down to T_{22PT} = 11 K can be reached. Mass selected H^+ ions are injected via the electrostatic entrance electrode (EN). For analyzing the ion cloud after various storage times t, the exit (EX) is opened using a suitable voltage. The ions pass a quadrupole mass spectrometer and are detected with a microchannel plate. The axial trapping potential, created by the rf field, can be corrected locally using five ring electrodes (RE). Right: normalized number of protons as a function of storage time. Without target gas, there is no change. Adding hydrogen (number density is in both cases 5.5×10^{13} cm^{-3}) leads to a decay of the number of protons due to formation of H_3^+. It is obvious that p-H_2 is more reactive than n-H_2.

In the following we give a short description of the instrument. New results for p-H_2 are presented and compared to results recently published for n-H_2.[24] Using well-prepared ortho−para mixtures allows us to extract state specific rate coefficients for radiative and ternary stabilization of $H^+ + H_2(j)$ collision complexes, $k_r(T;j)$ and $k_3(T;j)$. The discussion section emphasizes that the established models for explaining association processes are not able to provide sufficient explanations for the surprising result that k_r and k_3 show different temperature dependencies and that radiative association of protons with rotating H_2 is significantly faster than with ground state hydrogen.

EXPERIMENTAL SECTION

The measurements have been performed in the AB-22PT instrument the central part of which is the 22-pole rf ion trap, shown in Figure 1 on the left. It is surrounded by a copper box that is connected to the cold head of a closed-cycle helium refrigerator (Leybold RGD 210, lowest temperature 11 K). Because the principle of ion trapping[25] and the details of the 22-pole trap (first mentioned in ref 19) have been described often, only a few special hints are given below. Selected aspects of low temperature trapping have been discussed recently.[26,27]

Using magnetically suspended turbomolecular pumps, the vacuum chamber surrounding the trap is evacuated to a pressure below 10^{-7} Pa. Ultrahigh purity hydrogen gas has been used. In addition, traces of impurities are frozen out at low temperatures, with the exception of HD and D_2. As indicated in Figure 1, two separate gas inlets were installed, one for normal hydrogen (25% p-H_2, i.e., j = even and 75% o-H_2, i.e., j = odd) and one for para hydrogen. The purity of para hydrogen has been determined in situ using the reaction of N^+ with H_2.[28] Mixtures with a specific fraction of o-H_2, f, are set by adjusting the two separate leak valves. The gas density inside the trap is determined using an ionization gauge on the main chamber. This gauge is calibrated on a regular basis using a spinning rotor gauge that is connected to the interior of the 22-pole box.

For determining rate coefficients, the ion trap is periodically filled via the entrance electrode with a certain number of mass selected primary ions, in the present study typically a few hundred. The repetition period has been set to 10 s. Protons are created in a storage ion source via electron bombardment of hydrogen. After various storage times, t, the exit electrode is opened and the ions pass a quadrupole mass spectrometer and are detected with a microchannel plate. A typical set of raw data is shown in the right part of Figure 1. Without reactant gas, the number of stored ions (here normalized) is independent of the storage time. Adding n-H_2 through the left gas inlet or p-H_2 through the right one leads to a decrease of the number of protons. Because in both cases the same number density has been used (5.5×10^{13} cm^{-3}), it is immediately obvious that p-H_2 is more reactive than n-H_2.

A special difficulty in the present experiment is caused by the fact that the mass of the ion is only 1 u and, in addition, lower than the mass of the target gas, 2 u. Therefore, some remarks concerning the energy distributions of ions in rf traps must be made. In those applications where heavy ions are stored in H_2 or He, the influence of the rf field is very weak and can be neglected in most situations. One reason is that only small portions of energy are exchanged if the heavy ion hits the light buffer gas but cooling is finally very efficient. A second reason is that the translational temperature (i.e., the center of mass temperature) is determined by the mass weighted ratio of the cold gas temperature and the ion temperature (see eq 113 in ref 25). A simulation of the motion of protons stored in a ring electrode trap filled with H_2 indicate that, under similar conditions like here, 75% of the ions can be described with the nominal temperature, whereas 25% of them are at a 2.5 times higher temperature (see upper panel Figure 23 in ref 25). Unfortunately, real energy distributions of stored ions are usually less favorable due to potential distortions or parasitic time dependent fields which cause additional heating.

In the present experiment, the actual trapping conditions have been tested in situ via formation of He_2^+ dimers in $He^+ + 2$ He collisions, as discussed in detail by Plasil et al.[24] The results indicate *low* temperatures; however, deviations on the order of up to 10 K cannot be excluded. In addition, the ion to neutral mass ratio is 4:4 in this case and the trapping conditions have been superior because the test with He^+ has been performed with the same rf frequency (f = 19 MHz) used in the present work. Although the trap is still running in the safe operating mode (V_0 = 19 V, V^* = 34 meV, η = 0.15 at r_m/r_0 =

A.2

dx.doi.org/10.1021/jp400917v | J. Phys. Chem. A XXXX, XXX, XXX−XXX

0.80 for m = 1 u, for details see ref 25), further experiments will be performed with higher frequencies. Moreover, additional work is going on for determining the actual velocity distribution of protons trapped in a 22PT with H_2 and D_2 gas. Due to all uncertainties that may add up to an estimated temperature increase of 30 K, the present results are just reported as a function of the nominal temperature.

RESULTS

From the decay rates of primary ions at various hydrogen number densities (right part of Figure 1), apparent second-order rate coefficients for the formation of H_3^+ from H^+ have been determined, predominantly for p-H_2 in the present work. Figure 2 shows a collection of such results as a function of the number density of p-H_2, determined at nominal temperatures of 11, 22, and 33 K. The data points are averages over several iterations of filling the trap and analyzing the content after different storage times. The measured rate coefficients, k^*, have been fitted using the density dependence predicted by eq 3. The fits are plotted as solid lines, the obtained fit parameters, k_3 and k_r, are included in Table 1. To emphasize the temperature dependent differences in ternary association, the data are plotted here in a lin−lin scale, certainly at the disadvantage of radiative association which is discussed below. Against standard expectations, which are based on an increase of the lifetime of the collision complex with decreasing temperature, the data show clearly that ternary association becomes less efficient at lower temperatures.

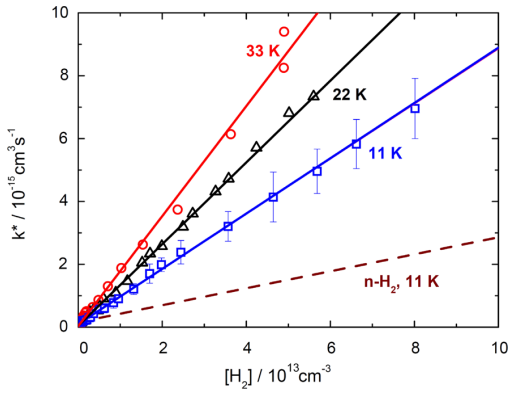

Figure 2. Apparent binary association rate coefficient k^* for T_{22PT} = 11, 22, and 33 K as a function of the p-H_2 number density. The data have been averaged over many iterations. For emphasizing the ternary rate coefficients, the results are plotted on a linear scale. The data are fitted with $k^* = k_r + k_3[H_2]$. The resulting parameters are in Table 1. The surprising result is that ternary association gets faster with increasing temperature. Concerning $k_r(T)$, see the text and Figure 3.

The obtained ternary and radiative rate coefficients are shown as a function of the nominal temperature in Figure 3 (rhomboids with crosses). To perform additional and faster measurements of the temperature dependence of k_r and k_3, it would be necessary to record H_3^+ formation at very low and very high number densities, respectively. In the present work, the apparent second-order rate coefficients k^* have been measured as a function of T_{22PT} between 11 and 45 K at the three different densities, given in Figure 3. The values for k_3 have been determined at 2.8 × 10^{13} cm^{-3} (squares, upper panel), by correcting k^* for the small contributions from

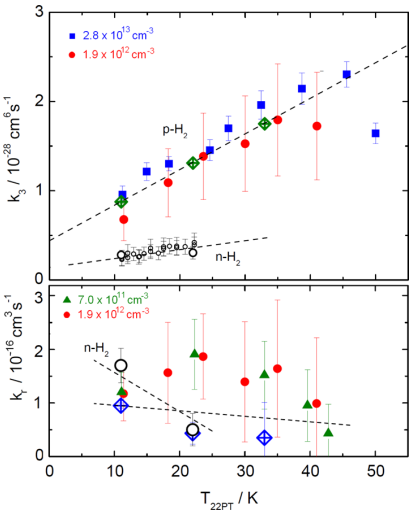

Figure 3. Temperature dependence of k_3 (upper panel) and k_r (lower panel). The large symbols (rhomboids with crosses inside) are results from fits to the density dependence of k^*. In addition, $k_3(T)$ has been determined at fixed p-H_2 densities (filled squares, 2.8 × 10^{13} cm^{-3}; filled circles, 1.9 × 10^{12} cm^{-3}) by correcting the measured k^* values individually for the small contribution from k_r. In analogy, $k_r(T)$ has been extracted from k^* measures at low densities (filled triangles, 7.0 × 10^{11} cm^{-3}; filled circles, 1.9 × 10^{12} cm^{-3}) and subtracting the contribution from ternary processes. For comparison, the previously published results[24] from experiments with n-H_2 are plotted as open circles. The trends (dashed lines) are discussed in the text.

radiative association. Correspondingly, the values for k_r have been obtained from k^* at 7.0 × 10^{11} cm^{-3} by subtracting the mean value of $k_3[H_2]$ (triangles, lower panel). The filled circles indicate that correction of k^* with nominal values of k_3 and k_r also works reasonably well at a density (1.9 × 10^{12} cm^{-3}) where the two contributions $k_3[H_2]$ and k_r are nearly equal. Also included in Figure 3 are dashed lines that indicate the temperature trend. The increase of k_3 for p-H_2, which follows the linear function

$$k_3(T;j{=}0) = (4.4 + 0.4 \times T/\mathrm{K}) \times 10^{-29}\ \mathrm{cm}^6\ \mathrm{s}^{-1} \quad (4)$$

is rather obvious but needs explanations (see below). For n-H_2 (data from Plasil et al.[24]), the trend is not so evident, partly due to the smaller temperature interval. The minor increase indicated by the dashed line,

$$k_3(T;\text{n-}H_2) = (1.4 + 0.1 \times T/\mathrm{K}) \times 10^{-29}\ \mathrm{cm}^6\ \mathrm{s}^{-1} \quad (5)$$

can be fully explained with the contribution of the 25% of $H_2(j{=}0)$ in n-H_2. This leads to the conclusion that $k_3(T;j{=}1)$ does not change with temperature. The results for radiative association (lower panel) are rather uncertain due to the large errors of the individual points. Therefore, the two functions

$$k_r(T;j{=}0) = (1 - 0.01 \times T/\mathrm{K}) \times 10^{-16}\ \mathrm{cm}^3\ \mathrm{s}^{-1} \quad (6)$$

$$k_r(T;\text{n-}H_2) = (2.3 - 0.07 \times T/\mathrm{K}) \times 10^{-16}\ \mathrm{cm}^3\ \mathrm{s}^{-1} \quad (7)$$

should not be overinterpreted. However, it is rather certain that radiative association decreases with temperature; i.e., it does not follow the temperature trend of ternary association.

Important for deriving state specific rate coefficients for j = 1 are the differences between p-H_2 and n-H_2. In Figure 4, the

A.2

dx.doi.org/10.1021/jp400917v | J. Phys. Chem. A XXXX, XXX, XXX−XXX

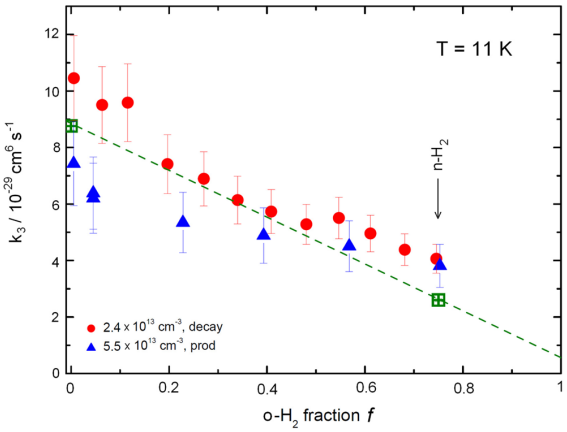

Figure 4. Ternary rate coefficients k_3 measured at T_{22PT} = 11 K as a function of the ortho fraction f (f = 0, p-H_2; f = 0.75, n-H_2). The squares with crosses inside have been determined from fits to the density dependence of k^*, and the other points have been measured at the indicated fixed densities and corrected for minor contributions from k_r. The filled circles have been derived from the decay of primary protons, and the triangles show rate coefficients determined from the products H_3^+. The slight systematic difference is discussed in the text. The dotted line indicates that the f dependence can be approximated with a linear function resulting in state specific rate coefficients for H_2 in j = 0 and j = 1 (see the text and Table 1).

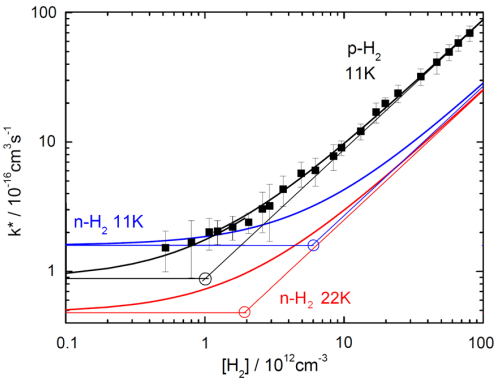

Figure 5. Apparent binary association rate coefficients k^*. For better comprehensibility only the T_{22PT} = 11 K data are shown for p-H_2. As in Figure 2, they are fitted with eq 3. Due to the log−log plot, the contributions from radiative association become apparent by the curvature of the fit. These results can be compared with the fitting curves, determined for n-H_2 at 11 and 22 K.[24] The circles mark the locations, where ternary and radiative association are equally efficient. It is obvious that ternary association with p-H_2 is significantly faster than with n-H_2 whereas the differences for radiative association are rather small and not so obvious because of the errors. For more detail, see the text and Table 1.

mean ternary rate coefficient is plotted as a function of the ortho fraction f. The two large symbols (squares with crosses inside) are the above presented results determined from the density dependence of k^* whereas the other points have been measured directly at the indicated f values. As discussed above, the contributions from k_r, which have been subtracted from k^*, are rather small at the indicated hydrogen densities. The rate coefficients plotted as filled circles have been derived from the decay of the protons, as most of the results presented in this work. The triangles show rate coefficients where the formation of H_3^+ products has been evaluated. Inspection reveals that they are smaller, which may be due to minor differences in the detection or trapping efficiency of H^+ and H_3^+. Remarkable is a systematic increase of the deviations toward pure p-H_2. This may be due to additional loss of H_3^+ because it is faster converted into H_5^+ ions. It is known from ion trap experiments[29] that, in pure p-H_2, H_5^+ clusters grow 4 times faster than in n-H_2. The overall dependence on f can be reasonably well described with a linear function (dashed line)

$$k_3(f) = (1 - f)k_3(j{=}0) + f\ k_3(j{=}1) \quad (8)$$

although one also could expect deviations from linearity because hydrogen plays a triple role: (i) thermalization of the ions, (ii) formation of the complexes, and (iii) stabilization of them. The fit with eq 8 results in the two state specific rate coefficients $k_3(11\ \mathrm{K}; j{=}0) = 8.8 \times 10^{-29}$ cm^6 s^{-1} and $k_3(11\ \mathrm{K}; j{=}1) = 0.6 \times 10^{-29}$ cm^6 s^{-1}. It is an open question whether this huge difference is due to complex formation or complex stabilization or due to both processes. Also the protons may be on average faster if more hydrogen molecules are rotationally excited (ortho−para transitions).

To illustrate the limitations in extracting radiative rate coefficients, Figure 5 compares selected results in a log−log presentation. As in Figure 2, the data (11 K, p-H_2) are fitted with the function given in eq 3. The results for n-H_2 at 11 and 22 K, reported by Plasil et al.,[24] are represented here only via their fit function for clarity. The thin straight lines mark the separate contributions from radiative (horizontal) and ternary (increasing) association. The circles indicate the locations, where they are equally efficient. Because all rate coefficients for radiative association are below 2×10^{-16} cm^3 s^{-1} and have rather large errors (see also Figure 3), future experiments should be extended to lower number densities. Note, however, that this requires very long storage times and no perturbations.

DISCUSSION

Collisions with hydrogen molecules are by far the most abundant processes in the universe, and therefore, it is of central importance to determine the ortho−para ratio in the various astrophysical environments and to understand how the 14.4 meV energy, provided by hydrogen in j = 1, and the total nuclear spin 1 affect physical and chemical processes. This is especially important at low temperatures. The result from the present work that ternary association is significantly more efficient with nonrotating hydrogen, is in accordance with previous ion trap studies performed with C^+, CH_3^+, and $C_2H_2^+$ ions, showing that both radiative and ternary association is several times faster with p-H_2 than with n-H_2.[30] Surprising on the new results is the temperature dependence of k_3 and the fact that radiative association is always very slow.

Previous measurements of ternary and radiative association rate coefficients have been evaluated using rather simple statistical models that have been reviewed by Gerlich and Horning.[19] The basic assumption is that the overall process can be described by the formation of a long-lived complex followed by (i) dissociation, (ii) ternary stabilization, or (iii) emission of a photon. The outcome of such calculations is that k^*, as defined in eq 3, can be approximated by the equation

$$k^* = k_c(1/\tau_{H_2} + 1/\tau_r)/(1/\tau_{diss} + 1/\tau_{H_2} + 1/\tau_r) \quad (9)$$

A.2

dx.doi.org/10.1021/jp400917v | J. Phys. Chem. A XXXX, XXX, XXX−XXX

Here k_c is the rate coefficient for forming the collision complex and the time constants τ_{diss}, τ_{H_2}, and τ_r describe its dissociation, its stabilization via the second H_2, and its radiative stabilization, respectively. It is also common to describe ternary stabilization by the product of a collision rate coefficient k_{H_2} and a stabilization factor f_s. Under such assumptions complex and radiative lifetimes can be inferred from the experimental data. Results for several systems are collected in the above-mentioned review[19] where one also finds for $H^+ + n\text{-}H_2$ at 80 K $\tau_{diss} = 5.5 \times 10^{-11}$ s and $\tau_r = 1.1$ ms. Using classical trajectory calculations,[31] the complex lifetime has been estimated to be $\tau_{diss} \sim 10^{-11}$ s at 0.1 eV and to change proportional to $T^{-1.9}$. This steep increase with falling temperature is in obvious contrast to our very small values of k_r. The question is whether this is due to k_c, τ_{diss}, or τ_r, the only parameters relevant at low densities. Concerning the radiative lifetime of highly excited H_3^+, an independent trapping experiment has provided additional information. It is based on CO_2 laser photofragmentation after different storage times; for details, see refs 10 and 19. The resulting lifetime, $\tau_r = 0.37$ ms, is in accordance with the expectation that IR emissions are in the millisecond range. The conclusion is that something must be wrong with the simple statistical concept of complex formation and decay.

For systems with many active internal degrees of freedom, statistical approaches are certainly useful; however, $H^+ + H_2$ collisions at translational energies of a few millielectronvolts populate only a rather small number of resonances. These scattering states may have quite different lifetimes and emission probabilities (dipole moments). Unfortunately, H_3^+ in the vicinity of the dissociation limit is still an unsolved problem, although there have been many theoretical activities, stimulated by the predissociation spectra reported by Carrington and co-workers.[32] For more than 25 years they have been unassigned! Can one expect under such conditions that modern theories are capable of predicting radiative association in $H^+ + H_2$ collisions?

To answer this question, it first should be emphasized that the Carrington states[32] are very specific ones, preselected by the experimental conditions. They have microsecond lifetimes and also excitation energies up to 3000 cm^{-1} above the dissociation limit. Because the ions are produced in reactive collisions of H_2^+ with H_2, angular momenta of 25 $\hbar$ or higher must be expected. In the present ion trap experiment, the energy interval of interest is 100 times smaller and the total orbital angular momenta J are restricted to a few $\hbar$. Based on the simple Langevin criterion and using just the polarization interaction, the maximum orbital angular momentum is $l_m = 6\ \hbar$ at 1 meV translational energy. All this leads to a rather low total number of H_3^+ continuum states populated in the collision complex. These quasibound states have been calculated rather often;[33] however, one of the problems is to get an accurate potential energy surface, describing also correctly the long-range part. Note that, in linear approach, the H^+-H_2 interaction has a 3.2 meV barrier at 11 a_0 and that, for C_{2v} geometry, it is still −1 meV attractive at 22 a_0.[16] A systematic investigation of the ground state potential energy surface of H_3^+ together with all bound vibrational states, including resonances above the dissociation limit has been reported recently by Jaquet and Khoma,[6] so far only for the total angular momentum $J = 0$. As already mentioned in the Introduction, first quantum mechanical scattering calculation have been reported for the $H^+ + H_2$ system and isotopic variants by Honvault et al.[14,15] For ortho−para transitions, the cross sections calculated at millielectronvolt translational energies, show a pronounced resonance structure (see Figure 1 in ref 12). It seems to be rather certain that such long-lived resonances are responsible for radiative association. Therefore, one can hope that theoreticians may find sooner or later explanations for the results from this work and especially for the fact that the largest value so far measured ($k_r = 1.8 \times 10^{-16}$ $cm^3\ s^{-1}$) is for the collision of a proton with the hydrogen molecule in the first rotational state!

Significantly more difficult than radiative association is to understand the measured ternary association rate coefficients and their temperature dependencies. In this case it is evident that the simple model mentioned above is not valid. Statistical theories always have predicted that the lifetime of a complex increases with decreasing temperature. In most model calculations, the proportionality $\sim T^{-s}$ is taken, where s is the so-called number of active degrees of freedom. At the moment we can only speculate that, from the few resonances populated under the conditions of our experiment, only selected ones can contribute to ternary association and that the number of such active resonances becomes bigger when the nominal temperature increases from 11 to 33 K. A second, even bigger uncertainty in ternary association is the stabilization of the intermediate complex by the collision with a second hydrogen molecule. This interaction takes place on the rather well-characterized potential energy surface of H_5^+.[34] One of the remarkable characteristics is that the proton can easily be exchanged between the two hydrogen molecules.[35] As a consequence of this "shared proton structure", one may suppose that the H_2 approaching the H_3^+ complex pulls out the proton in many cases instead of stabilizing the collision complex. Such specific processes certainly may have quite different temperature dependences. An interesting related information mentioned by Gerlich and Horning,[19] is that helium as stabilizer is more than four times more efficient than hydrogen.

CONCLUSIONS

With para- and normal-hydrogen new measurements have been performed at low temperatures for obtaining state specific rate coefficients for forming H_3^+ via radiative and ternary association. The extracted results, $k_r(T;j)$ and $k_3(T;j)$, show surprising temperature dependences that cannot be explained with simple statistical models. Due to the very unfavorable ion:neutral mass ratio, the actual velocity distribution deviates probably from the thermal one, and one needs at least two temperatures for describing it. Nonetheless, the interesting observations are unchanged, and it can be expected that the temperature dependences become even more pronounced. A significant improvement of the results can be achieved if the target gas is leaked in using a cold effusive or supersonic beam of hydrogen molecules. This is possible with the present instrument.[36]

It has been mentioned several times that more support from theory is needed for understanding the role of the $(H-H_2)^+$ scattering states populated at translational energies of a few millielectronvolts. Sufficiently accurate potential energy surfaces and the tools to solve the collision dynamics seem to be available today. Not mentioned so far but also of central importance are certainly the restrictions imposed by the nuclear spin of the three or five protons. For describing radiative

A.2

dx.doi.org/10.1021/jp400917v | J. Phys. Chem. A XXXX, XXX, XXX−XXX

association, a suitable dipole moment surface is needed for predicting the emission of photons. An experimental challenge is finally the laser induced association of the collision complex, allowing one to perform spectroscopy on it. All this finally may help also to understand the Carrington lines.[32]

A completely different theoretical approach for exploring H_3^+ close to the dissociation limit has been reported recently by Kylänpää and Rantala.[37] In this work, a quantum statistical method has been used to explore the structure and energetics of H_3^+ as a function of temperature up to the thermal dissociation limit which has been found to be around 4000 K. Corresponding trapping experiments are possible and are in preparation.

AUTHOR INFORMATION

Corresponding Author

*E-mail: gerlich@physik.tu-chemnitz.de.

Notes

The authors declare no competing financial interest.

ACKNOWLEDGMENTS

We thank the DFG and the TU Chemnitz for making these studies possible by lending the Charles University in Prague the AB-22PT instrument. This work was partly supported by GACR (P209/12/0233, 205/09/1183), GAUK 388811, GAUK 406011, and GAUK 659112.

REFERENCES

(1) Oka, T. H_3^+ from the Laboratory to the Galactic Center. *Faraday Discuss.* **2011**, *150*, 9−22.

(2) Morong, C. P.; Gottfried, J. L.; Oka, T. H_3^+ as the Benchmark for Rigorous ab initio Theory. *J. Mol. Spectrom.* **2009**, *255*, 13−23.

(3) Pavanello, M.; Adamowicz, L.; Alijah, A.; Zobov, N. F.; Mizus, I. I.; Polyansky, O. L.; Tennyson, J.; Szidarovszky, T.; Császár, A. G. Calibration-Quality Adiabatic Potential Energy Surfaces for H_3^+ and its Isotopologues. *J. Chem. Phys.* **2012**, *136*, 184303-1−184303-14.

(4) Polansky, O. L.; Alijah, A.; Zobov, N. F.; Mizus, I. I.; Ovsyannikov, R. I.; Tennyson, J.; Lodi, L.; Szidarovsky, T.; Császár, A. G. Spectroscopy of H_3^+ Based on a New High-accuracy Global Potential Energy Surface. *Philos. Trans. R. Soc. A* **2012**, *370*, 5014−5027.

(5) Pavanello, M.; Adamowicz, L.; Alijah, A.; Zobov, N. F.; Mizus, I. I.; Polyansky, O. L.; Tennyson, J.; Szidarovszky, T.; Császár, A. G; Berg, M.; et al. Precision Measurements and Computations of Transition Energies in Rotationally Cold Triatomic Hydrogen Ions up to the Midvisible Spectral Range. *Phys. Rev. Lett.* **2012**, *108*, 023002−023007.

(6) Jaquet, R.; Khoma, M. V. A Systematic Investigation of the Ground State Potential Energy Surface of H_3. *J. Chem. Phys.* **2012**, *136*, 154307-1−154307-11.

(7) Larsson, M. Dissociative Recombination of H_3^+: 10 Years in Retrospect. *Philos. Trans. R. Soc. A* **2012**, *370*, 5118−5129.

(8) Crabtree, K.; McCall, B. The Ortho:Para Ratio of H_3^+ in Laboratory and Astrophysical Plasmas. *Philos. Trans. R. Soc. A* **2012**, *370*, 5055−5056.

(9) Glover, S.; Savin, D. W. H_3^+ Cooling in Primordial Gas. *Philos. Trans. R. Soc. London, Ser. A* **2006**, *364*, 3107−3112.

(10) Gerlich, D. Ortho - Para Transitions in Slow $H^+ + H_2$ Collsions. *J. Chem. Phys.* **1990**, *92*, 2377−2388.

(11) Grozdanov, T. P.; McCarroll, R. Low-Energy $H^+ + H_2$ Reactive Collisions: Mean-Potential Statistical Model and Role of Permutation Symmetry. *J. Phys. Chem. A* **2012**, *116*, 4569−4577.

(12) Honvault, P.; Jorfi, M.; Gonzalez-Lezana, T.; Faure, A.; Pagani, L. Ortho-Para H_2 Conversion by Proton Exchange at Low Temperature: An Accurate Quantum Mechanical Study. *Phys. Rev. Lett.* **2011**, *107*, 023201-1−023201-4.

(13) Honvault, P.; Jorfi, M.; Gonzalez-Lezana, T.; Faure, A.; Pagani, L. Quantum Mechanical Study of the Proton Exchange in the Ortho−Para H_2 Conversion Reaction at low Temperature. *Phys. Chem. Chem. Phys.* **2011**, *13*, 19089−19100.

(14) Honvault, P.; Jorfi, M.; Gonzalez-Lezana, T.; Faure, A.; Pagani, L. Erratum: Otho-Para H_2 Conversion by Proton Exchange at Low Temperature: An Accurate Quantum Mechanical Study. *Phys. Rev. Lett.* **2012**, *108*, 109903-1.

(15) Jambrina, P. G.; Alvarino, J. M.; Gerlich, D.; Hankel, M.; Herrero, V. J.; Saez- Rabanos, V.; Aoiz, F. J. Dynamics of the $D^+ + H_2$ and $H^+ + D_2$ Reactions: A Detailed Comparison Between Theory and Experiment. *Phys. Chem. Chem. Phys.* **2012**, *14*, 3346−3359.

(16) Velilla, L.; Lepetit, B.; Aguado, A.; Beswick, J. A.; Paniagua, M. The H_3^+ Rovibrational Spectrum Revisited with a Global Electronic Potential Energy Surface. *J. Chem. Phys.* **2008**, *129*, 084307−1−084307−11.

(17) Graham, E.; James, D. R.; Keever, W. C.; Gatland, I. R.; Albritton, D. L.; McDaniel, E. W. Measurement of the Rate Coefficient of the Reactions $H^+ + 2H_2 \rightarrow H_3^+ + H_2$ and $D^+ + 2D_2 \rightarrow D_3^+ + D_2$ in a Drift Tube Mass Spectrometer. *J. Chem. Phys.* **1973**, *59*, 4648−4651.

(18) Johnson, R.; Huang, C.-M.; Biondi, M. A. Three-Body Association Reactions of H^+ and H_3^+ Ions in Hydrogen from 135 to 300 K. *J. Chem. Phys.* **1976**, *65*, 1539−1541.

(19) Gerlich, D.; Horning, S. Experimental Investigations of Radiative Association Processes as Related to Interstellar Chemistry. *Chem. Rev.* **1992**, *92*, 1509−1539.

(20) Barlow, S. E.; Luine, J. A.; Dunn, G. H. Measurement of Ion/Molecule Reactions Between 10 and 20 K. *Int. J. Mass. Spectrom. Ion Phys.* **1986**, *74*, 97−128.

(21) Gerlich, D.; Kaefer, G. Measurements of Extremely Small Rate Coefficients in an RF Trap: The Association Reaction of C^+ and H^+ with H_2 at 230 and 320 K. *Proceedings of the 5th International Swarm Seminar*; Adams, N. G., Smith, D., Eds.; Birmingham University: Birmingham, U.K., 1987; pp 133−137.

(22) Gerlich, D.; Kaefer, G.; Paul, W. Ion Trap Studies of Ternary and Radiative Association Processes. In *7th Symposium on Atomic and Suface Physics*; Märk, T. D. , Howorka, F., Eds.; University of Innsbruck: Innsbruck, 1990; pp 332−337; http://repository.uibk.ac.at/alo?objid=1026217.

(23) Gerlich, D. Ion-Neutral Collisions in a 22-Pole Trap at Very Low Energies. *Phys. Scr.* **1995**, *T59*, 256−263.

(24) Plašil, R.; Zymak, I.; Jusko, P.; Mulin, D.; Gerlich, D.; Glosík, J. Stabilization of H^+ - H_2 Collision Complexes Between 11 and 28 K. *Philos. Trans. R. Soc. A* **2012**, *370*, 5066−5073.

(25) Gerlich, D. Inhomogeneous Electrical Radio Frequency Fields: A Versatile Tool for the Study of Processes with Slow Ions. *Adv. Chem. Phys.* **1992**, *LXXXII*, 1−176.

(26) Gerlich, D. The Study of Cold Collisions Using Ion Guides and Traps. In *Low temperatures and cold molecules*; Smith, I. W. M., Ed.; World Scientific Publishing Co. Pte. Ltd.: Singapore, 2008; pp 121−174.

(27) Gerlich, D. The Production and Study of Ultra-Cold Molecular Ions. In *Low temperatures and cold molecules*; Smith, I. W. M., Eds.; World Scientific Publishing Co. Pte. Ltd.: Singapore, 2008; pp 295−343.

(28) Zymak, I.; Hejduk, M.; Mulin, D.; Plašil, R.; Glosík, J.; Gerlich, D. Low Temperature Ion Trap Studies of $N^+(^3P_{ja}) + H_2(j) \rightarrow NH^+ + H$. *Astrophys. J.* **2013**, in press.

(29) Paul, W.; Lücke, B.; Schlemmer, S.; Gerlich, D. On the Dynamics of the Reaction of Positive Hydrogen Cluster Ions (H_5^+ to H_{23}^+) with Para and Normal Hydrogen at 10 K. *Int. J. Mass. Spectrom. Ion Phys.* **1995**, *150*, 373−387.

(30) Gerlich, D. Recent Progress in Experimental Studies of Ion−Molecule Reactions Relevant to Interstellar Chemistry. In *Molecules and Grains in Space*; Nenner, I., Ed.; AIP Press: New York, 1994; pp 489−500.

(31) Schlier, Ch.; Vix, U. Lifetimes of Triatomic Collision Complexes. *Chem. Phys.* **1985**, *95*, 401−409.

A.2

(32) Carrington, A.; McNab, I. R.; West, Y. D. Infrared Predissociation Spectrum of the H_3^+ Ion. II. *J. Chem. Phys.* **1993**, *98*, 1073−1092.
(33) Tennyson, J.; Barletta, P.; Munro, J. J.; Silva, B. C. The Role of Asymptotic Vibrational States in H_3. *Philos. Trans. R. Soc. London, Ser. A* **2006**, *364*, 2903−2916.
(34) Aguado, A.; Barragán, P.; Prosmiti, R.; Delgado-Barrio, G.; Villarreal, P.; Roncero, O. A New Accurate and Full Dimensional Potential Energy Surface of H_5^+ Based on a Triatomics-in-Molecules Analytic Functional Form. *J. Chem. Phys.* **2010**, *133*, 024306-1−024306-15.
(35) de Tudela, R. P.; Barragán, P.; Prosmiti, R.; Villarreal, P.; Delgado-Barrio, G. Internal Proton Transfer and H_2 Rotations in the H_5^+ Cluster: A Marked Influence on its Thermal Equilibrium State. *J. Phys. Chem. A* **2011**, *115*, 2483−2488.
(36) Gerlich, D.; Borodi, G.; Luca, A.; Mogo, C.; Smith, M. Reactions Between Cold CH_n^+ with H and H_2. *Z. Phys. Chem.* **2011**, *252*, 475−492.
(37) Kylänpää, I.; Rantala, T. T. Finite Temperature Quantum Statistics of H_3^+ Molecular Ion. *J. Chem. Phys.* **2010**, *133*, 044312-1−044312-5.

A.2

B. SA-CRDS

B.1 Nuclear spin state-resolved cavity ring-down spectroscopy diagnostics of a low-temperature H_3^+-dominated plasma

M. Hejduk, P. Dohnal, J. Varju, P. Rubovič, R. Plašil and J. Glosík, *Plasma Sources Science & Technology*, 21 (2), 2012. doi:10.1088/0963-0252/21/2/024002.

IOP Publishing Plasma Sources Science and Technology
Plasma Sources Sci. Technol. **21** (2012) 024002 (9pp) doi:10.1088/0963-0252/21/2/024002

Nuclear spin state-resolved cavity ring-down spectroscopy diagnostics of a low-temperature H_3^+ -dominated plasma

Michal Hejduk, Petr Dohnal, Jozef Varju, Peter Rubovič, Radek Plašil and Juraj Glosík

Department of Surface and Plasma Physics, Faculty of Mathematics and Physics, Charles University, Prague, Czech Republic

E-mail: MichalLeeHejduk@matfyz.cz

Received 2 August 2011, in final form 31 October 2011
Published 4 April 2012
Online at stacks.iop.org/PSST/21/024002

Abstract
We have applied a continuous-wave near-infrared cavity ring-down spectroscopy method to study the parameters of a H_3^+-dominated plasma at temperatures in the range 77–200 K. We monitor populations of three rotational states of the ground vibrational state corresponding to para and ortho nuclear spin states in the discharge and the afterglow plasma in time and conclude that abundances of para and ortho states and rotational temperatures are well defined and stable. The non-trivial dependence of a relative population of para-H_3^+ on a relative population of para-H_2 in a source H_2 gas is described. The results described in this paper are valuable for studies of state-selective dissociative recombination of H_3^+ ions with electrons in the afterglow plasma and for the design of sources of H_3^+ ions in a specific nuclear spin state.

(Some figures may appear in colour only in the online journal)

B.1

1. Introduction

H_3^+ ions are one of the key components of interstellar space [1–3] and planetary atmospheres [4, 5]. For astrophysicists, it is crucial to understand how these ions are formed and destroyed [6, 7]. In the latter process, dissociative recombination (DR) of the H_3^+ ion with an electron plays one of the key roles.

Up to the end of the previous millennium, a number of mutually inconsistent experiments regarding DR were carried out [8–16] and no unifying theoretical explanation was available. This has changed recently when cross sections obtained at a storage ring [17–20] and theoretical values (calculated by going beyond the Born–Oppenheimer approximation and accounting for Jahn–Teller coupling [21–24]) started to converge. These experiments, however, succeeded in confirming different recombination cross sections for para and ortho nuclear spin states of the ion only qualitatively. The quantitative difference between the theory and the experiments was later explained to be caused by the fact that rotational temperatures were much higher [25] than those previously stated. Any further study about the recombination of H_3^+ would first have to show how well the internal temperature (population of internal states) is determined.

Our group has recently shown that, in addition to the two-body electron–ion recombination process, the ternary recombination process (He assisted, if helium buffer gas is used) plays a significant role in a laboratory afterglow plasma dominated by H_3^+ [26, 27]. Knowledge about both processes was exploited in our studies of the nuclear spin state-selective recombination of H_3^+ ions with electrons at a temperature of 77 K. Laser-aided continuous-wave cavity ring-down spectroscopy (cw-CRDS) was the chosen method. As a result of experiments with two different populations of para-nuclear spin states of H_3^+, we recently measured recombination rate coefficients for para and ortho H_3^+ ions [28], which are in quantitative accordance with the theoretical predictions [23].

In this paper, we describe our apparatus for the studies of the recombination and show how well the rotational and kinetic temperatures and population of the monitored states are determined. A description of the methods of precise determination of these parameters is useful not only for state-selective recombination studies but also for the investigation

of other nuclear spin state-selective processes involving H_3^+ ions in a low-temperature discharge plasma (nuclear spin conversion of H_3^+ ions in collision with H_2, for example, [29]). We also deal with the topic of production of an ensemble of H_3^+ ions with a specified population of para nuclear spin states, which may be interesting for the construction of para-H_3^+ ion sources.

In the following text, we use special notation for some terms. Para/ortho nuclear spin states of H_3^+, H_2 and H_2^+ are denoted by 'p'/'o' in the leading superscript position (like $^pH_3^+/^oH_3^+$). 'Normal' hydrogen gas ($^nH_2$) is defined as H_2 gas with 25% of molecules in the para state and 75% in the ortho state. H_2 gas with any higher population of $^pH_2$ is called para-enriched and is marked $^eH_2$. We refer to a relative population of $^pH_3^+$ among H_3^+ ions as $^pf_3$, i.e. $^pf_3 = [^pH_3^+]/[H_3^+]$. The abundance of $^pH_2$ in H_2 gas is marked similarly: $^pf_2 = [^pH_2]/[H_2]$. Apart from $^nH_2$, we mainly use $^eH_2$ with $^pf_2 = 0.87$ in our experiments; this $^eH_2$ is marked $^e_mH_2$ (m indicates the maximum).

2. Experimental setup

Our experimental apparatus can be naturally divided into two subsystems: one is responsible for the production of cold H_3^+-dominated plasma and the other is a system of spectroscopic detection of specific rovibrational states of H_3^+ ions. A thorough description of the apparatus can be found in [30]. Here we provide only the most important details.

2.1. Production of H_3^+-dominated plasma with ions in specific states

H_3^+ ions are produced by a microwave discharge in a He–Ar–H_2 mixture with typical concentrations of 10^{17}, 10^{14} and 10^{14} cm^{-3}. The frequency of the microwaves is 2.5 GHz and input power is set in the range 4–12 W. The discharge is switched on for 2–2.5 ms and then switched off for around 4 ms to let the plasma decay. The discharge tube is made of silica glass and its inner diameter is 1.5 cm. The tube can be cooled down to 77 K by immersing it in liquid nitrogen and temperatures above 135 K are achieved by exposing it to cold nitrogen vapour. Helium ions and metastable atoms created during the microwave discharge are rapidly converted to H_3^+ by a sequence of ion–molecule reactions involving Ar^+ and ArH^+ as intermediate ions (for details on the kinetics of formation see [30–32]). The method of examination of the afterglow is actually semi-stationary, because the source gas mixture is always flowing through the discharge tube: each repetition of discharge on–off cycle is carried out in a completely renewed environment with almost all reaction products removed (see the discussion in section 3.1.4).

As briefly mentioned in section 1 and fully described in [28], at least two different measurements with two different relative populations of $^pH_3^+$ ($^pf_3$) need to be carried out to study nuclear spin state-specific recombination. The value of $^pf_3$ is determined by H_2 and Ar densities, by the temperature and by nuclear spin selection rules of the reactions (see the discussions in [29, 33–37])

$$^{p,o}H_2^+ + {}^{p,o}H_2 \rightarrow {}^{p,o}H_3^+ + H, \quad (1)$$

$$^{p,o}H_3^+ + {}^{p,o}H_2 \rightarrow {}^{p,o}H_3^+ + {}^{p,o}H_2, \quad (2)$$

and

$$ArH^+ + {}^pH_2 \rightarrow {}^pH_3^+ + Ar \quad (3a)$$

$$+ {}^oH_2 \rightarrow {}^{p,o}H_3^+ + Ar, \quad (3b)$$

which allow the production of an ensemble of H_3^+ ions with higher or lower $^pf_3$ by raising or lowering the value of $^pf_2$. The maximal $^pf_2$ we are able to reach by conversion of $^nH_2$ in the presence of Fe_2O_3 catalyst at 10–18 K outside the discharge tube is 0.87 (value gained by nuclear magnetic resonance); we denote such a gas as $^e_mH_2$. The values of $^pf_3$ depend also on parameters other than $^pf_2$ as described in sections 3.1.4 and 3.1.5 of this paper.

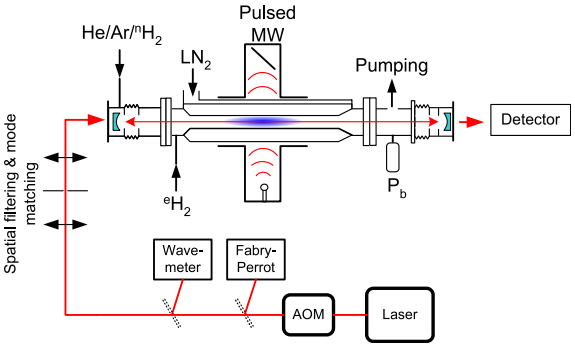

Figure 1. A scheme of the CRDS apparatus. The laser beam is directed into or out of the optical cavity by the acousto-optic modulator (AOM). The beam undergoes spatial filtering before it enters the optical cavity. The plasma is formed by the microwave discharge (MW) in the optical cavity. The pressure inside is measured by a baratron gauge (P_b). The discharge tube is cooled by liquid nitrogen (LN_2) or its vapour. The set wavelength is measured absolutely using a Michelson interferometer and relatively by a Fabry–Pérot interferometer. The inner diameter of the discharge tube is 15 mm.

2.2. Optical system—cavity ring-down spectroscopy

We have implemented cw-CRDS to track the population of specific rotational states of the ground vibrational state of H_3^+ ions in a discharge and an afterglow in time with high sensitivity and time resolution. Even though the concept of CRDS is widely known [38], its use in time spectroscopy is not common and requires a good synchronization of ring-down detection with other parts of the apparatus; for details about this topic, see [39].

A scheme of cw-CRDS, developed by Romanini *et al* [40], was employed in the construction of our spectrometer (see figure 1). A laser beam is coupled to an optical cavity whose highly reflective mirrors (reflectivity over 99.98%) are periodically swept until an optical resonator is formed. When the resonator is set up, the laser radiation power in the cavity

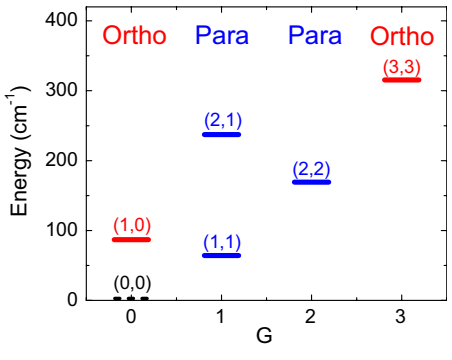

Figure 2. Lowest rotational levels (J, G) of the ground vibrational level of H_3^+. Populations of (1,1), (1,0) and (3,3) (corresponding to one para and two ortho states, respectively) are measured. For notation, see [41].

Table 1. Used transitions and their wavenumbers.

Transition	Wavenumber (cm^{-1})	Nuclear spin state
$3\nu_2^1(2,1) \leftarrow 0\nu_2^0(1,1)$	7237.285	Para
$3\nu_2^1(2,0) \leftarrow 0\nu_2^0(1,0)$	7241.245	Ortho
$3\nu_2^1(4,3) \leftarrow 0\nu_2^0(3,3)$	7234.957	Ortho

rises and the incoming laser beam is interrupted by an acousto-optic modulator as soon as the intensity measured by the PIN or avalanche diode behind one of the mirrors exceeds a threshold. After the laser beam is intercepted, the trapped light intensity decreases because of the losses at the mirrors and the absorption by the medium in the cavity. The characteristic time of the decrease in intensity is inversely proportional to the concentration of absorbing molecules in the medium. The frequency of ring-down events is ≈100 Hz.

As the light source, a fibre-coupled distributed feedback (DFB) laser diode was used. The central wavelength of the laser is 1381.55 nm. The line width of the laser is <2 MHz on 1 s timescales. The maximum output optical power is 20 mW. The beam from the laser undergoes spatial filtering to form Gaussian profile matching to the optical resonator. The set wavelength is measured absolutely using a Michelson interferometer and relatively by a Fabry–Pérot interferometer.

We were able to monitor three of the lowest rotational states of the ground vibrational state of H_3^+: $(J, G) = (1, 1)$, $(1, 0)$ and $(3, 3)$ corresponding to a para and two ortho states (respectively, see figure 2; for notation, see [41]). Specific transitions and their wavelengths are shown in table 1.

3. Experiment: examination of plasma parameters

As mentioned in section 1, our aim is to study the properties of the low-temperature discharge plasma in which we produce the ensemble of H_3^+ ions that is used to study the state-selective recombination of the eponymous ions. Apart from the discharge plasma, the early afterglow is also described in several places since the production processes can take place there as well. The CRDS method used in the presented experimental setup allows us to describe the plasma by kinetic and rotational temperatures of H_3^+ ions and by an abundance of these ions in para nuclear spin states (${}^{\mathrm{p}}f_3$). We need to study the relationships between the aforementioned parameters and experimental conditions to be able to reproduce the results at any time.

In particular, the following questions need to be answered if we want to describe the studied plasma satisfactorily:

(Q-1) How does the kinetic temperature (T_{Kin}) of the ions evolve? What is its relation to the temperature of the discharge tube and the He buffer gas?
(Q-2) How does the population of rotational states of the ions change in time in the discharge and the early afterglow?
(Q-3) Does any subsystem of an ensemble of H_3^+ ions reach equilibrium in the discharge to be able to define a rotational temperature? How does the rotational temperature correspond to T_{Kin}?
(Q-4) How does the population of nuclear spin states develop in the discharge and in the early afterglow?
(Q-5) How can we produce the plasma with a specified value of ${}^{\mathrm{p}}f_3$ (specified para-to-ortho ratio)?
  (a) What is the relationship between ${}^{\mathrm{p}}f_2$ and ${}^{\mathrm{p}}f_3$?
  (b) What is the relationship between T_{Kin} and ${}^{\mathrm{p}}f_3$?

To answer these questions, it is preferable to clarify the processes taking place in the discharge plasma. A list of them is given in table 2. Here are some comments on the table.

1. *Ambipolar diffusion.* We know from recombination studies [28, 42] carried out in the experimental setup described in figure 1 (with [He] ≈ $10^{17}\,\mathrm{cm}^{-3}$ and temperature range 77–300 K) that the characteristic diffusion time in the afterglow (τ_{DAG}) is of the order of 1 ms. The characteristic diffusion time is evaluated from the ion number density decays measured in the afterglow together with the recombination rate coefficient—see equation (4) and figure 1 in [28]. Its value can also be calculated [43] from the mobility of the ion [44]. We assume that the electron temperature (T_{e}) in the discharge is of the order of $T_{\mathrm{e}} \approx 1\,\mathrm{eV}$ and that ions have kinetic temperature $T_{\mathrm{Kin}} \approx 0.01\,\mathrm{eV}$. Then the value of the characteristic time of the ambipolar diffusion in the discharge is

$$\tau_1 \sim 2 \times \tau_{\mathrm{DAG}} \frac{T_{\mathrm{Kin}}}{T_{\mathrm{e}}} \approx 2\,\mathrm{ms} \times \frac{0.01\,\mathrm{eV}}{1\,\mathrm{eV}} = 0.02\,\mathrm{ms}.$$

2. *Recombination of H_3^+ ions.* For electron temperature $T_{\mathrm{e}} \approx 1\,\mathrm{eV}$ and electron density [e] ≈ $10^{11}\,\mathrm{cm}^{-3}$ in the discharge, the recombination rate will be $\alpha \leqslant 10^{-8}\,\mathrm{cm}^3\,\mathrm{s}^{-1}$ [20]. Hence the characteristic time of recombination is

$$\tau_2 = 1/(\alpha[\mathrm{e}]) \approx 1/(10^{-8}\,\mathrm{cm}^3\,\mathrm{s}^{-1} \times 10^{11}\,\mathrm{cm}^{-3}) = 1\,\mathrm{ms}.$$

4, 6 and 7. Ions are supposed to get *cooled vibrationally* after several collisions with He atoms or H_2 molecules. The variables τ in the table are the time between two successive quenching collisions, and estimation of their values in the table is based on the collisional frequencies. We assume that the main process of *rotational cooling* is a quenching

Table 2. Processes in the discharge plasma in which H_3^+ ions are involved. Rotational quantum numbers $J' > J$, $G' > G$, vibrational quantum number $v' > v$ (symmetric or degenerate antisymmetric stretch). Prsmp. stands for the presumption. Rate coefficients k are approximate values applicable to the range of temperatures 77–300 K unless otherwise specified. If k is given, $\tau_n = 1/(k\,[\mathrm{X}])$ (where X is a reactant) and it is called the 'characteristic time' of the process. See the text for the definition of τ in the case of missing k.

n	Process type $H_3^+ + X$	[X] (cm^{-3})	k ($cm^3\ s^{-1}$)	τ_n (ms)	References, comments
1	Ambipolar diffusion of H_3^+	—	—	0.02	[28, 42]
2	$H_3^+ + e \rightarrow$ neutral products	10^{11}	10^{-8}	1	$T_e \approx 1$ eV, [20]
3	$H_3^+(J, G) + e \leftrightarrow H_3^+(J', G') + e$	10^{11}	10^{-7} [a]	0.1	$T_e \approx 1$ eV, [45]
4	$H_3^+(J', G') + He \rightarrow H_3^+(J, G) + He$	10^{17}	—	$<\tau_6$	prsmp., [46]
5	$H_3^+(v' \geqslant 2) + Ar \rightarrow ArH^+ + H_2$	10^{14}	10^{-9}	0.01	[47]
6	$H_3^+(v') + He \rightarrow H_3^+(v = 0) + He$	10^{17}	—	$<10^{-3}$	prsmp., [47, 48]
7	$H_3^+(v') + H_2 \rightarrow H_3^+(v = 0) + H_2$	10^{14}	—	10^{-3}	[49]
8, (2)	$^{p,o}H_3^+ + {}^{p,o}H_2 \rightarrow {}^{p,o}H_3^+ + {}^{p,o}H_2$	10^{14}	10^{-10}	0.01 [b]	[36]

[a] Approximately same for both directions.
[b] Strongly dependent on the plasma temperature and initial nuclear spin states.

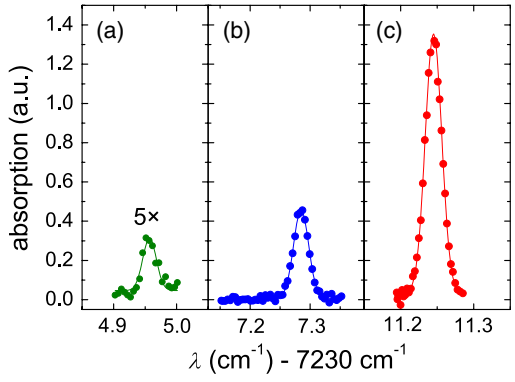

Figure 3. Doppler broadening of the monitored spectral lines in a $^nH_2$ discharge with the discharge tube immersed in LN_2. (*a*) transition $3\nu_2^1(4, 3) \leftarrow 0\nu_2^0(3, 3)$, (*b*) transition $3\nu_2^1(2, 1) \leftarrow 0\nu_2^0(1, 1)$, (*c*) transition $3\nu_2^1(2, 0) \leftarrow 0\nu_2^0(1, 0)$. The temperature evaluated from the broadening of the line corresponding to the (1,0) state is 80 ± 3 K. The mean values of temperature evaluated from all spectral lines are the same. The spectral line of the (3,3) state is multiplied by a factor of 5.

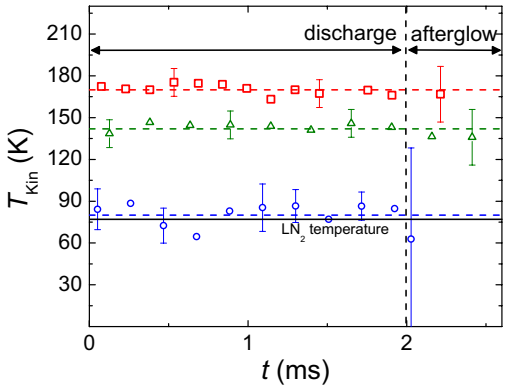

Figure 4. Evolution of kinetic temperatures for three different temperatures of the discharge tube (approximately 77, 140 and 170 K). Large errors in the early afterglow are caused by a fast decrease in the ion concentration due to the recombination with electrons. The mean values of the temperatures are shown as dashed lines. Note that data from a discharge tube cooled by LN_2 are close to the LN_2 temperature.

reaction of rotationally excited H_3^+ ions with He atoms and that this process has a higher rate than vibrational cooling. The CRDS method employed in our experimental setup should tell us whether H_3^+ ions are rotationally cooled down or not (see the discussion below).

From table 2 we can infer that mainly the ambipolar diffusion limits the lifetime of H_3^+ in the discharge. A significant fraction of H_3^+ ions have enough time to undergo rotational and vibrational cooling ($\tau_1 \approx \tau_5 > \tau_7 > \tau_6 > \tau_4$) and nuclear spin conversion (2): $\tau_8 \approx \tau_1$.

3.1. Answers to questions (Q-1)–(Q-5)

Measurements carried out to answer questions (Q-1)–(Q-5) and their results are discussed in this section.

3.1.1. (Q-1) Examination of kinetic temperature. The kinetic temperature of ions is evaluated from the Doppler broadening of the monitored transition lines given in table 1. An example of the broadening is shown in figure 3, which depicts the line profiles of all three used transitions in the $^nH_2$ discharge with the reaction area immersed in liquid nitrogen (LN_2). The value of the kinetic temperature (T_{Kin}) evaluated from the broadening of the line corresponding to the state (1,0) is 80 ± 3 K. The mean values of temperature corresponding to the other states are the same but the error is higher. In the graph, the (3,3) line is multiplied by a factor of 5 to be visible. The evaluated T_{Kin} agrees with the temperature of the discharge tube (77 K). Observations made in a $^e_mH_2$ discharge give similar results.

Figure 4 shows the evolution of T_{Kin} in the $^nH_2$ discharge and the early afterglow for three different temperatures of the tube (LN_2 temperature under standard conditions, 140 and 170 K). Data from the early afterglow are characterized by a large error because of a rapid decrease in the concentration due to the recombination. However, a significant change in T_{Kin} is not observed and the upper limit of the temperature given in the discharge seems to be preserved every time in the afterglow as well.

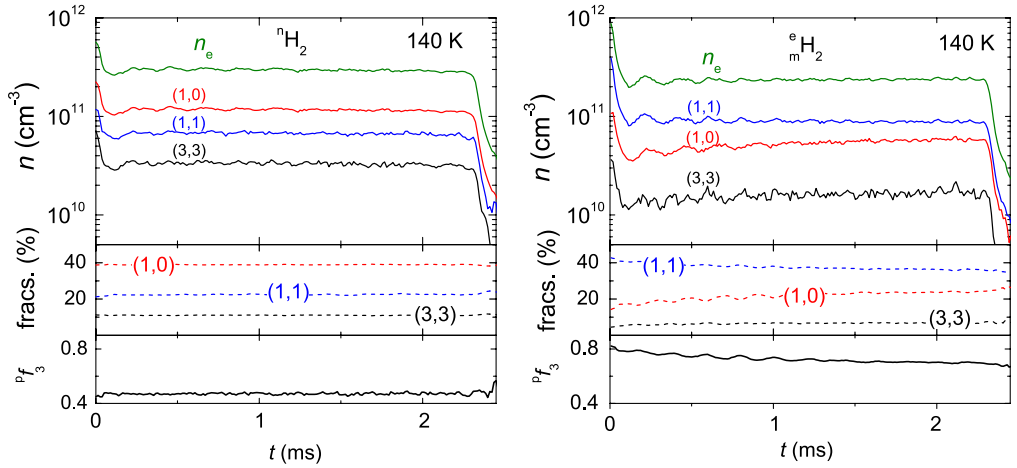

(a) discharge with $^{n}H_2$ (b) discharge with $^{e}_{m}H_2$

Figure 5. Evolution of the absolute and relative population of the states and the population of $^{p}H_3^+$ in the discharge and the early afterglow. Top panel: evolution of the concentrations of the ions in the indicated states and the corresponding electron density n_e. Middle panel: evolution of the fractions of the indicated states. Bottom panel: evolution of $^{p}f_3$.

Both figures 3 and 4 consist of data measured in the discharge with the microwave power in the range 4–8 W. During the discharge period, T_{Kin} maintains a more or less constant value, which means that collisional cooling of the translational degrees of freedom of the ions is very efficient. The agreement of T_{Kin} with the temperature of the discharge tube cooled by LN_2 allows us to take the measured T_{Kin} as a reference temperature for further experiments.

3.1.2. (Q-2) Evolution of populations of rotational states. Figure 5 shows the evolution of absolute and relative populations of the monitored states and an overall relative population $^{p}f_3$ of $^{p}H_3^+$ during the discharge and early afterglow for $^{n}H_2$ and $^{e}_{m}H_2$ discharges. These relative populations were computed by dividing the measured number density of the appropriate state by the number density of all H_3^+ ions. To calculate this overall number density, a Boltzmann distribution of rotational states was assumed. This assumption is justified later in the text (see section 3.1.3). The value of $^{p}f_3$ decreases slowly in the $^{e}_{m}H_2$ discharge, and in the $^{n}H_2$ discharge it is constant. Such a slow evolution of the value of $^{p}f_3$ towards a final constant (steady state) value observed in the $^{e}_{m}H_2$ discharge is common to all temperatures above 77 K, and it is discussed in section 3.1.4. In $^{n}H_2$ and $^{e}_{m}H_2$ discharges, the ratio of the fraction of the (1,0) state to the fraction of the (3,3) state is almost constant throughout the discharge period.

3.1.3. (Q-3) Definition of rotational temperature. In the previous section we concluded that relative populations of the rotational states within the ortho-nuclear spin manifold—states (1,0) and (3,3)—are constant (see figure 5). Most probably, this also holds for the para nuclear spin manifold. This allows us to define a rotational temperature $T_{Rot\text{-}ortho}$ based on the relative population of two ortho states. This rotational temperature is

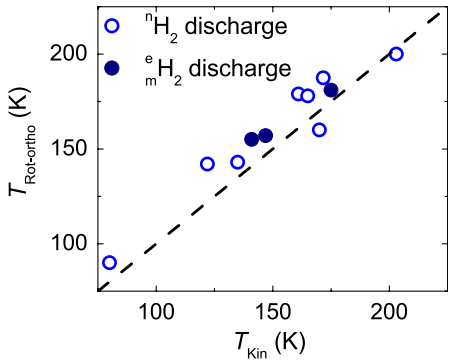

Figure 6. Comparison of the measured rotational $T_{Rot\text{-}ortho}$ and the kinetic T_{Kin} temperatures. Dashed line: $T_{Rot\text{-}ortho} = T_{Kin}$. The measurements were performed in discharges with $^{n}H_2$ and $^{e}_{m}H_2$.

compared with T_{Kin} in figure 6. Data from measurements with $^{e}_{m}H_2$ and $^{n}H_2$ are scattered along the $T_{Rot\text{-}ortho} = T_{Kin}$ line.

To examine under which conditions we can define a rotational temperature of the H_3^+ ensemble (i.e. the ensemble of $^{p}H_3^+$ ions and $^{o}H_3^+$ ions mixed together), we plot the population of rotational states against T_{Kin} for the discharge with $^{n}H_2$ and $^{e}_{m}H_2$ in figure 7 (the plotted values were measured at the end of the discharge period, $t \doteq 2$ ms). The measured populations are supplemented by lines showing the populations in thermodynamic equilibrium (TDE). We can see that populations of all three monitored states agree with the TDE values in the case of the discharge with $^{n}H_2$ despite the fact that the value of $^{p}f_2$ does not correspond to TDE (note that $^{p}f_2$ is approximately 0.5 at 77 K in TDE, while $^{p}f_2$ of $^{n}H_2$ is 0.25). The effect is clear if we redraw the data from figure 7 to show the dependence of $^{p}f_3$ on T_{Kin}, as is shown in figure 8: the fractions $^{p}f_3$ for TDE are close to the values of $^{p}f_3$ measured in the $^{n}H_2$ discharge (approximately 0.5) in the whole temperature range 75–300 K.

B.1

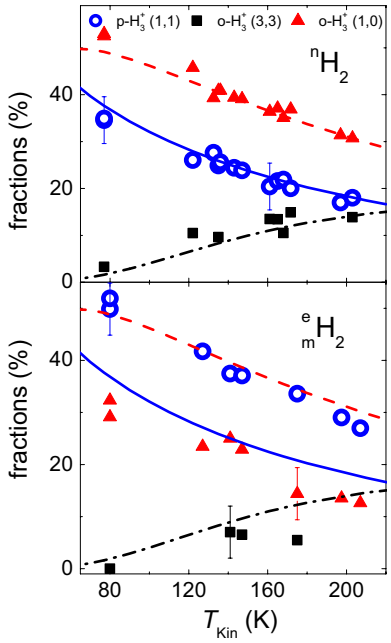

Figure 7. Dependence of the relative populations (fractions) of the monitored rotational states on T_{Kin} in the discharge with $^{\mathrm{n}}H_2$ (top panel) and with $^{\mathrm{e}}_{\mathrm{m}}H_2$ (bottom panel). Dashed lines, full lines, dashed-dotted lines: population of (1,0), (1,1) and (3,3) states corresponding to TDE, respectively. Note in the bottom panel that the measured values do not lie on the lines corresponding to TDE in the case of $^{\mathrm{e}}_{\mathrm{m}}H_2$ discharge; the fraction of $^{\mathrm{p}}H_3^+$ (1,1) (indicated by open circles) is substantially higher than the full line indicating the population at TDE.

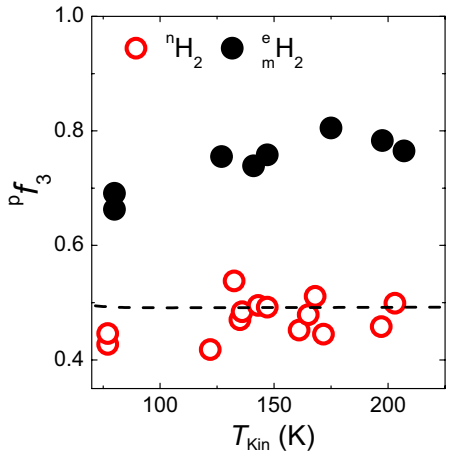

Figure 8. Measured dependence of $^{\mathrm{p}}f_3$ on T_{Kin} for the discharges with $^{\mathrm{n}}H_2$ and with $^{\mathrm{e}}_{\mathrm{m}}H_2$. Dashed line: $^{\mathrm{p}}f_3$ corresponding to TDE.

When using $^{\mathrm{e}}_{\mathrm{m}}H_2$ in the discharge, the population of the rotational states changes substantially against the values measured with $^{\mathrm{n}}H_2$ (see figure 7). The population of the states in the ortho sub-ensemble is thermalized, but the para-to-ortho ratio given by the value $^{\mathrm{p}}f_3$ is far from the TDE value (see figure 8).

Observations described in this section are useful for recombination studies. To compare the experimental recombination rate coefficients with theoretical values calculated for the distribution of the states in TDE for a temperature given in the range 77–300 K, we do not need to use $^{\mathrm{e}}H_2$ with $^{\mathrm{p}}f_2$ equal to the TDE value: the use of $^{\mathrm{n}}H_2$ is sufficient, because the resulting $^{\mathrm{p}}f_3 \approx 0.5$ is close to the value corresponding to TDE (see the dashed line in figure 8) and the rotational temperature is equilibrated with T_{Kin}.

Figures 6–8 show that it is possible to form plasmas with different values of $^{\mathrm{p}}f_3$ and with the rotational temperature defined well within each nuclear spin manifold by using H_2 with different values of $^{\mathrm{p}}f_2$ as a source gas. This is required in studies of the nuclear spin state-specific recombination of H_3^+ ions (see section 1, [28, 42])

3.1.4. (Q-4) Formation of the para–ortho steady state. The value of $^{\mathrm{p}}f_3$ in the discharge is determined by the nuclear spin selection rules of the processes (1), (2), (3*a*) and (3*b*). The evolution of $^{\mathrm{p}}f_3$ in time is given only by (2) if the value of $^{\mathrm{p}}f_2$ does not change in the discharge, i.e. if $^{\mathrm{e}}H_2$ does not convert to H_2 with a lower population of para states. This can happen because a certain amount of source $^{\mathrm{e}}H_2$ gas always stays in the discharge during the whole period, even though it is continuously supplied. In our experiments we could not observe the dependence of $^{\mathrm{p}}f_3$ on the length of the stay of the $^{\mathrm{e}}H_2$ gas in the discharge area. Moreover, data from experiments with density $[^{\mathrm{e}}_{\mathrm{m}}H_2]$ in the range from 5×10^{13} to 10^{15} cm^{-3} and with the temperature 130–210 K show that almost no dependence of $^{\mathrm{p}}f_3$ on $[^{\mathrm{e}}_{\mathrm{m}}H_2]$ exists—see figure 9. At each concentration, $^{\mathrm{p}}f_3$ from the beginning and from the end of the discharge period ('initial' and 'final value', respectively) is drawn (for an illustration of both terms, see the inset of the figure). The so-called 'nascent' fraction $^{\mathrm{p}}f_3$ originating from reaction (1) is also indicated (see also an extended discussion in [50]). The initial values are closer to the nascent values and change to the final value within the discharge period.

The slight slope of the lines fitted to data in the main frame of figure 9 seems to be an effect of temperature more than $[^{\mathrm{e}}_{\mathrm{m}}H_2]$ if we notice the error bar of $^{\mathrm{p}}f_3$ and where the mean values of data from each temperature range lie. The observation from this figure agrees with the trend of $^{\mathrm{e}}_{\mathrm{m}}H_2$ values in figure 8. Whether this effect is caused by the temperature dependence of the spin conversion reaction (2) is tested by measurements described in the next section.

3.1.5. (Q-5) Dependence of $^{\mathrm{p}}f_3$ on temperature. In the previous section we discussed figure 9 and introduced the idea that the slight slope of the line fitted to the experimental data can be caused by some temperature dependence, most probably by the temperature dependence of process (2). Such an effect can also be found in figure 8 (see the values for the discharge in $^{\mathrm{e}}_{\mathrm{m}}H_2$). To study this effect in detail we carried out measurements of the dependence of 'final' values of $^{\mathrm{p}}f_3$ on $^{\mathrm{p}}f_2$. Measurements were realized at temperatures of 77, 170 and 300 K. Data from 77 and 300 K are plotted in figure 10. The straight line marked 'nascent' shows the

B.1

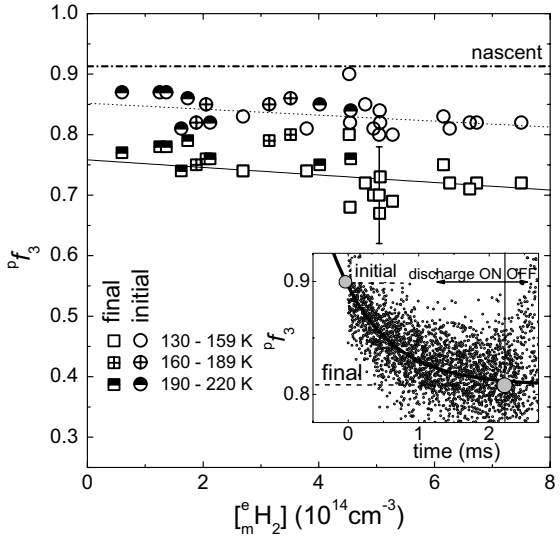

Figure 9. Dependence of the initial and final relative populations of $^pH_3^+$ on the concentration of $^e_mH_2$ in the discharge. The nascent value of $^pf_3$ originating from process (1) for $^pf_2 = 0.87$ (the value corresponding to $^e_mH_2$) is plotted by the dashed-dotted line. The inset serves as an illustration for the definition of the 'initial' and 'final' values.

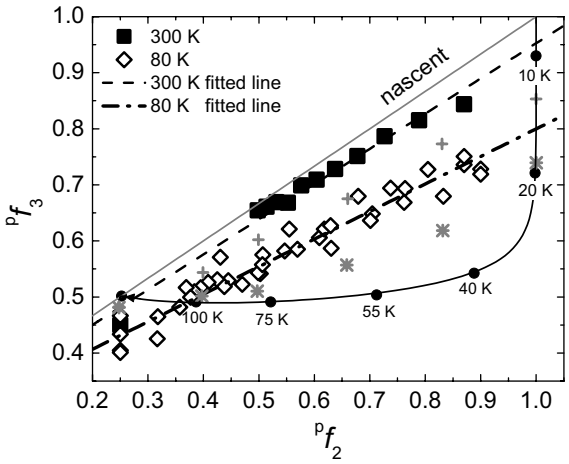

Figure 10. Dependence of the population of $^pH_3^+$ ($^pf_3$) on the para enrichment of $^eH_2$ ($^pf_2$) in experiments and TDE. Black dots: values corresponding to TDE at the indicated temperature (arrow shows the direction of rising temperature). The line marked as nascent is the population of $^pf_3$ and $^pf_2$ resulting from reaction (1) [50]. The experimental values come from measurements at 80 and 300 K. '+' and '$*$' symbols: values measured in pure H_2 discharge [29] at pressures above 400 mTorr and temperatures 300 K and 77 K, respectively.

combination of $^pf_2$ and $^pf_3$ resulting from reaction (1) [50]. The experiment at 300 K was carried out at a discharge power of 12 W, $[H_2] \approx 10^{14}$ cm^{-3} and $[Ar] = 2 \times 10^{13}$ cm^{-3}. Data from 80 K were acquired at two different discharge powers (4 and 8 W) and three different concentrations of Ar (1×10^{14}, 3×10^{14} and 1×10^{15} cm^{-3}) and $[H_2] = 2.5 \times 10^{14}$ cm^{-3}. Significant influence of the discharge power and concentration of Ar was not observed.

The black dots in figure 10 show the values of $^pf_3$ and $^pf_2$ at TDE at the indicated temperature. Experimental values of $^pf_3$ for all temperatures at $^pf_2 = 0.25$ are close to the corresponding TDE values, as was discussed in section 3.1.3. We can see that the slices of the graph for $^pf_2 = 0.25$ and $^pf_2 = 0.87$ are in agreement with figures 8 and 9. Since it was shown by figure 9 that the influence of $[^eH_2]$ is weak and all data were measured at similar values of $[^eH_2]$, we can state that we do observe an influence of temperature dependence of reaction (2) on the final $^pf_3$ in the graph, i.e. $^pf_3 = {}^pf_3(^pf_2, T_{Kin})$.

The experimental data in figure 10 resemble those from a recently published paper of the McCall group on the nuclear spin selection rules of reaction (2) [29]. Their data are also plotted in the figure (+ and $*$ symbols). Unlike in the case of the McCall group data, the dependence of $^pf_3$ on $^pf_2$ measured by us is linear, not convex. This difference is probably due to the H_2 concentration: in our case, $[H_2]$ is 100 times lower [29] and almost no H_5^+ ions are formed [51]. Therefore, the nuclear spin conversion processes within the H_3^+ ensemble can be described much more simply in our experiment. However, further discussion about figure 10 with respect to the nuclear spin selection rules of process (2) is beyond the scope of this paper.

4. Conclusion

We tracked the population of three of the lowest rotational states of H_3^+ ions (corresponding to one para nuclear spin state and two ortho states) in a H_3^+-dominated microwave discharge plasma and the early afterglow plasma by cavity ring-down spectroscopy (CRDS). The relative population of $^pH_3^+$ ($^pf_3$) was varied by using $^nH_2$ or $^eH_2$. We characterized the properties of the ensemble of H_3^+ ions by the kinetic and rotational temperatures and the relative population of para nuclear spin states ($^pf_3$). The following conclusions were drawn for the considered experimental conditions:

- the ensemble of H_3^+ ions in the plasma has a stable kinetic temperature equalling the temperature of the discharge tube;
- the rotational temperature can be determined from the relative population of the two ortho states and it is equal to the kinetic temperature, i.e. $T_{Rot\text{-}ortho} = T_{Kin}$;
- the population of H_3^+ in the para states is given by the population of the para states of H_2 and the temperature of the system, i.e. $^pf_3$ is a function of $^pf_2$ and T_{Kin};
- a steady-state population of para-H_3^+ is reached in our discharge plasma.

These conclusions confirm our previous assumptions that our measurements of H_3^+ recombination rate coefficients performed with a He–Ar–$^nH_2$ afterglow plasma ([26–28, 42], i.e. under experimental conditions similar to those described in this paper) give values close to those in TDE.

Acknowledgments

This work is a part of the research plan MSM 0021620834 and grant OC10046 financed by the Ministry of Education of the Czech Republic and was partly supported by GACR (202/07/0495, 202/08/H057, 205/09/1183, 202/09/0642), by GAUK 92410, GAUK 353811, GAUK 54010 and by COST Action CM0805 (The Chemical Cosmos). The authors would like to thank Mgr. Mojmír Jílek for the design of the para-H_2 generator and RNDr. Jan Lang, PhD, for NMR experiments.

References

[1] Herbst E 2000 The astrochemistry of H_3^+ *Phil. Trans. R. Soc. Lond.* A **358** 2523–34
[2] Geballe T R and Oka T 1996 Detection of H_3^+ in interstellar space *Nature* **384** 334
[3] McCall B J, Geballe T R, Hinkle K H and Oka T 1998 Detection of H_3^+ in the diffuse interstellar medium toward Cygnus OB2 No. 12 *Science* **279** 1910–13
[4] Trafton L, Lester D F and Thompson K L 1989 Unidentified emission lines in Jupiter's northern and southern 2 micron aurorae *Astrophys. J.* **343** 73–6
[5] Miller S *et al* 2000 The role of H_3^+ in planetary atmospheres *Phil. Trans. R. Soc. Lond.* A **358** 2485–502
[6] des Forêts G P and Roueff E 2000 H_3^+ recombination and bistability in the interstellar medium *Phil. Trans. R. Soc. Lond.* A **358** 2549–59
[7] Le Petit F, Roueff E and Herbst E 2004 H_3^+ and other species in the diffuse cloud towards ζ Persei: a new detailed model *Astron. Astrophys.* **417** 993–1002
[8] Leu M T, Biondi M A and Johnsen R 1973 Measurements of recombination of electrons with H_3^+ and H_5^+ ions *Phys. Rev.* A **8** 413
[9] Adams N G, Smith D and Alge E 1984 Measurements of dissociative recombination coefficients of H_3^+, HCO^+, N_2H^+, and CH_5^+ at 95 and 300 K using the FALP apparatus *J. Chem. Phys.* **81** 1778
[10] Larsson M and Orel A 2008 *Dissociative Recombination of Molecular Ions* (Cambridge: Cambridge University Press)
[11] Oka T 2000 Introductory remarks *Phil. Trans. R. Soc. Lond.* A **358** 2363–9
[12] Johnsen R 2005 A critical review of H_3^+ recombination studies *J. Phys.: Conf. Ser.* **4** 83
[13] Smith D and Španěl P 1993 Dissociative recombination of H_3^+ and some other interstellar ions: a controversy resolved *Int. J. Mass Spectrom. Ion Processes* **129** 163–82
[14] Amano T 1990 The dissociative recombination rate coefficients of H_3^+, HN_2^+, and HCO^+ *J. Chem. Phys.* **92** 6492–501
[15] Plašil R *et al* 2002 Advanced integrated stationary afterglow method for experimental study of recombination of processes of H_3^+ and D_3^+ ions with electrons *Int. J. Mass Spectrom.* **218** 105–30
[16] Laubé S *et al* 1998 New FALP-MS measurements of H_3^+, D_3^+ and HCO^+ dissociative recombination *J. Phys. B: At. Mol. Opt. Phys.* **31** 2111
[17] Kreckel H *et al* 2005 High-resolution dissociative recombination of cold H_3^+ and first evidence for nuclear spin effects *Phys. Rev. Lett.* **95** 263201
[18] McCall B J *et al* 2003 An enhanced cosmic-ray flux towards zeta persei inferred from a laboratory study of the H_3^+-e^- recombination rate *Nature* **422** 500
[19] Petrignani A *et al* 2009 Spectroscopy and dissociative recombination of the lowest rotational states of H_3^+ *J. Phys.: Conf. Ser.* **192** 012022
[20] Tom B A *et al* 2009 Dissociative recombination of highly enriched para-H_3^+ *J. Chem. Phys.* **130** 031101
[21] Kokoouline V, Greene C H and Esry B D 2001 Mechanism for the destruction of H_3^+ ions by electron impact *Nature* **412** 891
[22] Kokoouline V and Greene C H 2003 Unified theoretical treatment of dissociative recombination of D_{3h} triatomic ions: application to H_3^+ and D_3^+ *Phys. Rev.* A **68** 012703
[23] dos Santos S F, Kokoouline V and Greene C H 2007 Dissociative recombination of H_3^+ in the ground and excited vibrational states *J. Chem. Phys.* **127** 124309
[24] Pagani L *et al* 2009 Chemical modeling of L183 (= L134N) : an estimate of the ortho/para H_2 ratio *Astron. Astrophys.* **494** 623
[25] Petrignani A *et al* 2011 Resonant structure of low-energy H_3^+ dissociative recombination *Phys. Rev.* A **83** 032711
[26] Glosík J *et al* 2008 Recombination of H_3^+ ions in the afterglow of a He/Ar/H_2 plasma *J. Phys. B: At. Mol. Opt. Phys.* **41** 191001
[27] Glosík J *et al* 2009 Temperature dependence of binary and ternary recombination of H_3^+ ions with electrons *Phys. Rev.* A **79** 052707
[28] Varju J, Hejduk M, Dohnal P, Jílek M, Kotrík T, Plašil R, Gerlich D and Glosík J 2011 Nuclear spin effect on recombination of H_3^+ ions with electrons at 77 K *Phys. Rev. Lett.* **106** 203201
[29] Crabtree K N, Kauffman C A, Tom B A, Becka E, McGuire B A and McCall B J 2011 Nuclear spin dependence of the reaction of H_3^+ with H_2: II. Experimental measurements *J. Chem. Phys.* **134** 194311
[30] Macko P *et al* 2004 Afterglow studies of $H_3^+(v = 0)$ recombination using time resolved cw-diode laser cavity ring-down spectroscopy *Int. J. Mass Spectrom* **233** 299–304
[31] Glosík J, Novotný O, Pysanenko A, Zakouril P, Plašil R, Kudrna P and Poterya V 2003 The recombination of H_3^+ and H_5^+ ions with electrons in hydrogen plasma: dependence on temperature and on pressure of H_2 *Plasma Sources Sci. Technol.* **12** S117–22
[32] Poterya V *et al* 2002 Recombination of D_3^+ ions in the afterglow of a He–Ar–D_2 plasma *Phys. Rev. Lett.* **88** 044802
[33] Quack M 1977 Detailed symmetry selection rules for reactive collisions *Mol. Phys.* **34** 477–504
[34] Cordonnier M *et al* 2000 Selection rules for nuclear spin modifications in ion–neutral reactions involving H_3^+ *J. Chem. Phys.* **113** 3181–93
[35] Oka T 2004 Nuclear spin selection rules in chemical reactions by angular momentum algebra *J. Mol. Spectrosc.* **228** 635–9
[36] Park K and Light J C 2007 Microcanonical statistical study of ortho–para conversion in the reaction $H_3^+ + H_2 \rightarrow (H_5^+)^* \rightarrow H_3^+ + H_2$ at very low energies *J. Chem. Phys.* **126** 044305
[37] Hugo E, Asvany O and Schlemmer S 2009 $H_3^+ + H_2$ isotopic system at low temperatures: microcanonical and experimental study *J. Chem. Phys.* **130** 164302
[38] O'Keefe A and Deacon D A G 1988 Cavity ring-down optical spectrometer for absorption measurements using pulsed laser sources *Rev. Sci. Instrum.* **59** 2544–51
[39] Hlavenka P *et al* 2006 Near infrared second overtone cw-cavity ringdown spectroscopy of D_2H^+ ions *Int. J. Mass Spectrom.* **255–256** 170–6
[40] Romanini D, Kachanov A A and Stoeckel F 1997 Diode laser cavity ring down spectroscopy *Chem. Phys. Lett.* **270** 538–45
[41] Lindsay C M and McCall B J 2001 Comprehensive evaluation and compilation of H_3^+ spectroscopy *J. Mol. Spectrosc.* **210** 60–83
[42] Varju J *et al* 2010 Application of NIR-CRDS for state selective study of recombination of para and ortho H_3^+ ions with

electrons in low temperature plasma *J. Phys.: Conf. Ser.* **227** 012026
[43] Kotrík T, Dohnal P, Roučka Š, Jusko P, Plašil R, Glosík J and Johnsen R 2011 Collisional-radiative recombination $Ar^+ + e + e$: experimental study at 77–180 K *Phys. Rev.* A **83** 032720
[44] Lindinger W and Albritton D L 1975 Mobilities of various mass-identified positive ions in helium and argon *J. Chem. Phys.* **62** 3517–22
[45] Kokoouline V, Faure A, Tennyson J and Greene C H 2010 Calculation of rate constants for vibrational and rotational excitation of the H_3^+ ion by electron impact *Mon. Not. R. Astron. Soc.* **405** 1195–1202
[46] McCall B J *et al* 2004 Dissociative recombination of rotationally cold H_3^+ *Phys. Rev.* A **70** 052716
[47] Mikosch J, Kreckel H, Wester R, Plašil R, Glosík J, Gerlich D, Schwalm D and Wolf A 2004 Action spectroscopy and temperature diagnostics of H_3^+ by chemical probing *J. Chem. Phys.* **121** 11030–7
[48] Ferguson E E 1986 Vibrational quenching of small molecular ions in neutral collisions *J. Phys. Chem.* **90** 731–8
[49] Yousif F B, Hinojosa G, de Urquijo J, Cisneros C and Alvarez I 1997 Generation of an H_3^+ ($v = 0$) beam and its diagnosis from the observation of its polar dissociation in collision with He *Int. J. Mass. Spectrom.* **171** 127–34
[50] Crabtree K N, Indriolo N, Kreckel H, Tom B A and McCall B J 2011 On the ortho:para ratio of H_3^+ in diffuse molecular clouds *Astrophys. J.* **729** 15
[51] Crabtree K N, Tom B A and McCall B J 2011 Nuclear spin dependence of the reaction of H_3^+ with H_2. I. Kinetics and modeling *J. Chem. Phys.* **134** 194310

B.1

B.2 Binary and ternary recombination of para-H_3^+ and ortho-H_3^+ with electrons: State selective study at 77–200 K

P. Dohnal, M. Hejduk, J. Varju, P. Rubovič, Š. Roučka, T. Kotrík, R. Plašil, J. Glosík and R. Johnsen, *The Journal of Chemical Physics*, 136(24), 2012. doi:10.1063/1.4730162.

Binary and ternary recombination of para-H_3^+ and ortho-H_3^+ with electrons: State selective study at 77–200 K

Petr Dohnal,[1] Michal Hejduk,[1] Jozef Varju,[1] Peter Rubovič,[1] Štěpán Roučka,[1] Tomáš Kotrík,[1] Radek Plašil,[1] Juraj Glosík,[1] and Rainer Johnsen[2]
[1]*Department of Surface and Plasma Science, Faculty of Mathematics and Physics, Charles University, Prague 18000, Czech Republic*
[2]*Department of Physics and Astronomy, University of Pittsburgh, Pittsburgh, Pennsylvania 15260, USA*

(Received 13 April 2012; accepted 1 June 2012; published online 26 June 2012)

Measurements in H_3^+ afterglow plasmas with spectroscopically determined relative abundances of H_3^+ ions in the para-nuclear and ortho-nuclear spin states provide clear evidence that at low temperatures (77–200 K) para-H_3^+ ions recombine significantly faster with electrons than ions in the ortho state, in agreement with a recent theoretical prediction. The cavity ring-down absorption spectroscopy used here provides an *in situ* determination of the para/ortho abundance ratio and yields additional information on the translational and rotational temperatures of the recombining ions. The results show that H_3^+ recombination with electrons occurs by both binary recombination and third-body (helium) assisted recombination, and that both the two-body and three-body rate coefficients depend on the nuclear spin states. Electron-stabilized (collisional-radiative) recombination appears to make only a small contribution. © *2012 American Institute of Physics*. [http://dx.doi.org/10.1063/1.4730162]

I. INTRODUCTION

The present experiments were motivated by the fundamental character of the recombination of H_3^+ ions,[1] its relevance to modeling of astrophysical diffuse clouds,[2] and electrical discharges in hydrogen. In cold diffuse clouds (temperatures from 50 to 100 K), H_3^+ ions are formed by cosmic-ray ionization of H_2, followed by the reaction $H_2^+ + H_2 \rightarrow H_3^+ + H$.[3] The H_3^+ ions subsequently either recombine by dissociative recombination (DR) with electrons or transfer protons to other atoms or molecules.[4] The recombination of H_3^+ ions competes with the rate of molecule formation in diffuse clouds and plays a pivotal role in the chemical evolution. Even though H_3^+ is the "simplest" triatomic ion, its recombination is a rather subtle process that has challenged theorists and experimentalists for many years. It has become clear in recent years that the ortho-modifications and para-modifications of H_3^+, distinguished by their nuclear spins and allowed rotational states, may recombine differently at low temperatures. The experiments described in this paper focus on this question. Unlike other previous experiments, they incorporate *in situ* spectroscopic identification of the recombining ion species in the recombining medium.

The spin dependence of H_3^+ recombination also plays a role in the interpretation of spectra observed in astrophysical clouds. For instance, a recent analysis by Crabtree *et al.*[5] of several diffuse molecular clouds suggests that the observed differences between the rotational excitation temperatures of H_2 and H_3^+ (denoted as $T_{(01)}(H_2)$ and $T(H_3^+)$) can be explained by a kinetic model that includes both reactive collisions of H_3^+ or para-H_3^+ with H_2 and recombination with electrons. The model makes specific allowance for the dependence of all relevant reaction rates on the ortho/para states of both H_2 and H_3^+. Surprisingly, reasonable agreement between observed and calculated excitation temperatures was found only when the DR rate coefficients of para-H_3^+ (nuclear spin $I = 1/2$) and H_3^+ (nuclear spin $I = 3/2$) were assumed to be nearly equal, which, however, is in conflict with the theoretical prediction[6] that the low-temperature DR rate coefficient of para-H_3^+ is considerably larger than that of H_3^+.

The history of H_3^+ recombination studies has been extensively covered in a number of reviews[7–12] and in the book by Larsson and Orel.[13] Many of the once puzzling disagreements among measured recombination coefficients have either been resolved or can be rationalized by invoking third-body stabilized recombination processes that occur in plasmas but not in beam-type experiments. Also, earlier serious discrepancies between experimental results and theory were largely resolved in 2001 when it was shown that the Jahn–Teller mechanism can account for the observed magnitude of dissociative recombination rates of H_3^+ ions.[14] Subsequent improvements of the theory[15] yielded a thermal rate coefficient of the dissociative recombination at 300 K of $\alpha_{DR} = 5.6 \times 10^{-8}$ cm^{3}s^{-1} which comes close to the magnitude of many experimental values. Theoretical predictions also agree quite well with the temperature dependence of the thermal rate coefficients inferred from ion-storage-rings (ISR) experiments. The more recent ISR studies employed ion sources specifically designed to produce rotationally cold ions ("cold ion sources")[16–18] and the results supported the theoretical thermal rate coefficients.[19] At that time it appeared that a satisfactory solution to the "H_3^+ enigma," the often-cited term coined by Bates *et al.* in 1993,[20] had been found. However, it proved difficult to verify experimentally that the H_3^+ ions circulating in the storage rings were truly rotationally cold

and this problem has not been entirely solved. It had been assumed that the "cold" rotational distributions inferred from spectroscopic observations in the ion source survived extraction into the storage ring and were not altered further in the ring, but recent experiments using high-resolution storage-rings indicate that these assumptions were not necessarily correct.[21,22] The problem awaits clarification by further experiments. Also, high-resolution storage rings data exhibit resonances at particular collision energies that have not been clearly assigned to specific recombination paths and are not predicted by theory.[22] Thus, a truly satisfactory convergence of theory and experiment has not been achieved. Petrignani *et al.*[22] summed up the current situation of storage-ring experiments: *"Presently no rate coefficient measurement with a confirmed temperature below 300 K exists."* Plasma afterglow measurements at reduced temperatures have been made, but those, as will be discussed later, have their own set of complications. Paraphrasing Bates *et al.*[20] and Larsson *et al.*,[19] we can sum up the state of the art today in the words: *"... the saga of the* H_3^+ *enigma continues...."*

Recent theoretical calculations[6] predict that the low-temperature DR rate coefficients for para-H_3^+ are larger than those for H_3^+ ions, by a factor of about ten at temperatures below 10 K. This prediction has been qualitatively confirmed at low electron-ion collision energies in storage-ring experiments using para-enriched H_3^+,[17,23] but, as has been mentioned before, the actual para/ortho abundance ratio of the recombining ions was not experimentally verified. This problem, of course, is closely linked to that of the rotational populations. Further progress will require direct *in situ* determination of the para/ortho ratio and rotational excitation of the stored H_3^+ ions. Experimental photodissociation measurements on H_3^+ ions in the ring may be one feasible approach (see discussion in Refs. 24 and 25).

The experiments described here make use of the plasma afterglow technique but add spectroscopic capabilities. Here, the ion densities are many orders of magnitude larger than those in storage rings which enables *in situ* spectroscopic absorption measurements of rotational populations of H_3^+ ions under recombination-controlled conditions. The feasibility of such experiments was demonstrated by us in a recent study in which we measured binary recombination rate coefficients for para-H_3^+ and ortho-H_3^+ ions ($^{p}\alpha_{bin}$ and $^{o}\alpha_{bin}$) at buffer gas temperature ~77 K.[26,27] The present study extends this work and provides recombination rate coefficients for pure para-H_3^+ and pure ortho-H_3^+ over a wider range of temperatures from 77 K to 200 K. As before, the experiments were carried out in a stationary afterglow (SA) in conjunction with a near-infrared cavity-ring-down absorption spectrometer (NIR–CRDS) for direct *in situ* determination of the kinetic temperature, the rotational temperature, and the spin states of the ions.

In a SA experiment[28] electrons and ions undergo multiple collisions with buffer gas atoms (here He and Ar) and reagent molecules (here H_2) prior to their recombination. The early phase of the afterglow is dominated by ion-formation and ion-conversion reactions, electron thermalization, and equilibration of internal degrees of freedom of the ions. Ideally, this early phase should be completed rapidly so that the only relevant processes during the recombination phase are binary electron-ion recombination and ambipolar diffusion of ions and electrons. However, the neutral constituents (He, H_2, and Ar in our case) and ambient electrons and ions can affect the overall recombination process as well as the para/ortho ratio and this requires careful consideration. There are two known ternary recombination processes that contribute to the plasma decay, ternary neutral-assisted recombination (largely due to the helium buffer),[29] and ternary electron-assisted collisional radiative recombination (CRR).[30–32] We have recently studied the ternary helium-assisted recombination of H_3^+ and D_3^+ ions with electrons at conditions similar to those of the present experiments[8,33–37] and found that H_3^+ ions recombine by both the binary process with rate coefficient α_{bin} and by ternary ("He-assisted") process with ternary rate coefficient K_{He}. The observed plasma decay yields an "effective" rate coefficient α_{eff} given by the sum $\alpha_{eff} = \alpha_{bin} + K_{He}[He]$ that can be decomposed into its parts by measuring the dependence of α_{eff} on helium density [He].

The role of electron-assisted CRR is less clear because experimental data and theoretical calculations exist only for atomic ions but not for molecular ions. For atomic ions the predicted very strong negative temperature dependence, $\alpha_{CRR} \sim n_e T^{-4.5}$, of the CRR rate coefficient, has been confirmed for temperatures above 300 K,[30,38,39] and recently also for Ar^+ ions at temperatures below 300 K.[32,40] In low-temperature plasmas most molecular ions are removed by fast dissociative recombination (see, e.g., book by Larsson and Orel[13]) and the contribution from collisional radiative recombination is usually negligible. However, at temperatures approaching 77 K the effective binary rate of CRR (Refs. 38 and 39) becomes comparable to typical DR rate coefficients for electron densities $>10^{10}$ cm^{-3}. Somewhat surprisingly, the H_3^+ afterglow studies of Amano[41,42] at gas temperatures near 77 K and electron densities $>10^{11}$ cm^{-3} seemed to indicate that CRR did not play a significant role. However, as Bates[20] pointed out, the occurrence of CRR is "inevitable," and to make matters worse, the observed plasma decay due to CRR can give the appearance of binary recombination since the energy released by CRR can lead to a time-dependent electron temperature. A quantitative re-analysis of Amano's experiments is beyond the scope of this paper. It is far from obvious that CRR made only a negligible contribution. It is also difficult to accept the author's conclusion that clustering of H_3^+ to form fast recombining H_5^+ ions was entirely absent.

In our flowing afterglow (FA, FALP (Ref. 34)) and stationary afterglow (SA (Refs. 26 and 43)) experiments we can measure at gas temperatures close to 77 K and cover a wide range of electron and ion densities, from 10^8 to 10^{11} cm^{-3}. This makes it possible to separate binary and helium-assisted ternary recombination of H_3^+ ions from CRR. We will conclude (see Appendix) that CRR may have a slight effect at the lowest temperature (77 K), but most likely it is completely negligible at higher temperatures.

II. EXPERIMENTAL METHODS

The basic methods of measuring recombination rates in afterglow plasmas are well known and will not be

discussed here in great detail. This section focuses on the interconversion processes between para-H_3^+ and ortho-H_3^+ ions, and their recombination. Technical details of the experiments will be presented in Sec. III.

A. Afterglow processes in para-H_3^+ and ortho-H_3^+ dominated plasma

In the following upper left indices p, o, n, and e denote "para," "ortho," "normal," and "para-enriched" hydrogen (e.g., ${}^{\mathrm{p}}H_2$, ${}^{\mathrm{o}}H_2$, ${}^{\mathrm{n}}H_2$, and ${}^{\mathrm{e}}H_2$) and ${}^{\mathrm{p}}f_2$ and ${}^{\mathrm{o}}f_2$ denote their fractions. Para-H_3^+ and ortho-H_3^+ ions denote ${}^{\mathrm{p}}H_3^+$ and ${}^{\mathrm{o}}H_3^+$, while ${}^{\mathrm{p}}f_3$ and ${}^{\mathrm{o}}f_3$ stand for their fractions (i.e., ${}^{\mathrm{p}}f_3 = [{}^{\mathrm{p}}H_3^+]/[H_3^+]$ and ${}^{\mathrm{o}}f_3 = [{}^{\mathrm{o}}H_3^+]/[H_3^+]$ with ${}^{\mathrm{p}}f_3 + {}^{\mathrm{o}}f_3 = 1$). Absence of an index implies that the spin modification is not specified.

In a low-temperature afterglow plasma in a gas mixture of helium (the "buffer gas") with small additions of argon and hydrogen the principal processes affecting the densities of ${}^{\mathrm{p}}H_3^+$ and ${}^{\mathrm{o}}H_3^+$ are recombination, ambipolar diffusion, para/ortho conversion in reactions with H_2, and formation of H_5^+ in ternary association, i.e.:

$$ {}^{\mathrm{p}}H_3^+ + e^- \xrightarrow{{}^{\mathrm{p}}\alpha_{\mathrm{eff}}} \text{neutral products}, \tag{1a} $$

$$ {}^{\mathrm{o}}H_3^+ + e^- \xrightarrow{{}^{\mathrm{o}}\alpha_{\mathrm{eff}}} \text{neutral products}, \tag{1b} $$

$$ {}^{\mathrm{p}}H_3^+ + H_2 \xrightarrow{\nu_{\mathrm{po}}} {}^{\mathrm{o}}H_3^+ + H_2, \tag{1c} $$

$$ {}^{\mathrm{o}}H_3^+ + H_2 \xrightarrow{\nu_{\mathrm{op}}} {}^{\mathrm{p}}H_3^+ + H_2, \tag{1d} $$

$$ {}^{\mathrm{p}}H_3^+ + H_2 + He \xrightarrow{{}^{\mathrm{p}}\tau_{\mathrm{R}}} H_5^+ + He, \tag{1e} $$

$$ {}^{\mathrm{o}}H_3^+ + H_2 + He \xrightarrow{{}^{\mathrm{o}}\tau_{\mathrm{R}}} H_5^+ + He, \tag{1f} $$

where ${}^{\mathrm{p}}\alpha_{\mathrm{eff}}$ and ${}^{\mathrm{o}}\alpha_{\mathrm{eff}}$ stand for effective (apparent binary) recombination rate coefficients of pure para-H_3^+ and pure ortho-H_3^+ ions, respectively. ν_{po} and ν_{op} are the frequencies of para-H_3^+/ortho-H_3^+ conversion due to reactions with H_2. The spin state of the neutral hydrogen molecule in reactions (1c) and (1d) will change also, but because the neutral hydrogen is far more abundant than the ions, the resulting change in ${}^{\mathrm{p}}f_2$ can be neglected. ${}^{\mathrm{p}}\tau_{\mathrm{R}}$ and ${}^{\mathrm{o}}\tau_{\mathrm{R}}$ are time constants for ternary association, later we will assume that ${}^{\mathrm{p}}\tau_{\mathrm{R}} = {}^{\mathrm{o}}\tau_{\mathrm{R}}$ for simplification. The continuity equations for the ion densities $[{}^{\mathrm{p}}H_3^+]$ and $[{}^{\mathrm{o}}H_3^+]$ during the afterglow are:

$$ \frac{\mathrm{d}[{}^{\mathrm{p}}H_3^+]}{\mathrm{d}t} = -{}^{\mathrm{p}}\alpha_{\mathrm{eff}}[{}^{\mathrm{p}}H_3^+]n_{\mathrm{e}} - \frac{[{}^{\mathrm{p}}H_3^+]}{\tau_{\mathrm{D}}} - \nu_{\mathrm{po}}[{}^{\mathrm{p}}H_3^+] + \nu_{\mathrm{op}}[{}^{\mathrm{o}}H_3^+] - \frac{[{}^{\mathrm{p}}H_3^+]}{{}^{\mathrm{p}}\tau_{\mathrm{R}}}, \tag{2} $$

$$ \frac{\mathrm{d}[{}^{\mathrm{o}}H_3^+]}{\mathrm{d}t} = -{}^{\mathrm{o}}\alpha_{\mathrm{eff}}[{}^{\mathrm{o}}H_3^+]n_{\mathrm{e}} - \frac{[{}^{\mathrm{o}}H_3^+]}{\tau_{\mathrm{D}}} + \nu_{\mathrm{po}}[{}^{\mathrm{p}}H_3^+] - \nu_{\mathrm{op}}[{}^{\mathrm{o}}H_3^+] - \frac{[{}^{\mathrm{o}}H_3^+]}{{}^{\mathrm{o}}\tau_{\mathrm{R}}}, \tag{3} $$

where n_{e} is electron density and τ_{D} is the time constant for ambipolar diffusion, assumed to be equal for both spin modification of H_3^+. Three-body association of H_3^+ with H_2 to form H_5^+ is at the hydrogen and helium densities used in the present experiments relatively slow in comparison with the rate of the recombination (for details see Refs. 9, 34, and 44) and we can conclude $[H_5^+] \ll [H_3^+]$. Assuming that the plasma is quasineutral and that it contains no ions other than H_3^+ (i.e., $n_{\mathrm{e}} = [{}^{\mathrm{p}}H_3^+] + [{}^{\mathrm{o}}H_3^+]$), the continuity equation for the electron density (obtained by summing Eqs. (2) and (3)) becomes

$$ \frac{\mathrm{d}n_{\mathrm{e}}}{\mathrm{d}t} = -({}^{\mathrm{p}}f_3\,{}^{\mathrm{p}}\alpha_{\mathrm{eff}} + {}^{\mathrm{o}}f_3\,{}^{\mathrm{o}}\alpha_{\mathrm{eff}})n_{\mathrm{e}}^2 - \frac{n_{\mathrm{e}}}{\tau_{\mathrm{D}}} - \frac{n_{\mathrm{e}}}{\tau_{\mathrm{R}}}. \tag{4a} $$

The experimental data (see Sec. V) show that the fractions ${}^{\mathrm{p}}f_3$ and ${}^{\mathrm{o}}f_3$ are nearly constant during the afterglow. This implies that the para/ortho ratio is maintained by reactions (1c) and (1d) on a time scale that is short compared to the recombination time scale. In that case, one can define an overall effective (apparent binary) recombination rate coefficient for a given mixture of ortho and para ions by $\alpha_{\mathrm{eff}} = {}^{\mathrm{p}}f_3\,{}^{\mathrm{p}}\alpha_{\mathrm{eff}} + {}^{\mathrm{o}}f_3\,{}^{\mathrm{o}}\alpha_{\mathrm{eff}}$. Equation (4a) then simplifies to

$$ \frac{\mathrm{d}n_{\mathrm{e}}}{\mathrm{d}t} = -\alpha_{\mathrm{eff}}n_{\mathrm{e}}^2 - \frac{n_{\mathrm{e}}}{\tau_{\mathrm{L}}}, \tag{4b} $$

where $1/\tau_{\mathrm{L}} = 1/\tau_{\mathrm{D}} + 1/\tau_{\mathrm{R}}$. The time constant τ_{L} characterizes losses due to diffusion and reactions (1e) and (1f).

A measurement of α_{eff} for two or more different values of ${}^{\mathrm{p}}f_3$, but under otherwise identical conditions (temperature and density of He and H_2), then permits a determination of the individual recombination rate coefficients ${}^{\mathrm{p}}\alpha_{\mathrm{eff}}$ and ${}^{\mathrm{o}}\alpha_{\mathrm{eff}}$. These rate coefficients still do not necessarily represent purely binary recombination. In earlier work we observed that H_3^+ recombination in low-temperature (<300 K) helium-buffered afterglows occurs not only by binary recombination but also by ternary helium-assisted recombination.[8,33,34,36] In those studies ${}^{\mathrm{n}}H_2$ was used as a precursor gas to form H_3^+. It was then found that the effective recombination coefficient α_{eff} varies linearly with helium density [He], i.e.,

$$ \alpha_{\mathrm{eff}}(T, [\mathrm{He}]) = \alpha_{\mathrm{bin}}(T) + K_{\mathrm{He}}[\mathrm{He}], \tag{5} $$

where α_{bin} and K_{He} are the binary and ternary recombination rate coefficients. Previous experiments at 77 K (Ref. 27) showed that the same linear relation holds for the state-selected effective recombination rate coefficients ${}^{\mathrm{p}}\alpha_{\mathrm{eff}}$ and ${}^{\mathrm{o}}\alpha_{\mathrm{eff}}$. Hence, least-square fits to data of α_{eff} as a function of the helium density for two different values of ${}^{\mathrm{p}}f_3$ can be analyzed to obtain α_{bin} and K_{He} for each of the two spin states of H_3^+.

In experiment, ${}^{\mathrm{p}}f_3$ can be enhanced from about 0.5 to 0.8 by substituting para-enriched hydrogen for normal hydrogen. This was tested by a preliminary set of experiments, to be discussed next. Technical details of the para H_2 generator and the optical absorption measurements will be presented in Sec. III.

B.2

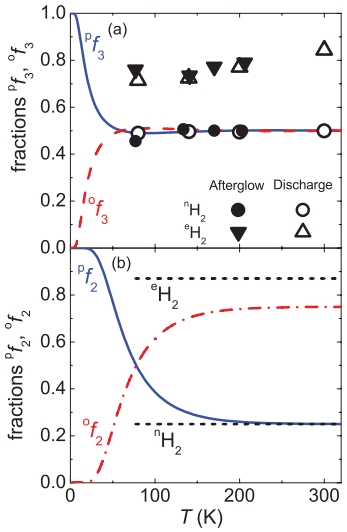

FIG. 1. Panel (a): Calculated temperature variation of the fractions $^{p}f_3$ and $^{o}f_3$ in thermal equilibrium, compared to measured values of $^{p}f_3$ during the discharge phase (open triangles) and during the afterglow (closed circles and triangles) in experiments with either $^{n}H_2$ or $^{e}H_2$. Panel (b): Calculated thermal-equilibrium fractions $^{p}f_2$ and $^{o}f_2$. The dashed horizontal lines indicate the values of $^{p}f_2$ in experiments with either $^{n}H_2$ or $^{e}H_2$ (measured by NMR).

B. Method of controlling the relative abundance of para-H_3^+ and ortho-H_3^+

In the experiment, normal $^{n}H_2$ is obtained by cooling normal hydrogen from 300 K to lower temperatures without ortho–para conversion, i.e., in a container without a catalyst. Hence, $^{n}H_2$ will have fraction $^{p}f_2 = 1/4$ and $^{o}f_2 = 3/4$. Para-enriched H_2 is produced by cooling normal hydrogen to cryogenic temperatures in the presence of a catalyst and then letting it warm up without the catalyst to the desired temperature. Our experiments confirmed earlier findings that an increase of $^{p}f_3$ in hydrogen discharges can be achieved by using $^{e}H_2$ instead of $^{n}H_2$ (see, e.g., Refs. 45 and 46), and that the increase of $^{p}f_3$ observed during the microwave discharge persists into afterglow phase.[26,27,43]

Figure 1 shows the equilibrium values $^{p}f_3$ and $^{o}f_3$ and $^{p}f_2$ and $^{o}f_2$ for temperatures from 0 to 300 K, calculated using published energy levels.[47,48] The same graph shows our experimental values of $^{p}f_3$ and $^{o}f_3$. In normal H_2 measured $^{p}f_3$ approach 0.5 at temperatures above ∼77 K, this is the value corresponding to thermal equilibrium at these temperatures. When para-enriched H_2 is used, measured $^{p}f_3$ becomes significantly larger (∼0.8).

III. EXPERIMENTAL APPARATUS

A. Stationary afterglow

The plasma is generated in a pulsed microwave discharge in a fused silica tube (inner diameter ∼ 1.5 cm) cooled by liquid nitrogen to nearly 77 K or by pre-cooled nitrogen gas for measurements in the range 80–220 K. The tube contains a mixture of He/Ar/H_2 with a typical composition

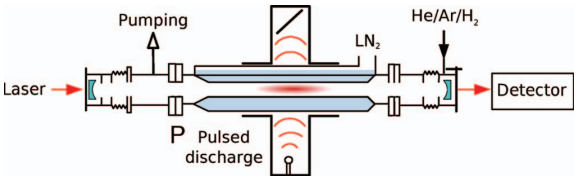

FIG. 2. Schematic diagram (not to scale) of the discharge tube and the optical resonator (cw–CRDS). The discharge tube at the center (containing a He/Ar/H_2 gas mixture) is immersed in liquid or pre-cooled gaseous nitrogen. The light signal exiting the optical cavity is measured by a photodetector (InGaAs avalanche photodiode).

$10^{17}/10^{14}/10^{14}$ cm^{-3} (details of the ion formation reactions are given in Refs. 8, 9, 34, 37, 44, and 49. The gas handling system includes a "para H_2 generator," used to prepare samples of para-enriched H_2, indicated here as $^{e}H_2$.[43] The microwave generator 2.45 GHz is equipped with an external fast high voltage switch to cut off the power to the magnetron within a fall time of < 30 μs. A fairly low microwave power in the range 5–15 W, with ∼50% duty cycle, was used to avoid excessive heating of the gas during the discharge.

B. CRDS spectroscopy

The principal diagnostic technique employs cavity ring down absorption spectroscopy in the continuous wave modification (cw-CRDS), based on the configuration described by Romanini *et al.*[50] The instrument used here was fabricated in our laboratory for spectroscopic time-resolved studies of elementary processes in plasmas, such as ion-electron recombination (see, e.g., Refs. 43 and 51–54). The light source is a fiber-coupled distributed feedback (DFB) laser diode with a central wavelength of 1381.55 nm, linewidth <2 MHz, and maximum output optical power of 20 mW. The wavelengths are measured by a wavemeter and a Fabry–Perot etalon. The ring-down signal exiting the optical cavity is detected by an InGaAs avalanche photodiode. A schematic picture of the apparatus is shown in Fig. 2.

The cw-CRDS instrument in conjunction with associated data processing electronics records the time-dependent optical absorption signals during the discharge and the afterglow. The observed absorption strengths are then converted to ion concentrations. By tuning the wavelength of the laser diode one can also determine the kinetic temperatures of the H_3^+ ions from the Doppler-broadened absorption line profiles, and their evolution during the discharge and in the early afterglow.

All spectroscopic absorption measurements were performed on the second overtone transitions originating from the ground vibrational level of H_3^+. The lowest rotational levels (1,0) (ortho) and (1,1) (para) of the vibrational ground state were monitored routinely, but the higher lying level (3,3) (ortho) was probed only occasionally. These first two transitions were chosen for routine scanning because they have closely spaced frequencies that can be covered by a single DFB laser. This made it possible to switch quickly from observing one to the other H_3^+ spin state. Figure 3 shows the relevant rotational levels and Table I lists the transitions. The

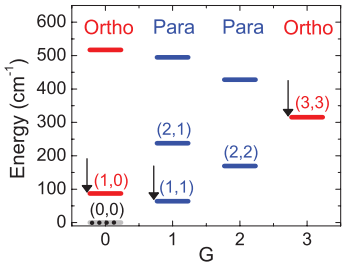

FIG. 3. Rotational energy levels of the ground vibrational state of H_3^+. The energy levels (J,G) are labeled by quantum numbers J and G.[55] The zero of the energy scale is taken at the forbidden (0,0) level, indicated by a dashed line. The rotational states, (1,0), (1,1), and (3,3) observed in the present study are indicated by arrows. Compiled from the data in Ref. 56.

energy levels are labeled (J,G) by their quantum numbers J and G.[55]

C. Para H_2 generator

Normal hydrogen gas at 300 K is a mixture of 1/4 para-hydrogen and 3/4 ortho-hydrogen (i.e., ${}^{\mathrm{p}}f_2 = 0.25$ and ${}^{\mathrm{o}}f_2 = 0.75$, see Fig. 1). It is well known that the composition changes extremely slowly when the hydrogen is cooled or heated, unless the gas is in contact with a suitable paramagnetic catalyst that facilitates re-alignment of the proton spins. By using a catalyst and cooling to low temperatures, nearly pure samples of para-hydrogen in the lowest rotational state ($J = 0$, $\nu = 0$) can be produced. When the catalyst is then removed and the gas is reheated, the hydrogen retains its low-temperature para/ortho composition for a sufficiently long time to carry out experiments with para-enriched hydrogen.

We produced para-enriched hydrogen in a closed-cycle helium cryostat that cools hydrogen in a conversion chamber[57] filled with the catalyst Fe_2O_3. Nuclear magnetic resonance (NMR) was used to check the actual para/ortho ratio in the enriched para-hydrogen ${}^{\mathrm{e}}H_2$. The experimental setup for measurement of para-hydrogen enrichment was similar to the one used in study by Tom.[58] The NMR measurements indicated (87 ± 5)% content of para-hydrogen, i.e., ${}^{\mathrm{p}}f_2 = 0.87$,[59] which is adequate for our experiments. In the following text we will use this value of ${}^{\mathrm{p}}f_2$ without explicitly mentioning its error. It suffices to enrich the hydrogen to a level where the fraction of para-H_3^+ significantly exceeds the value ${}^{\mathrm{p}}f_3 = 0.5$ in normal hydrogen. Figure 1 shows experimental data on the para-enrichment of H_3^+ measured in the discharge and in the afterglow for ${}^{\mathrm{e}}H_2$ and for ${}^{\mathrm{n}}H_2$.

B.2

IV. TEMPERATURES IN THE H_3^+ AFTERGLOW PLASMA

The different particles in a plasma afterglow and their internal degrees of freedom are not necessarily in complete thermal equilibrium with each other and with the walls of the plasma container. For instance, the electron temperature T_e can significantly exceed that of the ions T_{Kin} and gas atoms T_G because the energy transfer in electron collisions with heavy particles is inefficient. Also, the ion's rotational temperature T_{Rot} and vibrational temperature T_{Vib} do not have to be equal to the ion's translational temperature.

A. Ion and neutral gas kinetic temperatures

Since the exchange of translational energy between ions and neutral gas atoms is very efficient, the kinetic temperature of the H_3^+ ions during the afterglow should be nearly the same as the gas temperature, provided that the plasma is free of macroscopic electric fields that, in principle, can heat the ions. The ambipolar electric field is too weak to cause a significant heating. This expectation was confirmed by time-resolved scans of the Doppler-broadened absorption lines of H_3^+ ions over the experimental temperature range from 77 K to 220 K. The inferred temperatures of the H_3^+ ions during the discharge and the afterglow were equal to the wall temperature within ~10 K (see also Figs. 3 and 4 in Ref. 43). This also confirmed that the gas temperature in the discharge region approaches that of the walls. Previous afterglow studies in this lab performed under similar conditions,[60] but using absorption lines of H_2O rather than of H_3^+, led to the same conclusion.

B. Electron temperature T_e

The electron temperature T_e was not measured in these experiments. In previous FALP experiments[61–63] we used Langmuir probes to determine the electron energy distribution function in He and He/Ar buffered afterglow plasmas under conditions similar to those in the present study. It was found that the electrons gained a Maxwellian distribution with the gas temperature very quickly after the metastable helium atoms from the microwave discharge had been depleted by Penning ionization of argon atoms.[64] The electron cooling time constant at typical helium densities can also be estimated as the product of the electron-helium collision frequency (>1 GHz) and the mass ratio $2m_e/m_{He}$, which yields a cooling time of $\tau_\varepsilon < 10\ \mu$s.[65] We indirectly observed fast cooling of electrons by monitoring visible light emissions from the discharge and in the very early afterglow.[51] These estimates

TABLE I. Transitions monitored in the present study. For details on the spectroscopic notation see Ref. 55. Energy levels were taken from Ref. 56.

Wavenumber (cm^{-1})	Spin	Low. lvl. (cm^{-1})	Up. lvl. (cm^{-1})	Transition
7234.957	o	315.349	7550.316	$3\nu_2^1(4,3) \leftarrow 0\nu_2^0(3,3)$
7237.285	p	64.1234	7301.4084	$3\nu_2^1(2,1) \leftarrow 0\nu_2^0(1,1)$
7241.245	o	86.9591	7328.2041	$3\nu_2^1(2,0) \leftarrow 0\nu_2^0(1,0)$

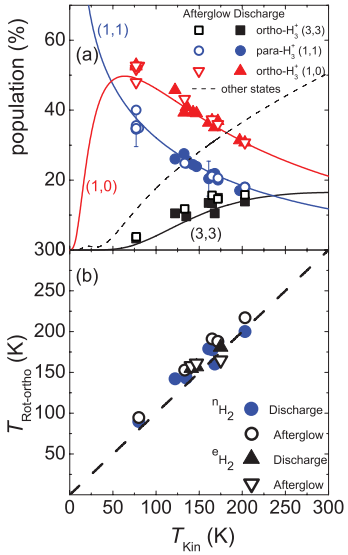

FIG. 4. Rotational temperatures of H_3^+ ions. Panel (a): Relative populations of H_3^+ ions in ortho (1,0) and (3,3) and para (1,1) states versus kinetic temperature of the ions measured in the experiments with normal H_2. The data obtained during the discharge (before switching it off) and during the afterglow (at ~ 150 μs) are indicated by the filled and the open symbols, respectively. The full lines indicate the calculated populations of the indicated states for ions in thermal equilibrium at temperatures equal to T_{Kin}. The dashed line indicates joint population of all other states. Panel (b): The measured rotational temperature of ortho manifold ($T_{Rot-ortho}$) versus measured kinetic temperature (T_{Kin}). The data were obtained in experiments with $^nH_2$ and with $^eH_2$. The dashed straight line indicates equality $T_{Rot-ortho} = T_{Kin}$.

need to be refined when the plasma contains energy sources that heat the electron gas, for instance, recombination of ions by collisional radiative recombination. It is shown in Appendix that this heating mechanism at used electron densities can elevate the electron temperature slightly in the early afterglow at gas temperatures near 77 K, but becomes unimportant at higher gas temperatures and lower electron densities.

C. Vibrational excitation of the H_3^+ ions

We expect that all excited vibrational states of H_3^+ are quenched in collisions with He, Ar, and H_2. The reaction $H_2^+ + H_2$ can produce H_3^+ ions with vibrational excitation up to $v = 5$ but the ions with internal energies above 0.57 eV are rapidly destroyed by proton transfer with Ar, leaving only ions in $v \leq 2$ (for details see Refs. 23 and 53). There is also a high probability that the vibrational excitation of H_3^+ will be quenched in collision with H_2. Kim *et al.*[66] obtained a rate coefficient 3×10^{-10} cm^{3}s^{-1} for vibrational relaxation of H_3^+ ions in H_2. At $[H_2] \sim 10^{14}$ cm^{-3} this leads to vibrational relaxation within 30 μs (see also discussion and references in Ref. 67). We conclude that at Ar and H_2 densities of the order of $\sim 10^{14}$ cm^{-3} vibrational excitation will be quenched within 30 μs after ion formation. Collisions with He atoms are more frequent by at least by three orders of magnitude, but vibrational quenching by helium can be very low, as it is, e.g., in collisions of He with vibrationally excited N_2^+ ions (see, e.g., Ref. 68). To estimate the rate of formation of H_3^+ ions (in reactions with H_2, Ar, and He) we studied the processes at very early afterglow at several He densities and at low H_2 and Ar densities ($[H_2]$, $[Ar] \sim 10^{12}$ cm^{-3}) in our previous study[69] and we found qualitative agreement with results obtained from kinetic model.

D. Rotational and nuclear spin states of the H_3^+ ions

The determination of the spin-dependent recombination rate coefficients of H_3^+ ions relies on accurate knowledge of the relative abundance of ions in the ortho-states and para-states and corresponding rotational states. In this experiment these quantities were measured by optical absorption, rather than by modeling the kinetic processes, but we will briefly describe the reactions of relevance.

The probability of changing the nuclear spin alignment by radiation is very low and likewise collisions with He or Ar atoms are inefficient in causing spin changes. The principal rotational equilibration and spin scrambling process is the proton-hopping or exchange reaction of H_3^+ with H_2 that proceeds via a short-lived $(H_5^+)^*$ reaction complex. The reaction has been studied in great detail.[5,27,70–75] It has been found that the ratio of $[^pH_3^+]/[^oH_3^+]$ in plasmas containing H_2 is constrained by nuclear spin selection rules and depends on the relative concentrations of $^pH_2$ and $^oH_2$ (Refs. 70–75) and on temperature. Rotational-state changes without changing the nuclear spin state, i.e., within the para or ortho manifold, are possible by radiation and in collisions with He or Ar. Electron collisions can change the rotational states within the para or the ortho manifold with rates approximately ten times faster than the rate of the dissociative recombination (for details see Ref. 76) which means than on average an H_3^+ ion has ten thermalizing collisions with electrons prior to its recombination at our conditions. For this reason, we expect that ions are rotationally thermalized within the para and ortho manifolds.

Rotational temperatures of the ions were inferred from measurements of absolute densities of ions in three rotational states. Panel (a) of Fig. 4 shows the populations of two ortho-states and one para-state, measured during the discharge and during the afterglow in experiments with normal H_2 at temperatures 77–200 K. The relative populations of the ortho- and para-states were computed by dividing the measured absolute ion densities in a given state by the density of all H_3^+ ions, assuming a thermal rotational state distribution. At temperatures where two H_3^+ absorption lines were observable, the rotational temperature $T_{Rot-ortho}$ within the ortho manifold was obtained also. The relation between the rotational temperature ($T_{Rot-ortho}$) and the kinetic temperature (T_{Kin}) of the ions is shown in panel (b) of Fig. 4. The data plotted in panel (b) were obtained in experiments with $^nH_2$ and with $^eH_2$. The agreement between $T_{Rot-ortho}$ and T_{Kin} is very good ($|T_{Rot-ortho} - T_{Kin}| < 15$ K). During the discharge, a slightly higher rotational temperature $T_{Rot-ortho}$ compared to the kinetic temperature T_{Kin} is expected since the ions are produced with higher rotational excitation and then relax by collisions to lower states. During the afterglow, the lifetime of the H_3^+ ions is longer (because ambipolar diffusion is slower) and

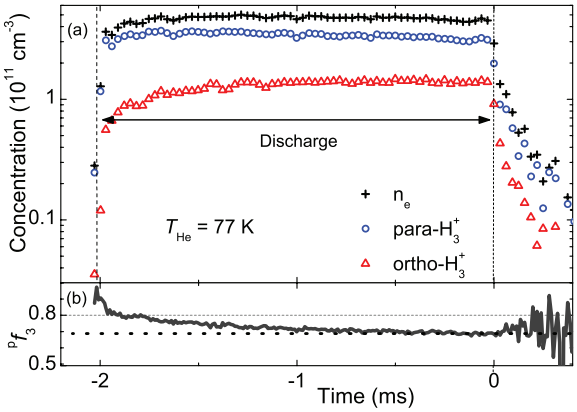

FIG. 5. Panel (a): Evolution of $[^pH_3^+]$, $[^oH_3^+]$, and n_e measured in experiments with enriched hydrogen, $^eH_2$, at $T_{He}\sim$ 77 K and [He] = 4 × 10^{17} cm^{-3}, $[^eH_2] = 3 \times 10^{14}$ cm^{-3}, [Ar] = 6 × 10^{13} cm^{-3}. The decay in the early afterglow is caused by recombination. Panel (b): Evolution of $^pf_3$. The final value of $^pf_3 \sim 0.7$ during the late discharge and in the early afterglow exceeds the equilibrium value of $^pf_3 \sim 0.5$ in normal hydrogen.

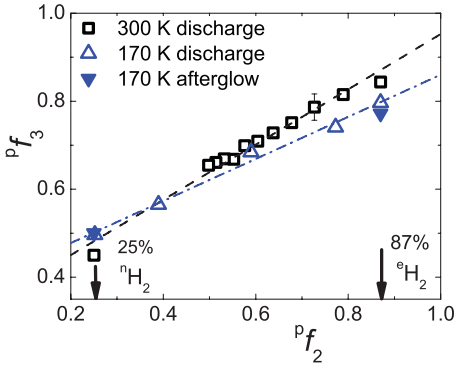

FIG. 6. Dependence of $^pf_3$ on $^pf_2$ measured in a He/Ar/H_2 mixture at 300 K (discharge) and 170 K (discharge and afterglow). Arrows point to the values of $^pf_2$ in $^nH_2$ and $^eH_2$ that were used in the recombination studies. Open symbols: Values in the discharge ($\tau_{Disch} \sim 2$ ms). Filled symbols: Values during the afterglow ($\tau_{Afterglow} \sim 150$ μs).

more time is available for rotational relaxation. Some production of rotationally excited H_3^+ ions may occur in very early afterglow. Therefore, in the determination of $T_{Rot-ortho}$ we excluded data obtained during the first $\sim$ 150 μs after switching off the discharge.

We concluded that the ions under study were kinetically and internally thermalized in plasmas containing $^nH_2$, within the experimental uncertainties of $T_{Rot-ortho}$, T_{Kin}, and $^pf_3$(see Figs. 1 and 4). In plasmas containing $^eH_2$, we also found that $T_{Rot-ortho} \sim T_{Kin} \sim T_{He}$ (see panel (b) of Fig. 4), but in this case the relative abundances of para-H_3^+ and ortho-H_3^+ ($^pf_3$ and $^of_3$) are not in thermal equilibrium (see panel (a) of Fig. 1). The enrichment of para-H_3^+ will be discussed next.

E. H_3^+ para to ortho ratio

We measured absolute densities $[^pH_3^+]$ and $[^oH_3^+]$ during the discharge and during the afterglow to determine the dependence of the para-H_3^+ and ortho-H_3^+ fractions on experimental conditions. The time resolution in our experiment suffices to record the temporal evolution during the discharge and during the early afterglow. Typical evolutions of $[^pH_3^+]$, $[^oH_3^+]$ and electron densities are plotted in panel (a) of Fig. 5 for the case where $^eH_2$ was the precursor gas. The electron density n_e is taken as the sum $[^pH_3^+] + [^oH_3^+]$. Panel (b) of Fig. 5 shows the measured fraction $^pf_3$ of $[^pH_3^+]$. After the rapid change in the early discharge the variation during the discharge becomes slow. The faster change of $^pf_3$ at the beginning reflects the transition from the nascent H_3^+, formed by proton transfer from ArH^+ or H_2^+ to H_2, to the steady state established in subsequent reactions with H_2. A thorough discussion of the reactions is contained in two recent papers by Crabtree *et al.*[45,46]). During the discharge, the para/ortho composition of H_2 ($^pf_2$) changes slowly as a consequence of H_2 dissociation and recombination and hence $^pf_3$ also changes during the discharge. When we refer to values (e.g., $T_{Rot-ortho}$, T_{Kin}) measured "during the discharge" we mean values measured shortly before switching off the discharge ($\tau_{Disch} \sim 2$ ms), unless stated otherwise (see also discussion in Ref. 43).

Our systematic measurements of the evolution of the para/ortho composition show that, under the conditions of this set of experiments, the fraction $^pf_3$ remains nearly constant during the afterglow, and that it can be varied by using normal or para enriched hydrogen. We also measured the dependence of $^pf_3$ on $^pf_2$ which was varied from $^pf_2$= 0.25 to ∼0.87 by mixing $^nH_2$ with $^eH_2$, while keeping the overall hydrogen density ($[^nH_2] + [^eH_2]$) constant. The dependence of $^pf_3$ on $^pf_2$ measured at 300 K and at 170 K (see Fig. 6) is linear and the same was found to be true at other temperatures (for details see Ref. 43). The linearity is a consequence of the spin-scrambling reaction with hydrogen.[70–73] Crabtree *et al.*[45,46] have recently discussed in great detail the general dependence of $^pf_3$ on $^pf_2$ and other experimental conditions. For the present study of H_3^+ recombination a quantitative understanding of the reaction kinetics is not required; it is only important that $^pf_3$ is known and can be varied over a significant range.

V. EXPERIMENTAL RESULTS – STATE SELECTIVE RECOMBINATION

The measured electron-density decay curves were analyzed to obtain apparent binary recombination rate coefficients for two particular values of $^pf_3$(see Eqs. (2)—(4)). Further details can also be found in Ref. 27. We carried out a systematic set of measurements which differed only in the value of $^pf_2$, but employed otherwise very similar conditions. The densities of para (1,1), ortho (1,0), and ortho (3,3) states of H_3^+ were monitored. Examples of data measured at 170 K with $^nH_2$ and with $^eH_2$ are plotted in Figs. 7 and 8, respectively. Note the large difference in measured populations of particular rotational states of H_3^+ in both experiments (see panels (b) of both figuers). In this set of experiments we obtained $^pf_3$ ∼ 0.5 for $^nH_2$ and $^pf_3 \sim$ 0.7–0.8 for $^eH_2$ (see panels (c) of both figures). Note also that in both experiments the values of $^pf_3$ are nearly constant during the afterglow.

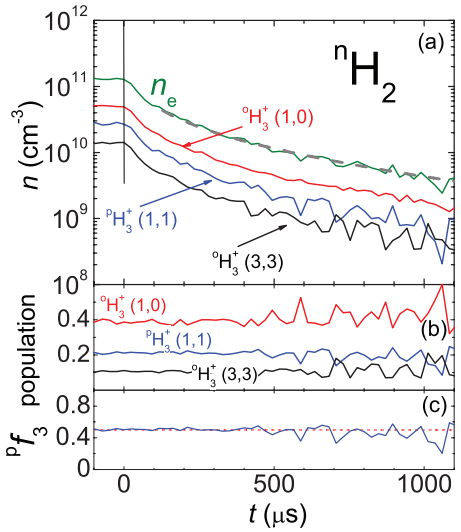

FIG. 7. Panel (a): Example of decay curves of densities of ions in para (1,1), ortho (1,0), and ortho (3,3) states of H_3^+, measured during the afterglow in a He/Ar/$^{n}H_2$ gas mixture at 170 K, 1440 Pa of He, $[H_2] = 1 \times 10^{14}$ cm^{-3}, and $[Ar] = 2 \times 10^{14}$ cm^{-3}. Time is set to zero at the beginning of the afterglow. The vertical bar shows the end of the discharge period and the beginning of the afterglow. Electron density is obtained as a sum of ion densities. Panel (b): The measured relative populations of para (1,1), ortho (1,0), and ortho (3,3) states of H_3^+, note the nearly constant values during whole afterglow. Panel (c): Measured fraction $^{p}f_3$ of para-H_3^+.

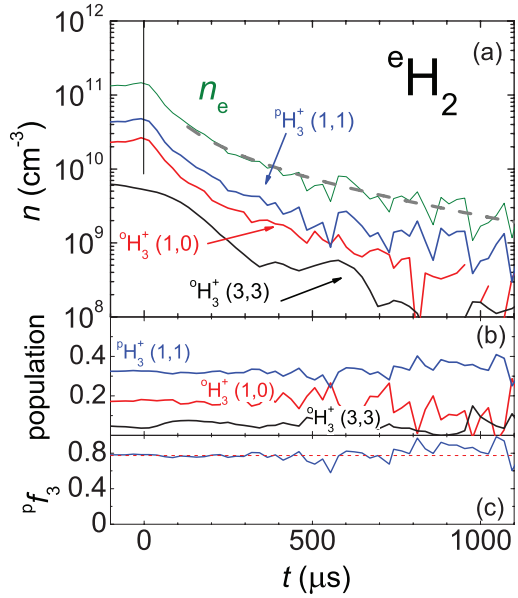

FIG. 8. Panel (a): Example of decay curves of densities of ions in para (1,1), ortho (1,0), and ortho (3,3) states of H_3^+, measured during the afterglow in a He/Ar/$^{e}H_2$ gas mixture at 170 K, 1550 Pa of He, $[H_2] = 1 \times 10^{14}$ cm^{-3}, and $[Ar] = 2 \times 10^{14}$ cm^{-3}. The vertical bar shows the end of the discharge period and the beginning of the afterglow. Panel (b): The measured relative populations of para (1,1), ortho (1,0), and ortho (3,3) states of H_3^+. Panel (c): Measured fraction $^{p}f_3$ of para-H_3^+.

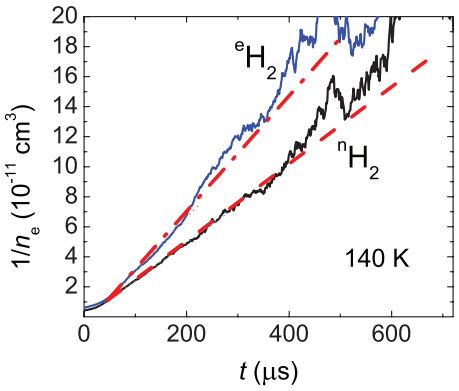

FIG. 9. Examples of the evolutions of the reciprocal number density $1/n_e$ during the afterglow when using normal $^{n}H_2$ or para-enriched $^{e}H_2$ at otherwise identical conditions. The effective (apparent) binary recombination rate coefficient is given by the slope of the linear part of the plot.

From the densities of the ions in (1,1) and (1,0) states we calculated, assuming thermal equilibrium (TDE) within the para-manifolds and ortho-manifolds, the total densities $[^{p}H_3^+]$ and $[^{o}H_3^+]$ and their sum, i.e., the electron density. The electron-density decay curves can be approximately analyzed by graphing $1/n_e$ versus decay time. The slope of the linear part of the plot yields the effective (apparent) binary recombination rate (for details see Ref. 61). Examples of such graphs of data obtained with $^{n}H_2$ and $^{e}H_2$ are shown in Fig. 9.

This simple form of analysis demonstrates that recombination in afterglows containing para-enriched hydrogen $^{e}H_2$, i.e., with higher relative population of para-H_3^+, is faster than when normal hydrogen is used. However, it neglects ambipolar diffusion and eventual reactive losses characterized in Eqs. (2) and (3). Hence, we used the more advanced "integral analysis" of the measured electron density decay curves (for details of "integral analysis" see Refs. 61 and 77). This analysis can separate α_{eff} from τ_L and minimize influence of ternary association (1e) and (1f) on determination of α_{eff}. The first 50–150 μs of the afterglow decay were excluded because probably new ions were still being formed (for details see Refs. 8, 27, 43, and 69. At 77 K special attention was paid to analysis of the decay curves because of a possible influence of the CRR process, which is discussed in Appendix.

The dependences of $^{n}\alpha_{\text{eff}}$ and $^{e}\alpha_{\text{eff}}$ on He density measured at 170 K are shown in panel (a) of Fig. 10. Panel (c) shows values of the corresponding fractions $^{p}f_3$. Note that the fractions $^{p}f_3$ are different in $^{n}H_2$ and in $^{e}H_2$, but are independent on helium density [He]. Both, $^{n}\alpha_{\text{eff}}$ and $^{e}\alpha_{\text{eff}}$ increase linearly with increasing [He]. Therefore (see Eq. (5)), we can obtain separate binary and ternary recombination rate coefficients for known para/ortho ratios. The values obtained with normal hydrogen refer to the thermal equilibrium H_3^+ with $^{p}f_3 \sim 0.5$. In our previous FALP experiments using $^{n}H_2$ we assumed but did not prove that $^{p}f_3 = 0.5$. The present experiments with $^{n}H_2$ confirmed that $^{p}f_3 = 0.5$ and $T_{\text{Rot-ortho}} = T_{\text{Kin}}$. In other words, the values of α_{bin} and K_{He} recombination rate coefficients obtained in our previous FALP experiments were the values appropriate for thermal equilibrium.[8,33–37]

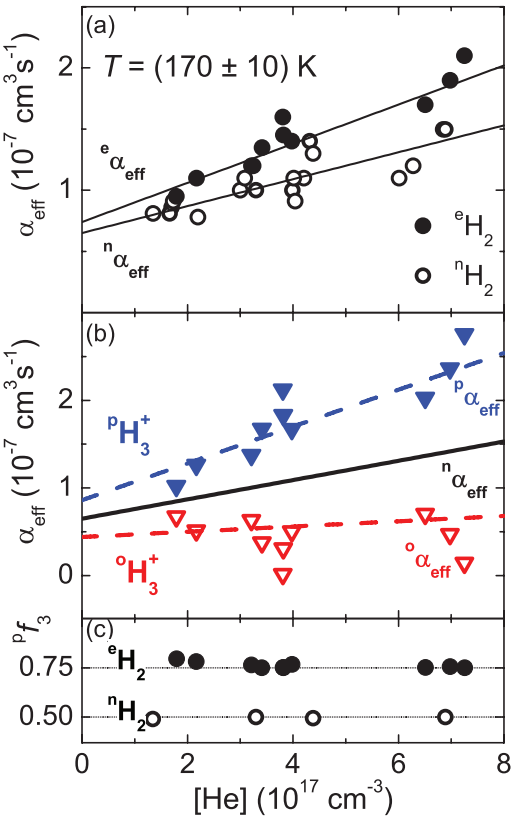

FIG. 10. Measured dependence of effective recombination rate coefficients α_{eff} on He density at 170 K. Panel (a): The values α_{eff} measured using $^nH_2$ as the precursor gas ($^n\alpha_{eff}$, open circles) and the values measured using $^eH_2$ ($^e\alpha_{eff}$, filled circles). Panel (b): The calculated values $^p\alpha_{eff}$ and $^o\alpha_{eff}$ for pure para-H_3^+ (filled triangles) and pure H_3^+ (open triangles), respectively. For comparison straight line obtained by fit of values $^n\alpha_{eff}$ in panel (a) is also plotted. Panel (c): The $^pf_3$ fractions of para-H_3^+ measured in the experiments with $^nH_2$ and $^eH_2$.

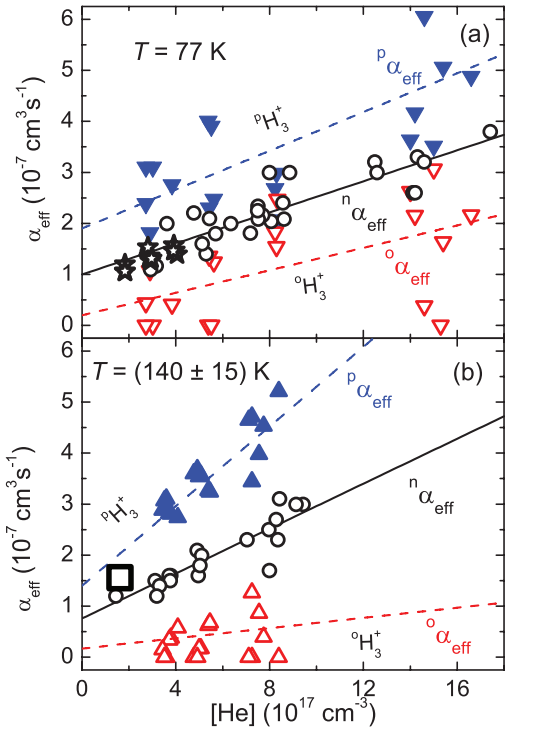

FIG. 11. Measured effective recombination rate coefficients $^p\alpha_{eff}$ and $^o\alpha_{eff}$ (closed and open triangles, respectively) as a function of He density at 77 K (panel (a), for details see also Ref. 27) and at 140 K (panel (b)). The full lines indicate $^n\alpha_{eff}$. The stars in panel (a) are data measured in previous FALP experiment at 77 K (Ref. 34) and the large square in panel (b) represents data measured in previous FALP and stationary afterglow experiments at 130 K.[34,79] The slopes of the straight-line fits yield the corresponding ternary recombination rate coefficients (K_{He}) while the intercept for [He] → 0 gives the corresponding α_{bin}.

We measured the dependences of $^n\alpha_{eff}$ and $^e\alpha_{eff}$ on [He] for temperatures in the range 77–200 K. From the dependences of $^n\alpha_{eff}$ and $^e\alpha_{eff}$ on [He] and the corresponding values of $^pf_3$ we calculated values $^p\alpha_{eff}$ and $^o\alpha_{eff}$ for pure para-H_3^+ and for pure ortho-H_3^+, respectively. In these calculations, linear fits to the data measured with $^nH_2$ were used as a reference (the full lines in panels (a) and (b) of the Fig. 10 indicated as $^n\alpha_{eff}$). The obtained negative values of $^o\alpha_{eff}$ were truncated to zero and the corresponding values of $^p\alpha_{eff}$ were corrected accordingly. By fitting the data $^p\alpha_{eff}$ and $^o\alpha_{eff}$ (panel (b) of Fig. 10) with a linear dependence (Eq. (5)) we obtained the corresponding binary ($^p\alpha_{bin}$ and $^o\alpha_{bin}$) and ternary ($^pK_{He}$ and $^oK_{He}$) recombination rate coefficients for pure para-H_3^+ and for pure ortho-H_3^+. This form of data analysis is also described in Ref. 27.

VI. RESULTS—TERNARY HE ASSISTED RECOMBINATION OF PARA-H_3^+ AND ORTHO-H_3^+

The present SA–CRDS experiments cover a range of pressures from 200 to 1600 Pa, corresponding to maximum He densities of 1.6×10^{18} cm^{-3} at 77 K and $\sim 6 \times 10^{17}$ cm^{-3} at 200 K. The ability to vary the He density over a large range of nearly a factor of 10 improves the accuracy of the inferred ternary rate coefficients. The dependences of α_{eff} on [He] were measured at four temperatures (77, 140, 170, and 200 K) using $^nH_2$ and $^eH_2$. The dependences of $^p\alpha_{eff}$ and $^o\alpha_{eff}$ on helium density obtained for 170 K are shown in panel (b) of Fig. 10 and dependences obtained for 77 K and for 140 K can be found in our previous papers[27,78] and are shown in Fig. 11 (the values of $^p\alpha_{eff}$ were omitted in Fig. 11 for better clarity). From the dependences of $^p\alpha_{eff}$ and $^o\alpha_{eff}$ on [He] we obtained (using Eq. (5)) the corresponding binary and ternary recombination rate coefficients α_{bin} and K_{He}. In spite of the fairly large scatter in the data it is clear that ternary recombination depends on the spin state of recombining ions (on $^pf_3$). This large scatter is mirrored in error bars of the values shown in Figs. 12 and 13. As can be seen from Fig. 11, zero values of extrapolated $^o\alpha_{bin}$ cannot be excluded at the lowest temperatures. For all three temperatures the ternary helium-assisted recombination of para-H_3^+ is faster than the recombination of H_3^+.

Figure 12 shows the ternary recombination rate coefficients $^pK_{He}$ and $^oK_{He}$ as a function of temperature, as

B.2

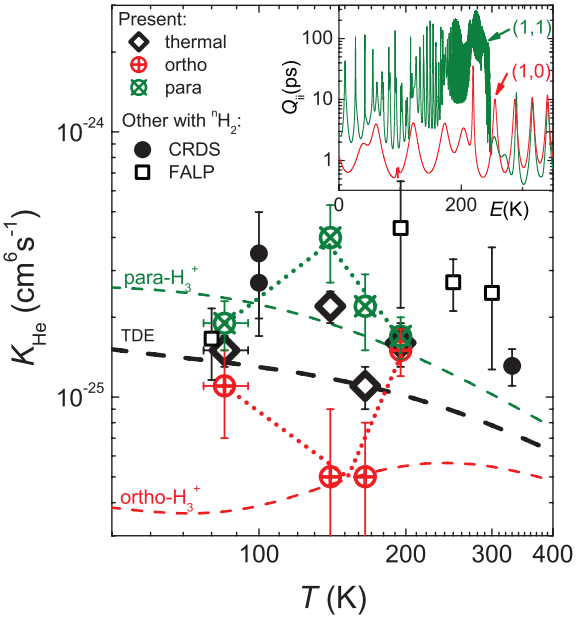

FIG. 12. Ternary recombination rate coefficients $^pK_{He}$, $^oK_{He}$, and $^nK_{He}$. The data obtained in previous CRDS (closed circles) and FALP/SA (open squares) experiments[33,34] are also shown. The dotted lines drawn through the para and ortho data are only meant to guide the eye. In the insert diagonal elements Q_{ii} of lifetime Matrix **Q** for the two lowest initial rotational states of H_3^+ are plotted. Each curve is labeled with the corresponding quantum numbers (J,G).[8,34]

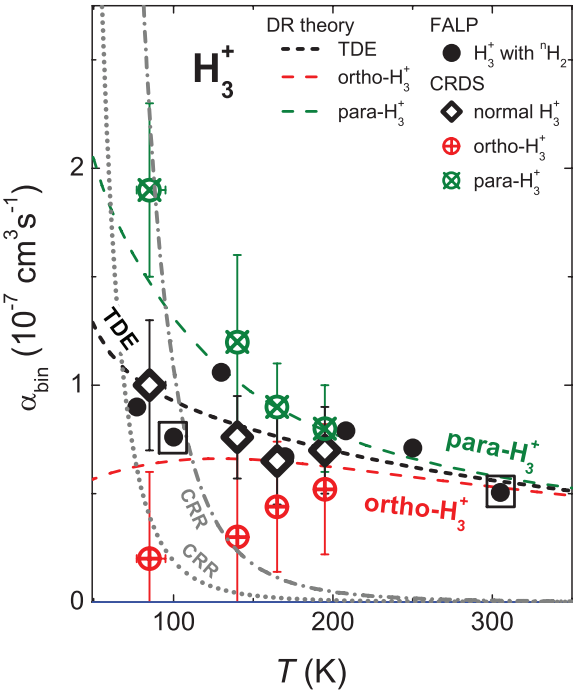

FIG. 13. Measured temperature dependences of the binary recombination rate coefficients $^n\alpha_{bin}$, $^p\alpha_{bin}$, and $^o\alpha_{bin}$ for normal-H_3^+ (measured in experiments with $^nH_2$), para-H_3^+, and ortho-H_3^+, respectively (see also Ref. 78). Previous FALP data[8,33,34] measured with $^nH_2$ are indicated by full circles. Combined SA–CRDS/FALP data at 100 K and 305 K (Refs. 8 and 34) are indicated by a full circle in a square. The temperature T in the SA–CRDS experiments is given by T_{Kin}, while in the FALP it is the temperature of the flow tube. That is why we use $T = 82$ K for data obtained in experiment made with discharge tube (SA–CRDS) immersed in liquid nitrogen, otherwise we indicate it as 77 K (e.g., in Fig. 5). Error bars (present CRDS data) represent statistical errors (see linear fits in Figs. 10 and 11). The dashed lines indicate the theoretical rate coefficients for para-H_3^+, ortho-H_3^+, and for H_3^+ ions in the thermal equilibrium (TDE).[6] The curves labeled CRR are the effective binary rate coefficients of collisional radiative recombination (CRR) calculated from the Stevefelt formula (see Refs. 31, 32, and 38) for electron densities $n_e = 5 \times 10^9$ cm^{-3} (dotted line) and $n_e = 3 \times 10^{10}$ cm^{-3} (dash-dotted line). For details see the Appendix.

obtained from the slopes of graphs of the kind shown in Figs. 10 and 11. The values $^nK_{He}$ corresponding to thermal equilibrium at 77, 140, 170, and 200 K (open rhomboids in Fig. 12) were obtained in the same way from $^n\alpha_{eff}$ (see Figs. 10 and 11). Particular attention was paid to experiments at 77 and 140 K (see Fig. 11) where we obtained high accuracy by measuring at larger helium density range (when comparing current CRDS data to FALP data, see Fig. 11). The CRDS data at 100 and 330 K (closed circles in Fig. 12) and FALP data at 200 K were measured in previous experiments and were obtained from the measured dependences of $^n\alpha_{eff}$ on hydrogen number density in the "saturated region." For details see Ref. 34. Values of K_{He} at 250 K and 300 K were obtained from the slopes of the linear dependence on helium number density from the data collection of SA and FALP data.[34] Because of the lower electron density in FALP experiment plasma decay is longer and formation of H_5^+ can influence the decay at higher helium densities. We have taken this effect into the account by enlarging error bars of the FALP data. Having in mind high He density and low temperature we used kinetic models to verify our assumptions on influence of H_5^+ formation on plasma decay and on determination of α_{eff}. Note that H_5^+ formed in association (1e) and (1f) is in used experimental conditions removed from plasma within $\sim 10\,\mu$s and the association is loss determining process. Possible error caused by H_5^+ formation is within statistical error of the data, as was confirmed by the chemical kinetics model. In Fig. 12 we did not include the data previously measured in "continuous regime" where FALP was first cooled to 77 K and after stopping cooling effective rate coefficients were measured at continuously increasing temperature (for details see Ref. 8). The accuracy of data obtained in "continuous regime" is lower when comparing with accuracy of present data obtained from dependences on helium density (Figs. 10 and 11).

In our previous studies[8,33,34] of recombination of H_3^+ with electrons we discussed the ternary recombination rate coefficient K_{He} in terms of the lifetimes of excited metastable Rydberg states H_3^* formed in collision of H_3^+ ion with electron.[8,33,34] At low collision energies the calculated values of the lifetimes depend on the spin state of the recombining ions and on collision energy. In the inset in Fig. 12 the calculated diagonal elements Q_{ii} of the lifetime Matrix **Q** for the two lowest initial rotational states of H_3^+ are plotted. The calculated lifetimes are long enough to enable l-changing collision of H_3^* molecule with helium buffer gas atom. The calculated ternary recombination rate coefficients[34] for para-H_3^+ and ortho-H_3^+, shown as dashed lines in Fig. 12,

are in qualitative agreement with measured values. ${}^{\mathrm{p}}K_{\mathrm{He}}$ is greater than ${}^{\mathrm{o}}K_{\mathrm{He}}$ due to the longer lifetimes of para-H_3^* Rydberg resonances. Although some rather rough assumptions were made in the theoretical calculations (mainly the independence of the rate coefficient of *l*-changing collision on temperature) the overall agreement with the measured data is quite good in comparison with older theories of ternary assisted recombination.[29,80] An alternative explanation of ternary recombination of H_3^+ has been suggested by Johnsen and Guberman.[12]

More accurate theory should address decrease of ternary rate coefficients at temperature decreasing towards 77 K and also observed small difference between ${}^{\mathrm{p}}K_{\mathrm{He}}$ and ${}^{\mathrm{o}}K_{\mathrm{He}}$ at 77 K (see also Ref. 27), which are in contradiction with calculated dependences.

VII. RESULTS—BINARY RECOMBINATION OF PARA-H_3^+ AND ORTHO-H_3^+

The values of ${}^{\mathrm{p}}\alpha_{\mathrm{bin}}$ and ${}^{\mathrm{o}}\alpha_{\mathrm{bin}}$ for pure para-H_3^+ and pure ortho-H_3^+ and values of ${}^{\mathrm{n}}\alpha_{\mathrm{bin}}$ measured in the present experiment are plotted versus temperature in Fig. 13. Plotted are also values ${}^{\mathrm{n}}\alpha_{\mathrm{bin}}$ for H_3^+ ions in thermal equilibrium obtained in our previous FALP experiments.[8,33,34] The theoretical rate coefficients for pure para-H_3^+, pure ortho-H_3^+, and for H_3^+ ions in thermal equilibrium[6] are also shown in Fig. 13. The agreement between experimental and theoretical binary recombination rate coefficients ${}^{\mathrm{n}}\alpha_{\mathrm{bin}}$, ${}^{\mathrm{p}}\alpha_{\mathrm{bin}}$, and ${}^{\mathrm{o}}\alpha_{\mathrm{bin}}$ is very good. Also, the agreement between the present ${}^{\mathrm{n}}\alpha_{\mathrm{bin}}$ values and those obtained in our earlier FALP experiments using Langmuir probes is very good over the whole temperature range, even though in the present experiments the electron densities in the early afterglow were higher by at least a factor of 20.[34] The agreement at higher temperatures (140, 170, and 200 K) indicates that the measured rate coefficients at 77 K do not depend on electron density (see overlap of FALP and CRDS data plotted in Fig. 11), which means that CRR has little effect on the binary recombination rate coefficients ${}^{\mathrm{p}}\alpha_{\mathrm{bin}}$ and ${}^{\mathrm{o}}\alpha_{\mathrm{bin}}$ (for details see discussion in the Appendix).

VIII. POSSIBLE CONTRIBUTION OF CRR

The afterglow experiments described here had to be performed at high ion and electron densities (approaching 10^{11} cm^{-3}) in order to obtain adequate optical absorption. Hence, we were concerned that electron-stabilized recombination (CRR) might contribute to the recombination loss, especially at the lowest gas temperature of 77 K. The dominant term in the "classical" treatment of CRR for atomic ions by Stevefelt *et al.*[30,38] yields a three-body CRR rate coefficient $K_{\mathrm{CRR}} = 3.8 \times 10^{-9}\, T_{\mathrm{e}}^{-4.5}$ cm^{6}s^{-1}. The formula (hereinafter referred to as the "Stevefelt formula") has been experimentally verified for recombination of atomic argon ions at temperatures down to 60 K (Refs. 32 and 40)). Its validity for molecular ions seems plausible but has not been tested.

An uncritical application of the commonly used "Stevefelt formula"[38] results in an effective binary CRR rate coefficient of 3×10^{-7} cm^{3}s^{-1} (at $T_{\mathrm{e}} = 77$ K and an electron density $n_{\mathrm{e}} = 3 \times 10^{10}$ cm^{-3}, see Fig. 13), larger than the binary H_3^+ recombination coefficient measured in normal H_2 at the same temperature. At later afterglow times, e.g., when the electron density has dropped below 5×10^9 cm^{-3}, the contribution of CRR becomes much smaller (see Fig. 13). However, the real situation is more complicated because the electrons that are captured by CRR transfer energy to other electrons, thereby raise the temperature of the electron gas, and reduce the rate of the strongly temperature-dependent CRR. The estimates of the electron heat balance described in the Appendix indicate that the electron temperature in the very early afterglow may be as high as 100 K, when the gas temperature is 77 K. This would reduce the contribution of CRR considerably but not make it entirely negligible. The model calculations described in the Appendix suggest that the effect of CRR is negligible, even at 77 K.

The fact that the present data for normal hydrogen are very close to those measured by us in flow tubes (FALP) at ten times smaller electron densities[34] supports our conclusion that CRR makes only a small contribution to recombination. While the exact contribution of CRR is difficult to determine, our main conclusion, namely that para-H_3^+ and ortho-H_3^+ recombine with different rates, remains unaffected since CRR should not distinguish between nuclear spin states, however this question is in need of further clarification. Under preparation is the SA–CRDS experiment where wall temperature will be below liquid nitrogen temperature, i.e., below 77 K.

IX. DISCUSSION AND CONCLUSION

Our investigations show that the low-temperature recombination of H_3^+ ions depends strongly on the nuclear spin states of the ions. CRDS proved eminently capable of quantifying the populations of para-H_3^+ and ortho-H_3^+ in the discharge and during the afterglow and to verify that the afterglow plasma was in thermal equilibrium with the He buffer gas. By adding normal and para enriched hydrogen to He buffer gas we were able to form plasmas with different partial populations of para-H_3^+ (fractions, ${}^{\mathrm{p}}f_3$) and ortho-H_3^+ (fractions, ${}^{\mathrm{o}}f_3$) and to deduce both binary and ternary (He-assisted) recombination rate coefficients for pure para-H_3^+ and ortho-H_3^+ ions. The rate coefficients were measured at temperatures from 77 to 200 K. As far as applications to astrophysical clouds are concerned, the binary rate coefficients are the most important. Applications to laboratory hydrogen plasmas will have to include the ternary coefficients as well. It is worth mentioning here that the recent observation of laser lines in hydrogen/rare gas discharge was explained by three-body recombination of H_3^+.[81]

This is the first time that binary and ternary recombination rate coefficients have been determined for H_3^+ ions with *in situ* measured abundances of the para and ortho nuclear spin state and actual kinetic and rotational temperature. The results support theoretical predictions and are compatible with the partial results obtained in storage-ring experiments.

ACKNOWLEDGMENTS

We would like to thank Mgr. Mojmir Jilek for the design of para-H_2 generator and RNDr. Jan Lang, Ph.D. for

B.2

TABLE II. Electron processes and corresponding characteristic times calculated for a plasma at $T_{He} = T_{Kin} = T_{Rot} = 77$ K, $T_e = 82$ K, $n_e = 5 \times 10^{10}$ cm^{-3}, and [He] $= 5 \times 10^{17}$ cm^{-3} (~500 Pa). Definition of symbols: v: electron velocity; $\sigma_{e/He}(v)$: tabulated cross section of electron-He elastic scattering; $\langle \ldots \rangle$: average over relative velocity distribution; λ_D: Debye length; Λ: impact parameter for 90° coulombic scattering; m_{He}: mass of He atom; m_e: electron mass; λ: coulombic logarithm; $\Delta_{1,2}$: energy difference between rotational states (1,1) and (2,1); n_1, n_2: number density of H_3^+ ions in rotational states (1,1) and (2,1); α_{21}, α_{12}: rate coefficients for electron (de)excitation between the states 2 → 1 and vice versa; K_{He}: ternary rate coefficient of helium assisted dissociative recombination; α_{bin}: rate coefficient of binary dissociative recombination.

Reactants	Process	τ [μs]	Remark	Reference
e + He	Elastic scattering	0.0008	${}^c\tau_{e/He} = 1/[He]\langle\sigma_{e/He} \cdot v\rangle$	85
e + e	Coulombic scattering	0.004	${}^c\tau_{e/e} = 1/n_e\langle v\pi\Lambda^2\ln(\lambda_D/\Lambda)\rangle$	83,84
e + He	Elastic cooling	2.9	${}^\varepsilon\tau_{e/He} = {}^c\tau_{e/He}(m_{He}/2m_e)$	65
e + H_3^+	Coulombic cooling	3.4	${}^\varepsilon\tau_{e/i} = \frac{6\sqrt{2m_e}\varepsilon_0^2(\pi k_B T_e)^{3/2}}{n_e e^4 \lambda}\frac{m_i}{2m_e}$	86
e + e + H_3^+	CRR	43	$\tau_{CRR} = 1/n_e^2 K_{CRR}$	38
e + H_3^+	Rotational cooling	140	${}^\varepsilon\tau_{Rot} = \frac{3}{2}\frac{k_B(T_{Rot}-T_e)}{\Delta_{1,2}(n_2\alpha_{21}-n_1\alpha_{12})}$	76,87
e + H_3^+ + He	Ternary recombination	200	$\tau_{ternary} = 1/K_{He}[He]n_e$	34
e + H_3^+	Binary recombination	250	$\tau_{bin} = 1/\alpha_{bin}n$	34

NMR measurements of para enrichment of ${}^eH_2$ gas. This work was partly financed by the research Grant No. OC10046 from the Ministry of Education of the Czech Republic and was partly supported by GACR (205/09/1183, P209/12/0233), SV 265 302, GAUK 92410, GAUK 353811, GAUK 54010, and COST Action CM0805 (The Chemical Cosmos).

APPENDIX A: ELECTRON HEATING AND EFFECT OF COLLISIONAL RADIATIVE RECOMBINATION

In this appendix we consider the heat balance for electrons in low temperature plasma. First we consider the heat balance between the heat released by CRR and heat transfer to ions and neutrals and the resulting increase of the electron temperature. In the second step we consider the effect of electron heating on the afterglow decay.

We denote characteristic times between electron collisions as ${}^c\tau$ (left superscript c) and characteristic times for equipartition of energy as ${}^\varepsilon\tau$ (left superscript ε). Right subscript will be used to denote collision partners. For example, the characteristic time for electron/He collisions is denoted as ${}^c\tau_{e/He}$ and the electron temperature relaxation time due to electron/He collisions is denoted as ${}^\varepsilon\tau_{e/He}$. Both quantities are related by the equation: ${}^\varepsilon\tau_{e/He} = {}^c\tau_{e/He}(m_{He}/2m_e)$.[65]

In these calculations we do not distinguish between the para and ortho nuclear spin states of H_3^+. In this approximation we treat the interactions as spin independent. The relevant collision processes are listed in Table II together with calculated characteristic times for conditions typical in our experiment: $T_{He} = T_{Kin} = T_{Rot} = 77$ K, $T_e = 82$ K, $n_e = 5 \times 10^{10}$ cm^{-3}, and [He] $= 5 \times 10^{17}$ cm^{-3} (~500 Pa). Collisional radiative recombination adds ΔE_{CRR} to the internal energy of the electron gas. We assume that this energy is of the order of $\Delta E_{CRR} = 0.13$ eV per recombined electron. This corresponds to the ionization potential of the lowest Rydberg state recombining predominantly by collisions rather than radiative transitions.[38,82] Varying the ΔE_{CRR} by a factor of 2 had no qualitative effect on the conclusions of our simulations. The CRR ternary rate coefficient is taken as $K_{CRR} = 3.8 \times 10^{-9} T_e^{-4.5}$ cm^{6}s^{-1}.[38] Heat transfer from the electron gas to neutrals (He) and ions occurs via electron/He collisions, electron-ion coulombic collisions, and by rotational excitation of H_3^+ between the rotational levels (1,1) and (2,1). We use recently calculated thermal rates (see Ref. 76) for rotational energy transfer. Electron-electron collisions establish and maintain a maxwellian energy distribution of the electron gas.

The maxwellization of the electron gas by electron-electron coulombic collisions[83,84] is much faster than the cooling processes under our conditions. Hence, we can define an electron temperature and write a simple equation for the internal energy of the electron gas U:

$$\frac{dU}{dt} = Q_{CRR} - Q_{elastic} - Q_{e/i} - Q_{Rot}, \tag{A1}$$

where the Q_{CRR}, $Q_{elastic}$, $Q_{e/i}$, and Q_{Rot} terms represent the heating by CRR, cooling by elastic collisions with neutrals, cooling by coulombic collisions with ions, and cooling by rotational excitation of ions, respectively. This equation can be rewritten in terms of relaxation times defined in Table II:

$$\frac{dT_e}{dt} = \frac{2\Delta E_{CRR}/3k_B}{\tau_{CRR}} - \frac{T_e - T_G}{{}^\varepsilon\tau_{e/He}} - \frac{T_e - T_{Kin}}{{}^\varepsilon\tau_{e/i}} - \frac{T_e - T_{Rot}}{{}^\varepsilon\tau_{Rot}}. \tag{A2}$$

In determining the electron temperature, the time derivative term can be neglected, because the relaxation processes are fast enough to maintain the equilibrium temperature at each time during the afterglow. The electron temperature is then obtained by numerically solving Eq. (A2) with zero time derivative.

For the beginning we use the theory of CRR of atomic ions[38] to estimate a rate of CRR of H_3^+ ions, then the effective binary rate of CRR should be comparable to the rate of effective binary recombination at 77 K and $n_e > 10^{10}$ cm^{-3} (see plots in Figs. 11 and 13). We deliberately chose conditions where a large influence of CRR can be expected. We then numerically model afterglow recombination in the presence of electron heating by CRR and compare the results to our experimental data. The evolution of electron density on axis of

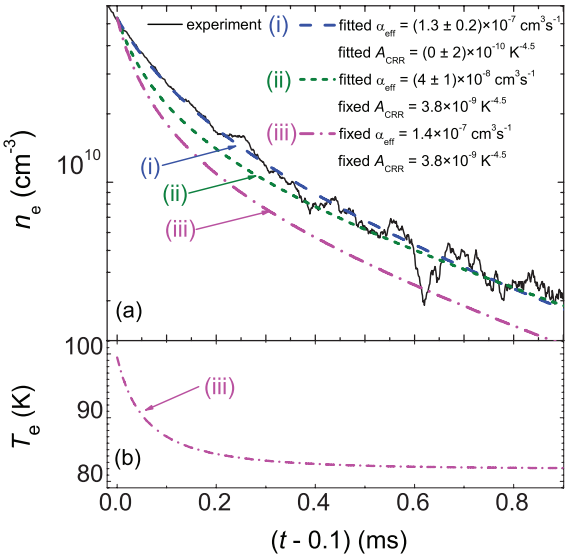

FIG. 14. Model fits of sample data measured in normal hydrogen at 77 K. Panel (a): The dashed line (i) shows the best fit to the data when α_{eff} and A_{CRR} are treated as free parameters. The short dashed line (ii) indicates the best fit when α_{eff} is treated as a free parameter, but A_{CRR} is taken as that given by the Stevefelt formula.[38] The dashed-dotted line (iii) shows model results assuming that both the Stevefelt value of A_{CRR} and the FALP values of α_{eff} (Ref. 34) are correct. Panel (b): The corresponding evolution of the electron temperature calculated for conditions corresponding to fit (iii).

the discharge tube is given by the differential equation (4b) augmented with the CRR term

$$\frac{dn_e}{dt} = -K_{CRR}(T_e)\, n_e^3 - \alpha_{eff} n_e^2 - \frac{n_e}{\tau_D}, \qquad \text{(A3)}$$

where T_e is given by Eq. (A2) and is dependent on n_e. In the numerical models, the value of K_{CRR} was taken as $K_{CRR} = A_{CRR} T_e^{-4.5}$ cm^{6}s^{-1} with either $A_{CRR} = 3.8 \times 10^{-9}$ K$^{4.5}$ or with A_{CRR} as a free fitting parameter.[38] The latter choice is permissible since no accurate measurement or theory of CRR for H_3^+ ions is available. Figure 14 compares numerical fits to sample data measured in normal hydrogen at 77 K. As before, the first 100 μs of the afterglow were excluded to eliminate possible effects of ion formation in the early afterglow.

B.2

It can be seen in Fig. 14 that the best fit to the data is obtained for a value of the CRR coefficient close to zero (line (i) in Fig. 14). The fit obtained under the constraint that K_{CRR} is given by the Stevefelt formula is noticeably worse, even when α_{eff} is reduced (line (ii)). An even worse agreement is obtained when α_{eff} is taken as the FALP value measured previously[34] (see panel (a) of Fig. 11) and the Stevefelt value is used for K_{CRR} (line (iii)). Since the previous FALP measurements were performed at lower electron densities, they should not be affected by CRR even if the Stevefelt value of K_{CRR} is appropriate for H_3^+.

The same fitting procedures were applied to several of our normal and enriched hydrogen datasets and led to the same conclusion that CRR has only a negligible effect. Hence, we did not correct the measured values of α_{eff} for CRR contributions. The apparent absence of CRR is surprising. It is known to occur for atomic ions and the high Rydberg states involved in CRR are essentially the same for molecular ions. On the other hand, it is also possible that the electron temperature in the experimental afterglow plasmas was somewhat higher than we estimate. This would greatly reduce the rate of CRR but make only a minor difference in the dissociative recombination coefficient of H_3^+.

[1] T. Oka, Philos. Trans. R. Soc. London, Ser. A **364**, 2847 (2006).
[2] E. Herbst and W. Klemperer, Astrophys. J. **185**, 505 (1973).
[3] N. Indriolo, G. A. Blake, M. Goto, T. Usuda, T. Oka, T. R. Geballe, B. D. Fields, and B. J. McCall, Astrophys. J. **724**, 1357 (2010).
[4] J. Glosik, Int. J. Mass Spectrom. **1369**, 15 (1994).
[5] K. N. Crabtree, N. Indriolo, H. Kreckel, B. A. Tom, and B. J. McCall, Astrophys. J. **729**, 15 (2011).
[6] S. F. dos Santos, V. Kokoouline, and C. H. Greene, J. Chem. Phys **127**, 124309 (2007).
[7] M. Larsson, Philos. Trans. R. Soc. London, Ser. A **358**, 2433 (2000).
[8] J. Glosik, R. Plasil, T. Kotrik, P. Dohnal, J. Varju, M. Hejduk, I. Korlov, S. Roucka, and V. Kokoouline, Mol. Phys. **108**, 2253 (2010).
[9] R. Plasil, J. Glosik, V. Poterya, P. Kudrna, J. Rusz, M. Tichy, and A. Pysanenko, Int. J. Mass Spectrom. **218**(2), 105 (2002).
[10] D. Smith and P. Spanel, Int. J. Mass Spectrom. **129**, 163 (1993).
[11] R. Johnsen, J. Phys.: Conf. Ser. **4**, 83 (2005).
[12] R. Johnsen and S. L. Guberman, Adv. At., Mol., Opt. Phys. **59**, 75 (2010).
[13] M. Larsson and A. Orel, *Dissociative Recombination of Molecular Ions* (Cambridge University Press, Cambridge, England, 2008).
[14] V. Kokoouline, C. H. Greene, and B. D. Esry, Nature (London) **412**, 891 (2001).
[15] V. Kokoouline and C. H. Greene, Phys. Rev. A **68**, 012703 (2003).
[16] B. J. McCall, A. J. Honeycutt, R. J. Saykally, T. R. Geballe, N. Djuric, G. H. Dunn, J. Semaniak, O. Novotny, A. Al-Khalili, A. Ehlerding, F. Hellberg, S. Kalhori, A. Neau, R. Thomas, F. Osterdahl, and M. Larsson, Nature (London) **422**, 500 (2003).
[17] H. Kreckel, M. Motsch, J. Mikosch, J. Glosik, R. Plasil, S. Altevogt, V. Andrianarijaona, H. Buhr, J. Hoffmann, L. Lammich, M. Lestinsky, I. Nevo, S. Novotny, D. A. Orlov, H. B. Pedersen, F. Sprenger, A. S. Terekhov, J. Toker, R. Wester, D. Gerlich, D. Schwalm, A. Wolf, and D. Zajfman, Phys. Rev. Lett. **95**, 263201 (2005).
[18] B. J. McCall, A. J. Huneycutt, R. J. Saykally, N. Djuric, G. H. Dunn, J. Semaniak, O. Novotny, A. Al-Khalili, A. Ehlerding, F. Hellberg, S. Kalhori, A. Neau, R. Thomas, A. Paal, F. Osterdahl, and M. Larsson, Phys. Rev. A **70**, 052716 (2004).
[19] M. Larsson, B. McCall, and A. Orel, Chem. Phys. Lett. **462**, 145 (2008).
[20] D. R. Bates, M. F. Guest, and R. A. Kendall, Planet. Space Sci. **41**(1), 9 (1993).
[21] H. Kreckel, O. Novotny, K. N. Crabtree, H. Buhr, A. Petrignani, B. A. Tom, R. D. Thomas, M. H. Berg, D. Bing, M. Grieser, C. Krantz, M. Lestinsky, M. B. Mendes, C. Nordhorn, R. Repnow, J. Stutzel, A. Wolf, and B. J. McCall, Phys. Rev. A **82**, 042715 (2010).
[22] A. Petrignani, S. Altevogt, M. H. Berg, D. Bing, M. Grieser, J. Hoffmann, B. Jordon-Thaden, C. Krantz, M. B. Mendes, O. Novotny, S. Novotny, D. A. Orlov, R. Repnow, T. Sorg, J. Stutzel, A. Wolf, H. Buhr, H. Kreckel, V. Kokoouline, and C. H. Greene, Phys. Rev. A **83**, 032711 (2011).
[23] J. Mikosch, H. Kreckel, R. Wester, J. Glosik, R. Plasil, D. Gerlich, D. Schwalm, and A. Wolf, J. Chem. Phys. **121**(22), 11030 (2004).
[24] A. Petrignani, D. Bing, O. Novotny, M. H. Berg, H. Buhr, M. Grieser, B. Jordon-Thaden, C. Krantz, M. B. Mendes, S. Menk, S. Novotny, A. D. A. Orlov, R. Repnow, J. Stutzel, X. Urbain, and A. Wolf, J. Phys. Chem. A **114**, 4864 (2010).
[25] U. Hechtfischer, Z. Amitay, P. Forck, M. Lange, J. Linkemann, M. Schmitt, U. Schramm, D. Schwalm, R. Wester, D. Zajfman, and A. Wolf, Phys. Rev. Lett. **80**, 2809 (1998).
[26] J. Varju, S. Roucka, T. Kotrik, R. Plasil, and J. Glosik, J. Phys.: Conf. Ser. **227**, 012026 (2010).
[27] J. Varju, M. Hejduk, P. Dohnal, M. Jilek, T. Kotrik, R. Plasil, D. Gerlich, and J. Glosik, Phys. Rev. Lett. **106**, 203201 (2011).
[28] D. Smith and P. Spanel, Methods Exp. Phys. **29**(A), 273 (1995).
[29] D. Bates and S. Khare, Proc. Phys. Soc. Lond. **85**, 231 (1965).
[30] D. R. Bates, A. E. Kingston, and W. P. McWhirter, Philos. Trans. R. Soc. London, Ser. A **267**, 297 (1962).

[31] E. W. McDaniel, J. B. A. Mitchell, and M. E. Rudd, *Atomic Collisions, Heavy Partricle Projectiles* (Wiley Interscience, New York, 1993).
[32] T. Kotrik, P. Dohnal, S. Roucka, P. Jusko, R. Plasil, J. Glosik, and R. Johnsen, Phys. Rev. A **83**, 032720 (2011).
[33] J. Glosik, I. Korolov, R. Plasil, O. Novotny, T. Kotrik, P. Hlavenka, J. Varju, I. A. Mikhailov, V. Kokoouline, and C. H. Greene, J. Phys. B **41**, 191001 (2008).
[34] J. Glosik, R. Plasil, I. Korolov, T. Kotrik, O. Novotny, P. Hlavenka, P. Dohnal, J. Varju, V. Kokoouline, and C. Greene, Phys. Rev. A **79**, 052707 (2009).
[35] J. Glosik, I. Korolov, R. Plasil, T. Kotrik, P. Dohnal, O. Novotny, J. Varju, S. Roucka, C. Greene, and V. Kokoouline, Phys. Rev. A **80**, 042706 (2009).
[36] J. Glosik, R. Plasil, I. Korolov, O. Novotny, and T. Kotrik, J. Phys.: Conf. Ser. **192**, 012005 (2009).
[37] T. Kotrik, P. Dohnal, I. Korolov, R. Plasil, S. Roucka, J. Glosik, C. Greene, and V. Kokoouline, J. Chem. Phys. **133**, 034305 (2010).
[38] J. Stevefelt, J. Boulmer, and J. Delpech, Phys. Rev. A **12**, 1246 (1975).
[39] T. Pohl, D. Vrinceanu, and H. R. Sadeghpour, Phys. Rev. Lett. **100**, 223201 (2008).
[40] T. Kotrik, P. Dohnal, P. Rubovic, R. Plasil, S. Roucka, S. Opanasiuk, and J. Glosik, Eur. Phys. J. Appl. Phys. **56**, 24011 (2011).
[41] T. Amano, J. Chem. Phys. **92**, 6492 (1990).
[42] T. Amano, Astrophys. J. **329**, L121 (1988).
[43] M. Hejduk, P. Dohnal, J. Varju, P. Rubovic, R. Plasil, and J. Glosik, Plasma Sources Sci. Technol. **21**, 024002 (2012).
[44] J. Glosik, O. Novotny, A. Pysanenko, P. Zakouril, R. Plasil, P. Kudrna, and V. Poterya, Plasma Sci. Technol. **12**, S117 (2003).
[45] K. N. Crabtree, B. A. Tom, and B. J. McCall, J. Chem. Phys. **134**, 194310 (2011).
[46] K. N. Crabtree, C. Kauffman, B. Tom, E. Beçka, B. McGuire, and B. J. McCall, J. Chem. Phys. **134**, 194311 (2011).
[47] J. Tennyson, see http://www.tampa.phys.ucl.ac.uk/ftp/astrodata/h3+/ for a list of H_3^+ transitions (2011).
[48] P. F. Goldsmith, T. Velusamy, D. Li, and W. D. Langer, Astrophys. J. **715**, 1370 (2010).
[49] J. Glosik, R. Plasil, V. Poterya, P. Kudrna, M. Tichy, and A. Pysanenko, J. Phys. B **34**(15), L485 (2001).
[50] D. Romanini, A. A. Kachanov, N. Sadeghi, and F. Stoeckel, Chem. Phys. Lett. **264**(3-4), 316 (1997).
[51] P. Macko, G. Bano, P. Hlavenka, R. Plasil, V. Poterya, A. Pysanenko, O. Votava, R. Johnsen, and J. Glosik, Int. J. Mass Spectrom. **233**, 299 (2004).
[52] P. Hlavenka, R. Plasil, G. Bano, I. Korolov, D. Gerlich, J. Ramanlal, J. Tennyson, and J. Glosik, Int. J. Mass Spectrom. **255-256**, 170 (2006).
[53] J. Glosik, P. Hlavenka, R. Plasil, F. Windisch, D. Gerlich, A. Wolf, and H. Kreckel, Philos. Trans. R. Soc. London, Ser. A **364**(1848), 2931 (2006).
[54] P. Hlavenka, I. Korolov, R. Plasil, J. Varju, T. Kotrik, and J. Glosik, Czech J. Phys. **56**, B749 (2006).
[55] C. M. Lindsay and B. J. McCall, J. Mol. Spectrosc. **210**, 60 (2001).
[56] L. Neale, S. Miller, and J. Tennyson, Astrophys. J. **464**, 516 (1996).
[57] S. Tam and M. Fajardo, Rev. Sci. Instrum. **70**, 1926 (1999).
[58] B. A. Tom, S. Bashler, Y. Miyamoto, T. Momose, and B. J. McCall, Rev. Sci. Instrum. **80**, 016108 (2009).
[59] J. Lang, private communication (2011).
[60] R. Plasil, P. Hlavenka, P. Macko, G. Bano, A. Pysanenko, and J. Glosik, J. Phys.: Conf. Ser. **4**, 118 (2005).
[61] I. Korolov, T. Kotrik, R. Plasil, J. Varju, M. Hejduk, and J. Glosik, Contrib. Plasma Phys. **48**(5–7), 521 (2008).
[62] R. Plasil, I. Korolov, T. Kotrik, J. Varju, P. Dohnal, Z. Donko, G. Bano, and J. Glosik, J. Phys.: Conf. Ser. **192**, 012023 (2009).
[63] R. Plasil, I. Korolov, T. Kotrik, P. Dohnal, G. Bano, Z. Donko, and J. Glosik, Eur. Phys. J. D **54**, 391 (2009).
[64] J. Glosik, G. Bano, R. Plasil, A. Luca, and P. Zakouril, Int. J. Mass Spectrom. **189**, 103 (1999).
[65] Y. P. Raizer, *Gas Discharge Physics* (Springer–Verlag, Berlin, 1991) p. 14.
[66] J. Kim, L. Theard, and W. Huntres, Int. J. Mass Spectrom. **15**, 223 (1974).
[67] F. B. Yousif, G. Hinojosa, J. de Urquijo, C. Cisneros, and I. Alvarez, Int. J. Mass Spectrom. **171**(1–3), 127 (1997).
[68] E. Ferguson, J. Phys. Chem. **90**, 731 (1986).
[69] R. Plasil, J. Varju, M. Hejduk, P. Dohnal, T. Kotrik, and J. Glosik, J. Phys.: Conf. Ser. **300**(1), 012023 (2011).
[70] M. Quack, Mol. Phys. **34**, 477 (1977).
[71] M. Cordonnier, D. Uy, R. M. Dickson, K. E. Kerr, Y. Zhang, and T. Oka, J. Chem. Phys. **113**, 3181 (2000).
[72] T. Oka and E. Epp, Astrophys. J. **613**, 349 (2004).
[73] D. Gerlich, F. Windisch, P. Hlavenka, R. Plasil, and J. Glosik, Philos. Trans. R. Soc. London, Ser. A **364**, 3007 (2006).
[74] K. Park and J. C. Light, J. Chem. Phys. **126**, 044305 (2007).
[75] E. Hugo, O. Asvany, and S. Schlemmer, J. Chem. Phys. **130**, 164302 (2009).
[76] V. Kokoouline, A. Faure, J. Tennyson, and C. Greene, Mon. Not. R. Astron. Soc. **405**, 1195 (2010).
[77] R. Plasil, I. Korolov, T. Kotrik, and J. Glosik, Int. J. Mass Spectrom. **275**, 80 (2008).
[78] P. Dohnal, M. Hejduk, J. Varju, P. Rubovic, S. Roucka, T. Kotrik, R. Plasil, R. Johnsen, and J. Glosik, "Binary recombination of para and ortho-H_3^+ with electrons at low temperatures," Philos. Trans. R. Soc. London, Ser. A (in press) (Conference Proceeding 2012).
[79] J. Glosik, R. Plasil, A. Pysanenko, O. Novotny, P. Hlavenka, P. Macko, and G. Bano, J. Phys.: Conf. Ser. **4**, 104 (2005).
[80] M. R. Flannery, J. Chem. Phys. **95**(11), 8205 (1991).
[81] R. J. Saykally, E. A. Michael, J. Wang, and C. H. Greene, J. Chem. Phys. **133**, 234302 (2010).
[82] S. Byron, R. C. Stabler, and P. I. Bortz, Phys. Rev. Lett. **8**, 376 (1962).
[83] F. F. Chen, *Introduction to Plasma Physics* (Plenum, New York, 1974).
[84] D. Trunec, P. Spanel, and D. Smith, Chem. Phys. Lett. **372**, 728 (2003).
[85] A. V. Phelps, see http://jila.colorado.edu/~avp/collision_data/ for compilation of electron cross sections (2011)
[86] A. A. Dougal and L. Goldstein, Phys. Rev. **109**, 615 (1958).
[87] J. Ramanlal and J. Tennyson, Mon. Not. R. Astron. Soc. **354**, 161 (2004).

B.3 Binary recombination of para- and ortho-H_3^+ with electrons at low temperatures

P. Dohnal, M. Hejduk, J. Varju, P. Rubovič, Š. Roučka, T. Kotrík, R. Plašil, R. Johnsen and J. Glosík, *Philosophical Transactions of the Royal Society A – Mathematical Physical and Engineering Sciences*, 370(1978):5101–5108, 2012. doi:10.1098/rsta.2012.0097.

PHILOSOPHICAL TRANSACTIONS OF THE ROYAL SOCIETY A

CrossMark click for updates

Phil. Trans. R. Soc. A (2012) **370**, 5101–5108
doi:10.1098/rsta.2012.0097

Binary recombination of para- and ortho-H_3^+ with electrons at low temperatures

By P. Dohnal[1], M. Hejduk[1], J. Varju[1], P. Rubovič[1,*], Š. Roučka[1], T. Kotrík[1], R. Plašil[1], R. Johnsen[2] and J. Glosík[1]

[1]*Faculty of Mathematics and Physics, Department of Surface and Plasma Science, Charles University, Prague, Czech Republic*
[2]*Department of Physics and Astronomy, University of Pittsburgh, Pittsburgh, PA 15260, USA*

Results of an experimental study of binary recombination of para- and ortho-H_3^+ ions with electrons are presented. Near-infrared cavity-ring-down absorption spectroscopy was used to probe the lowest rotational states of H_3^+ ions in the temperature range of 77–200 K in an H_3^+-dominated afterglow plasma. By changing the para/ortho abundance ratio, we were able to obtain the binary recombination rate coefficients for pure para-H_3^+ and ortho-H_3^+. The results are in good agreement with previous theoretical predictions.

Keywords: H_3^+; dissociative recombination; cavity ring down spectroscopy; afterglow plasma

1. Introduction

The fundamental characteristics of the H_3^+ dissociative recombination (DR) [1] have been the subject of much interest for both theoretical and experimental physicists [2]. The discrepancies between measurements of the binary dissociative reaction rate and the theoretical complexity of this seemingly simple reaction led to a great deal of fruitful research on this process. The history of H_3^+ recombination studies has been adequately covered in several review articles [3–9]. Recently, both theory and experiment have converged to a value for the rate of this particular reaction. The theoretical treatment took a crucial leap forward in the understanding of the DR process after including the Jahn–Teller mechanism as the critical step in the initial electron-capture step of the DR reaction [10]. This resulted in a convergence with experimental DR data reported from ion storage rings where experimentalists had realized the impact of rotational excitation of the H_3^+ ions on the DR reaction rate, especially with respect to the importance of the DR process in interstellar molecular clouds [11–13]. Final convergence between theory and the remaining important experimental techniques, stationary and flowing afterglow, was reached after recognizing that a

*Author for correspondence (peter.rubovic@gmail.com).

One contribution of 21 to a Theo Murphy Meeting Issue ‘Chemistry, astronomy and physics of H_3^+’.

fast third-body reaction, not previously considered, stabilizes the recombination process in such plasmas [4,14,15]. However, recently it has been shown [16,17] that the assumption of rotationally cold H_3^+ ions in storage rings was not entirely correct [17]. This is important if we realize that the quantum mechanical calculations [18] predict a large difference in the low-temperature recombination of ions in para-H_3^+ and ortho-H_3^+ states. This has been qualitatively confirmed in storage-ring experiments using hydrogen with an enriched para fraction [12,13,19]. However, as has just been stated, the actual rotational population of the recombining ions has not been proved experimentally. In the present experiments, the stationary afterglow (SA) technique with spectroscopic *in situ* determination of the abundances of the recombining ions was used. Near-infrared cavity-ring-down absorption spectroscopy (NIR-CRDS) enabled *in situ* determination of the spin states, together with the kinetic and the rotational temperatures of the recombining ions. A similar approach was used in our recent study of binary recombination of para-H_3^+ and ortho-H_3^+ ions at temperatures close to 77 K [20]. In the present studies, we have extended the range of temperatures up to 200 K. Our previous measurements in H_3^+- and D_3^+-dominated plasmas at conditions similar to those in the present experiment [4,14,15,21,22] have shown that the H_3^+ ions recombine by both a binary process with a rate coefficient α_{bin}, and a ternary helium-assisted recombination mechanism, with a rate coefficient K_{He}. The plasma decay can then be described by an overall effective recombination rate coefficient:

$$\alpha_{\mathrm{eff}} = \alpha_{\mathrm{bin}} + K_{\mathrm{He}}[\mathrm{He}]. \tag{1.1}$$

Both rate coefficients can be obtained by measuring the dependence of α_{eff} on the helium density [He]. The possible effects of another ternary process—collisional radiative recombination (CRR) [23,24]—are discussed in detail elsewhere [25].

In the following, we will use left indices p, o, n and e to denote 'para', 'ortho', 'normal' and 'para-enriched' hydrogen (i.e. ${}^{\mathrm{p}}H_2$, ${}^{\mathrm{o}}H_2$, ${}^{\mathrm{n}}H_2$ and ${}^{\mathrm{e}}H_2$) and ${}^{\mathrm{p}}f_2$ and ${}^{\mathrm{o}}f_2$ to denote para and ortho fractions. ${}^{\mathrm{p}}H_3^+$ and ${}^{\mathrm{o}}H_3^+$ stand for para-H_3^+ and ortho-H_3^+, while ${}^{\mathrm{p}}f_3$ and ${}^{\mathrm{o}}f_3$ denote their fractions (i.e. ${}^{\mathrm{p}}f_3 = [{}^{\mathrm{p}}H_3^+]/[H_3^+]$ and ${}^{\mathrm{o}}f_3 = [{}^{\mathrm{o}}H_3^+]/[H_3^+]$). If an index is missing, then the spin modification is not specified. Assuming that the plasma is quasi-neutral and that it contains no ions other than H_3^+ (i.e. $n_{\mathrm{e}} = [{}^{\mathrm{p}}H_3^+] + [{}^{\mathrm{o}}H_3^+]$), then following the derivation in the study of Varju *et al.* [20], we can write the continuity equation for the electron number density n_{e}:

$$\frac{\mathrm{d}n_{\mathrm{e}}}{\mathrm{d}t} = -({}^{\mathrm{p}}\alpha_{\mathrm{eff}}\,{}^{\mathrm{p}}f_3 + {}^{\mathrm{o}}\alpha_{\mathrm{eff}}\,{}^{\mathrm{o}}f_3)\,n_{\mathrm{e}}^2 - \frac{n_{\mathrm{e}}}{\tau_{\mathrm{D}}} = -\alpha_{\mathrm{eff}}\,n_{\mathrm{e}}^2 - \frac{n_{\mathrm{e}}}{\tau_{\mathrm{D}}}, \tag{1.2}$$

where ${}^{\mathrm{o}}\alpha_{\mathrm{eff}}$ and ${}^{\mathrm{p}}\alpha_{\mathrm{eff}}$ are the state-selected effective recombination rate coefficients for ${}^{\mathrm{o}}H_3^+$ and ${}^{\mathrm{p}}H_3^+$, respectively, $\alpha_{\mathrm{eff}} = {}^{\mathrm{p}}f_3\,{}^{\mathrm{p}}\alpha_{\mathrm{eff}} + {}^{\mathrm{o}}f_3\,{}^{\mathrm{o}}\alpha_{\mathrm{eff}}$ is the overall (apparent binary) recombination rate coefficient for a given mixture of ortho and para ions, and τ_{D} is the characteristic time constant of the ambipolar diffusion. A linear relation similar to equation (1.2) holds also for ${}^{\mathrm{p}}\alpha_{\mathrm{eff}}$ and ${}^{\mathrm{o}}\alpha_{\mathrm{eff}}$ [20].

The data (see §3) show that at the H_2 and He densities used in the experiment, the fractions ${}^{\mathrm{p}}f_3$ and ${}^{\mathrm{o}}f_3$ are nearly constant during the afterglow. A measurement of α_{eff} for two or more different values of ${}^{\mathrm{p}}f_3$, but under otherwise identical conditions (temperature, and density of He and H_2), then permits a determination

of the individual recombination rate coefficients ${}^{\mathrm{p}}\alpha_{\mathrm{eff}}$ and ${}^{\mathrm{o}}\alpha_{\mathrm{eff}}$. The fraction ${}^{\mathrm{p}}f_3$ can be enhanced from about 0.5 to 0.8 by using para-enriched hydrogen instead of normal hydrogen (for details, see [20,26]).

2. Experimental apparatus

The experimental apparatus is the same as that in our previous studies [20,26]. A pulsed microwave discharge generates a plasma in a tube (inner diameter of approx. 1.5 cm) cooled by liquid nitrogen. A mixture of He/Ar/H_2 with a typical composition $10^{17}/10^{14}/10^{14}\,\mathrm{cm}^{-3}$ flows continuously along the discharge tube. Details of the ion formation reactions are given elsewhere [4,5,27]. 'A para-hydrogen generator' prepares samples of para-enriched H_2 (${}^{\mathrm{e}}H_2$) [26]. The enrichment was measured by nuclear magnetic resonance spectroscopy (RNDr Jan Lang PhD 2010, personal communication). NIR-CRDS in the continuous wave modification (based on the configuration described by Romanini *et al.* [28]) was developed in our laboratory for time-resolved studies [26,29,30]. The light source is a fibre-coupled distributed feedback laser diode with a central wavelength of 1381.55 nm, line-width less than 2 MHz, and maximum output optical power of 20 mW. During the experiment, the time-dependent optical absorption signals from the discharge and the afterglow are recorded. The measured absorption is then converted to ion concentrations. The kinetic temperature of the H_3^+ ions and its evolution during the discharge and in the early afterglow were determined from the Doppler-broadened absorption line profiles by tuning the wavelength of the laser diode. All spectroscopic absorption measurements were performed on the second overtone transitions originating from the ground vibrational level of H_3^+. The lowest rotational levels (1,0) (ortho, transition $3v_2^1(2,0) \leftarrow 0v_2^0(1,0)$) and (1,1) (para, transition $3v_2^1(2,1) \leftarrow 0v_2^0(1,1)$) of the vibrational ground state were monitored routinely. In some experiments, we also probed the higher-lying level (3,3) (ortho, transition $3v_2^1(4,3) \leftarrow 0v_2^0(3,3)$). Here, and in the following discussion, the energy levels are labelled (J, G) by their quantum numbers J and G.

B.3

3. Experimental results: binary recombination of para-H_3^+ and ortho-H_3^+

The measured electron density decay curves were analysed to obtain α_{eff} for two particular values of ${}^{\mathrm{p}}f_3$ (further details can also be found in the study of Varju *et al.* [20]). We carried out a systematic set of measurements that differed only in the value of ${}^{\mathrm{p}}f_2$ (${}^{\mathrm{p}}f_2 = 0.25$ when using ${}^{\mathrm{n}}H_2$ and ${}^{\mathrm{p}}f_2 = 0.87$ using ${}^{\mathrm{e}}H_2$), but under otherwise very similar conditions. The densities of the para (1,1), ortho (1,0) and ortho (3,3) states of H_3^+ were monitored. Examples of data measured at 140 K with ${}^{\mathrm{n}}H_2$ and with ${}^{\mathrm{e}}H_2$ are plotted in figure 1*a*,*b*, respectively. The middle panels of figure 1*a*,*b* show a large difference in the measured populations of the particular rotational states of H_3^+ in both experiments. In this set of experiments, we obtained ${}^{\mathrm{p}}f_3 \sim 0.5$ for ${}^{\mathrm{n}}H_2$, and ${}^{\mathrm{p}}f_3 \sim 0.7$ for ${}^{\mathrm{e}}H_2$ (see the lower panels). Note that in both experiments, the values of ${}^{\mathrm{p}}f_3$ are nearly constant during the afterglow.

Assuming thermal equilibrium (TDE) within the para and ortho manifolds, we calculated from the densities of the ions in the (1,1) and (1,0) states the

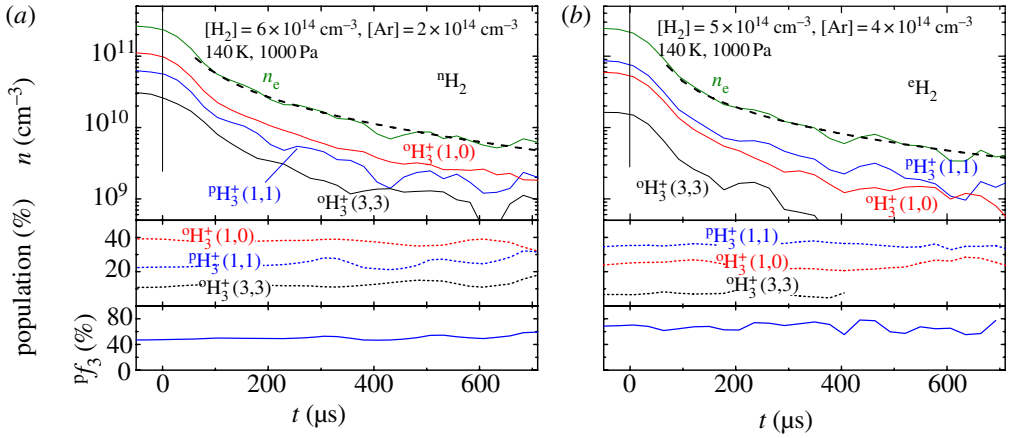

Figure 1. (*a*) Upper panel: a typical example of the ion and electron decay curves measured during the afterglow in a He/Ar/$^{n}H_2$ gas mixture. The time $t = 0$ is taken to be at the beginning of the afterglow when the discharge is switched off. The measurements were made at 140 K and 1000 Pa of He and at the indicated densities of H_2 and Ar. Middle panel: the measured relative populations of the para (1,1), ortho (1,0) and ortho (3,3) states of H_3^+. Lower panel: the measured fraction of $^{p}f_3$ of $^{p}H_3^+$. Note the constant value of $^{p}f_3$ during the afterglow. (*b*) Similar to (*a*), but for data measured in a He/Ar/$^{e}H_2$ gas mixture. (Online version in colour.)

total densities [$^{p}H_3^+$], [$^{o}H_3^+$] and n_e. We have proved experimentally [25,26] that the assumption of TDE under our experimental conditions is correct. To obtain α_{eff} from the measured electron density decay curves, we used direct fits to the data and, in addition, the more advanced 'integral analysis' technique [31]. We deliberately excluded the first 50–150 μs of the afterglow decay from the data analysis because some new ions were probably still being formed (for details see [4,20,26,31]). The observed dependences of $^{n}\alpha_{eff}$ and $^{e}\alpha_{eff}$ on [He] at 140 K are shown in figure 2*a*. The corresponding fractions $^{p}f_3$ are shown in figure 2*c*. Because $^{n}\alpha_{eff}$ and $^{e}\alpha_{eff}$ increase linearly with increasing [He], we can use equation (1.1) to obtain binary and ternary recombination rate coefficients for known para/ortho ratios. The values obtained with normal hydrogen ($^{p}f_3 = 0.5$) correspond to those expected under TDE. The present experiments with $^{n}H_2$ also confirmed that $^{p}f_3$ was 0.5 in our previous flowing afterglow with Langmuir probe (FALP) experiments [4,14,15,32]. Hence, the values of α_{bin} and K_{He} from these experiments correspond to TDE.

The dependences of $^{n}\alpha_{eff}$ and $^{e}\alpha_{eff}$ on [He] were measured for four temperatures in the 77–200 K range. From those dependences and from the corresponding $^{p}f_3$, we calculated the values of $^{p}\alpha_{eff}$ and $^{o}\alpha_{eff}$ for pure $^{p}H_3^+$ and for pure $^{o}H_3^+$, respectively. The binary recombination rate coefficients for pure $^{p}H_3^+$ and for pure $^{o}H_3^+$ were obtained by fitting the values of $^{p}\alpha_{eff}$ and $^{o}\alpha_{eff}$ (figure 2*b*) using equation (1.1). For further details on the data analysis, see Varju *et al.* [20]. The measured values of $^{p}\alpha_{bin}$, $^{o}\alpha_{bin}$, $^{n}\alpha_{bin}$ and values of $^{n}\alpha_{bin}$ from previous FALP experiments [4,14,15] are plotted in figure 3. The displayed errors of rate coefficients are 1σ errors, and systematic errors (mainly from determination of ion number densities) were estimated to be less than 10 per cent.

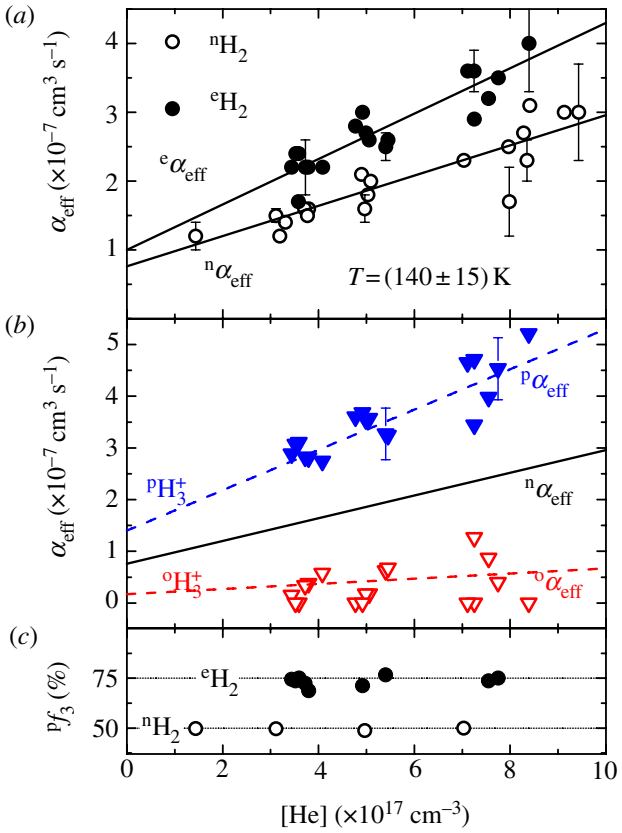

Figure 2. The measured dependences of the effective recombination rate coefficients on the He density at 140 K. (*a*) α_{eff} measured using $^{n}H_2$ (open circles) and α_{eff} measured using $^{e}H_2$ (filled circles). (*b*) The measured values $^{p}\alpha_{eff}$ and $^{o}\alpha_{eff}$ for pure $^{p}H_3^+$ (filled triangles) and pure $^{o}H_3^+$ (open triangles), respectively. (*c*) The fractions $^{p}f_3$ of $^{p}H_3^+$ measured in the experiments with $^{n}H_2$ and $^{e}H_2$. (Online version in colour.)

4. Discussion and conclusion

B.3

By using either normal or para-enriched hydrogen gas, we were able to form plasmas with different partial populations of $^{p}H_3^+$ (fractions, $^{p}f_3$) and $^{o}H_3^+$, and from the measured decay of the ion density, we evaluated the binary recombination rate coefficients for pure $^{p}H_3^+$ and $^{o}H_3^+$ ions. The temperature range covered in this study was 77–200 K. The results of this study show a strong dependence of the low-temperature binary recombination of H_3^+ ions on the nuclear spin states of the ions. The agreement between the experimental values ($^{n}\alpha_{bin}$, $^{p}\alpha_{bin}$ and $^{o}\alpha_{bin}$) and the theoretical values ($^{n}\alpha_{DR}$, $^{p}\alpha_{DR}$ and $^{o}\alpha_{DR}$) [18] is very good. Moreover, though the electron number density used in the present experiment was by an order of magnitude higher than in our previous FALP experiments using Langmuir probes [14], the agreement between the present $^{n}\alpha_{bin}$ values and those from the FALP experiments is very good over the whole temperature range. Because of this agreement at higher temperatures, where CRR is negligible, we conclude that the measured rate coefficients at 77 K do not depend on the electron density. From this, it follows that CRR has little to no effect on the plasma decay and that the obtained recombination rate coefficients

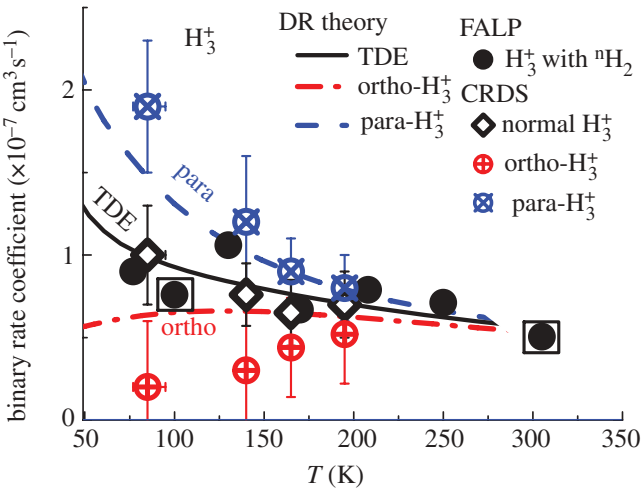

Figure 3. The measured temperature dependences of the binary recombination rate coefficients $^n\alpha_{bin}$, $^p\alpha_{bin}$ and $^o\alpha_{bin}$. 'Normal-H_3^+' refers to data measured in the present experiments with $^nH_2$. Previous FALP data [4,14,15] measured with $^nH_2$ are indicated by filled circles. Combined SA-CRDS/FALP data at 100 K and 305 K [4,14] are indicated by a filled circle in a square. The lines indicate the theoretical rate coefficients for $^pH_3^+$, $^oH_3^+$ and for H_3^+ ions in TDE [18]. (Online version in colour.)

$^p\alpha_{bin}$ and $^o\alpha_{bin}$ correspond to the binary DR (for details see discussion in the study of Dohnal *et al.* [25]). Further results concerning ternary recombination have been published elsewhere [25], together with a detailed discussion of the equilibrium conditions in the recombining afterglow plasma and with an estimation of the effect of the CRR process.

This work was partly financed by the research grant OC10046 from the Ministry of Education of the Czech Republic and was partly supported by GACR (205/09/1183, P209/12/0233), by SV 265 302, by GAUK 92410, GAUK 353811, GAUK 54010 and by COST Action CM0805 (The Chemical Cosmos).

B.3

References

1 Oka, T. 2006 Introductory remarks. *Phil. Trans. R. Soc. A* **364**, 2847–2853. (doi:10.1098/rsta.2006.1870)
2 Herbst, E. & Klemperer, W. 1973 The formation and depletion of molecules in dense interstellar clouds. *Astrophys. J.* **185**, 505–533. (doi:10.1086/152436)
3 Larsson, M. 2000 Experimental studies of the dissociative recombination of H_3^+. *Phil. Trans. R. Soc. Lond. A* **358**, 2433–2444. (doi:10.1098/rsta.2000.0658)
4 Glosík, J., Plašil, R., Kotrík, T., Dohnal, P., Varju, J., Hejduk, M., Korolov, I., Roučka, Š. & Kokoouline, V. 2010 Binary and ternary recombination of H_3^+ and D_3^+ ions with electrons in low temperature plasma. *Mol. Phys.* **108**, 2253–2264. (doi:10.1080/00268976.2010.507555)
5 Plašil, R., Glosík, J., Poterya, V., Kudrna, P., Rusz, J., Tichý, M. & Pysanenko, A. 2002 Advanced integrated stationary afterglow method for experimental study of recombination of processes of H_3^+ and D_3^+ ions with electrons. *Int. J. Mass Spectrom.* **218**, 105–130. (doi:10.1016/S1387-3806(02)00714-5)
6 Smith, D. & Španěl, P. 1993 Dissociative recombination of H_3^+ and some other interstellar ions: a controversy resolved. *Int. J. Mass Spectrom. Ion Process.* **129**, 163–182. (doi:10.1016/0168-1176(93)87040-Y)

7 Johnsen, R. 2005 A critical review of H_3^+ recombination studies. *J. Phys. Conf. Ser.* **4**, 83–91. (doi:10.1088/1742-6596/4/1/011)
8 Johnsen, R. & Guberman, S. L. 2010 Dissociative recombination of H_3^+ ions with electrons: theory and experiment. In *Advances in atomic, molecular, and optical physics*, vol. 59 (eds E. Arimondo, P. R. Berman & C. C. Lin), pp. 75–128. New York, NY: Academic Press.
9 Larsson, M. & Orel, A. E. 2008 *Dissociative recombination of molecular ions*. Cambridge, UK: Cambridge University Press.
10 Kokoouline, V. & Greene, C. H. 2003 Unified theoretical treatment of dissociative recombination of D_{3h} triatomic ions: application to H_3^+ and D_3^+. *Phys. Rev. A* **68**, 012703. (doi:10.1103/PhysRevA.68.012703)
11 McCall, B. J. *et al.* 2003 An enhanced cosmic-ray flux towards ζ Persei inferred from a laboratory study of the H_3^+–e^- recombination rate. *Nature* **422**, 500–502. (doi:10.1038/nature01498)
12 Kreckel, H. *et al.* 2005 High-resolution dissociative recombination of cold H_3^+ and first evidence for nuclear spin effects. *Phys. Rev. Lett.* **95**, 263201. (doi:10.1103/PhysRevLett.95.263201)
13 McCall, B. J. *et al.* 2004 Dissociative recombination of rotationally cold H_3^+. *Phys. Rev. A* **70**, 052716. (doi:10.1103/PhysRevA.70.052716)
14 Glosík, J. *et al.* 2009 Temperature dependence of binary and ternary recombination of H_3^+ ions with electrons. *Phys. Rev. A* **79**, 052707. (doi:10.1103/PhysRevA.79.052707)
15 Glosík, J. *et al.* 2008 Recombination of H_3^+ ions in the afterglow of a He–Ar–H_2 plasma. *J. Phys. B* **41**, 191001. (doi:10.1088/0953-4075/41/19/191001)
16 Kreckel, H. *et al.* 2010 High-resolution storage-ring measurements of the dissociative recombination of H_3^+ using a supersonic expansion ion source. *Phys. Rev. A* **82**, 042715. (doi:10.1103/PhysRevA.82.042715)
17 Petrignani, A. *et al.* 2011 Resonant structure of low-energy H_3^+ dissociative recombination. *Phys. Rev. A* **83**, 032711. (doi:10.1103/PhysRevA.83.032711)
18 dos Santos, S. F., Kokoouline, V. & Greene, C. H. 2007 Dissociative recombination of H_3^+ in the ground and excited vibrational states. *J. Chem. Phys.* **127**, 124309. (doi:10.1063/1.2784275)
19 Mikosch, J., Kreckel, H., Wester, R., Glosík, J., Plašil, R., Gerlich, D., Schwalm, D. & Wolf, A. 2004 Action spectroscopy and temperature diagnostics of H_3^+ by chemical probing. *J. Chem. Phys.* **121**, 11 030–11 037. (doi:10.1063/1.1810512)
20 Varju, J., Hejduk, M., Dohnal, P., Jílek, M., Kotrík, T., Plašil, R., Gerlich, D. & Glosík, J. 2011 Nuclear spin effect on recombination of H_3^+ ions with electrons at 77 K. *Phys. Rev. Lett.* **106**, 203201. (doi:10.1103/PhysRevLett.106.203201)
21 Glosík, J. *et al.* 2009 Binary and ternary recombination of D_3^+ ions with electrons in He–D_2 plasma. *Phys. Rev. A* **80**, 042706. (doi:10.1103/PhysRevA.80.042706)
22 Kotrík, T., Dohnal, P., Korolov, I., Plašil, R., Roučka, S., Glosík, J., Greene, C. H. & Kokoouline, V. 2010 Temperature dependence of binary and ternary recombination of D_3^+ ions with electrons. *J. Chem. Phys.* **133**, 034305. (doi:10.1063/1.3457940)
23 Bates, D. R., Kingston, A. E. & McWhirter, R. W. P. 1962 Recombination between electrons and atomic ions. I. Optically thin plasmas. *Proc. R. Soc. Lond. A* **267**, 297–312. (doi:10.1098/rspa.1962.0101)
24 Kotrík, T., Dohnal, P., Roučka, Š., Jusko, P., Plašil, R., Glosík, J. & Johnsen, R. 2011 Collisional-radiative recombination $Ar^+ + e + e$: experimental study at 77–180 K. *Phys. Rev. A* **83**, 032720. (doi:10.1103/PhysRevA.83.032720)
25 Dohnal, P., Hejduk, M., Varju, J., Rubovič, P., Roučka, Š., Kotrík, T., Plašil, R., Glosík, J. & Johnsen, R. 2012 Binary and ternary recombination of para- and ortho-H_3^+ with electrons: state selective study at 77–200 K. *J. Chem. Phys.* **136**, 244304. (doi:10.1063/1.4730162)
26 Hejduk, M., Dohnal, P., Varju, J., Rubovič, P., Kotrik, T., Plašil, R. & Glosík, J. 2012 Nuclear spin state-resolved cavity ring-down spectroscopy diagnostics of a low-temperature H_3^+-dominated plasma. *Plasma Sources Sci. Technol.* **21**, 024002. (doi:10.1088/0963-0252/21/2/024002)
27 Glosík, J., Plašil, R., Poterya, V., Kudrna, P., Tichý, M. & Pysanenko, A. 2001 Experimental study of recombination of H_3^+ ions with electrons relevant for interstellar and planetary plasmas. *J. Phys. B* **34**, L485–L494. (doi:10.1088/0953-4075/34/15/104)

28 Romanini, D., Kachanov, A. A., Sadeghi, N. & Stoeckel, F. 1997 CW cavity ring down spectroscopy. *Chem. Phys. Lett.* **264**, 316–322. (doi:10.1016/S0009-2614(96)01351-6)
29 Macko, P., Bano, G., Hlavenka, P., Plašil, R., Poterya, V., Pysanenko, A., Votava, O., Johnsen, R. & Glosík, J. 2004 Afterglow studies of H_3^+ ($\nu = 0$) recombination using time resolved cw-diode laser cavity ring-down spectroscopy. *Int. J. Mass Spectrom.* **233**, 299–304. (doi:10.1016/j.ijms.2003.12.035)
30 Hlavenka, P., Plašil, R., Bano, G., Korolov, I., Gerlich, D., Ramanlal, J., Tennyson, J. & Glosík, J. 2006 Near infrared second overtone cw-cavity ringdown spectroscopy of D_2H^+ ions. *Int. J. Mass Spectrom.* **255**–**256**, 170–176. (doi:10.1016/j.ijms.2006.02.002)
31 Plašil, R., Korolov, I., Kotrík, T. & Glosík, J. 2008 Recombination of KrD^+ and XeD^+ ions with electrons. *Int. J. Mass Spectrom.* **275**, 80–85. (doi:10.1016/j.ijms.2008.05.037)
32 Glosík, J., Plašil, R., Korolov, I., Novotný, O. & Kotrík, T. 2009 Multicollision character of recombination of H_3^+ ions in afterglow plasma. *J. Phys. Conf. Ser.* **192**, 012005. (doi:10.1088/1742-6596/192/1/012005)

B.3

B.4 Nuclear Spin Effect on Recombination of H_3^+ Ions with Electrons at 77 K

J. Varju, M. Hejduk, P. Dohnal, M. Jílek, T. Kotrík, R. Plašil, D. Gerlich and J. Glosík, *Physical Review Letters*, 106(20), 2011. doi:10.1103/PhysRevLett.106.203201.

Nuclear Spin Effect on Recombination of H_3^+ Ions with Electrons at 77 K

J. Varju, M. Hejduk, P. Dohnal, M. Jílek, T. Kotrík, R. Plašil, D. Gerlich, and J. Glosík
Charles University, Faculty of Mathematics and Physics, Prague, Czech Republic
(Received 13 September 2010; published 17 May 2011)

Utilizing different ratios of para to ortho H_2 in normal and para enriched hydrogen, we varied the population of para-H_3^+ in an H_3^+ dominated plasma at 77 K. Absorption spectroscopy was used to measure the densities of the two lowest rotational states of H_3^+. Monitoring plasma decays at different populations of para-H_3^+ allowed us to determine the rate coefficients for binary recombination of para-H_3^+ and ortho-H_3^+ ions: ${}^p\alpha_{\mathrm{bin}}(77\,\mathrm{K}) = (1.9 \pm 0.4) \times 10^{-7}\,\mathrm{cm^3\,s^{-1}}$ and ${}^o\alpha_{\mathrm{bin}}(77\,\mathrm{K}) = (0.2 \pm 0.2) \times 10^{-7}\,\mathrm{cm^3\,s^{-1}}$.

DOI: 10.1103/PhysRevLett.106.203201 PACS numbers: 34.80.Lx, 34.80.Nz, 52.72.+v, 95.30.Ft

Introduction.—H_3^+ is the dominant ion in many types of hydrogen-containing plasmas including astrophysically relevant plasmas [1,2]. It is the simplest polyatomic ion; its properties are well known [3,4]. The recombination of H_3^+ has been studied for over 50 years [5,6]. Only recently, the process of binary dissociative recombination (DR) of H_3^+ was described by going beyond the Born-Oppenheimer approximation and accounting for Jahn-Teller coupling [7]. The calculated cross sections [8,9] and the cross sections measured recently in storage ring experiments are approaching each other [10,11]. Presently, no reliable rate coefficient measured with storage rings below 300 K exists [12,13]. Only two years ago, it was demonstrated that the recombination rate coefficients (effective α_{eff}) determined from plasma decay during an afterglow are composed of the binary and ternary process [14]. Taking this into the account, an agreement between experimental and calculated (DR) rate coefficients has been achieved for 77–300 K [15–19].

For temperatures below 300 K, the theory [9] of DR of H_3^+ predicts different values of recombination rate coefficients for different nuclear spin states of H_3^+ (${}^p\alpha_{\mathrm{DR}}$ and ${}^o\alpha_{\mathrm{DR}}$ for para-H_3^+ with a total nuclear spin quantum number $I = 1/2$ and ortho-H_3^+ with $I = 3/2$, respectively). The qualitative reason is that at small collisional energies there are more Rydberg resonances of the neutral para-H_3 that can be populated during the electron-ion collisions. It is because there are more low energy rotational states of the ground vibrational state of para-H_3^+, for example, $(J, K) = (2, 2)$ and $(2, 1)$ (corresponding to energy of $\sim$151 and 249 K). For ortho-H_3^+, the lowest rotational states of the ground vibrational state have relatively higher energies [for example, $(3, 0)$ corresponds to $\sim$650 K]. More Rydberg resonances in para-H_3 enhances DR cross sections in para-H_3^+ more than in ortho-H_3^+ at low temperatures (< 200 K). The difference between ${}^p\alpha_{\mathrm{DR}}$ and ${}^o\alpha_{\mathrm{DR}}$ was partly confirmed by storage ring experiments [10].

The recent observations made towards several diffuse molecular clouds showed a large difference between excitation temperatures $T_{10}(H_2)$ and $T(H_3^+)$ derived from the relative intensities of lowest rotational levels of H_2 and H_3^+, respectively (for details, see Ref. [20]). These observations lead to the conclusion that in a reliable chemical model the nuclear spin dependences of the reactions, including recombination of para- and ortho-H_3^+, have to be considered. The dependences on spin, rotational excitation, and temperature have to be measured.

In this Letter, we report results of our pursuit of measuring the recombination rate coefficients ${}^p\alpha$ and ${}^o\alpha$ of pure para-H_3^+ and pure ortho-H_3^+. This is achieved by *in situ* determination of para-H_3^+ and ortho-H_3^+ densities in an H_3^+ dominated and recombination governed plasma in a He-Ar-H_2 mixture at 77 K. In the following, we will use upper left index p, o, n, and e to indicate "para," "ortho," "normal," and "para enriched," respectively, e.g., ${}^pH_2$, ${}^oH_2$, ${}^nH_2$, and ${}^eH_2$. For para-H_3^+ and ortho-H_3^+ ions we use ${}^pH_3^+$ and ${}^oH_3^+$. Symbols ${}^pf$ and ${}^of$ denote relative populations (fractions, ${}^pf + {}^of = 1$) of H_3^+ ions in the para and ortho state, respectively (i.e., ${}^pf = [{}^pH_3^+]/[H_3^+]$ and ${}^of = [{}^oH_3^+]/[H_3^+]$). Normal (${}^nH_2$) and para enriched (${}^eH_2$) hydrogen were used in the experiments. In ${}^nH_2$, 1/4 of the H_2 molecules are in para and 3/4 in ortho states. In a low temperature hydrogen afterglow plasma, the main processes determining the density of ${}^pH_3^+$ and ${}^oH_3^+$ are diffusion and the following processes:

$$\begin{aligned} {}^pH_3^+ + e &\xrightarrow{{}^p\alpha_{\mathrm{eff}}} \text{neutral products}, \\ {}^oH_3^+ + e &\xrightarrow{{}^o\alpha_{\mathrm{eff}}} \text{neutral products}, \\ {}^pH_3^+ &\underset{\nu_{op}}{\overset{\nu_{po}}{\rightleftarrows}} {}^oH_3^+, \end{aligned} \tag{1}$$

where ${}^p\alpha_{\mathrm{eff}}$ and ${}^o\alpha_{\mathrm{eff}}$ are the effective rate coefficients of the overall recombination of ${}^pH_3^+$ and ${}^oH_3^+$, respectively. ν_{po} and ν_{op} are frequencies of ${}^pH_3^+$ to ${}^oH_3^+$ transitions and vice versa. If collisions with ${}^pH_2$ and ${}^oH_2$ dominate such processes, then ν_{po} and ν_{op} can be expressed as $\nu = k[{}^{p,o}H_2]$ where k is a rate coefficient of the corresponding

B.4

nuclear spin changing reaction. The balance equations for ${}^{p}H_3^+$ and ${}^{o}H_3^+$ are

$$\frac{d[{}^{p}H_3^+]}{dt} = -{}^{p}\alpha_{\text{eff}}[{}^{p}H_3^+]n_e - \frac{[{}^{p}H_3^+]}{\tau_D} - \nu_{\text{po}}[{}^{p}H_3^+] + \nu_{\text{op}}[{}^{o}H_3^+], \quad (2)$$

$$\frac{d[{}^{o}H_3^+]}{dt} = -{}^{o}\alpha_{\text{eff}}[{}^{o}H_3^+]n_e - \frac{[{}^{o}H_3^+]}{\tau_D} - \nu_{\text{op}}[{}^{o}H_3^+] + \nu_{\text{po}}[{}^{p}H_3^+], \quad (3)$$

where τ_D is the time constant of ambipolar diffusion. If $[{}^{p}H_3^+] + [{}^{o}H_3^+] = n_e$, then we obtain by summing Eqs. (2) and (3)

$$\frac{dn_e}{dt} = -({}^{p}\alpha_{\text{eff}}{}^{p}f + {}^{o}\alpha_{\text{eff}}{}^{o}f)n_e^2 - \frac{n_e}{\tau_D} = -\alpha_{\text{eff}}n_e^2 - \frac{n_e}{\tau_D}. \quad (4)$$

We see that α_{eff} determined from the decay of n_e [21] depends on ${}^{p}f$, ${}^{o}f$, ${}^{p}\alpha_{\text{eff}}$, and ${}^{o}\alpha_{\text{eff}}$. If ${}^{p}f$ and ${}^{o}f$ are constant during the afterglow, the decay can be described by an effective recombination rate coefficient $\alpha_{\text{eff}} = {}^{p}\alpha_{\text{eff}}{}^{p}f + {}^{o}\alpha_{\text{eff}}{}^{o}f$. If α_{eff} is measured at least for two different values of ${}^{p}f$, one can derive ${}^{p}\alpha_{\text{eff}}$ and ${}^{o}\alpha_{\text{eff}}$. The overall recombination includes a binary and a ternary helium assisted recombination [15–18]. In the first approximation we can write

$$\alpha_{\text{eff}}(T, [\text{He}]) = \alpha_{\text{bin}}(T) + K_{\text{He}}(T)[\text{He}], \quad (5)$$

where α_{bin} and K_{He} are the corresponding rate coefficients; a similar relation can be written for ${}^{p}\alpha_{\text{eff}}$ and ${}^{o}\alpha_{\text{eff}}$.

Because of the weak coupling of the nuclear spin to the remaining degrees of freedom in H_3^+ and H_2, the probability of changing the nuclear spin by radiation is very low. In the present experiment, the main nuclear spin scrambling process is the reaction with H_2 via the formation of an $(H_5^+)^{\#}$ reaction complex [20,22–27]. This reaction allows efficient scrambling of the protons. Besides the dynamical details, rather stringent nuclear spin selection rules affect the ratio of $[{}^{p}H_3^+]$ and $[{}^{o}H_3^+]$ in the plasma [20,22–28]. Therefore the change in ${}^{p}f$ can be achieved by using ${}^{e}H_2$ instead of ${}^{n}H_2$ [20,23,29]. By performing the measurements with different [He], the values α_{bin} and K_{He} for the individual spin states have been obtained. For a detailed discussion of experiments with ${}^{n}H_2$, see Refs. [14,15,19].

Experiment.—In the experiment, the plasma is formed in a pulsed microwave discharge in a fused silica tube cooled by liquid nitrogen to 77 K. The discharge was ignited in a mixture of He-Ar-H_2 (a typical composition 10^{18}, 10^{14}, 10^{13} cm^{-3} [30]). Para enriched ${}^{e}H_2$ was produced from ${}^{n}H_2$ by using a Fe_2O_3 catalytic converter cooled below 20 K. Nuclear magnetic resonance spectroscopy was used to determine the fraction of ${}^{p}H_2$ [$> (87 \pm 5)\%$].

The ion density was measured with a near infrared cavity ring down absorption spectrometer [31,32]. The densities of the two lowest rotational states of the ground vibrational state of H_3^+ were measured by using the transition $3\nu_2^1(2,0) \leftarrow 0\nu_2^0(1,0)$ for ${}^{o}H_3^+$ and $3\nu_2^1(2,1) \leftarrow 0\nu_2^0(1,1)$ for ${}^{p}H_3^+$; for notation and details, see Refs. [31,32]. In a thermodynamic equilibrium at 77 K, these two lowest rotational states contain $\approx 86\%$ of the population of H_3^+. The Doppler broadening of the absorption lines was measured to obtain the kinetic temperature of H_3^+. The measured kinetic temperature of ions in the active discharge was (80 ± 15) K. Because of the high helium density [[He] $= (2\text{–}18) \times 10^{17}$ cm^{-3})], the relaxation time for the electron temperature is below 1 μs. In the early afterglow, the electron and ion temperatures relax, and in the later afterglow (≥ 50 μs), we can expect that the temperature of electrons and ions is 77 K.

Because of high [He], [H_2], and n_e, any ion has on average 10^5 collisions with He, 10 collisions with electrons [33], and more than 10 collisions with H_2 prior to its recombination. This is why it is safe to assume that during the afterglow the population of states within the ${}^{p}H_3^+$ and

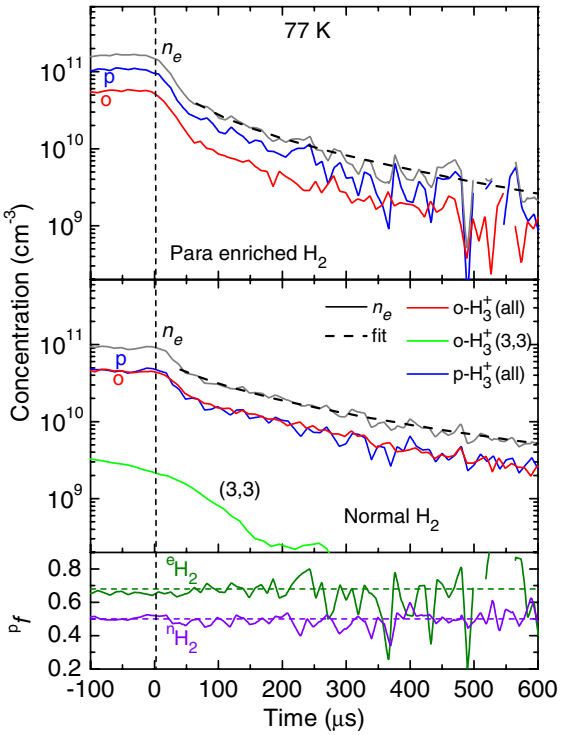

FIG. 1 (color online). The decay curves measured for ${}^{p}H_3^+$ and ${}^{o}H_3^+$ using para enriched H_2 (${}^{e}H_2$, top panel) and normal H_2 (${}^{n}H_2$, middle panel). Obtained n_e are also plotted. The line indicated as (3, 3) in the middle panel is a decay curve for H_3^+ in the eponymous state. The fractions ${}^{p}f$ of ${}^{p}H_3^+$ measured in experiments with ${}^{n}H_2$ and ${}^{e}H_2$ are plotted in the lower panel.

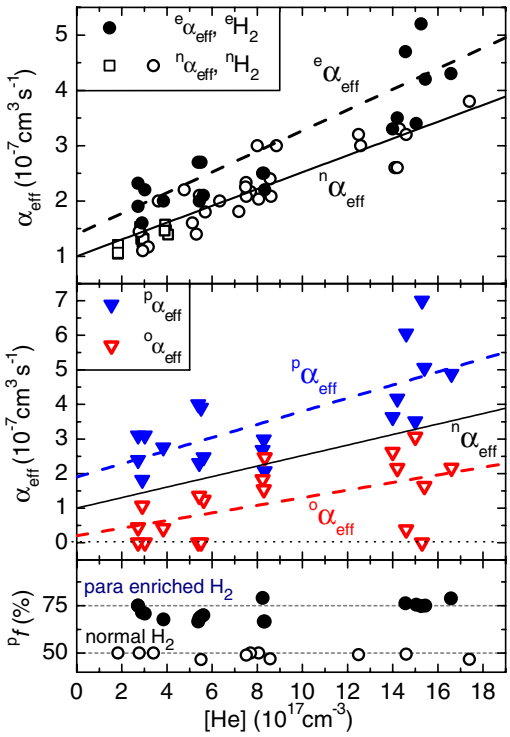

FIG. 2 (color online). Dependencies of effective recombination rate coefficients on He density. Upper panel: Data from experiments with $^nH_2$ and $^eH_2$ ($^n\alpha_{eff}$ and $^e\alpha_{eff}$). Included are data obtained in the FALP experiment using $^nH_2$ (at 82 ± 5 K, open squares). Lower panel: Relative populations of $^pH_3^+$ (fraction ^pf) measured in experiments using $^nH_2$ and $^eH_2$. Middle panel: The effective recombination rate coefficients $^p\alpha_{eff}$ and $^o\alpha_{eff}$ for $^pH_3^+$ and $^oH_3^+$ calculated from measured $^e\alpha_{eff}$, $^n\alpha_{eff}$, and ^pf.

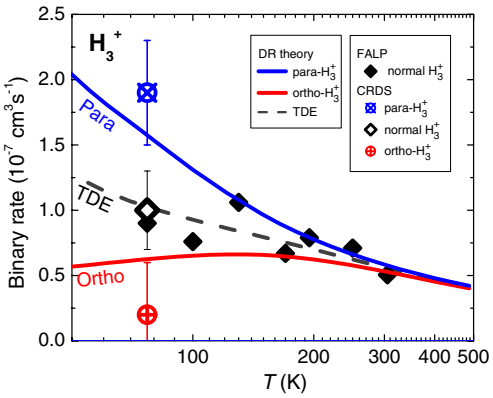

FIG. 3 (color online). Measured binary recombination rate coefficients for normal H_3^+, ortho-H_3^+, and para-H_3^+ in comparison with FALP data for normal H_3^+ [14,15,19] and theoretical predictions [9]. Normal H_3^+ indicates data measured with normal H_2. TDE stands for thermodynamic equilibrium.

$^oH_3^+$ manifold is thermalized to 77 K and it is sufficient to measure densities of H_3^+ in the lowest rotational states, i.e., (1, 1) of $^pH_3^+$ and (1, 0) of $^oH_3^+$. This assumption was confirmed also by the measurement of a population distribution among (3, 3) metastable ortho state [24] and two aforementioned states in the $^nH_2$ discharge for temperatures in the 77–200 K range.

Results and discussion.—When using $^nH_2$ as precursor, we observed $^pf \approx {}^of \approx 0.5$; see Figs. 1 and 2. That holds for the whole H_2 density range used in the present experiments [(0.5–5) × 10^{14} cm^{-3}].

For each set of experimental conditions, the evolutions of [$^pH_3^+$] and [$^oH_3^+$] were measured and n_e were calculated (Fig. 1). From these evolutions, we extracted α_{eff} and ^pf. The first 50–100 μs of the decay are excepted from the analysis to exclude the formation-relaxation region. In Fig. 2 (upper panel), rate coefficients measured with $^nH_2$ at 77 K are plotted as a function of [He]. The data were fitted by using Eq. (5), and the recombination rate coefficients of H_3^+ with $^pf \approx {}^of \approx 0.5$ were obtained: $^n\alpha_{bin}(77\ \mathrm{K}) = (1.0 \pm 0.2) \times 10^{-7}$ cm^3 s^{-1} for the binary and $^nK_{He}(77\ \mathrm{K}) = (1.5 \pm 0.2) \times 10^{-25}$ cm^6 s^{-1} for the ternary process. Earlier data obtained with a Langmuir probe in the flowing afterglow experiment (FALP) at (82 ± 5) K are also plotted for comparison [15].

Using $^eH_2$ as a precursor, we increased the fraction of $^pH_3^+$. The obtained $^e\alpha_{eff}$ and ^pf are plotted in Fig. 2. It is evident already from these plots that the recombination of $^pH_3^+$ is faster. From $^e\alpha_{eff}$ and ^pf, measured with $^eH_2$, the values $^p\alpha_{eff}$ and $^o\alpha_{eff}$ for $^pH_3^+$ and $^oH_3^+$ were calculated. In these calculations, the dependence fitted through data measured with $^nH_2$ was used as a reference (full lines in Fig. 2 indicated as $^n\alpha_{eff}$). By fitting the data $^p\alpha_{eff}$ and $^o\alpha_{eff}$ with a linear dependence [Eq. (5)], we obtained corresponding binary and ternary recombination rate coefficients. For $^pH_3^+$, $^p\alpha_{bin} = (1.9 \pm 0.4) \times 10^{-7}$ cm^3 s^{-1} and $^pK_{He} = (1.9 \pm 0.4) \times 10^{-25}$ cm^6 s^{-1}. For $^oH_3^+$, $^o\alpha_{bin} = (0.2 \pm 0.2) \times 10^{-7}$ cm^3 s^{-1} and $^oK_{He} < (1.1 \pm 0.4) \times 10^{-25}$ cm^6 s^{-1}. The results are summarized in Fig. 3–the agreement with FALP experiments [15,19] and with the theory [9] is excellent.

Summary.—By using a cavity ring down absorption spectrometer, the evolution of ortho-H_3^+ and para-H_3^+ densities has been monitored *in situ* during the afterglow. From such measurements, effective rate coefficients of recombination of H_3^+, for a particular para-H_3^+/ortho-H_3^+ ratio at 77 K, have been determined and the effective recombination rate coefficients of both spin modifications ($^p\alpha_{eff}$ and $^o\alpha_{eff}$) were obtained. The rate coefficients of the binary recombination of para-H_3^+ and ortho-H_3^+ ($^p\alpha_{bin}$ and $^o\alpha_{bin}$) were determined by measuring at different [He].

To our knowledge, this is the first study of H_3^+ recombination with *in situ* determination of the composition of the decaying plasma with respect to para and ortho states of

B.4

H_3^+. Since the majority of the ions is in the lowest rotational states of para and ortho modifications [(1, 1) and (1, 0)] at 77 K, it is the first time that binary recombination rate coefficients were obtained for ions in the ground vibrational, specific nuclear, and rotational states. The theoretical prediction made for binary DR [9] is in excellent agreement with our data. No reliable storage ring data below 300 K exists [13].

This work is a part of the research plan MSM 0021620834 and Grant No. OC10046 financed by the Ministry of Education of the Czech Republic and was partly supported by GACR (202/07/0495, 202/08/H057, 205/09/1183, and 202/09/0642), by GAUK 92410, GAUK 353811, and GAUK 54010, and by COST Action CM0805 (The Chemical Cosmos).

[1] S. Miller *et al.*, Phil. Trans. R. Soc. A **358**, 2485 (2000).
[2] E. Herbst, Phil. Trans. R. Soc. A **358**, 2523 (2000).
[3] C. P. Morong, J. L. Gottfried, and T. Oka, J. Mol. Spectrosc. **255**, 13 (2009).
[4] O. L. Polyansky and J. Tennyson, J. Chem. Phys. **110**, 5056 (1999).
[5] M. Larsson and A. Orel, *Dissociative Recombination of Molecular Ions* (Cambridge University Press, Cambridge, England, 2008).
[6] R. Plašil *et al.*, Int. J. Mass Spectrom. **218**, 105 (2002).
[7] V. Kokoouline, C. H. Greene, and B. D. Esry, Nature (London) **412**, 891 (2001).
[8] V. Kokoouline and C. H. Greene, Phys. Rev. A **68**, 012703 (2003).
[9] S. F. dos Santos, V. Kokoouline, and C. H. Greene, J. Chem. Phys. **127**, 124309 (2007).
[10] H. Kreckel *et al.*, Phys. Rev. Lett. **95**, 263201 (2005).
[11] B. J. McCall *et al.*, Nature (London) **422**, 500 (2003).
[12] H. Kreckel *et al.*, Phys. Rev. A **82**, 042715 (2010).
[13] A. Petrignani *et al.*, Phys. Rev. A **83**, 032711 (2011).
[14] J. Glosík *et al.*, J. Phys. B **41**, 191001 (2008).
[15] J. Glosík *et al.*, Phys. Rev. A **79**, 052707 (2009).
[16] J. Glosík *et al.*, Phys. Rev. A **80**, 042706 (2009).
[17] J. Glosík *et al.*, J. Phys. Conf. Ser. **192**, 012005 (2009).
[18] T. Kotrík *et al.*, J. Chem. Phys. **133**, 034305 (2010).
[19] J. Glosík *et al.*, Mol. Phys. **108**, 2253 (2010).
[20] K. N. Crabtree, N. Indriolo, H. Kreckel, B. A. Tom, and B. J. McCall, Astrophys. J. **729**, 15 (2011).
[21] I. Korolov *et al.*, Contrib. Plasma Phys. **48**, 521 (2008).
[22] M. Quack, Mol. Phys. **34**, 477 (1977).
[23] M. Cordonnier *et al.*, J. Chem. Phys. **113**, 3181 (2000).
[24] T. Oka and E. Epp, Astrophys. J. **613**, 349 (2004).
[25] D. Gerlich *et al.*, Phil. Trans. R. Soc. A **364**, 3007 (2006).
[26] K. Park and J. C. Light, J. Chem. Phys. **126**, 044305 (2007).
[27] E. Hugo, O. Asvany, and S. Schlemmer, J. Chem. Phys. **130**, 164302 (2009).
[28] T. Oka, J. Mol. Spectrosc. **228**, 635 (2004).
[29] B. A. Tom *et al.*, J. Chem. Phys. **132**, 081103 (2010).
[30] J. Varju *et al.*, J. Phys. Conf. Ser. **227**, 012026 (2010).
[31] P. Macko *et al.*, Int. J. Mass Spectrom. **233**, 299 (2004).
[32] P. Hlavenka *et al.*, Int. J. Mass Spectrom. **255–256**, 170 (2006).
[33] V. Kokoouline *et al.*, Mon. Not. R. Astron. Soc. **405**, 1195 (2010).

B.5 Binary and ternary recombination of D_3^+ ions at 80–130 K: Application of laser absorption spectroscopy

P. Dohnal, M. Hejduk, P. Rubovič, J. Varju, Š. Roučka, R. Plašil and J. Glosík, *The Journal of Chemical Physics*, 137 (19), 2012. doi:10.1063/1.4767396.

Binary and ternary recombination of D_3^+ ions at 80–130 K: Application of laser absorption spectroscopy

Petr Dohnal, Michal Hejduk, Peter Rubovič, Jozef Varju, Štěpán Roučka, Radek Plašil, and Juraj Glosík
Department of Surface and Plasma Science, Faculty of Mathematics and Physics, Charles University, Prague, Czech Republic

(Received 14 August 2012; accepted 24 October 2012; published online 20 November 2012)

Recombination of D_3^+ ions with electrons at low temperatures (80–130 K) was studied using spectroscopic determination of D_3^+ ions density in afterglow plasmas. The use of cavity ring-down absorption spectroscopy enabled an *in situ* determination of the abundances of the ions in plasma and the translational and the rotational temperatures of the recombining ions. Two near infrared transitions at $(5792.70 \pm 0.01)\,cm^{-1}$ and at $(5793.90 \pm 0.01)\,cm^{-1}$ were used to probe the number densities of the lowest ortho state and of one higher lying rotational state of the vibrational ground state of D_3^+ ion. The results show that D_3^+ recombination with electrons consists of the binary and the third-body (helium) assisted process. The obtained binary recombination rate coefficients are in agreement with a recent theoretical prediction for electron-ion plasma in thermodynamic equilibrium with $\alpha_{bin}(80\,K) = (9.2 \pm 2.0) \times 10^{-8}\,cm^3\,s^{-1}$. The measured helium assisted ternary rate coefficients K_{He} are in agreement with our previously measured flowing afterglow data giving a value of $K_{He}(80\,K) = (1.2 \pm 0.3) \times 10^{-25}\,cm^6\,s^{-1}$. © *2012 American Institute of Physics*. [http://dx.doi.org/10.1063/1.4767396]

I. INTRODUCTION

The astronomical importance of trihydrogen cation H_3^+ has been driving research in many areas of both physics and chemistry[1] for a long time. This simplest of all polyatomic ions and its isotopologues are also very important for theory, because their properties including interactions with electrons, can be calculated. Processes leading to formation and destruction of H_3^+ ions and similar processes in which deuterated isotopologues are formed or destroyed are important for astronomy and fundamental physics. Deuteration of H_3^+ and formation of H_2D^+, HD_2^+, and D_3^+ are important processes that enable us to characterize the environment in which the deuteration takes place.[2] This also includes interstellar plasma and plasmas under physical conditions believed to be appropriate for pre-protostellar cores.[2,3] The particular importance of H_3^+, but also of H_2D^+ and HD_2^+, was recognized and they were detected in interstellar plasma.[4–7] These detections confirm expectations that multiple deuterated ions play a key role in the chemistry of the early universe.[2] The inclusion of HD_2^+ and D_3^+ in the models leads to predictions of higher values of the D/H ratio in the gas phase.[4] Unfortunately, D_3^+ has not been directly observed in the interstellar medium or in other astronomical object up to now.

Because of its fundamental character, the recombination of H_3^+ and D_3^+ ions with electrons has been studied for over 60 years with emphasis on H_3^+ (see, e.g., the book by Larsson and Orel[8]). For details on recombination studies of the D_3^+ ion, see Refs. 9–19. For both H_3^+ and D_3^+ significant differences between recombination rate coefficients were obtained in different types of experiments[10,12–15,19,20] over many years and the differences between the experimental values and the theoretical ones were very large.[21] Moreover, recombination studies of H_2D^+ and HD_2^+ ions are very rare.[22–25]

Only in the early 2000s the modern theory of binary dissociative recombination (DR) of these ions was formulated.[24–28] Agreement between this theory and experiments achieved in the late 1990s and in the years 2000–2003 was only partial. The remaining discrepancies were assumed to be in internal excitation of recombining ions, which can play a role at low collision energies. Because of this assumption ion storage rings were equipped with "cold ion sources" and better agreement was obtained for H_3^+ recombination.[29–31] In these experiments, it had been assumed that the "cold" rotational distributions measured in the ion source, survived the injection and storage in the ring. Recent high-resolution storage ring experiments indicate that these assumptions were not necessarily correct.[32,33] At this moment, there are no reliable storage ring data for H_3^+ recombination below 300 K (see discussion in Refs. 32 and 33). We assume that the situation with D_3^+ is similar to H_3^+ (i.e., no reliable data from storage ring experiments exist for low temperature recombination of the D_3^+ ion).

In our laboratory, we have studied D_3^+ recombination using stationary afterglow (AISA experiment[14,34]) and also flowing afterglow (FALP).[15] In our recent studies, we discovered a fast ternary neutral assisted recombination of H_3^+ and D_3^+ ions in plasma.[16–18,35–37] At temperatures between 77 and 300 K in helium buffer gas, the losses due to this ternary process are comparable with the losses due to binary dissociative recombination already at a buffer gas pressure of few hundred Pa. When this process is accounted for, then the rate coefficient of binary process can be obtained from afterglow experiments. In H_3^+ experiments, we obtained very good agreement

B.5

of the measured binary recombination rate coefficients with the ones theoretically predicted for thermodynamic equilibrium (TDE) and for pure para- and pure ortho-H_3^+.[38–41]

Among the H_3^+ studies only few were made using spectroscopic identification of the recombining ions (e.g., Refs. 42–46). The study by Amano done in pure hydrogen[42,43] is well known. Nevertheless, his value of the recombination rate coefficient is up to three times larger than other measured values.[30,37,41] We can speculate that in his experiments the H_3^+ recombination was enhanced by the ternary H_2 assisted process.

The situation with D_3^+ is different. To our knowledge, there was no spectroscopic study of D_3^+ recombination up to now. Only few studies were made using afterglow experiments[9,10,12,14,15] and storage ring experiments.[13,19] There are few storage ring experiments[22] and no afterglow experiments with H_2D^+ and HD_2^+. Usable, near infrared (NIR) absorption frequencies are known[47,48] and we have made spectroscopic investigation of plasma containing a mixture of these ions.[47] Recombination study of these ions using cavity ring down spectroscopy (CRDS) in the afterglow experiment is possible, but it would be very complicated. As was already mentioned, there are no recent storage ring studies of these ions and none at all with "cold ion source". The recent theory predicts the rate coefficients for DR of these ions to be smaller than the one of H_3^+ at temperatures ~300 K.[27,49,50]

In the present study, we formed D_3^+ dominated plasma in local thermodynamic equilibrium and we measured the binary recombination rate coefficient α_{bin} and the helium assisted ternary recombination rate coefficient K_{He} of D_3^+ recombination with electrons. To our knowledge, this is the first spectroscopic study concerning recombination of D_3^+ ions with electrons.

II. EXPERIMENTAL METHODS

The method of measuring the recombination rate coefficients in stationary afterglow plasma is well known, so only a very short description will be given here (see, e.g., Refs. 14 and 34). In pulsed discharge, quasi-neutral D_3^+ dominated plasma is formed and when the discharge is switched off a decrease of the ion number density is monitored during the afterglow. At these conditions the decay of the afterglow plasma is governed by ambipolar diffusion to the walls and by electron-ion recombination. Here, in addition to the mentioned processes, we also consider the conversion of D_3^+ ions to D_5^+ in ternary helium assisted association reaction.[15] The main processes are

$$D_3^+ + e^- \xrightarrow{\alpha_{bin}} \text{neutral products}, \quad (1)$$

$$D_3^+ + e^- + He \xrightarrow{K_{He}} \text{neutral products}, \quad (2)$$

$$D_3^+ + D_2 + He \xrightarrow{k_5} D_5^+ + He, \quad (3)$$

$$D_5^+ + e^- \xrightarrow{\alpha_5} \text{neutral products}, \quad (4)$$

where α_{bin} is the binary recombination rate coefficient of D_3^+ ions, K_{He} is the ternary recombination rate coefficient of He assisted recombination, k_5 is the ternary rate coefficient of He assisted association, and α_5 is the binary recombination rate coefficient of D_5^+ ions with electrons.[15,51] If the recombination of D_5^+ is fast and the ternary association (3) is the rate determining reaction in the sequence of processes (3) and (4), then the balance equation can be written in the form

$$\frac{d[D_3^+]}{dt} = -\alpha_{bin}[D_3^+]n_e - K_{He}[He][D_3^+]n_e - \frac{n_e}{\tau_D} - \frac{n_e}{\tau_R}, \quad (5)$$

where τ_D is the characteristic diffusion time, τ_R the time constant characterizing losses due to ternary association followed by a rapid recombination of D_5^+. If we assume quasineutrality and if we introduce the time constant τ_L for "linear losses" by equation $1/\tau_L = 1/\tau_D + 1/\tau_R$, then the balance equation can be rewritten as

$$\frac{dn_e}{dt} = -\alpha_{eff} n_e^2 - \frac{n_e}{\tau_L}, \quad (6)$$

where we introduced the effective binary recombination rate coefficient α_{eff} which can be written in the form

$$\alpha_{eff}(T, [He]) = \alpha_{bin}(T) + K_{He}(T)[He]. \quad (7)$$

We have demonstrated in our previous studies[16–18] and here we will demonstrate again, that the overall recombination of D_3^+ in afterglow plasma can be described in this way. To obtain α_{bin} and K_{He} one has to measure the dependence of α_{eff} on [He] at fixed temperature T.

III. EXPERIMENT

The plasma is generated in a pulsed microwave discharge in a fused silica tube (inner diameter ~1.5 cm). The tube is cooled to 80 K by liquid nitrogen or by pre-cooled nitrogen vapors for measurements in the temperature range of 80–220 K. To form a D_3^+ dominated plasma a mixture of He/Ar/D_2 with a typical composition $10^{17}/10^{14}/10^{14}\,cm^{-3}$ is flowing through the discharge tube. The D_3^+ ions are formed in a sequence of ion molecule reactions. The details of the kinetics of the ion formation are well known (see Refs. 14, 15, 18, 34, and 52). The microwave generator ($f = 2.45$ GHz) is equipped with an external fast high-voltage switch to cut off the HV power to the magnetron. The switch off transient time is less than 30 μs. This was indirectly confirmed by monitoring the spontaneous emission of the plasma.[45] A fairly low microwave power in the range 5–15 W, with ~50% duty cycle, was used to avoid excessive heating of the gas during the discharge. A NIR-CRDS was used as the main diagnostic tool, the principal layout is shown in Figure 1. The discharge tube, equipped with an optical resonator (not in scale), forms the main part of the continuous wave modification of CRDS. Because the apparatus was described elsewhere (see Refs. 38–41, 45, and 46) only a short description will be given here.

A distributed feedback laser diode covering the spectral range of 5788–5798 cm^{-1} was used in the present study. During the measurement the laser current was kept constant and wavelength change was done by means of computer controlled temperature change. An interference signal from the Fabry-Perot etalon was used to linearize the wavenumber

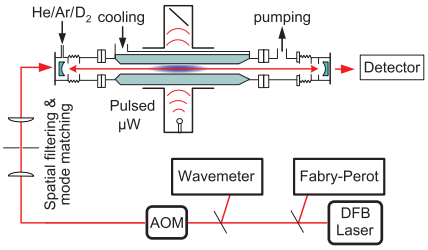

FIG. 1. Stationary afterglow with the CRDS absorption spectrometer. A discharge is periodically ignited in the microwave resonator (μW) in the middle part of the discharge tube. A He/Ar/D_2 gas mixture is used to form a D_3^+ dominated afterglow plasma. The laser light modulated by the acousto-optic modulator (AOM) is injected through the mirror on one side and photons exiting the cavity through the mirror on the other side are detected by an InGaAs avalanche photodiode. The absolute wavelength is measured using a Michelson wavemeter and relatively by a Fabry-Perot etalon.

scale. Two H_2O lines at 5789.65 cm^{-1} and 5793.03 cm^{-1} (line positions taken from HITRAN database[53]) were used to transform the relative value given by Fabry-Perot etalon to absolute wavelength. The resulting precision of wavelength determination is better than 0.01 cm^{-1}. At conditions used in the present experiment, where D_3^+ was the dominant ion, only two absorption lines $(5792.70 \pm 0.01)\,cm^{-1}$ and $(5793.90 \pm 0.01)\,cm^{-1}$ were visible during the discharge and early afterglow. The difference between the measured line positions and those predicted by quantum mechanical calculations is less than 0.02 cm^{-1}.[54] Given this fact and that those two absorption lines were only in plasma with D_2 present, we concluded that they belong to D_3^+ ion. The conclusion was also supported by measuring the temperature dependence of the intensities of both lines. The examples of measured profiles of absorption lines are shown in Figure 2. In this study we used the transitions, which we assigned (after discussion with Tennyson[54]) as $3\nu_2^1(1,0) \leftarrow 0\nu_2^0(0,0)$ and $3\nu_2^1(3,2) \leftarrow 0\nu_2^0(4,2)$ for ortho-D_3^+ (0,0) and meta-D_3^+ (4,2), respectively. The rotational levels are labeled by corresponding quantum numbers (J,G), for details on notation and calculations of transitions frequencies see Ref. 55.

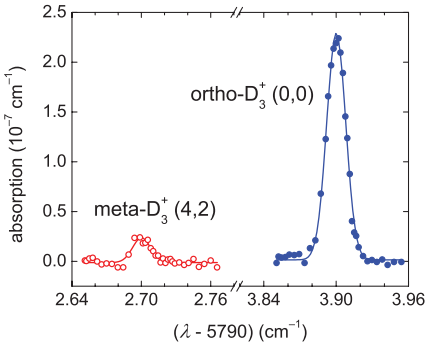

FIG. 2. Example of absorption line profiles of D_3^+ ions measured at the wall temperature of $T_{Wall} = 112$ K and $P = 560$ Pa of He. The kinetic temperature $T_{Kin} = (112 \pm 10)$ K was obtained from the Doppler broadening of the absorption lines. The line center positions are: $(5793.90 \pm 0.01)\,cm^{-1}$ and $(5792.70 \pm 0.01)\,cm^{-1}$ for ortho-D_3^+ (0,0) and meta-D_3^+ (4,2), respectively. The calculated values are 5793.92 cm^{-1} for $3\nu_2^1(1,0) \leftarrow 0\nu_2^0(0,0)$ and 5792.68 cm^{-1} for $3\nu_2^1(3,2) \leftarrow 0\nu_2^0(4,2)$ for ortho-D_3^+ (0,0) and meta-D_3^+ (4,2), respectively.[54,55]

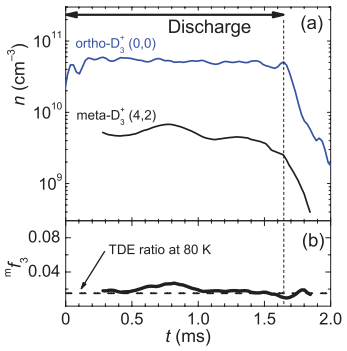

FIG. 3. Panel (a) Measured number densities of the ions in ortho (0,0) and meta (4,2) states of D_3^+ during the discharge and early afterglow. Panel (b) Measured fraction $^m f_3$ of meta-D_3^+ (4,2), $^m f_3 = [\text{meta-}D_3^+\,(4,2)]/[D_3^+]$. The value of the ratio corresponding to the TDE at 80 K is indicated by the dashed horizontal line. Used conditions are $T_{He} = 80$ K, $P = 400$ Pa of He, $[D_2] = 4 \times 10^{14}$ cm^{-3} and $[Ar] = 2 \times 10^{14}$ cm^{-3}.

An example of measured ion number density evolutions in discharge and early afterglow is shown in panel (a) of Figure 3. The dashed vertical line indicates the end of the discharge and the beginning of the afterglow. The measured evolution of the fraction $^m f_3$ of the number density of the meta-D_3^+ (4,2) to the number density of D_3^+ is shown in the lower panel of Figure 3. The horizontal dashed line indicates the calculated ratio corresponding to the TDE at 80 K.

IV. TEMPERATURE IN THE D_3^+ DOMINATED AFTERGLOW PLASMA

In general, in an afterglow plasma the different particles and their internal degrees of freedom are not necessarily in complete thermal equilibrium with each other and with the walls of the plasma container. For instance, the electron temperature T_e can significantly exceed the kinetic temperature of the ions T_{Kin} and the buffer gas atoms temperature T_{He} because the transfer of kinetic energy in electron collisions with heavy particles is less efficient than the kinetic energy transfer in collisions of ions and gas atoms. Also, the ions' rotational temperature T_{Rot} and vibrational temperature T_{Vib} do not have to be equal to the ions' translational temperature if the corresponding relaxation times are long in comparison with the characteristic time of the ion density decay. We have discussed this problem for H_3^+ dominated plasma in Refs. 40, 41, and 56. In the present studies, we determine kinetic temperature (T_{Kin}) of ions from the Doppler broadening of measured absorption lines. In Figure 4 an example of the evolution of T_{Kin} measured at a wall temperature of $T_{Wall} = (112 \pm 1)$ K is plotted. The obtained equality $T_{Wall} = T_{Kin}$ means also $T_{Wall} = T_{He}$. We have made such measurements for the whole range of pressures and temperatures used in the present study with the same conclusion.

The electron temperature T_e in the afterglow was not measured in these experiments. The time constant for

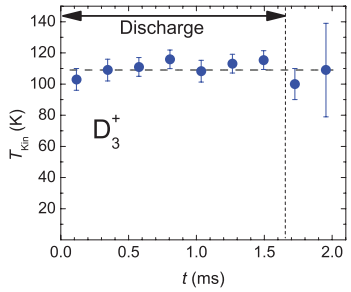

FIG. 4. The measured evolution of the kinetic temperature of the ions (T_{Kin}) during the discharge and during the early afterglow, while a wall temperature was $T_{Wall} = (112 \pm 1)$ K and rotational temperature was $T_{Rot} = (112 \pm 3)$ K. Used helium buffer gas concentration was [He] $= 3.6 \times 10^{17}$ cm^{-3}. The mean value of the measured T_{Kin} is indicated by a horizontal dashed line.

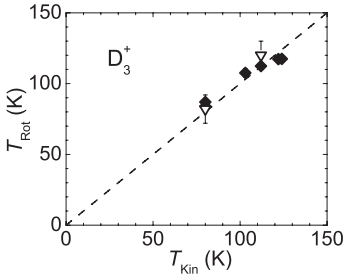

FIG. 5. The measured rotational temperature T_{Rot} of the D_3^+ ions versus the measured kinetic temperature T_{Kin}. The dashed straight line indicates the equality $T_{Rot} = T_{Kin}$. The open triangles and filled rhomboids indicate data measured during the early afterglow and during the discharge, respectively.

electron cooling at a typical helium density used in the experiment can be estimated from the electron-helium collision frequency (>1 GHz) and the mass ratio $2m_e/m_{He}$. The calculated time constant for electron cooling is $\tau_\varepsilon < 10\,\mu$s. In previous FALP experiments, we measured the electron energy distribution function (EEDF) in He and He/Ar buffered afterglow plasmas under conditions similar to those in the present study.[57–59] It was found that EEDF is close to a Maxwellian distribution with a temperature close to the buffer gas temperature.[60] In stationary afterglow with CRDS, we indirectly observed fast cooling of electrons after switching off the discharge by monitoring visible light emissions from the discharge and very early afterglow. Using analogy with H_3^+, we also expect that all excited vibrational states of D_3^+ are quenched in multiple collisions with He, Ar, and D_2 (see discussion for H_3^+ in Ref. 41).

Using FALP, we also studied the collisional radiative recombination (CRR) in an Ar^+ dominated plasma in a He/Ar gas mixture and we measured the corresponding ternary recombination rate coefficient K_{CRR} which has a very pronounced temperature dependence, $K_{CRR} \sim T_e^{-9/2}$.[61–63] In this study, we also measured the temperature dependence of ambipolar diffusion. In both cases, we obtained very good agreement with theory for temperatures of 77–300 K.[62,63] This is an excellent confirmation that at the given experimental conditions $T_e = T_{He} = T_{Wall}$. These estimates need to be refined when the plasma contains energy sources that can lead to heating of the electron gas. One such source can be He metastables.[59,60] In the present experiments, metastables are destroyed in reaction with Ar (by Penning ionization[58,60]). At low temperatures and high electron densities the electron heating can be caused by CRR; we will discuss this possibility later. In our previous studies of H_3^+ recombination,[41] we showed that at the used electron densities, the CRR can elevate the electron temperature only slightly in the early afterglow at gas temperatures near 77 K, but becomes unimportant at higher gas temperatures and lower electron densities.

From the measured relative population of the ions in the two monitored states we determined the rotational temperature T_{Rot}. The rotational temperature T_{Rot} was measured not only during the discharge but also during the early afterglow when the signal from meta-D_3^+ (J,G) = (4,2) was still sufficient. The measured dependence of T_{Rot} on T_{Kin} is shown in Figure 5.

Recently, we studied relaxation processes and equilibrium in H_3^+ dominated plasma using very similar experimental conditions, the only difference being that now we use D_2 instead of H_2.[38–41,56] In H_3^+ studies, we monitored the population of two ortho states and one para state and the used transitions were more suitable for measurements of rotational temperatures at He buffer gas temperatures in the range of 80–200 K. We were also able to monitor the para to ortho ratio, [para-H_3^+]/[ortho-H_3^+]. In addition, in the H_3^+ experiments we used normal and para enriched hydrogen to manipulate the fraction of para-H_3^+ in the plasma. From the obtained results we also concluded that $T_{Rot} = T_{Kin} = T_{He} = T_{Wall}$ for H_3^+. Later on, for present experiments we will use temperature measured from the Doppler broadening of the absorption lines (mean value from several measurements at the same wall temperature). For previous FALP data, we will use the measured temperature of the flow tube. On the basis of the present experiments and using comparison and analogy with the results obtained in H_3^+ experiments, we concluded that the plasma in the afterglow is in the thermodynamic equilibrium at a temperature given by the wall of the discharge tube.

V. RESULTS AND DISCUSSION

We measured the variation of light absorption in afterglow plasma using CRDS. Under the assumption that the plasma is in thermal equilibrium and D_3^+ is the dominant ion we calculated the electron density decay. Examples of data measured at 112 K are plotted in Figure 6. The measured number densities of the ions in ortho (0,0) and meta (4,2) states of D_3^+, the calculated electron density and the partial density of ions in (4,2) state (fraction $^m f_3$ of meta-D_3^+ (4,2), $^m f_3$ = [meta-D_3^+ (4,2)]/[D_3^+]) are plotted.

We studied plasma decay at temperatures of 80–130 K over a wide range of He pressures. The decay curves were analyzed using "integral analysis" (for details see Refs. 57 and 64). This analysis can separate α_{eff} from τ_L (see Eqs. (5) and (6)) and minimize the influence of D_5^+ formation followed by a rapid recombination on the determination of α_{eff}. The first 50–150 μs of the afterglow decay were not taken into

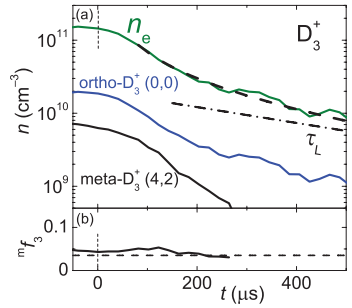

FIG. 6. Panel (a) Example of the decay of densities of ions in ortho (0,0) and meta (4,2) states of D_3^+, measured during the afterglow in a He/Ar/D_2 gas mixture at 112 K, 550 Pa of He, $[D_2] = 1.7 \times 10^{14}$ cm^{-3} and $[Ar] = 8.4 \times 10^{13}$ cm^{-3}. Time is set to zero at the beginning of the afterglow (indicated by vertical dashed line). The electron density (n_e) is obtained from the partial density of ions in the (0,0) state under assumption of TDE. The dashed-dotted line indicates losses due to diffusion and reactions with the time constant τ_L, the dashed line indicates the fit of the electron number density decay, see Eqs. (5) and (6). Panel (b) Measured fraction $^mf_3$ of meta-D_3^+ (4,2), $^mf_3$ = [meta-D_3^+ (4,2)]/[D_3^+].

account from the analysis to exclude eventual formation of D_3^+ in very early afterglow (for details see Refs. 18, 39, and 65). Dependencies of the effective recombination rate coefficient α_{eff} on [He], measured at 80 and 100 K are shown in panels (a) and (b) of Figure 7, respectively. Linear dependence of α_{eff} on [He] is obvious. Similar dependencies were measured also at 112 and 125 K. The data from previous FALP experiment are plotted in Figure 7 as open squares.[17] In addition, we performed series of experiments using new Cryo-FALP II apparatus (for details on experimental setup see Ref. 63) at

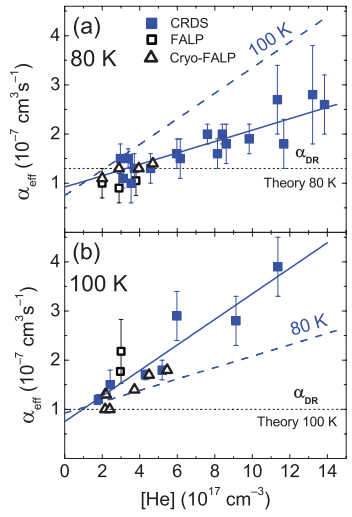

FIG. 7. Measured dependence of the effective recombination rate coefficients on [He] at 80 K - panel (a) and 100 K - panel (b). The data indicated by filled squares were measured in present experiments using CRDS and the data indicated by open squares were measured using a Langmuir probe in previous FALP experiment (see compilation in Ref. 17). The data indicated by open triangles were measured in this study using a new Cryo-FALP II apparatus. For comparison straight lines obtained by a fit of CRDS data at indicated temperatures are plotted in both panels. The horizontal dotted lines indicate theoretical values of α_{DR} at corresponding temperatures.[27,50]

the same conditions (temperature, number density of Ar and D_2) as in the already mentioned FALP experiment but in a broader pressure range and with better temperature control. These data are plotted in Figure 7 as open triangles.

Special attention was paid to the analysis of the decay curves measured at 80 and 100 K because of a possible influence of CRR process described by Bates.[66,67] To demonstrate and evaluate the effect of CRR we used the fact that the overall binary rate coefficient α_{CRR} of the ternary CRR process is dependent on the electron density, $\alpha_{CRR} = K_{CRR} \cdot n_e$, where K_{CRR} is the ternary rate coefficient, only dependent on the temperature. We measured α_{eff} in two types of experiments, in FALP with a typical initial electron density of $n_{e_0} = 2 \times 10^9$ cm^{-3} and in SA-CRDS with a typical initial electron density $n_{e_0} = 3 \times 10^{10}$ cm^{-3}. The measured α_{eff} are plotted in Figure 7. Within experimental accuracy, the data measured at the same temperature but with very different electron densities give the same value of α_{eff}. From this we concluded that CRR contribution, which should be dependent on n_{e_0} is small in comparison with the contribution from processes with their rate coefficients independent of electron density. This conclusion can be surprising, but it agrees with conclusions from more detailed studies of this phenomenon made for recombination of H_3^+ ions, for details see Ref. 41. For comparison if one uses the classical Stevefelt formula for calculation of α_{CRR} at $T = 77$ K and $n_e = 3 \times 10^{10}$ cm^{-3} then the value of $\alpha_{CRR} \sim 3 \times 10^{-7}$ cm^3 s^{-1} is obtained (for details see Refs. 41 and 61). From the data plotted in Figure 7 it is clear that Stevefelt's calculated value of α_{CRR}[61] is three times higher than the measured overall recombination rate coefficient α_{eff} at low [He]. We experimentally verified the validity of Stevefelt formula for atomic ions by measuring α_{CRR} in Ar^+ dominated plasma at temperature range of 60–300 K and we obtained a good agreement.[62,63] Up to now we do not have an explanation for not observing CRR for H_3^+ nor D_3^+ molecular ions while we can observe it for atomic Ar^+(bearing in mind the differences between both the experiments).

We calculated binary and ternary recombination rate coefficients α_{bin} and K_{He} from the measured dependencies of α_{eff} on [He] (see Eq. (7)). Present measurements are made over a broad range of [He], so the accuracy of obtained α_{bin} and K_{He} is higher in comparison with previous FALP and AISA studies.[17] The obtained values of α_{bin} and K_{He} are plotted in Figures 8 and 9 as a function of the temperature and summarized in Table I. The thermal rate coefficients α_{DR} calculated for binary dissociative recombination[27,28,50] are also plotted in Figure 8 (recombination rate coefficient plotted in Figure 8 as theory of Pratt and Jungen was calculated from the dependence of the recombination rate on energy published in Ref. 28). We also included several values of rate coefficients measured in previous afterglow experiments at 300 K.[10–12] These rate coefficients were corrected by taking the He density into account in particular experiments and the actual values of ternary rate coefficients as measured in the FALP experiment.[17] We also plotted the rate coefficients calculated from the corresponding cross section measured in storage ring experiment CRYRING.[13,19] For comparison of the measured α_{bin} with α_{CRR}, we also plotted expected

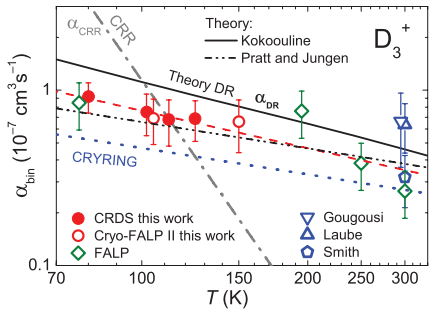

FIG. 8. D_3^+ binary recombination rate coefficients. The solid line and the dashed double dotted line indicate the values for the binary dissociative recombination (α_{DR}) at a thermal population of the para-/ortho-/meta-states of D_3^+ calculated by Kokoouline[27,50] and by Pratt and Jungen,[28] respectively. The values α_{bin} indicated by filled circles were obtained in present study from the dependencies of α_{eff} on [He] at particular T. The open circles denote the data obtained in this study using Cryo-FALP II apparatus. The values indicated by open diamonds were obtained in previous FALP experiments from dependencies of α_{eff} on [He] at fixed T.[16–18] The dotted line indicates the rate coefficients measured in storage ring experiment CRYRING.[13,19] Previous FALP data obtained in other laboratories are indicated as Gougousi,[11] Laube,[10] and Smith;[12] these data were corrected (see text). The steep dashed-dotted line labeled CRR is the effective binary rate coefficient α_{CRR} of CRR calculated using Stevefelt formula (see Refs. 41 and 61) for electron density $n_e = 3 \times 10^{10}$ cm^{-3}). The dashed line is a fit to FALP, Cryo-FALP II, and CRDS data.

α_{CRR} in Figure 8 calculated for $n_e = 3 \times 10^{10}$ cm^{-3} using the Stevefelt formula.[41,61]

The measured ternary recombination rate coefficients K_{He} are in good agreement with previous data measured in FALP experiments. In our previous studies, we discussed the ternary helium assisted recombination in terms of the life-times of excited Rydberg states D_3^* formed in the collision of D_3^+ ions with electrons.[16–18] Because of long life-time of D_3^* (up to several hundreds of picoseconds) the process can be, depending on the temperature, hundred times more effective

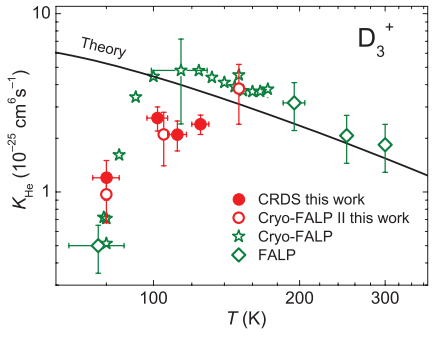

FIG. 9. The ternary recombination rate coefficient, $K_{He}(T)$, for He assisted ternary recombination of D_3^+ ions. The filled circles indicate the present values obtained from the measured linear dependencies of α_{eff} on [He] at fixed T, see full lines in Figure 7. The open circles were obtained in present study with Cryo-FALP II apparatus from the dependence of α_{eff} on [He]. The open diamonds indicate data obtained from dependence of α_{eff} on [He] measured in FALP experiment (for more details see Refs. 16–18). The data measured using Cryo-FALP with the continuously increasing temperature are labeled by stars.[17,18] The full line indicates theoretical ternary rate coefficients calculated for D_3^+ ions in thermal equilibrium.[16–18]

TABLE I. Measured binary α_{bin} and ternary K_{He} recombination rate coefficients of D_3^+. The displayed temperature T is the temperature obtained from Doppler broadening of absorption lines in the present study and temperature of the metal wall of the flow tube in FALP experiments.[17]

T[K]	α_{bin} (10^{-8} cm^3 s^{-1})	K_{He} (10^{-25} cm^6 s^{-1})	Reference
77	8.5 ± 2.5	0.5 ± 0.2	FALP[17]
80	9.2 ± 2.0	1.2 ± 0.3	This study
100	7.5 ± 2.0	2.6 ± 0.4	This study
112	6.5 ± 2.0	2.1 ± 0.4	This study
125	6.9 ± 1.8	2.4 ± 0.3	This study
300	2.7 ± 0.8	1.8 ± 0.6	FALP[17]

than classical neutral assisted ternary recombination predicted by Thomson[68] and by Bates and Khare.[69] The process is essentially different from the process considered by Thomson. The present studies confirmed the previously measured strong increase of K_{He} with temperatures starting from 80 K.

VI. CONCLUDING REMARKS

We studied electron-ion recombination in D_3^+ dominated afterglow plasma in He/Ar/D_2 gas mixture using CRDS for measuring ion density decays during the afterglow and for characterizing kinetic and rotational temperature of ions. From this measurements and using similarity with H_3^+ dominated afterglow plasma[39,41,56] we concluded that at used conditions D_3^+ dominated afterglow plasma is in thermal equilibrium with He buffer gas. The study confirmed that the decay of D_3^+ dominated afterglow plasma is controlled by the binary recombination and in parallel by the three body helium assisted recombination process. The magnitude and temperature dependence of rate coefficients of these processes as measured with CRDS are in agreement with our previous flowing afterglow studies using Langmuir probe.[16–18] The binary and the ternary recombination rate coefficients were obtained in the temperature range of 80–130 K yielding $\alpha_{bin}(80\,K) = (9.2 \pm 2.0) \times 10^{-8}$ cm^3 s^{-1}, $\alpha_{bin}(125\,K) = (6.9 \pm 1.8) \times 10^{-8}$ cm^3 s^{-1}, $K_{He}(80\,K) = (1.2 \pm 0.3) \times 10^{-26}$ cm^6 s^{-1} and $K_{He}(125\,K) = (2.4 \pm 0.3) \times 10^{-26}$ cm^6 s^{-1}.

As in our previous recombination study of H_3^+ dominated plasma, neither for recombination of D_3^+ ions we have seen any substantial dependence of recombination rate coefficient on electron number density as predicted by theory of collisional radiative recombination.[61] This rather surprising result is supported by comparison of effective recombination rate coefficients obtained at the temperature of 80 K in this study and in previous flowing afterglow measurement[17] (see Figure 7 for details) at electron number densities different by an order of magnitude.

This is the first study on the recombination of D_3^+ ions with electrons with spectroscopically resolved abundances of the recombining ions. The results support theoretical predictions and are in agreement with previous flowing afterglow measurements[16–18] and with storage ring data.[13,19]

B.5

ACKNOWLEDGMENTS

This work was partly financed by the research grant OC10046 from the Ministry of Education of the Czech Republic and was partly supported by GACR (205/09/1183, P209/12/0233), by SV 265 302, by GAUK 92410, GAUK 353811, GAUK 54010, and by COST Action CM0805 (The Chemical Cosmos).

[1]T. R. Geballe and T. Oka, Science **312**, 1610 (2006).
[2]C. D. Gay, P. C. Stancil, S. Lepp, and A. Dalgarno, Astrophys. J. **737**, 44 (2011).
[3]D. R. Flower, G. P. des Forets, and C. M. Walmsley, Astron. Astrophys. **427**, 887 (2004).
[4]C. Vastel, T. G. Phillips, and H. Yoshida, Astrophys. J. **606**, L127 (2004).
[5]R. Stark, F. F. S. van der Tak, and E. F. van Dishoeck, Astrophys. J. **521**, L67 (1999).
[6]R. Stark, G. Sandell, S. C. Beck, M. R. Hogerheijde, E. F. van Dishoeck, P. van der Wal, F. F. S. van der Tak, F. Schafer, G. J. Melnick, M. L. N. Ashby, and G. de Lange, Astrophys. J. **608**, 341 (2004).
[7]E. Roueff, J. Phys.: Conf. Ser. **4**, 1 (2005).
[8]M. Larsson and A. Orel, *Dissociative Recombination of Molecular Ions* (Cambridge University Press, Cambridge, 2008).
[9]P. van der Donk, F. B. Yousif, and J. B. A. Mitchell, Phys. Rev. A **43**, 5971 (1991).
[10]S. Laube, A. L. Padellec, O. Sidko, C. Rebrion-Rowe, J. B. A. Mitchell, and B. R. Rowe, J. Phys. B **31**, 2111 (1998).
[11]T. Gougousi, R. Johnsen, and M. F. Golde, Int. J. Mass Spectrom. **149-150**, 131 (1995).
[12]D. Smith and P. Spanel, Int. J. Mass Spectrom. **129**, 163 (1993).
[13]M. Larsson, H. Danared, A. Larson, A. L. Padellec, J. R. Peterson, S. Rosen, J. Semaniak, and C. Stromholm, Phys. Rev. Lett. **79**, 395 (1997).
[14]V. Poterya, J. Glosik, R. Plasil, M. Tichy, P. Kudrna, and A. Pysanenko, Phys. Rev. Lett. **88**, 044802 (2002).
[15]O. Novotny, R. Plasil, A. Pysanenko, I. Korolov, and J. Glosik, J. Phys. B **39**, 2561 (2006).
[16]J. Glosik, I. Korolov, R. Plasil, T. Kotrik, P. Dohnal, O. Novotny, J. Varju, S. Roucka, C. Greene, and V. Kokoouline, Phys. Rev. A **80**, 042706 (2009).
[17]T. Kotrik, P. Dohnal, I. Korolov, R. Plasil, S. Roucka, J. Glosik, C. Greene, and V. Kokoouline, J. Chem. Phys. **133**, 034305 (2010).
[18]J. Glosik, R. Plasil, T. Kotrik, P. Dohnal, J. Varju, M. Hejduk, I. Korlov, S. Roucka, and V. Kokoouline, Mol. Phys. **108**, 2253 (2010).
[19]A. L. Padellec, M. Larsson, H. Danared, A. Larson, J. R. Peterson, S. Rosen, J. Semaniak, and C. Stromholm, Phys. Scr. **57**, 215 (1998).
[20]T. Tanabe, I. Katayama, and H. Kamegaya, *Dissociative Recombination: Theory, Experiments and Applications III* (World Scientific, Singapore, 1996), pp. 84–93.
[21]A. E. Orel, I. F. Schneider, and A. Suzor-Weiner, Philos. Trans. R. Soc. London, Ser. A **358**, 1445 (2000).
[22]J. B. A. Mitchell, C. T. Ng, L. Forand, R. Janseen, and J. W. McGowan, J. Phys. B **17**, L909 (1984).
[23]V. Zhaunerchyk, R. D. Thomas, W. D. Geppert, M. Hamberg, M. Kaminska, E. Vigren, and M. Larsson, Phys. Rev. A **77**, 034701 (2008).
[24]V. Kokoouline and C. H. Greene, Phys. Rev. A **72**, 022712 (2005).
[25]C. Jungen and S. T. Pratt, Phys. Rev. Lett **1021**, 023201 (2009).
[26]V. Kokoouline, C. H. Greene, and B. D. Esry, Nature (London) **412**, 891 (2001).
[27]V. Kokoouline and C. H. Greene, Phys. Rev. A **68**, 012703 (2003).
[28]S. T. Pratt and C. Jungen, J. Phys.: Conf. Ser. **300**, 012019 (2011).
[29]B. J. McCall, A. J. Honeycutt, R. J. Saykally, T. R. Geballe, N. Djuric, G. H. Dunn, J. Semaniak, O. Novotny, A. Al-Khalili, A. Ehlerding, F. Hellberg, S. Kalhori, A. Neau, R. Thomas, F. Osterdahl, and M. Larsson, Nature (London) **422**, 500 (2003).
[30]H. Kreckel, M. Motsch, J. Mikosch, J. Glosik, R. Plasil, S. Altevogt, V. Andrianarijaona, H. Buhr, J. Hoffmann, L. Lammich, M. Lestinsky, I. Nevo, S. Novotny, D. A. Orlov, H. B. Pedersen, F. Sprenger, A. S. Terekhov, J. Toker, R. Wester, D. Gerlich, D. Schwalm, A. Wolf, and D. Zajfman, Phys. Rev. Lett. **95**, 263201 (2005).
[31]B. J. McCall, A. J. Huneycutt, R. J. Saykally, N. Djuric, G. H. Dunn, J. Semaniak, O. Novotny, A. Al-Khalili, A. Ehlerding, F. Hellberg, S. Kalhori, A. Neau, R. Thomas, A. Paal, F. Osterdahl, and M. Larsson, Phys. Rev. A **70**, 052716 (2004).
[32]H. Kreckel, O. Novotny, K. N. Crabtree, H. Buhr, A. Petrignani, B. A. Tom, R. D. Thomas, M. H. Berg, D. Bing, M. Grieser, C. Krantz, M. Lestinsky, M. B. Mendes, C. Nordhorn, R. Repnow, J. Stutzel, A. Wolf, and B. J. McCall, Phys. Rev. A **82**, 042715 (2010).
[33]A. Petrignani, S. Altevogt, M. H. Berg, D. Bing, M. Grieser, J. Hoffmann, B. Jordon-Thaden, C. Krantz, M. B. Mendes, O. Novotny, S. Novotny, D. A. Orlov, R. Repnow, T. Sorg, J. Stutzel, A. Wolf, H. Buhr, H. Kreckel, V. Kokoouline, and C. H. Greene, Phys. Rev. A **83**, 032711 (2011).
[34]R. Plasil, J. Glosik, V. Poterya, P. Kudrna, J. Rusz, M. Tichy, and A. Pysanenko, Int. J. Mass Spectrom. **218**(2), 105 (2002).
[35]J. Glosik, R. Plasil, I. Korolov, O. Novotny, and T. Kotrik, J. Phys.: Conf. Ser. **192**, 012005 (2009).
[36]J. Glosik, I. Korolov, R. Plasil, O. Novotny, T. Kotrik, P. Hlavenka, J. Varju, I. A. Mikhailov, V. Kokoouline, and C. H. Greene, J. Phys. B **41**, 191001 (2008).
[37]J. Glosik, R. Plasil, I. Korolov, T. Kotrik, O. Novotny, P. Hlavenka, P. Dohnal, J. Varju, V. Kokoouline, and C. Greene, Phys. Rev. A **79**, 052707 (2009).
[38]J. Varju, S. Roucka, T. Kotrik, R. Plasil, and J. Glosik, J. Phys.: Conf. Ser. **227**, 012026 (2010).
[39]J. Varju, M. Hejduk, P. Dohnal, M. Jilek, T. Kotrik, R. Plasil, D. Gerlich, and J. Glosik, Phys. Rev. Lett. **106**, 203201 (2011).
[40]M. Hejduk, P. Dohnal, J. Varju, P. Rubovic, T. Kotrik, R. Plasil, and J. Glosik, Plasma Sources Sci. Technol. **21**, 024002 (2012).
[41]P. Dohnal, M. Hejduk, J. Varju, P. Rubovic, S. Roucka, T. Kotrik, R. Plasil, J. Glosik, and R. Johnsen, J. Chem. Phys. **136**, 244304 (2012).
[42]T. Amano, J. Chem. Phys. **92**, 6492 (1990).
[43]T. Amano, Astrophys. J. **329**, L121 (1988).
[44]M. Feher, A. Rohrbacher, and J. P. Maier, Chem. Phys. **185**, 357 (1994).
[45]P. Macko, G. Bano, P. Hlavenka, R. Plasil, V. Poterya, A. Pysanenko, O. Votava, R. Johnsen, and J. Glosik, Int. J. Mass Spectrom. **233**, 299 (2004).
[46]P. Macko, R. Plasil, P. Kudrna, P. Hlavenka, V. Poterya, A. Pysanenko, G. Bano, and J. Glosik, Czech. J. Phys. **52**, 695 (2002).
[47]P. Hlavenka, R. Plasil, G. Bano, I. Korolov, D. Gerlich, J. Ramanlal, J. Tennyson, and J. Glosik, Int. J. Mass Spectrom. **255**, 170 (2006).
[48]J. Glosik, P. Hlavenka, R. Plasil, F. Windisch, D. Gerlich, A. Wolf, and H. Kreckel, Philos. Trans. R. Soc. London, Ser. A **364**(1848), 2931 (2006).
[49]S. F. dos Santos, V. Kokoouline, and C. H. Greene, J. Chem. Phys. **127**, 124309 (2007).
[50]L. Pagani, C. Vastel, E. Hugo, V. Kokoouline, C. H. Greene, A. Bacmann, E. Bayet, C. Ceccarelli, R. Peng, and S. Schlemmer, Astron. Astrophys. **494**, 623 (2009).
[51]M. T. Leu, M. A. Biondi, and R. Johnsen, Phys. Rev. A **8**, 413 (1973).
[52]J. Glosik, R. Plasil, V. Poterya, P. Kudrna, M. Tichy, and A. Pysanenko, J. Phys. B **34**(15), L485 (2001).
[53]L. S. Rothman, I. E. Gordon, A. Barbe, D. C. Benner, P. F. Bernath, M. Borik, V. Boudon, L. R. Brown, A. Campargue, J.-P. Champion, K. Chance, L. H. Coudert, V. Dana, V. M. Devi, S. Fally, J.-M. Flaud, R. R. Gamache, A. Goldman, D. Jacquemart, I. Kleiner, N. Lacome, W. J. Lafferty, J.-Y. Mandin, S. T. Massie, S. N. Mikhailenko, C. E. Miller, N. Moazzen-Ahmadi, O. V. Naumenko, A. V. Nikitin, J. Orphai, V. I. Perevalov, A. Perrin, A. Predoi-Cross, C. P. Rinsland, M. Rotger, M. Simeckova, M. A. H. Smith, K. Sung, S. A. Tashkun, J. Tennyson, R. A. Toth, A. C. Vandaele, and J. V. Auwera, J. Quant. Spectrosc. Radiat. Transf. **110**, 533 (2009).
[54]J. Tennyson, private communication (2012).
[55]J. Ramanlal and J. Tennyson, Mon. Not. R. Astron. Soc. **354**, 161 (2004).
[56]P. Dohnal, M. Hejduk, J. Varju, P. Rubovic, S. Roucka, T. Kotrik, R. Plasil, R. Johnsen, and J. Glosik, Philos. Trans. R. Soc. London, Ser. A **370**, 5101 (2012).
[57]I. Korolov, T. Kotrik, R. Plasil, J. Varju, M. Hejduk, and J. Glosik, Contrib. Plasma Phys. **48**(5−7), 521 (2008).
[58]R. Plasil, I. Korolov, T. Kotrik, J. Varju, P. Dohnal, Z. Donko, G. Bano, and J. Glosik, J. Phys.: Conf. Ser. **192**, 012023 (2009).
[59]R. Plasil, I. Korolov, T. Kotrik, P. Dohnal, G. Bano, Z. Donko, and J. Glosik, Eur. Phys. J. D **54**, 391 (2009).
[60]J. Glosik, G. Bano, R. Plasil, A. Luca, and P. Zakouril, Int. J. Mass Spectrom. **189**, 103 (1999).
[61]J. Stevefelt, J. Boulmer, and J. Delpech, Phys. Rev. A **12**, 1246 (1975).
[62]T. Kotrik, P. Dohnal, S. Roucka, P. Jusko, R. Plasil, J. Glosik, and R. Johnsen, Phys. Rev. A **83**, 032720 (2011).
[63]T. Kotrik, P. Dohnal, P. Rubovic, R. Plasil, S. Roucka, S. Opanasiuk, and J. Glosik, Eur. Phys. J.: Appl. Phys. **56**, 24011 (2011).
[64]R. Plasil, I. Korolov, T. Kotrik, and J. Glosik, Int. J. Mass Spectrom. **275**, 80 (2008).

[65]R. Plasil, J. Varju, M. Hejduk, P. Dohnal, T. Kotrik, and J. Glosik, J. Phys.: Conf. Ser. **300**(1), 012023 (2011).
[66]D. R. Bates, A. E. Kingston, and W. P. McWhirter, Philos. Trans. R. Soc. London, Ser. A **267**, 297 (1962).
[67]E. W. McDaniel, J. B. A. Mitchell, and M. E. Rudd, *Atomic Collisions, Heavy Partricle Projectiles* (Wiley Interscience, New York, 1993).
[68]J. J. Thomson, Philos. Mag. **47**, 337 (1924).
[69]D. Bates and S. Khare, Proc. Phys. Soc. London **85**, 231 (1965).

C. Cryo-FALP II

C.1 Binary Recombination of H_3^+ and D_3^+ Ions with Electrons in Plasma at 50–230 K

P. Rubovič, P. Dohnal, M. Hejduk, R. Plašil and J. Glosík, *The Journal of Physical Chemistry A*, 0(0):null, 0, 2013. doi:10.1021/jp3123192.

THE JOURNAL OF PHYSICAL CHEMISTRY A

Article

pubs.acs.org/JPCA

Binary Recombination of H_3^+ and D_3^+ Ions with Electrons in Plasma at 50−230 K

Peter Rubovič, Petr Dohnal, Michal Hejduk, Radek Plašil,* and Juraj Glosík

Department of Surface and Plasma Science, Faculty of Mathematics and Physics, Charles University, Prague 18000, Czech Republic

ABSTRACT: The results of an experimental study of the H_3^+ and D_3^+ ions recombination with electrons in afterglow plasmas in the temperature range 50−230 K are presented. A flowing afterglow apparatus equipped with a Langmuir probe was used to measure the evolution of the electron number density in the decaying plasma. The obtained values of the binary recombination rate coefficient are $\alpha_{\mathrm{bin}H_3^+} = (6.0 \pm 1.8) \times 10^{-8}(300/T)^{0.36\pm0.09}$ cm^3 s^{-1} for H_3^+ ions in the temperature range 80−300 K and $\alpha_{\mathrm{bin}D_3^+} = (3.5 \pm 1.1) \times 10^{-8}(300/T)^{0.73\pm0.09}$ cm^3 s^{-1} for D_3^+ ions in the temperature range 50−300 K. This is the first measurement of the binary recombination rate coefficient of H_3^+ and D_3^+ ions in a plasma experiment down to 50 K.

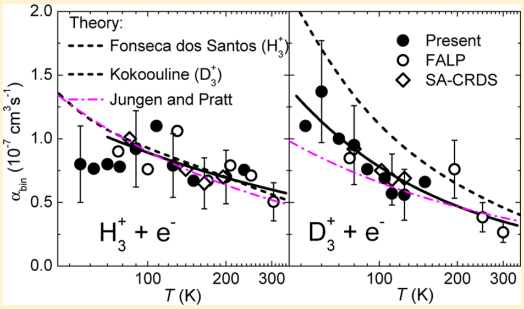

I. INTRODUCTION

The recombination of the simplest polyatomic ion H_3^+ (and to some extent of its deuterated isotopologues) with electrons has been the subject of extensive study by both experimental and theoretical physicists during the previous fifty years.[1] This process is fundamental for modeling of astrophysical diffuse clouds[2] and other hydrogen containing plasmas. The long history of H_3^+ recombination studies has been summarized in a number of reviews[3−8] and in the thorough book by Larsson and Orel.[9] The once puzzling disagreements in magnitude of recombination rate coefficients obtained in different types of experiments have been largely resolved by taking into account third-body stabilized recombination processes that can substantially enhance the overall recombination in plasmas over the pure binary recombination rate coefficients measured in beam type experiments.[10,11] Moreover, the large discrepancy between experimentally obtained recombination rate coefficients and some early quantum mechanical calculations[12] has been successfully resolved by including the role of the Jahn−Teller effect.[13−16] Theoretical predictions now agree very well with values obtained in ion-storage-rings experiments[17−20] and in afterglow experiments.[4,10,11,21,22]

In comparison, the neutral assisted ternary recombination of H_3^+ and D_3^+ ions with electrons as found in helium buffered afterglow experiments is still not fully understood. The recombining H_3^+ and D_3^+ ions form long living metastable Rydberg states[11,21] with lifetimes in the order of hundreds of picoseconds. At pressures above 100 Pa, this is long enough for several collisions with particles of the buffer gas prior to recombination. Although some mechanisms for these interactions have been proposed,[8,11] none of them fully explains the experimental data. This topic is thoroughly discussed in another article in this volume[23] together with new experimental data on the ternary helium assisted recombination of H_3^+ or D_3^+ ions with electrons.

The theory of the dissociative recombination of H_3^+ ions with electrons also predicts a large difference between the recombination of *ortho*- and *para*-H_3^+ (more than 10 times at 10 K, 2.5 times at 80 K and no difference above 300 K).[15] This was partially confirmed by storage ring measurements conducted using normal and para-enriched hydrogen (normal hydrogen contains 25% of *para*-H_2 and 75% of *ortho*-H_2—i.e., the population of the rotational states of H_2 in thermodynamic equilibrium at 300 K).[18,24−26] Tom et al.[25] found that *para*-H_3^+ recombines about twice as fast as *ortho*-H_3^+ at low collisional energies (10 K). The rotational temperature of H_3^+ ions in this experiment was probably higher than 300 K (see discussion in refs 20 and 26). In recent stationary afterglow experiments[27−29] a cavity ring down spectrometer (CRDS) was used to probe the decay of ions in specific rotational states and to determine the state specific recombination coefficients. According to these experiments at 77 K *para*-H_3^+ ions recombine three to 10 times faster (if the error bars are taken into account) than *ortho*-H_3^+ ions. In these experiments, the H_3^+ ions were in thermodynamic equilibrium (TDE) with the helium buffer gas; i.e., the measured kinetic and rotational temperatures of the H_3^+ ions were close to the wall temperature, $T_{\mathrm{kin}} = T_{\mathrm{rot}} = T_{\mathrm{He}} = T_{\mathrm{wall}}$.

Another afterglow experiment with spectroscopically resolved number densities of the recombining H_3^+ ions was conducted by Amano in pure hydrogen in the early nineties.[30]

Special Issue: Oka Festschrift: Celebrating 45 Years of Astrochemistry

Received: December 14, 2012
Revised: March 6, 2013

C.1

   dx.doi.org/10.1021/jp3123192 | J. Phys. Chem. A XXXX, XXX, XXX−XXX

His value of recombination rate coefficient $\alpha = 1.8 \times 10^{-7}$ cm^3 s^{-1} at 273 K and measured at pressure below 100 Pa is rather high and it probably indicates a very effective H_2 assisted ternary recombination.

The recombination of D_3^+ ions with electrons was also studied in storage ring experiments[31] and in plasmatic experiments.[4,21,32] Up to now there is only one study in a D_3^+ dominated plasma with spectroscopically resolved recombining ions.[33] In that experiment the measured kinetic and rotational temperatures of the recombining ions was also close to the buffer gas temperature (for details see ref 33).

In addition to the ternary neutral assisted recombination, an entirely different ternary process that can enhance the overall recombination rate in low temperature afterglow plasma is electron assisted ternary recombination (collisional radiative recombination, E-CRR).[34] At 80 K and an electron number density of $n_e = 5 \times 10^{10}$ cm^{-3} the predicted effective binary recombination rate coefficient due to E-CRR is 5×10^{-7} cm^3 s^{-1}—much larger than the actual values measured in H_3^+ or D_3^+ dominated afterglow plasmas under the same conditions.[28,33] The thorough analysis of experimental data made by Dohnal et al.[28] has shown that the E-CRR contribution to the overall recombination rate in their experiments is more than order of magnitude lower than that predicted by the theory of E-CRR.[34] We have recently studied the E-CRR of Ar^+ ions in the temperature range 50−200 K,[35,36] and we have obtained reasonable agreement with the theory. It is rather puzzling that we can measure value for the recombination rate coefficient close to the calculated one for the atomic ion Ar^+ and not for the molecular ion H_3^+. Recently, Shuman et al.[37] observed the dependence of the mutual neutralization of Ar^+ ions with various molecular anions on electron number density. Although the process they proposed is different than E-CRR (and 10−100 times faster), it is clear that the magnitude of the electron induced enhancement of the recombination rate of more complicated species (e.g., molecular ions) is still an open question (especially given the lack of experimental data on the subject). One of the motivations for the present experiments was to study the role of E-CRR on the overall recombination of H_3^+/D_3^+ ions in an afterglow plasma.

In this article we will present the results of our study of the recombination of H_3^+ and D_3^+ ions with electrons in the temperature range 50−230 K, extending our previous measurement down to 50 K. The present measurements were performed with better temperature stability and over a broader range of pressures than in our previous flowing afterglow experiments[10,11,21] to gain better accuracy of obtained binary and ternary recombination rate coefficients. To the best of our knowledge this is the first study of recombination of these molecular ions in an afterglow plasma below 80 K.

II. EXPERIMENT

In this study we used a Cryo-FALP II apparatus—a modification of the standard FALP (Flowing Afterglow with Langmuir Probe) device. The details of the FALP technique may be found in refs 9 and 38. The current experimental setup is described in ref 36 so only a short description will be given here.

The helium buffer gas is ionized in a microwave discharge in the upstream glass section of the flow tube, enters the stainless steel flow tube, and is pumped out by a Roots pump located at the other end of the flow tube. Argon is added a few centimeters downstream from the discharge to remove metastable helium atoms and to form an Ar^+ dominated plasma. Further downstream, H_2 or D_2 is added to form H_3^+ or D_3^+ dominated plasmas. The sequence of ion−molecule reactions leading to the formation of H_3^+ (D_3^+) dominated plasma is discussed, e.g., in refs 5 and 39. The decrease of the electron number density along the flow tube is measured by means of axially movable Langmuir probe.

In our previous SA-CRDS (stationary afterglow with cavity ring down spectrometer) experiments[27−29,33,40] conducted under conditions (pressure, temperature, and gas composition) similar to those in the present experiment, the measured kinetic and rotational temperatures of the H_3^+ or D_3^+ ions in the afterglow were close to the buffer gas temperature. Therefore, we have good reason to suppose that the internal temperature of the recombining ions is close to the buffer gas temperature also in the presented study which essentially extends previous measurements down to 50 K. Nevertheless, as discussed below, the actual *para*-H_3^+ to *ortho*-H_3^+ ratio could have been slightly shifted in favor of *ortho*-H_3^+ at temperatures below 80 K.

The electron temperature T_e was not directly measured in these (SA-CRDS and Cryo-FALP II) experiments. Recently, we have studied the collisional radiative recombination of Ar^+ ions with electrons, a process with a steep dependence on electron temperature.[35,36] The results were in overall agreement with the theory of E-CRR[34] indicating that T_e was not significantly higher than the buffer gas temperature. Another indirect measure of the value of T_e is the rate of ambipolar diffusion. Ambipolar diffusion time constants measurements for the Ar^+ ions in helium gas, performed using the same experimental setup as in present study,[35] confirmed that in the studied range 80−200 K the measured ambipolar diffusion is close to the expected value, i. e. again that the electron temperature is not higher than the buffer gas temperature (within experimental error of 10%).

III. DETERMINATION OF THE BINARY RECOMBINATION RATE COEFFICIENTS

Here and in the following text we will refer to the recombining ions as H_3^+, but the same considerations apply to D_3^+ ions unless stated otherwise.

It has been shown in previous afterglow experiments[4,10,11,21] that the recombination losses due to the ternary helium assisted recombination of H_3^+ or D_3^+ ions can be comparable to that due to the dissociative recombination at buffer gas pressures of a few hundred pascals. Furthermore, at low temperatures and high densities of H_2 and He, H_5^+ cluster ions, which quickly recombine with electrons with a recombination rate coefficient $\alpha_5 \sim 10^{-6}$ cm^3 s^{-1}, are formed in three body association reactions.[41,42]

The overall losses of charged particles in a H_3^+ dominated plasma with a small fraction of H_5^+ ions, following the derivation in refs 35 and 42 can be described by the equation

$$\frac{dn_e}{dt} = \frac{d[H_3^+]}{dt} = -\alpha_{bin}[H_3^+]n_e - \alpha_5 R[H_3^+]n_e - K_{He}[He][H_3^+]n_e - K_{E\text{-}CRR}[H_3^+]n_e^2 - \frac{n_e}{\tau_D} - \frac{n_e}{\tau_R} \quad (3)$$

where n_e is the electron number density, $[H_3^+]$ is the number density of H_3^+ ions, [He] is the number density of neutral buffer gas atoms (helium in this experiment), α_{bin} is the binary

C.1

dx.doi.org/10.1021/jp3123192 | J. Phys. Chem. A XXXX, XXX, XXX−XXX

recombination rate coefficient of H_3^+ ions, α_5 is the H_5^+ binary recombination rate coefficient, $R = [H_5^+]/[H_3^+] \approx K_C[H_2]$ (K_C is the equilibrium constant, the ratio R is equal to $K_C[H_2]$ if R does not change in time), K_{He} is the ternary recombination rate coefficient of neutral assisted ternary recombination (N-CRR), $K_{E\text{-}CRR}$ is the ternary recombination rate coefficient of electron assisted collisional radiative recombination (E-CRR), τ_D is the time constant of ambipolar diffusion, and τ_R is the time constant of losses due to reactions with impurities and consequent fast recombination of formed ions. Assuming that H_3^+ is the dominant ion in the decaying plasma, and that the plasma is quasineutral, eq 3 can be then simplified:

$$\frac{dn_e}{dt} = -\alpha_{eff} n_e^2 - \frac{n_e}{\tau_L} \quad (4)$$

where

$$\alpha_{eff} = \alpha_{extrap} + \alpha_5 K_C[H_2] = \alpha_{eff0} + K_{He}[He] + \alpha_5 K_C[H_2] \quad (5)$$

is the effective binary recombination rate coefficient, and $1/\tau_L = 1/\tau_D + 1/\tau_R$. The α_{extrap} is part of the effective recombination rate coefficient independent of hydrogen number density. In the limit of vanishing helium and hydrogen densities, α_{eff} ($[H_2] \rightarrow 0$, $[He] \rightarrow 0$) = $\alpha_{eff0} = (\alpha_{bin} + K_{E\text{-}CRR} n_e)$.

In the previous paragraph we have assumed that losses by N-CRR and E-CRR can be linearly added. This assumption might not be necessarily correct because of competition between both ternary processes.[43] At temperatures above 100 K and electron number densities $n_e \sim 10^9$ cm^{-3}, the predicted losses due to E-CRR[34] are negligible in comparison with the losses due to dissociative recombination of H_3^+ (or D_3^+). At lower temperatures the losses due to E-CRR could be comparable with those from the dissociative recombination reaction. Nevertheless, we decided not to evaluate the $K_{E\text{-}CRR}$ from the measured decay of the electron number density. If the E-CRR is present, it would be included in the α_{eff0} term of eq 5, because the H_2 and He dependent terms are evaluated separately (see below).

The "integral data analysis" described in ref 44 enables us to evaluate the effective recombination rate coefficient, α_{eff}, and the time constant, τ_L, from the measured evolution of the electron number density.

To correct for the presence of H_5^+ ions, we measured the dependence of the effective recombination rate coefficient, α_{eff}, on the H_2 number density at each temperature and pressure. Examples of such dependences are plotted in Figure 1.

The recombination rate coefficients of H_3^+ ions with electrons at a given temperature and pressure $\alpha_{extrap}(T, [He]) = \alpha_{eff}(T,[He],[H_2]\rightarrow 0)$, are then obtained by linear extrapolation of the measured α_{eff} to $[H_2] = 0$, as shown in Figure 1. The steepness of the slope fitted to these data increased with helium density and decreasing temperature. The number density of H_2 was always kept above 5×10^{11} cm^{-3} because it has to be high enough to form H_3^+ rapidly from the Ar^+ precursor ions and to maintain a constant *para*- to *ortho*-H_3^+ ratio. Otherwise, the faster recombining species would be depleted preferentially. We perform calculations of the chemical kinetics to determine the best conditions for the experiment. The discussions in refs 4 and 11 suggest that at conditions similar to the present experiment, the number density of H_2 should be greater than 10^{12} cm^{-3}. In this study $[H_2]$ was in the range 5×10^{11} to 2×10^{13} cm^{-3}, sufficient to maintain the *para*-

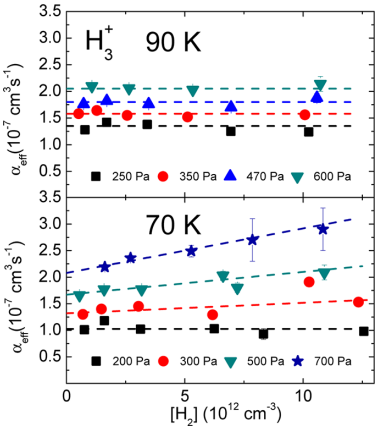

Figure 1. Dependence of the measured effective recombination rate coefficient of recombination of H_3^+ ions with electrons on H_2 number density at 90 K (upper panel) and 70 K (lower panel). Dashed lines are linear fits to the data. The extrapolation of these fits to $[H_2] = 0$ gives the value of $\alpha_{extrap}(T,[He])$ at the given temperature and pressure.

H_3^+ to *ortho*-H_3^+ ratio at the value appropriate for the *para*/*ortho* composition of the H_2 gas used.[40,45]

Examples of measured dependences of α_{eff} on the helium number density for H_3^+ and for D_3^+ are plotted in Figure 2.

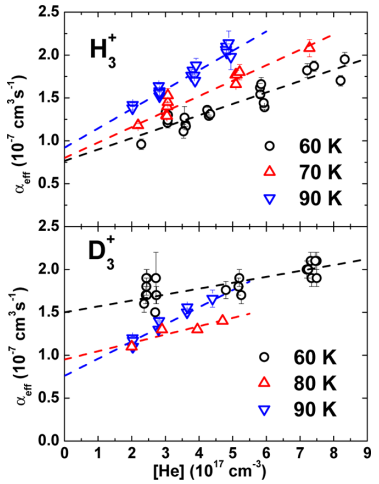

Figure 2. Upper panel: dependence of the effective recombination rate coefficient of recombination of H_3^+ ions with electrons on the helium buffer gas density measured at each of the following temperatures: 60, 70, and 90 K. Lower panel: as in the upper panel but for D_3^+ ions at the temperatures 60, 80, and 90 K. The dashed lines are linear fits to the data. The displayed errors are statistical errors.

These data were obtained at number densities of H_2 in the range 1×10^{12} to 7×10^{12} cm^{-3}. In general, the binary and the ternary recombination rate coefficients can be obtained from the dependences plotted in Figure 2, as is discussed, e.g., in ref 28. At low temperatures (especially at 50 K) and at higher helium densities the formation of H_5^+ (D_5^+) would cause an additional increase in the effective recombination rate

C.1

dx.doi.org/10.1021/jp3123192 | J. Phys. Chem. A XXXX, XXX, XXX–XXX

coefficient. The binary α_{eff0} and the ternary K_{He} recombination rate coefficients at a given temperature were thus obtained using eq 5 from the dependence of $\alpha_{extrap}(T,[He])$ on the helium number density. The errors displayed in Figures 1 and 2 are statistical errors of the fit to the time decay of electron number density.

IV. RESULTS AND DISCUSSION

The measured dependence of the binary recombination rate coefficient α_{bin} (α_{eff0}, see below) of the recombination of H_3^+ ions with electrons on temperature is plotted in Figure 3. The present data are plotted as full circles. Values from previous FALP,[11] SA-CRDS,[27,28] and CRYRING[19] experiments are also plotted in Figure 3 together with the thermal dissociative recombination rate coefficients calculated by Fonseca dos Santos et al.[15] and by Pratt and Jungen.[16,46] We computed the thermal values from the energy dependent recombination rate coefficients published by Pratt and Jungen.[46] The estimated errors of the measured recombination rate coefficients α_{bin} are ±30%.[47] The main contributions of the systematic errors arise from the electron number density measurement by Langmuir probe and from uncertainties in the determination of pressure and gas flows. The statistical error from the aforementioned fitting steps (less than 10%) is negligible in comparison with the systematic one.

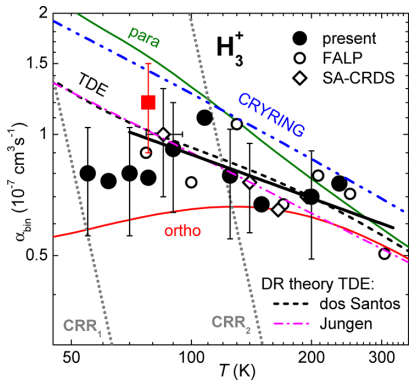

Figure 3. Temperature dependence of the binary recombination rate coefficient for the recombination of H_3^+ ions with electrons. Present Cryo-FALP II data are indicated by full circles. Open rhomboids indicate values measured by Varju et al.[27] and Dohnal et al.[28] using the SA-CRDS apparatus with spectroscopic identification of the recombining ions. Open circles are binary recombination rate coefficients measured in this laboratory using the FALP technique (see discussion in refs 11 and 28). The dashed double dotted line shows data measured at the storage ring CRYRING.[19] The dashed, and the dot dashed, lines marked TDE are theoretical calculations by Fonseca dos Santos[15] and Pratt and Jungen,[46] respectively. The dotted lines marked CRR_1 and CRR_2 indicate calculated[34] recombination rate coefficient for E-CRR at electron number densities of 10^9 and 5×10^{10} cm^{-3}, respectively. The thick full straight line is a fit to the FALP, Cryo-FALP II, and SA-CRDS data in the range 80−300 K: $\alpha_{binH_3^+} = (6.0 \pm 1.8) \times 10^{-8}(300/T)^{0.36\pm0.09}$ cm^3 s^{-1}. The full lines labeled para and ortho are recombination rate coefficients calculated by Fonseca dos Santos[15] for *para*-H_3^+ and *ortho*-H_3^+ ions. The full square is the value of α_{bin} measured using the Cryo-FALP II apparatus with para-enriched H_2 instead of normal H_2.

The dotted lines in Figure 3 labeled CRR_1 and CRR_2 are effective binary recombination rate coefficients of E-CRR ($\alpha_{E\text{-}CRR}$) at electron number density of 10^9 cm^{-3} (a typical value for the present Cryo-FALP II experiment) and 5×10^{10} cm^{-3} (a typical value for the SA-CRDS experiment), calculated from the dependence $\alpha_{E\text{-}CRR} = 3.8 \times 10^{-9}\ T^{-4.5}\ n_e$ cm^3 s^{-1} (see ref 34), respectively. Note that at $T \sim 80$ K, the difference between the values of α_{bin} obtained in the present study and in the previous SA-CRDS experiment[27] is less than 2×10^{-8} cm^3 s^{-1}. This suggests that the effect of E-CRR on the recombination of H_3^+ ions with electrons is at least 20 times lower than predicted by theory of E-CRR.[34] A substantial increase of the recombination rate coefficient below 80 K (in accordance with the $T^{-4.5}$ temperature dependence of $\alpha_{E\text{-}CRR}$) was not observed. This leads to the conclusion that under our experimental conditions $\alpha_{eff0} = \alpha_{bin}$.

We have previously measured the rate coefficients of E-CRR of Ar^+ ions using the same setup as in current experiment[35,36] and we have found good agreement with theory of E-CRR.[34] We do not have an explanation for the seeming absence of E-CRR in the H_3^+ dominated plasma investigated here.

The thick full straight line plotted in Figure 3 is the fit of the FALP, Cryo-FALP II, and SA-CRDS data in the temperature range 80−300 K giving the value $\alpha_{binH_3^+} = (6.0 \pm 1.8) \times 10^{-8}(300/T)^{0.36\pm0.09}$ cm^3 s^{-1}. We included in the fit only the data for which we have information about the internal state of the recombining ions. The agreement of the present data with our previous afterglow experiments, storage ring values and with the theoretical calculations is very good. Below 80 K the experimental values begin to deviate from the theoretical ones. To form H_3^+ ions, we used normal H_2 from a 300 K reservoir, with a *para*- to *ortho*-H_2 ratio of 1:3. The *para*- to *ortho*-H_2 equilibrium ratio at 50 K is approximately 3:1. We suspect that this huge difference could shift the population of H_3^+ ions toward *ortho*-H_3^+. At 77 K where the *para*- to *ortho*-H_2 equilibrium ratio is 1:1, the resulting percentage of *para*-H_3^+ states was 45 ± 2% depending on conditions (see Figure 10 in Hejduk et al.[40]). There is a difference in magnitude of the recombination rate coefficients of *para*- and *ortho*-H_3^+ below 300 K. *para*-H_3^+ recombines 2 times faster than *ortho*-H_3^+ at 10 K as measured in storage ring experiment CRYRING[25] or 3−10 times faster at 80 K as measured in our stationary afterglow experiment.[27] The theory[15] suggests that *para*-H_3^+ recombines 2.5 times faster than *ortho*-H_3^+ at 80 K (Figure 3). This would lead to substantial decrease of measured α_{bin} if the fraction of *ortho*-H_3^+ ions was enhanced with respect to the equilibrium population of states of the H_3^+ ions.

To see the influence of the different *para*- to *ortho*-H_3^+ ratios on the overall recombination in plasma, we used hydrogen with an enriched fraction of *para*-H_2 at otherwise identical conditions as in presented experiments with normal H_2. The para-enriched hydrogen was produced using apparatus described in ref 40. According to the measurements of the reaction rate coefficient of the reaction of N^+ with H_2,[48] the produced H_2 gas contained 99.5 ± 0.5% molecules in *para*-H_2 states. Using this *para*-H_2-enriched gas to form the H_3^+ dominated plasma, the obtained value of the binary recombination rate coefficient was $(1.2 \pm 0.3) \times 10^{-7}$ cm^3 s^{-1} at 80 K in comparison with the value of $(0.8 \pm 0.3) \times 10^{-7}$ cm^3 s^{-1} obtained using normal H_2. The result is plotted in Figure 3 as a full square. Unfortunately, we are not able to measure in situ the *para*- to *ortho*-H_3^+ ratio in the present Cryo-

C.1

dx.doi.org/10.1021/jp3123192 | J. Phys. Chem. A XXXX, XXX, XXX−XXX

FALP II setup. The fraction of *para*-H_3^+ ions obtained in SA-CRDS experiment at 80 K when para-enriched H_2 was used was 70−75%.[40] We suppose that the *para*-H_3^+ fraction in our Cryo-FALP II experiment is similar.

The experiments with D_3^+ dominated plasmas were similar to those with H_3^+ dominated plasmas. We measured the dependence of the effective recombination rate coefficient on the D_2 number density at particular temperatures and pressures and obtained the binary α_{bin} and the ternary K_{He} recombination rate coefficients for the recombination of D_3^+ ions with electrons. The measured binary recombination rate coefficients of recombination of D_3^+ ions with electrons are plotted in Figure 4 together with values from previous SA-CRDS,[33]

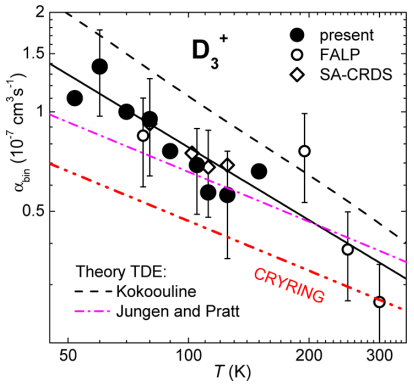

Figure 4. Temperature dependence of the measured binary recombination rate coefficient for the recombination of D_3^+ ions with electrons. Full circles indicate the present data obtained in the Cryo-FALP II experiment. Open rhomboids are the values obtained in SA-CRDS experiment.[33] Open circles are data from previous FALP[21] experiments. The dashed double dot line indicates results from the storage ring CRYRING.[31] The theoretical calculations of Kokoouline[49] and Pratt and Jungen[46] are plotted as dashed lines and dot dashed lines, respectively. The full straight line is a fit to the FALP, Cryo-FALP II, and SA-CRDS data in the range 50−300 K: $\alpha_{bin D_3^+} = (3.5 \pm 1.1) \times 10^{-8}(300/T)^{0.73\pm0.09}$ cm^3 s^{-1}.

FALP,[21] and CRYRING[31] experiments. The theoretical dependences calculated by Kokoouline[49] and by Pratt and Jungen[46] are also plotted in Figure 4. We calculated the recombination rate coefficients labeled Jungen and Pratt in Figure 4 by thermally averaging their energy dependent recombination rates published in ref 46. The full straight line plotted in Figure 4 is the fit to the FALP, Cryo-FALP II, and SA-CRDS data in the range 50−300 K, giving a value for recombination rate coefficient $\alpha_{bin D_3^+} = (3.5 \pm 1.1) \times 10^{-8}(300/T)^{0.73\pm0.09}$ cm^3 s^{-1}. The theory[49] predicts that the difference between the recombination rate coefficients of each nuclear spin state modification of D_3^+ (ortho, para, and meta) is only small and not so pronounced as in the case of H_3^+. For example at 50 K *ortho*-D_3^+ should recombine 1.5 times faster than *meta*-D_3^+. Moreover, the relative population of nuclear spin modifications in the D_2 gas used in the experiment is close to the equilibrium value even at 60 K due to the closer spacing of the rotational energy levels of D_2 in comparison with H_2. At 300 K the *para*-D_2 to *ortho*-D_2 equilibrium ratio is 2, at 60 K the *para*-D_2 to *ortho*-D_2 equilibrium ratio is 1.8. Therefore, we suppose that the *ortho*/*para*/*meta*-D_3^+ ratio is maintained in the whole temperature range used in this study. This is probably why the values for the D_3^+ recombination rate coefficient obtained below 80 K continue to follow the $T^{-0.73}$ dependence (the full line plotted in Figure 4). As in the case of H_3^+, the results obtained for D_3^+ are in good agreement with theoretical calculations and with other experiments. No substantial difference between present values and values obtained in SA-CRDS experiment[33] conducted at order of magnitude higher n_e was observed. As in the case of H_3^+ dominated plasma we have seen no substantial influence of E-CRR on the overall recombination of D_3^+ ions with electrons over the range of experimental conditions.

Together with binary recombination rate coefficients α_{bin} we also evaluated the ternary recombination rate coefficients K_{He} for the recombination of H_3^+ and D_3^+ ions with electrons in the temperature range 50−230 K. These results are published elsewhere[23] together with a thorough discussion of possible ternary recombination processes occurring in low temperature plasmas. The temperature range 80−300 K was already covered in our previous experiments;[11,21,28,33] the present data were measured over wider temperature and pressure ranges than in the FALP[11,21] experiments and with better accuracy and temperature stability. The agreement with these previous studies is good.

V. CONCLUSION

We have measured the binary and the ternary recombination rate coefficient for the recombination of H_3^+ and D_3^+ ions with electrons in the temperature range 50−230 K. The results are in good agreement with previous afterglow experiments (FALP and SA-CRDS), storage ring data, and theoretical calculations. The obtained binary recombination rate coefficients follow the dependence $\alpha_{bin H_3^+} = (6.0 \pm 1.8) \times 10^{-8}(300/T)^{0.36\pm0.09}$ cm^3 s^{-1} for H_3^+ in the temperature range 80−300 K and $\alpha_{bin D_3^+} = (3.5 \pm 1.1) \times 10^{-8}(300/T)^{0.73\pm0.09}$ cm^3 s^{-1} for D_3^+ in the temperature range 50−300 K. We have seen no enhancement of the measured recombination rate coefficient of H_3^+ and D_3^+ ions due to E-CRR even at the lowest temperature. This is in agreement with our previous SA-CRDS experiments[27,33] conducted at higher electron number densities than in present study. The addition of para-enriched H_2 instead of normal H_2 led to the increase of the binary recombination rate coefficient at 80 K from $(0.8 \pm 0.3) \times 10^{-7}$ cm^3 s^{-1} with normal H_2 to $(1.2 \pm 0.3) \times 10^{-7}$ cm^3 s^{-1} with para-enriched H_2. This is the first measurement of the recombination rate coefficient of H_3^+ and D_3^+ ions in a plasma experiment down to 50 K.

AUTHOR INFORMATION

Corresponding Author

*Phone: +420221912224. E-mail: radek.plasil@mff.cuni.cz.

Author Contributions

The manuscript was written through contributions of all authors. All authors have given approval to the final version of the manuscript.

Notes

The authors declare no competing financial interest.

ACKNOWLEDGMENTS

We thank Rainer Johnsen for helpful discussion and comments. This work was partly supported by GACR (205/09/1183, P209/12/0233), SV 267 302, GAUK 353811, GAUK 406011,

C.1

GAUK 659112, and COST Action CM0805 (The Chemical Cosmos).

REFERENCES

(1) Oka, T. in *Dissociative Recombination of Molecular Ions with Electrons*; Guberman, S. L., Ed.; Kluwer Academic/Plenum Publishers: New York, USA, 2003; pp 209−220

(2) Herbst, E.; Klemperer, W. The Formation and Depletion of Molecules in Dense Interstellar Clouds. *Astrophys. J.* **1973**, *185*, 505−533.

(3) Larsson, M. Experimental Studies of the Dissociative Recombination of H_3^+. *Philos. Trans. R. Soc. A* **2000**, *358*, 2433−2444.

(4) Glosik, J.; Plasil, R.; Kotrik, T.; Dohnal, P.; Varju, J.; Hejduk, M.; Korolov, I.; Roucka, S.; Kokoouline, V. Binary and Ternary Recombination of H_3^+ and D_3^+ Ions with Electrons in Low Temperature Plasma. *Mol. Phys.* **2010**, *108*, 2253−2264.

(5) Plasil, R.; Glosik, J.; Poterya, V.; Kudrna, P.; Rusz, J.; Tichy, M.; Pysanenko, A. Advanced Integrated Stationary Afterglow Method for Experimental Study of Recombination of Processes of H_3^+ and D_3^+ Ions with Electrons. *Int. J. Mass Spectrom.* **2002**, *218*, 105−130.

(6) Smith, D.; Spanel, P. Dissociative Recombination of H_3^+ and Some Other Interstellar Ions: a Controversy Resolved. *Int. J. Mass Spectrom.* **1993**, *129*, 163−182.

(7) Johnsen, R. A Critical Review of H_3^+ Recombination Studies. *J. Phys.: Conf. Ser.* **2005**, *4*, 83−91.

(8) Johnsen, R.; Guberman, S. L. Dissociative Recombination of H_3^+ Ions with Electrons: Theory and Experiment. *Adv. At., Mol., Opt. Phys.* **2010**, *59*, 75−128.

(9) Larsson, M.; Orel, A. *Dissociative Recombination of Molecular Ions*; Cambridge University Press: Cambridge, U.K., 1995.

(10) Glosik, J.; Korolov, I.; Plasil, R.; Novotny, O.; Kotrik, T.; Hlavenka, P.; Varju, J.; Mikhailov, I. A.; Kokoouline, V.; Greene, C. H. Recombination of H_3^+ Ions in the Afterglow of a He-Ar-H_2 Plasma. *J. Phys. B-At. Mol. Opt.* **2008**, *41*, 191001.

(11) Glosik, J.; Plasil, R.; Korolov, I.; Kotrik, T.; Novotny, O.; Hlavenka, P.; Dohnal, P.; Varju, J.; Kokoouline, V.; Greene, C. H. Temperature Dependence of Binary and Ternary Recombination of H_3^+ Ions with Electrons. *Phys. Rev. A* **2009**, *79*, 052707.

(12) Michels, H. H.; Hobbs, R. H. Low-Temperature Dissociative Recombination of e + H_3^+. *Astrophys. J.* **1984**, *286*, L27−L29.

(13) Kokoouline, V.; Greene, C. H.; Esry, B. D. Mechanism for the Destruction of H_3^+ Ions by Electron Impact. *Nature* **2001**, *412*, 891−894.

(14) Kokoouline, V.; Greene, C. H. Unified Theoretical Treatment of Dissociative Recombination of D_{3h} Triatomic Ions: Application to H_3^+ and D_3^+. *Phys. Rev. A* **2003**, *68*, 012703.

(15) Fonseca dos Santos, S.; Kokoouline, V.; Greene, C. H. Dissociative Recombination of H_3^+ in the Ground and Excited Vibrational States. *J. Chem. Phys.* **2007**, *127*, 124309.

(16) Jungen, Ch.; Pratt, S. T. Jahn-Teller Interactions in the Dissociative Recombination of H_3^+. *Phys. Rev. Lett.* **2009**, *102*, 023201.

(17) McCall, B. J.; Honeycutt, A. J.; Saykally, R. J.; Geballe, T. R.; Djuric, N.; Dunn, G. H.; Semaniak, J.; Novotny, O.; Al-Khalili, A.; Ehlerding, A.; et al. An Enhanced Cosmic-Ray Flux Towards ζ Persei Inferred from a Laboratory Study of the H_3^+-e^- Recombination Rate. *Nature* **2003**, *422*, 500−502.

(18) Kreckel, H.; Motsch, M.; Mikosch, J.; Glosik, J.; Plasil, R.; Altevogt, S.; Andrianarijaona, V.; Buhr, H.; Hoffman, J.; Lammich, L.; et al. High-Resolution Dissociative Recombination of Cold H_3^+ and First Evidence for Nuclear Spin Effects. *Phys. Rev. Lett.* **2005**, *95*, 263201.

(19) McCall, B. J.; Honeycutt, A. J.; Saykally, R. J.; Djuric, N.; Dunn, G. H.; Semaniak, J.; Novotny, O.; Al-Khalili, A.; Ehlerding, A.; Hellberg, F.; et al. Dissociative Recombination of Rotationally Cold H_3^+. *Phys. Rev. A* **2004**, *70*, 052716.

(20) Petrignani, A.; Altevogt, S.; Berg, M. H.; Bing, D.; Grieser, M.; Hoffman, J.; Jordon-Thaden, B.; Krantz, C.; Mendes, M. B.; Novotny, O.; et al. Resonant Structure of Low-Energy H_3^+ Dissociative Recombination. *Phys. Rev. A* **2011**, *83*, 032711.

(21) Kotrik, T.; Dohnal, P.; Korolov, I.; Plasil, R.; Roucka, S.; Glosik, J.; Greene, C. H.; Kokoouline, V. Temperature Dependence of Binary and Ternary Recombination of D_3^+ Ions with Electrons. *J. Chem. Phys.* **2010**, *133*, 034305.

(22) Glosik, J.; Plasil, R.; Korolov, I.; Novotny, O.; Kotrik, T. Multicollision Character of Recombination of H_3^+ Ions in Afterglow Plasma. *J. Phys.: Conf. Ser.* **2009**, *192*, 012005.

(23) Johnsen, R.; Rubovic, P.; Dohnal, P.; Hejduk, M.; Plasil, R.; Glosik, J. Ternary Recombination of H_3^+ and D_3^+ with Electrons in He-H_2 (D_2) Plasmas at Temperatures from 50 to 300 K. Elsewhere in this volume. *J. Phys. Chem. A* **2013**, DOI: 1021/jp311978n.

(24) Wolf, A.; Kreckel, H.; Lammich, L.; Strasser, D.; Mikosch, J.; Glosik, J.; Plasil, R.; Altevogt, S.; Andrianarijaona, V.; Buhr, H.; et al. Effects of Molecular Rotation in Low-Energy Electron Collisions of H_3^+. *Philos. Trans. R. Soc. A* **2006**, *364*, 2981−2997.

(25) Tom, B. A.; Zhaunerchyk, V.; Wiczer, M. B.; Mills, A. A.; Crabtree, K. N.; Kaminska, M.; Geppert, W. D.; Hamberg, M.; af Ugglas, M.; Vigren, E.; et al. Dissociative Recombination of Highly Enriched Para-H_3^+. *J. Chem. Phys.* **2009**, *130*, 031101.

(26) Kreckel, H.; Novotny, O.; Crabtree, K. N.; Buhr, H.; Petrignani, A.; Tom, B. A.; Thomas, R. D.; Berg, M. H.; Bing, D.; Grieser, M.; et al. High-Resolution Storage-Ring Measurements of the Dissociative Recombination of H_3^+ Using a Supersonic Expansion Ion Source. *Phys. Rev. A* **2010**, *82*, 042715.

(27) Varju, J.; Hejduk, M.; Dohnal, P.; Jilek, M.; Kotrik, T.; Plasil, R.; Gerlich, D.; Glosik, J. Nuclear Spin Effect on Recombination of H_3^+ Ions with Electrons at 77 K. *Phys. Rev. Lett.* **2011**, *106*, 203201.

(28) Dohnal, P.; Hejduk, M.; Varju, J.; Rubovic, P.; Roucka, S.; Kotrik, T.; Plasil, R.; Glosik, J.; Johnsen, R. Binary and Ternary Recombination of Para-H_3^+ and Ortho-H_3^+ with Electrons: State Selective Study at 77−200 K. *J. Chem. Phys.* **2012**, *136*, 244304.

(29) Dohnal, P.; Hejduk, M.; Varju, J.; Rubovic, P.; Roucka, S.; Kotrik, T.; Plasil, R.; Johnsen, R.; Glosik, J. Binary Recombination of Para- and Ortho-H_3^+ with Electrons at Low Temperatures. *Philos. Trans. R. Soc. A* **2012**, *370*, 5101−5108.

(30) Amano, T. The Dissociative Recombination Rate Coefficients of H_3^+, HN_2^+ and HCO^+. *J. Chem. Phys.* **1990**, *92*, 6492−6501.

(31) Le Padellec, A.; Larsson, M.; Danared, H.; Larson, A.; Peterson, J. R.; Rosen, S.; Semaniak, J.; Stromholm, C. A Storage Ring Study of Dissociative Excitation and Recombination of D_3^+. *Phys. Scr.* **1998**, *57*, 215−221.

(32) Poterya, V.; Glosik, J.; Plasil, R.; Tichy, M.; Kudrna, P.; Pysanenko, A. Recombination of D_3^+ ions in the Afterglow of a He-Ar-D_2 Plasma. *Phys. Rev. Lett.* **2002**, *88*, 044802.

(33) Dohnal, P.; Hejduk, M.; Rubovic, P.; Varju, J.; Roucka, S.; Plasil, R.; Glosik, J. Binary and Ternary Recombination of D_3^+ Ions at 80−130 K: Application of Laser Absorption Spectroscopy. *J. Chem. Phys.* **2012**, *137*, 194320.

(34) Stevefelt, J.; Boulmer, J.; Delpech, J. F. Collisional-Radiative Recombination in Cold Plasmas. *Phys. Rev. A* **1975**, *12*, 1246−1251.

(35) Kotrik, T.; Dohnal, P.; Roucka, S.; Jusko, P.; Plasil, R.; Glosik, J.; Johnsen, R. Collisional-Radiative Recombination $Ar^+ + e + e$: Experimental Study at 77−180 K. *Phys. Rev. A* **2011**, *83* (3), 032720.

(36) Kotrik, T.; Dohnal, P.; Rubovic, P.; Plasil, R.; Roucka, S.; Opanasiuk, S.; Glosik, J. Cryo-FALP Study of Collisional-Radiative Recombination of Ar^+ Ions at 40−200 K. *Eur. Phys. J. Appl. Phys.* **2011**, *56*, 24011.

(37) Shuman, S.; Miller, T. M.; Bemish, R. J.; Viggiano, A. A. Electron-Catalyzed Mutual Neutralization of Various Anions with Ar^+: Evidence of a New Plasma Process. *Phys. Rev. Lett.* **2011**, *106*, 018302.

(38) Smith, D.; Adams, N. G.; Dean, A. G.; Church, M. J. The Application of the Langmuir Probes to the Study of the Flowing Afterglow Plasmas. *J. Phys. D: Appl. Phys.* **1975**, *8*, 141−152.

(39) Novotny, O.; Plasil, R.; Pysanenko, A.; Korolov, I.; Glosik, J. The Recombination of D_3^+ and D_5^+ Ions with Electrons in Deuterium Containing Plasma. *J. Phys. B-At. Mol. Opt. Phys.* **2006**, *39*, 2561−2569.

(40) Hejduk, M.; Dohnal, P.; Varju, J.; Rubovic, P.; Plasil, R.; Glosik, J. Nuclear Spin State-Resolved Cavity Ring-Down Spectroscopy

C.1

Diagnostics of a Low-Temperature H_3^+ Dominated Plasma. *Plasma Sources Sci. Technol.* **2012**, *21*, 024002.
(41) Hiraoka, K. A determination of the Stabilities of $H_3^+(H_2)_n$ with n = 1−9 from Measurements of the Gas Phase Ion Equilibria $H_3^+(H_2)_{n-1} + H_2 = H_3^+(H_2)_n$. *J. Chem. Phys.* **1987**, *87*, 4048−4055.
(42) Glosik, J.; Novotny, O.; Pysanenko, A.; Zakouril, P.; Plasil, R.; Kudrna, P.; Poterya, V. The Recombination of H_3^+ and H_5^+ Ions with Electrons in Hydrogen Plasma: Dependence on Temperature and on Pressure of H_2. *Plasma Sources Sci. Technol.* **2003**, *12*, S117−S122.
(43) Bates, D. R. Recombination and Electrical Networks. *Proc. R. Soc. London A* **1974**, *337*, 15−20.
(44) Korolov, I.; Kotrik, T.; Plasil, R.; Varju, J.; Hejduk, M.; Glosik, J. Application of Langmuir Probe in Recombination Dominated Afterglow Plasma. *Contrib. Plasma Phys.* **2008**, *48*, 521−526.
(45) Grussie, F.; Berg, M. H.; Crabtree, K. N.; Gartner, S.; McCall, B. J.; Schlemmer, S.; Wolf, A.; Kreckel, H. The Low-Temperature Nuclear Spin Equilibrium of H_3^+ in Collisions with H_2. *Astrophys. J.* **2012**, *759*, 21.
(46) Pratt, T.; Jungen, Ch. Dissociative Recombination of Small Polyatomic Molecules. *J. Phys.: Conf. Ser.* **2011**, *300*, 012019.
(47) Glosik, J.; Bano, G.; Plasil, R.; Luca, A.; Zakouril, P. Study of the Electron Ion Recombination in High Pressure Flowing Afterglow: Recombination of $NH_4^+(NH_3)_2$. *Int. J. Mass Spectrom.* **1999**, *189*, 103−113.
(48) Zymak, I.; Hejduk, M.; Mulin, D.; Plasil, R.; Glosik, J.; Gerlich, D. Low Temperature Ion Trap Studies of $N^+(^3P_{ja}) + H_2(j) \rightarrow NH^+ + H$. *Astrophys. J.* **2013**, in press.
(49) Pagani, L.; Vastel, C.; Hugo, E.; Kokoouline, V.; Greene, C. H.; Backmann, A.; Bayet, E.; Ceccarelli, C.; Peng, R.; Schlemmer, S. Chemical Modeling of L183 (L134N): an Estimate of the Ortho/Para H_2 Ratio. *Astron. Astrophys.* **2009**, *494*, 623−636.

C.1

C.2 Ternary Recombination of H_3^+ and D_3^+ with Electrons in He-H_2 (D_2) Plasmas at Temperatures from 50 to 300 K

R. Johnsen, P. Rubovič, P. Dohnal, M. Hejduk, R. Plašil and J. Glosík, *The Journal of Physical Chemistry A*, 0(0):null, 0, 2013. doi:10.1021/jp311978n.

THE JOURNAL OF PHYSICAL CHEMISTRY A

Article

pubs.acs.org/JPCA

Ternary Recombination of H_3^+ and D_3^+ with Electrons in He–H_2 (D_2) Plasmas at Temperatures from 50 to 300 K

R. Johnsen,*[,†] P. Rubovič,[‡] P. Dohnal,[‡] M. Hejduk,[‡] R. Plašil,[‡] and J. Glosík[‡]

[†]Department of Physics and Astronomy, University of Pittsburgh, Pittsburgh, Pennsylvania 15260, United States

[‡]Faculty of Mathematics and Physics, Department of Surface and Plasma Science, Charles University, Prague, Czech Republic

ABSTRACT: We present results of plasma afterglow experiments on ternary electron-ion recombination rate coefficients of H_3^+ and D_3^+ ions at temperatures from 50 to 300 K and compare them to possible three-body reaction mechanisms. Resonant electron capture into H_3* Rydberg states is likely to be the first step in the ternary recombination, rather than third-body-assisted capture. Subsequent interactions of the Rydberg molecules with ambient neutral and charged particles provide the rate-limiting step that completes the recombination. A semiquantitative model is proposed that reconciles several previously discrepant experimental observations. A rigorous treatment of the problem will require additional theoretical work and experimental investigations.

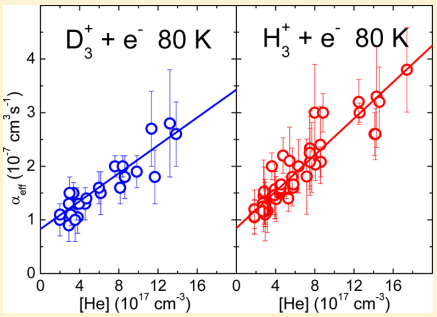

1. INTRODUCTION

The recombination of H_3^+ ions and their deuterated analogs with thermal electrons has been studied for more than four decades, motivated largely by its pivotal role in the chemistry and physics of astrophysical clouds and the atmospheres of the outer planets, applications to man-made discharges, and basic interest. However, a true reconciliation of often discrepant experimental data, and a convergence of theory and experiment have not been achieved, as has been pointed out in recent reviews of the subject (see, e.g., Johnsen and Guberman[1]). This article focuses on three-body recombination of H_3^+ ions, i.e., the enhancement of recombination by collisions with ambient plasma particles, such as electrons, ions, and neutrals. Theoretical[2−5] and experimental[6−8] work on purely binary recombination of H_3^+ has made enormous progress since the advent of storage rings, advanced afterglow techniques, and the modern Jahn–Teller type theories.[2] At this time, the theory reproduces the experimental values of the thermal (Maxwellian) rate coefficients very well, but discrepancies still exist between the calculated resonances and the structures seen in high-resolution storage-ring data, as has been discussed in great detail by Petrignani et al.[9] Some of these resonances may also play a role in the three-body effects discussed here (see section 5).

It is important to realize that third-body assisted recombination does not always lead to experimentally detectable dependences on ambient gas density. We briefly illustrate this point by revisiting the early experiment of Leu et al.[10,11] Their microwave-afterglow measurements yielded an H_3^+ recombination coefficient (2.4×10^{-7} cm^3/s at 300 K) that is far larger (by a factor of nearly 4) than that obtained later (about 0.6×10^{-7} cm^3/s) in low-pressure afterglows[12−14] and storage-ring experiments.[6−8] Leu et al. employed helium as buffer gas, at densities from 4.4×10^{17} to 8.6×10^{17} cm^{-3} at T = 300 K, and from 4.1×10^{17} to 7.8×10^{17} cm^{-3} at 205 K. They found that the recombination rates were independent (within about 5%) of density and that they were independent of the experimental electron densities from 5×10^9 to about 1/20 of that density. Over the limited range of temperatures the measured recombination coefficients varied with temperature as $T^{-1/2}$, exactly what was expected for binary recombination, and hence the authors were confident that they had observed binary recombination of H_3^+, but as we will discuss later, they probably measured a "saturated" three-body reaction that only gives the appearance of binary recombination. A crude estimate of the three-body rate coefficient at 300 K would be given by the ratio $(2.4 \times 10^{-7} - 0.6 \times 10^{-7})/ 4.4 \times 10^{17} = 4 \times 10^{-25}$ cm^6/s, a rather large value that cannot be ascribed to known three-body mechanism[15] such as collisional radiative recombination in which atoms act as third bodies. We emphasize that the large body of data for ions other than H_3^+ collected by the microwave technique was confirmed later and that three-body effects are not at all common. The gas phase recombination of H_3^+, the simplest triatomic ion, clearly has some unusual features!

Systematic measurements of the neutral-assisted recombination have been carried out in the Prague laboratory over a period of about four years and have recently been extended to unprecedented low temperatures (50 K). Both stationary and

Special Issue: Oka Festschrift: Celebrating 45 Years of Astrochemistry

Received: December 5, 2012
Revised: February 6, 2013

C.2

   dx.doi.org/10.1021/jp311978n | J. Phys. Chem. A XXXX, XXX, XXX–XXX

flowing afterglow apparatus were employed, always in conjunction with mass spectrometric identification of the recombining ions. In some measurements the traditional Langmuir probe technique was used to determine electron densities. Although accurate recombination coefficients can be obtained by this method, the internal state of the ions remains unspecified. Hence, optical absorption (cavity-ring-down-spectroscopy, CRDS) was added to observe the decay of H_3^+ (D_3^+) ions in known vibrational/rotational states and to measure the dependence of the recombination on the nuclear spin modification (para, ortho, meta). Complete descriptions of the earlier experiments can be found in Glosík et al.,[16−19,22] Varju et al.,[20,23] Kotrík et al.,[21] Plašil et al.,[29] Rubovič et al.,[24] and Dohnal et al.[25−27]

The earliest such measurements,[28] carried out over a small range of helium densities, were consistent with a lack of density dependence. However, as the accuracy of the data improved, and the density range was increased, a dependence of the recombination on neutral (helium) density was invariably observed. The measurements revealed that the three-body coefficients vary with temperature and that they also depend on the nuclear spin states of the H_3^+ (D_3^+) ions (see Varju et al.,[20,23] Plašil et al.,[29] and Dohnal et al.[25,27]).

We limit the discussion to plasmas in which helium is the dominant neutral gas and ignore possible effects of the minority gases that are often present in afterglow experiments, typically argon and hydrogen. Tests showed that small additions of argon have no significant effect. The hydrogen density is kept small ($<10^{13}$ cm^{-3}), sufficient to maintain thermal equilibrium among rotational states (within either the para or ortho manifolds) and to convert precursor ions (mainly Ar^+) rapidly to H_3^+ (D_3^+). We digress briefly to discuss one important measurement that was performed in pure hydrogen to assess the possible effect of H_2.

Amano's[30] pioneering and very influential optical absorption measurements in pure hydrogen afterglows yielded a large recombination coefficient of 1.8×10^{-7} cm^3/s at 300 K, about 3 times larger than the now accepted binary value. Amano did not observe a dependence of the recombination coefficient on hydrogen density in the range from 3.2×10^{15} cm^{-3} to 10 times that value, which seems to indicate an absence of a three-body contribution due to hydrogen. However, as was pointed out earlier, the absence of a density dependence is not conclusive proof that three-body effects are not present. If one were to ascribe the larger observed recombination coefficient entirely to H_2-stabilized recombination (ignoring possible contributions from electrons), the three-body rate would have to be larger than $(1.8 \times 10^{-7} - 0.6 \times 10^{-7})/3.2 \times 10^{15} = 3.75 \times 10^{-23}$ cm^6/s, about 100 times faster than the estimate made earlier for He as third body. This estimate is compatible with that obtained in the experiments of Gougousi et al.[31] In the afterglow experiments described here, the H_2 density was kept below 10^{13} cm^{-3} and hence H_2-assisted recombination should have been negligible. In later work Amano[32] extended his measurements to low temperatures (~110 K) and found even larger recombination coefficients. Under those conditions, conversion of H_3^+ to H_5^+ is not negligible (see Johnsen[33]) and there is the further complication that the electron densities in Amano's studies were unusually high ($\sim 3 \times 10^{11}$ cm^{-3}).

Neutral particles are probably not the only third bodies that affect H_3^+ recombination. Two afterglow experiments,[31,34] both performed at low helium densities, indicated that the H_3^+ recombination slowed down in the later afterglow (i.e., at smaller electron densities), but the same was not observed in recombination studies of O_2^+ ions, the "benchmark" ion often used to test experimental procedures. However, this observation has also been ascribed to vibrationally excited H_3^+ ions.[34]

In the following, we will present experimental data on the temperature dependence of neutral assisted recombination, followed by a discussion of possible reaction mechanisms. The proposed mechanisms have in common that they invoke high molecular Rydberg states with principal quantum number n, formed either by third-body assisted capture or by resonant capture into autoionizing states. If such states are sufficiently long-lived, their interactions with third bodies may induce dissociation into stable recombination products, thus making the recombination irreversible. In the case of molecular ions, the ionic core may be rotationally (or vibrationally) excited so that several sets of Rydberg states exist that converge to different ionization limits. One should also be aware that the electron "orbits" can be quite large so that many ambient gas particles will be closer to the ion core than the Rydberg electron. For instance, at gas densities of 3×10^{17} cm^{-3} (~10 Torr at 300 K), the spherical volume of an $n = 50$ state contains several thousand atoms. The density of charged particles is typically much lower, but above the Inglis−Teller limit[35,36] ($n_{max} \sim 80$ at $n_e = 1 \times 10^9$ cm^{-3}, $n_{max} \sim 60$ at $n_e = 1 \times 10^{10}$ cm^{-3}) the Stark broadening due to neighboring charged particles is on the same order as the energy difference between adjacent Rydberg states.

2. EXPERIMENTAL DATA ON THE TEMPERATURE DEPENDENCE OF THE HELIUM-ASSISTED RECOMBINATION COEFFICIENT

A comprehensive set of rate coefficients of H_3^+ and D_3^+ has been collected in helium-buffered afterglow plasmas in the Prague laboratory. Some of the data were measured earlier, and some were obtained as part of the present investigation. The instruments used and the methods of analysis are the same as those employed in determinations of the binary recombination coefficients and there is no need to repeat detailed descriptions (see, e.g., Kotrík et al.,[37] Dohnal et al.,[38] and Rubovič et al.[24]). In all these measurements the electron and ion temperatures were the same as the gas temperature, the hydrogen and deuterium gases were taken from room-temperature reservoirs, and their nuclear spin states have their "normal" abundances. We will not discuss recent measurements with para-enriched gases (see Varju et al.,[23] Dohnal et al.,[25−27] and Hejduk et al.[39]).

As a precaution, a series of measurements was performed (Dohnal et al.[38]) to rule out the unlikely possibility that the measured dependences on helium density were due to unrecognized systematic errors, for instance in the determinations of electron densities or in the corrections for diffusion losses. In these tests the well-known recombination coefficient of O_2^+ ions was measured at $T = 230$ K for helium densities (in units of cm^{-3}) from 3.8×10^{17} to 5×10^{17}, and at $T = 155$ K from 2.7×10^{17} to 5.6×10^{17}. No detectable variation with density was observed and the absolute values agreed with the known recombination coefficients.

The three-body (ternary) H_3^+ (D_3^+) rate coefficients K_{He} are derived from graphs of the measured "effective" rate coefficient vs the density of helium, assuming that binary recombination (α_{bin}) and ternary recombination simply add, i.e., that

$$\alpha_{eff} = \alpha_{bin} + K_{He}[He] \quad (1)$$

C.2

dx.doi.org/10.1021/jp311978n | J. Phys. Chem. A XXXX, XXX, XXX−XXX

Experimental values of α_{eff} (Figure 1), collected by the SA-CRDS (stationary afterglow −cavity ring-down spectrometer)

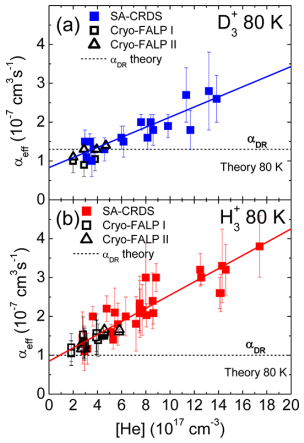

Figure 1. Dependence α_{eff} on helium density at T = 80 ± 3 K, as measured in a stationary afterglow in conjunction with cavity-ring-down spectroscopy (SA-CRDS) and in flowing afterglows (Cryo-FALP I and Cryo-FALP II). (a) D_3^+ data (from Dohnal et al.,[26] Kotrík et al.[21]). (b) H_3^+ data (from Glosík et al.,[18] Varju et al.[23]). The dashed horizontal lines show theoretical values of the binary coefficients (Pagani et al.,[4] Fonseca dos Santos et al.[3]).

and the flowing afterglow (CRYO- FALP I and II), are consistent with a linear dependence over the differing density ranges covered by the experiments. No measurable dependence on electron density was observed, even though the Cryo-FALP I and II data were obtained at low electron densities (typically $n_e = 2 \times 10^9$ cm^{-3}) in the afterglow plasma and the SA-CRDS data were obtained at much higher electron densities (typically 3×10^{10} cm^{-3}).

However, the linear addition of binary and ternary recombination implied by eq 1 is valid only when the two recombination mechanisms occur in parallel, but not when binary and ternary recombination share the same "finite resource", for instance, an intermediate excited state that is formed by electron capture (see section 5). The observations discussed in the Introduction suggest that α_{eff} is more likely to approach a constant value at higher [He]. Hence, the experimental values of K_{He} maybe only approximate first-order values that are valid in the limit of small helium densities.

Figure 2 shows measured K_{He} data for H_3^+ in the temperature range from T = 50 K to T = 350 K, the first such data ever obtained for molecular ions at temperatures below 77 K.

It has been verified in additional studies (Dohnal et al.,[25−27,38] Kotrík et al.[37]) that such plasmas are close to thermal equilibrium ($T_{He} = T_e = T_{ion}$). Although the consistency of the present data with those obtained in earlier experiments is not perfect, the overall temperature dependences are similar. The present experiments covered a wider range of densities and have better accuracy. At temperatures below about 100 K the three-body coefficient falls off with decreasing temperature and then approaches the three-body coefficient for neutral-stabilized recombination. For comparison, we have added experimental data points obtained by Dohnal et al.[38] in plasmas that contained only atomic Ar^+ ions

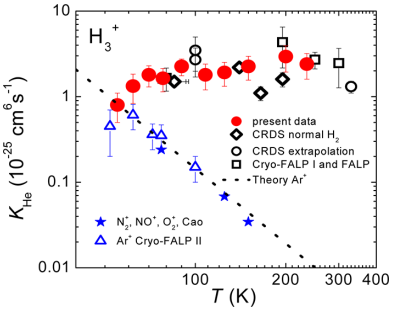

Figure 2. Upper data set: measured variation of K_{He} of H_3^+ ions with gas temperature, obtained when normal hydrogen was used (Varju et al.,[23] Dohnal et al.,[25] Glosík et al.[18]). Lower data set: measured helium-assisted collisional radiative recombination rate coefficient of Ar^+ ions (Dohnal et al.[38]), and earlier results of Cao and Johnsen.[40] Dashed line: theoretical values of the Ar^+ rate coefficient (Bates and Khare[15]).

(in the absence of hydrogen) and those agree very well with earlier data[40] and with theory of neutral assisted collisional radiative recombination (N-CRR, see section 3). At higher temperatures, the latter recombination mechanism makes only a negligible recombination.

Figure 3 shows a similar data set for D_3^+ ions. Here, the rapid decline of the rate coefficient below 100 K is more obvious. In

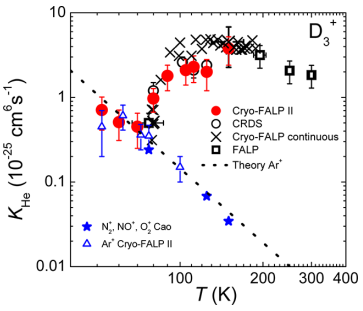

Figure 3. Upper data set: measured variation of K_{He} of D_3^+ ions with gas temperature (Kotrík et al.,[21] Dohnal et al.[26]). Lower data set: measured helium-assisted collisional radiative recombination rate coefficient of Ar^+ ions (Dohnal et al.[38]) and earlier results of Cao and Johnsen.[40] Dashed line: theoretical values of the Ar^+ rate coefficient (Bates and Khare[15]).

these data it is also clear that the D_3^+ ternary rate coefficient rises again below ~70 K, exactly as is observed for atomic argon ions, removing all doubt that neutral collisional radiative recombination occurs in both cases.

Although H_3^+ and D_3^+ are similar in many respects, there is no reason to believe that they recombine with the same rates or that the three-body rate coefficients should be identical because their rotational and vibrational levels are different. The three-body coefficients exceed those of collisional radiative recombination in both cases at all but the lowest temperatures. Also, the temperature dependence clearly does not obey a simple inverse power-law dependence on temperature, such as is often seen in three-body reactions such as ion−molecule association reactions. A casual inspection of the data, especially those for D_3^+, suggests that the three-body recombination

C.2

dx.doi.org/10.1021/jp311978n | J. Phys. Chem. A XXXX, XXX, XXX−XXX

involves an activation energy or a resonance that requires a minimum energy.

3. MODELS OF THREE-BODY ELECTRON-ION RECOMBINATION OF H_3^+ AND D_3^+

Many, if not most, molecular ions recombine by the direct mechanism. Here, the captured electron induces rapid dissociation and there is insufficient time for stabilizing collisions with third bodies. When, as is the case in indirect recombination, the electron is first captured into autoinizing Rydberg states, collisions with third bodies can affect their subsequent evolution, if the lifetime of such states is long enough. The density of third bodies here enters in the "stabilizing" step. It is also possible, though, that the third bodies play a role in the formation of Rydberg states, as in collisional radiative recombination. It is not obvious which of the two mechanisms is more important and whether the capture step or the stabilization step are rate-limiting.

The earliest attempts[31] to explain the peculiar recombination in H_3^+ containing afterglow plasmas (at low helium densities of 3×10^{16} cm^{-3} at $T = 300$ K) were made at a time when theoretical calculations predicted a very small binary recombination coefficient. Gougousi et al.[31] observed that the recombination rate coefficient declined in the late afterglow, a finding that was quite similar to that found in earlier afterglow experiments by Smith and Španěl.[34] Gougousi et al. proposed a model in which an electron was captured into a long-lived Rydberg state with a vibrationally excite core, followed by electron induced l-mixing (l being the Rydberg electron's angular momentum) and eventual stabilization by a reaction with ambient hydrogen. In hindsight, the lifetimes used in their model were probably too long, and improved theories[2] showed that binary recombination was not as slow as earlier theories had suggested. The experimental observations of Gougousi et al. and Smith and Španěl, however, should not be dismissed as "early data".

When later afterglow experiments (Glosík et al.,[16−19,22] Kotrík et al.,[21] Dohnal et al.[25]) showed that the recombination rate increased with the density of the buffer gas (helium), the authors developed an approximate model in which electrons of low angular momentum ($l = 1$) are captured into rotationally excited Rydberg states, subsequently suffer l-mixing in collisions with helium, and are eventually stabilized. As will be discussed later, rather large l-mixing rates for high Rydberg states have to be invoked to obtain agreement with experiment. An alternate mechanism (Johnsen and Guberman[1]) invokes three-body capture into lower Rydberg states that have higher l-mixing rates. This estimate, however, relies on the approximation that states with binding energies less than $-4kT$ (the so-called "bottleneck") are in thermal Saha equilibrium, which is not necessarily true if those states are subject to stabilization other than by collisional energy loss.

In the following, we will use the following abbreviations: E-CRR and N-CRR denote electron or neutral assisted collisional radiative recombination of atomic ions. We use E-CDR and N-CDR (electron or neutral collisional dissociative recombination) for molecular ions that can be stabilized by dissociation. In reality, all these processes can occur together, do not add in a simple manner, and are difficult to separate.

We begin with a brief introduction to the essential properties of collisional radiative recombination for ions with an atomic core. Though neither of these processes provides an adequate explanation for the three-body effect observed in the case of recombining H_3^+ plasmas, some aspects of the problem are best understood by first considering atomic ions before examining modifications that should be made in the case of molecular ions. Electron assisted collisional radiative recombination (E-CRR) involves three-body capture of an electron by the ion in the presence of other electrons. One of the electrons is captured into a high Rydberg state whereas the second electron carries away the excess energy. Subsequent collisions with ambient electrons then cause a net downward cascade that eventually makes reionization impossible.

The rate coefficient for E-CRR is given by (see, e.g., Stevefelt et al.[41])

$$\alpha_{\text{E-CRR}} = 2.7 \times 10^{-20} (T_e/300)^{-4.5} n_e \ [\text{cm}^3/\text{s}] \tag{2}$$

Here and in the following we will ignore the additional terms that represent radiative effects. The validity of eq 2 at very low temperatures T_e (down to 52 K) was recently verified for Ar^+ ions in a helium-buffered afterglow plasma in a Cryo-FALP II experiment (Kotrík et al.,[27,42] Dohnal et al.[38]). Excellent agreement of experimental and theoretical values was obtained.

The capture into high Rydberg states (a few kT below the ionization limit) is much faster than that given by the formula above, but most of the Rydberg atoms will be reionized, rather than recombined. The capture rate coefficient can be calculated from the detailed balance between capture of free electrons and ionization of Rydberg atoms in thermal Saha equilibrium as

$$\alpha_{\text{cap}}(n) = n^2 \lambda_{\text{th}}{}^3 e^{\varepsilon_n} k_{\text{ion}} n_e \ [\text{cm}^3/\text{s}] \tag{3}$$

Here λ_{th} is the thermal de Broglie wavelength

$$\lambda_{\text{th}}{}^3 = (h^2/(2\pi m_e kT))^{3/2} \tag{4}$$

and ε_n is the ionization energy of a Rydberg atom (13.6 [eV]/n^2) with principal quantum number n, divided by kT_e [eV], i.e.

$$\varepsilon_n = \frac{13.6}{n^2 kT_e} \tag{5}$$

The electron ionization coefficient k_{ion} in eq 3 is quite accurately known. Vriens and Smeets[43] derived the semi-empirical analytical formula

$$k_{\text{ion}} = \frac{9.56 \times 10^{-6} (kT_e)^{-1.5} \exp(-\varepsilon_n)}{\varepsilon_n^{2.33} + 4.38\varepsilon_n^{1.72} + 1.32\varepsilon_n} \ [\text{cm}^3/\text{s}] \tag{6}$$

Here, kT_e has to be inserted in units of electronvolts. More elaborate calculations by Pohl et al.[44] have confirmed the validity of this formula, and Vrinceanu[45] has shown that the ionization coefficient is only weakly dependent on the electronic angular momentum. If one now makes the simple assumption that low Rydberg states with binding energies above kT cannot be reionized, the capture rate coefficient of eq 3 in conjunction with eq 6 provides a rather good estimate of the E-CRR rate of eq 2 that, however, is somewhat fictitious because it ignores the contribution of downward n-changing collisions. Capture into higher Rydbergs is much faster than α_{CRR} of eq 2. For instance, capture into a range of Rydberg states from $n = 40$ to $n = 80$ at $n_e = 1 \times 10^{10}$ cm^{-3} proceeds with an effective binary capture rate coefficients of $\alpha_{\text{cap}} \sim 1 \times 10^{-6}$ cm^3/s at $T_e = 300$ K, $\alpha_{\text{cap}} \sim 5 \times 10^{-6}$ cm^3/s at $T_e = 100$ K. Note that the equilibrium between capture and collisional ionization will be maintained on a time scale of $1/k_{\text{ion}}\, n_e$, about 10^{-8} s for $n = 80$ (at 300 K and $n_e = 1 \times 10^{10}$ cm^{-3}), which is

C.2

dx.doi.org/10.1021/jp311978n | J. Phys. Chem. A XXXX, XXX, XXX−XXX

much shorter than the recombination time scale of afterglow experiments.

In the case of atomic ion cores the capture into high Rydberg states is almost entirely compensated by reionization, but the same need not be true for molecular cores that, at least in principle, can be stabilized by predissociation into fragments that can no longer be ionized. This is the basic idea of the collisional dissociative recombination (E-CDR), first prosed by Collins.[46] If one assumes that all Rydberg atoms with p from 40 to 80 predissociate rapidly, the effective recombination coefficient approaches the capture coefficient that rises linearly with n_e and is very large, $\sim 1 \times 10^{-6}$ cm^3/s at T_e = 300 K and n_e = 1×10^{10} cm^{-3}, $\sim 5 \times 10^{-6}$ cm^3/s at 100 K. The effective recombination coefficient will rise with n_e until the reionization rate exceeds the predissociation rate and then levels off. However, the assumption that a large fraction of the Rydberg predissociate rapidly is probably not realistic. The capture populates all allowed angular momentum states evenly (because the inverse, ionization, is only weakly l-dependent) but only very few of those, namely those with small l are likely to predissociate (see Chupka[47]). If only ions with low l, e.g., in l = 1, are capable of predissociating, the estimates of the E-CDR rate coefficient will be reduced by the factor $(2l + 1)/n^2$, approximately 10^{-3} at n = 50. One might presume that l-mixing by electrons would be effective in converting high-l ions to predissociating l-states. The l-mixing rate by electrons from a given l' to a different l is indeed very large (Dutta et al.[48]), but the rate for converting a random l to a given l' is smaller by the factor $(2l' + 1)/[n^2 - (2l' + 1)]$, again a number on the order of 10^{-3}. Thus, it appears unlikely that E-CDR is an important process under the conditions of the afterglow experiments, unless Rydberg molecules in high l-states dissociate rapidly or are destroyed by some other reaction. If E-CDR were important, its rate should increase quite fast with decreasing temperature and lead to a strong dependence on electron density. This, however, is not what is experimentally observed.

Collisional radiative recombination, however, should become noticeable at very low temperatures and high electron densities. For instance, at 100 K and $n_e = 1 \times 10^{10}$ cm^{-3} eq 2 gives $\alpha_{CRR} \sim 4 \times 10^{-8}$ cm^3/s.

Similar considerations apply to neutral-assisted recombination processes. The approximation made in the above estimates of the electron-assisted three-body capture is not applicable in the case of neutral-assisted capture. Ionization of Rydberg states by helium atoms as opposed to electrons is slower by about 10 orders of magnitude (see Lebedev[49]). Hence, one would obtain extremely small rates of capture into high Rydberg states. This estimate is inappropriate because those states are populated predominantly by multiple electron-atom collisions that gradually reduce the total energy. A more reasonable estimate can be based on the treatment by Flannery,[50] who obtained the following rate coefficient for the neutral assisted recombination of atomic ions:

$$\alpha = 8\pi \frac{m_e}{M_{atom}} R_0 R_e^2 \left(\frac{8kT}{\pi m_e}\right)^{1/2} \sigma_{e,atom} n_{atom} \quad (7)$$

Here, m_e and M_{atom} denote the masses of the electron and gas atoms (e.g., helium), $\sigma_{e,atom}$ is the electron-atom momentum transfer cross section, and $R_e = e^2/kT$ (=5×10^{-6} cm at 300 K). R_0 is the trapping radius. The assumption is made that an electron that collides with an atom inside this radius recombines with unit probability, whereas those colliding outside that radius will escape recombination. If R_0 is taken as $2R_e/3$, the recombination coefficient decreases with temperature as $T^{-2.5}$ and agrees with the energy-diffusion model of Pitaevskii.[51] In the case of recombination in ambient helium (using $\sigma_{e,atom} = 5 \times 10^{-16}$ cm^2), one obtains

$$\alpha(T) = 2.1 \times 10^{-27} (T/300)^{-2.5} n(\mathrm{He})\ [\mathrm{cm}^3/\mathrm{s}] \quad (8)$$

A smaller (by about 40%) rate coefficient was obtained by Bates and Khare[15] in their classical treatment of the problem. At temperatures above 100 K, this recombination coefficient is far smaller than what is needed to explain the neutral assisted coefficient in the H_3^+ recombination studies. However, at temperatures below 50 K and n(He) = 6×10^{17} cm^{-3} $\alpha(T)$ of eq 8 exceeds 1×10^{-7} cm^3/s, which is clearly not negligible.

It is difficult to construct a general theory of third-body assisted recombination of molecular ions because the decay of molecular ions in high Rydberg states depends critically on the specific molecule. However, one can estimate the relative efficiencies of helium and electrons in leading to recombination from the ratio of the rates in eqs 2 and 8. At T_e = 300 K, one ambient electron has about the same stabilizing effect as 10^7 helium atoms. If one now, as before, assumes that high Rydberg atoms can also be stabilized by predissociation, it seems reasonable to expect that the flux into such states is controlled by helium atoms with an efficiency that is smaller by 10^7 compared to that of electrons. For example, a density of ambient electrons of $n_e = 1 \times 10^{10}$ cm^{-3} would have an effect similar to that of helium with density n(He) = 1×10^{17} cm^{-3}. Such conditions are fairly typical in experiments. Again, however, the magnitude of N-DRR is expected to be significant only if a very large number of Rydbergs states can predissociate, which seems unlikely. Also, the N-DRR rate coefficient would increase as the temperature is reduced, rather than exhibiting a drastic decline, such as that seen in the D_3^+ data below 100 K (Figure 3).

We conclude that that neither E-CDR nor N-CDR provides a compelling or even plausible explanation for the experimental findings. However, at very low temperatures collisional radiative recombination, given by eqs 2 and 8, becomes competitive with binary recombination. It may seem surprising that collisional dissociative recombination is less important than collisional radiative recombination. The reason is that dissociation is effective only for states of low l, whereas collisional stabilization also occurs for states with high l and much higher statistical weights.

4. RESONANT CAPTURE AND L-MIXING MODEL

A more promising mechanism of the helium-assisted recombination may be electron capture of a p-electron into an autoionizing resonance with a rotationally excited core, followed by a helium-induced change of the Rydberg electron's angular momentum (l-mixing), and final stabilization by predissociation or perhaps some other stabilizing mechanism. This is the model that has been invoked in several earlier publications.[16,21] Calculations of the lifetimes (or "time delays") of such resonances show that they can be indeed quite large (100−1000 ps) but the subsequent collisions that lead to irreversible recombination are more difficult to quantify. Essentially, the effective rate coefficient is estimated as

$$\alpha_{eff} = f\alpha_{cap} k_l n(\mathrm{He})/\nu_a\ [\mathrm{cm}^3/\mathrm{s}] \quad (9)$$

C.2

dx.doi.org/10.1021/jp311978n | J. Phys. Chem. A XXXX, XXX, XXX−XXX

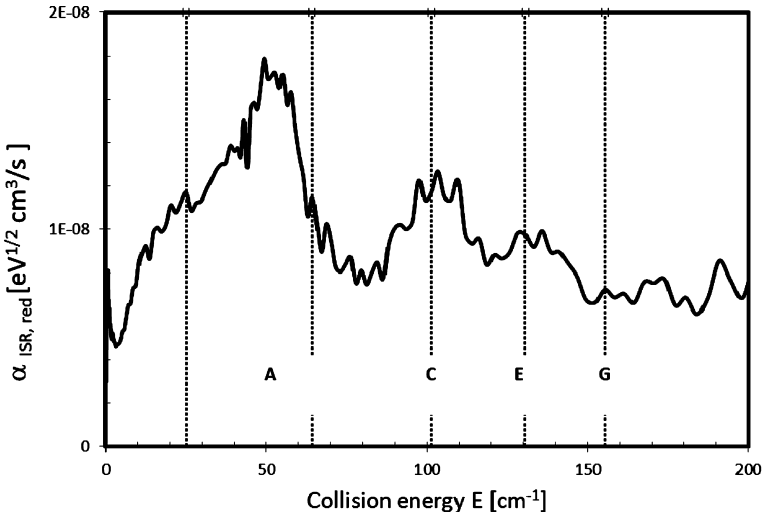

Figure 4. Reduced H_3^+ rate coefficient observed in storage-ring experiments as a function of collision energy, drawn from data supplied by Petrignani.[53] Vertical dashed lines indicate the energies at which the calculated lifetimes[16] of (1, 1) to (2, 1) resonances have maxima. The energies C, E, and G correspond to resonant capture into n = 39, 50, and 78, respectively.

where $\nu_a = 1/\tau_a$ is the reciprocal of the autoionizing lifetime, α_{cap} denotes the capture coefficient, and k_l is the l-mixing rate from the initial p-state to higher angular momenta. The factor f denotes the fraction of the H_3^+ ions that are capable of capturing electrons, e.g., are in an appropriate rotational state. That number is estimated to be about 0.25. If one uses $\tau_a = 10^{-10}$ s, $\alpha_{cap} = 3 \times 10^{-7}$ cm^3/s, and $k_l = 3 \times 10^{-8}$ cm^3/s, one obtains a three-body rate coefficient of 2.25×10^{-25} cm^6/s, in good agreement with the experimental value assuming that Rydberg states from p = 40−80 contribute. Equation 9 is valid only in the limit of vanishing helium density. At finite helium densities, l-mixing also depletes the resonant state. Hence, eq 9 should be replaced by

$$\alpha_{eff} = f\alpha_{cap}\frac{k_l n(\mathrm{He})}{k_l n(\mathrm{He}) + \nu_a} \quad (10)$$

which agrees with formula 9 in the limit n(He) = 0. At a helium density of 3×10^{17} cm^{-3}, α(He) is now only about 50% of that given by eq 9. At higher helium densities it "saturates" at $f\alpha_{cap}$ and the differential three-body rate ($d\alpha_{eff}/dn$(He) approaches zero. The saturation should be taking into account in comparisons of experimental data to model calculations. We note also that eq 10 only considers l-mixing by helium atoms. If one includes the much faster l-mixing by electrons, the "saturation" would set in at lower helium densities under many experimental conditions.

The assumption that the l-mixing rate coefficient due to helium is given by $k_l = 3 \times 10^{-8}$ cm^3/s, independent of the principal quantum number, is in conflict with the theoretical conclusion of Hickman[52] that for higher n it should decline as $n^{-2.7}$. Also, the theories of l-mixing consider only mixing from $l \geq 2$. The rates for mixing from l = 0, 1 to higher l are actually smaller because the quantum defects are larger. Unfortunately, there are no direct measurements of l-mixing coefficients for high p for molecular ions to reach a clear decision.

The assumption that the autoionizing high-l Rydberg states formed by l-mixing predissociate much faster than they autoionize is also not obvious, and there is no good argument that rules out the opposite assumption. In the following section we will explore a modification of the resonant-capture model that is, in part, based on experimental observations. In a more rigorous treatment, multiple capture resonances should be considered and their contributions should be added.

5. COMPLEX MODEL

At low electron densities binary rotational capture will always be a faster route to Rydberg states than three-body assisted capture. Hence, we will neglect contributions due to three-body capture. The resonant lifetimes that were used in earlier treatments were calculated from the matrix that describes the rotational capture of p-electrons and their release assuming that the ionic core, except for changing its rotational state, remains unaffected. Other channels, such as predissociation or vibrational excitation were deemed to play no significant role. It seems possible, however, that the rotational resonances lead to more complicated complexes, in which the ionic core becomes highly vibrationally excited and eventually decays into dissociating channels. This conjecture motivated us to examine the energy dependence of the H_3^+ recombination that has been observed in storage-ring experiments

The high-resolution storage-ring data on H_3^+ recombination Petrignani et al.[9,53] show several recombination peaks at energies from 40 to 160 cm^{-1} (0.005−0.02 eV) that are not predicted by theory. As shown in Figure 4, their positions correlate with the calculated[16] positions of the lifetime maxima for the rotational resonances from the (1, 1) to the (2, 1) (excitation energy of 173 cm^{-1}) rotational states of para-H_3^+. In Figure 5 of Petrignani et al. the peaks are labeled C and E (we labeled the next higher peak "G"). In this graph, the "raw" (referring to narrow, non-Maxwellian energy distributions) rate coefficients have been reduced by multiplying with the square root of the collision energy to remove the overall energy dependence. It is still not entirely clear whether or not H_3^+ recombination measurements in storage rings are free from possible effects due to electric stray fields.

C.2

dx.doi.org/10.1021/jp311978n | J. Phys. Chem. A XXXX, XXX, XXX−XXX

One could dismiss the correlation as coincidence, but resonant capture by H_3^+ in the (1, 1) state, the rotational ground state of para-H_3^+, is a natural first step in complex formation. Helium, of course is absent in the storage ring, and the electron density is much lower than in afterglow experiments. Hence, it appears that some of the long-lived rotational resonances actually lead to binary recombination. The largest (very broad) peak in the storage ring data at 50 cm^{-1} (labeled A) has no counterpart in the lifetime graph of (1, 1) to (2, 1) resonances and probably has a different origin. Storage ring data by Kreckel et al.[54] (see their Figure 8) indicate that the central part of peak "A" remained the same when para-enriched rather than normal hydrogen was fed to the ISR ion source. Peak "A" may reflect a rotational resonance from the para (2, 1) to the (3, 1) rotational state. If this assignment is correct, this resonance could contribute to afterglow recombination at T = 300 K, but it should not play a role at very low temperatures, because the abundance of the (2, 1) rotational state would be small.

Returning to three-body effects, we now assume that the Rydberg states formed by rotational capture of a p-electron actually interact with the ion core and form an ensemble of complexes with lifetimes that exceed those given by the lifetime matrix. We further assume that the complexes can autoionize, dissociate in the absence of third-body interactions, and that the dissociation rate can be enhanced by third bodies. The resulting recombination rate coefficient in terms of several, however not well-known, rate coefficients has the form

$$\alpha_{\mathrm{eff}}(He) = \alpha_{\mathrm{cap}} \frac{k_{\mathrm{He}} n(\mathrm{He}) + k_e n_e + \nu_{\mathrm{diss},0}}{k_{\mathrm{He}} n(\mathrm{He}) + k_e n_e + \nu_{\mathrm{diss},0} + \nu_a} \qquad (11)$$

The effective recombination coefficient is the product of a capture rate coefficient and the ratio of recombination channels to all decay channels. It is similar to eq 10, but the rate coefficients have different meanings. Here, k_{He} and k_e denote the net rate coefficients for complex stabilization (i.e., leading to predissociation rather than collisional ionization) by helium atoms or electrons, respectively. $\nu_{\mathrm{diss},0}$ is the predissociation rate in the absence of third bodies, and ν_a is the autoionization frequency. We prefer to use decay frequencies rather than lifetimes, because an ensemble of complexes does not necessarily decay with a single exponential time constant.

The coefficients in eq 11 are not known and it is not likely that they can be deduced from simple theoretical arguments. However, it is easy to find values that approximately reproduce the experimental data. Figure 5 shows a fit of eq 11 to data obtained at T = 300 K for three different electron densities. The autoionization rate has been chosen as $\nu_a = 8 \times 10^8$ 1/s such that the model agrees with those of the Prague experiments rather than with those of Leu et al.[10]

The data by Smith and Španěl[34] and by Gougousi et al.[31] are shown with upward arrows, from the values that they observed at low n_e (late afterglow) to those at high n_e (early afterglow). If one chooses $k_e = 10^7 k_{\mathrm{He}}$, the same "efficiency factor" used in section 3, the model roughly reproduces the range of rate coefficients observed in those experiments at different n_e. A precise fitting of those data is not possible and would be pointless because the accuracy of those data at low n_e is considerably worse than at high electron densities. At high n(He) the model gives a weaker dependence on n_e, in agreement with the findings by both Leu et al.[10] and the Prague experiments. Although a linear extrapolation of the Prague data

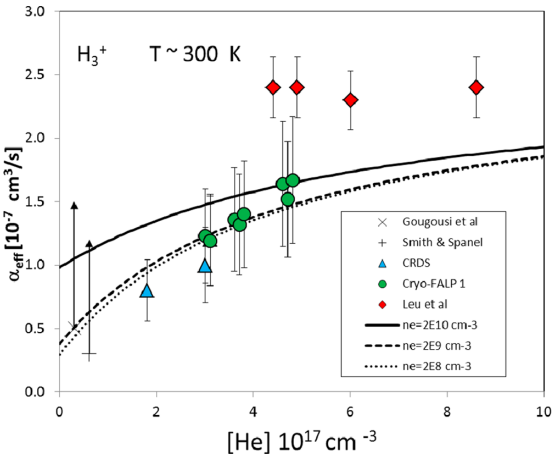

Figure 5. Comparison of eq 11 to experimental data at T = 300 K. The following values were used for the rate coefficients and decay rates: $\alpha_{\mathrm{cap}} = 2.55 \times 10^{-7}$ cm^3/s, $k_{\mathrm{He}} = 2 \times 10^{-9}$ cm^3/s, $k_e = 5 \times 10^{-2}$ cm^3/s, $\nu_{\mathrm{diss},0} = 1 \times 10^8$ 1/s, $\nu_a = 8 \times 10^8$ 1/s. See text for additional explanations. Data points from Gougousi et al.,[31] Smith and Spanel,[34] CRDS and Cryo-FALP I from Glosik et al.[18] and Leu et al.[11]

to n(He) = 0 is not strictly compatible with the model, it results in a binary value that is only slightly too high.

Our exploratory model provides a common framework that makes the apparent discrepancies between experimental data easier to accept. Obviously, the model is crude because it uses the same rate coefficients for all members of the ensemble of complexes. This is unavoidable, given the severe lack of knowledge of the relevant parameters. It is also difficult to estimate how the effective recombination coefficients would vary with temperature. At low electron temperatures resonant capture can only occur into Rydberg states with smaller principal quantum numbers and the spacing between states will increase. Thus, one might expect that three-body effect would become smaller at low temperatures. The changing rotational distribution of H_3^+ is likely to have an effect also.

In the complex model, collisions with third bodies enhance the recombination rate at the expense of the autoionization rate ν_a. If ν_a is vanishingly small, however, then (see eq 11) the recombination rate is limited by electron capture and third-body effects disappear. In the simplified theory of Jungen and Pratt[5] electrons are captured by vibrational excitation mediated by the linear Jahn–Teller effect and autoionization is assumed to be negligible. Because their theory reproduces the rate coefficients measured in storage rings quite well, the agreement can be seen as a possible argument against the complex model. However, in a later and more detailed paper Jungen and Pratt[55] conclude that purely rotational capture into autoionizing states should also be considered and that recombination in that case would not be capture limited. It is difficult to go further without knowing the relative efficiencies of the capture mechanisms.

6. CONCLUSIONS

The multiyear efforts to elucidate the ternary recombination of H_3^+ and D_3^+ ions, in particular the novel extension to very low temperatures, have resulted in a rather unique set of data. It is particularly pleasing to see that the traditional three-body reaction (i.e., the Bates and Khare mechanism[15]) becomes

C.2

dx.doi.org/10.1021/jp311978n | J. Phys. Chem. A XXXX, XXX, XXX–XXX

detectable at temperatures below 70 K. This observation strongly supports the validity of the afterglow methods used here.

It appears that many of the seeming discrepancies between afterglow recombination data on H_3^+ (D_3^+) can be traced to third-body effects involving both neutral and charged particles. Although these measurements of third-body assisted recombination have narrowed the range of plausible mechanisms, developing a quantitative theoretical model is seriously hampered by the lack of needed data, especially on rates of predissociation, their dependence on angular momentum, and coupling between electronic and core degrees of freedom. The tentative model proposed here presents an attempt to develop a common framework that seeks to reconcile experimental observations.

The data obtained in helium-buffered plasmas are nearly complete, but there is a lack of data in other rare gases. Neon might be a good choice for further work because the momentum transfer between electrons and neon is far smaller than with helium. The only experiment in neon buffer[56] was done at a single pressure and does not permit any inferences regarding pressure dependences. Hence, we did not discuss this work but note that it resulted in smaller recombination coefficients than those obtained with helium buffer gas.

There remains some doubt about the role that electrons play as stabilizing body because the only two experiments[34,31] that point to electron-stabilized recombination may have alternate explanations. Additional experiments, especially measurements at very low temperatures, may be worth the effort.

Finally, it would certainly be highly desirable to have more theoretical information on the configuration interaction between electronic and core excitations in H_3^+ Rydberg states, and to identify clearly the origin of the resonance peaks that are seen in storage-ring experiments.

AUTHOR INFORMATION

Corresponding Author

*Phone: 412-624-9285. E-mail: rj@pitt.edu.

Notes

The authors declare no competing financial interest.

ACKNOWLEDGMENTS

This work was partly financed by the research grant OC10046 from the Ministry of Education of the Czech Republic and was partly supported by GACR (205/09/1183, P209/12/0233), by SV 267 302, by GAUK 353811, GAUK 406011, GAUK 659112, and by COST Action CM0805 (The Chemical Cosmos). We thank A. Petrignani for supplying numerical data on the storage ring results

REFERENCES

(1) Johnsen, R.; Guberman, S. L. Dissociative Recombination of H_3^+ Ions with Electrons: Theory and Experiment. *Adv. At., Mol., Opt. Phys.* **2010**, *59*, 75−127.

(2) Kokoouline, V.; Greene, C. H. Unified Theoretical Treatment of Dissociative Recombination of D3h Triatomic Ions: Application to H_3^+ and D_3^+. *Phys. Rev. A: At., Mol., Opt. Phys.* **2003**, *68*, 012703-1−23.

(3) Fonseca dos Santos, S.; Kokoouline, V.; Greene, C. H. Dissociative Recombination of H_3^+ in the Ground and Excited Vibrational States. *J. Chem. Phys.* **2007**, *127*, 124309-1−8.

(4) Pagani, L.; Vastel, C.; Hugo, E.; Kokoouline, V.; Greene, C. H.; Bacmann, A.; Bayet, E.; Ceccarelli, C.; Peng, R.; Schlemmer, S. Chemical Modeling of L183 (L134N): An Estimate of the Ortho/Para H_2 ratio. *Astron. Astrophys.* **2009**, *494*, 623−636.

(5) Jungen, Ch.; Pratt, S. T. Jahn-Teller Interactions in the Dissociative Recombination of H_3. *Phys. Rev. Lett.* **2009**, *102*, 023201-1−4.

(6) McCall, B. J.; Huneycutt, A. J.; Saykally, R. J.; Djuric, N.; Dunn, G. H.; Semaniak, J.; Novotny, O.; Al-Khalili, A.; Ehlerding, A.; Hellberg, F.; et al. Dissociative Recombination of Rotationally Cold H_3^+. *Phys. Rev. A: At., Mol., Opt. Phys.* **2004**, *70*, 052716-1−12.

(7) Wolf, A.; Kreckel, H.; Lammich, L.; Strasser, D.; Mikosch, J.; Glosík, J.; Plašil, R.; Altevogt, S.; Andrianarijaona, V.; Buhr, H.; et al. Effects of Molecular Rotation in Low-Energy Electron Collisions of H_3^+. *Philos. Trans. R. Soc. A.* **2006**, *364*, 2981−2997.

(8) Kreckel, H.; Motsch, M.; Mikosch, J.; Glosík, J.; Plašil, R.; Altevogt, S.; Andrianarijaona, V.; Buhr, H.; Hoffmann, J.; Lammich, L.; et al. High-Resolution Dissociative Recombination of Cold H_3^+ and First Evidence for Nuclear Spin Effects. *Phys. Rev. Lett.* **2005**, *95*, 263201-1−4.

(9) Petrignani, A.; Altevogt, S.; Berg, M. H.; Bing, D.; Grieser, M.; Hoffmann, J.; Jordon-Thaden, B.; Krantz, C.; Mendes, M.; Novotny, O.; et al. Resonant Structure of Low-Energy H_3^+ Dissociative Recombination. *Phys. Rev. A: At., Mol., Opt. Phys.* **2011**, *83*, 032711-1−10.

(10) Leu, M. T.; Biondi, M. A.; Johnsen, R. Measurements of Recombination of Electrons with H_3^+ and H_5^+ Ions. *Phys. Rev. A: At., Mol., Opt. Phys.* **1973**, *8*, 413−419.

(11) Leu, M. T. *Ph.D. thesis*, University of Pittsburgh, Pittsburgh, PA, USA, 1972.

(12) Macko, P.; Bánó, G.; Hlavenka, P.; Plašil, R.; Poterya, V.; Pysanenko, A.; Votava, O.; Johnsen, R.; Glosík, J. Afterglow Studies of H_3^+(v = 0) Recombination Using Time Resolved CW-Diode Laser Cavity Ring-Down Spectroscopy. *Int. J. Mass Spectrom.* **2004**, *233*, 299−304.

(13) Plašil, R.; Glosík, J.; Poterya, V.; Kudrna, P.; Rusz, J.; Tichý, M.; Pysanenko, A. Advanced Integrated Stationary Afterglow Method for Experimental Study of Recombination processes of H_3^+ and D_3^+ Ions With electrons. *Int. J. Mass Spectrom.* **2002**, *218*, 105−130.

(14) Laubé, S.; Le Padellec, A.; Sidko, O.; Rebrion-Rowe, C.; Mitchell, J. B. A.; Rowe, B. R. New FALP-MS Measurements of H_3+, D_3^+ and HCO^+ Dissociative Recombination. *J. Phys. B: At., Mol. Opt. Phys.* **1998**, *31*, 2111−2128.

(15) Bates, D. R.; Khare, S. P. Recombination of Positive Ions with Electrons in a Dense Gas. *Proc. Phys. Soc.* **1965**, *85*, 231−243.

(16) Glosík, J.; Korolov, I.; Plašil, R.; Novotny, O.; Kotrík, T.; Hlavenka, P.; Varju, J.; Mikhailov, I. A.; Kokoouline, V.; Greene, C. H. Recombination of H_3^+ ions in the Afterglow of a He−Ar−H_2 Plasma. *J. Phys. B: At., Mol. Opt. Phys.* **2008**, *41*, 191001−191009.

(17) Glosík, J.; Plašil, R.; Korolov, I.; Novotny, O.; Kotrík, T. Multicollision Character of Recombination of H_3^+ Ions in Afterglow Plasma. *J. Phys.: Conf. Ser.* **2009**, *192*, 012005 (8 pages).

(18) Glosík, J.; Plašil, R.; Korolov, I.; Kotrík, T.; Novotny, O.; Hlavenka, P.; Dohnal, P.; Varju, J.; Kokoouline, V.; Greene, C. H. Temperature Dependence of Binary and Ternary Recombination of H_3^+ ions with Electrons. *Phys. Rev. A: At., Mol., Opt. Phys.* **2009**, *79*, 052707-1−10.

(19) Glosík, J.; Korolov, I.; Plašil, R.; Kotrík, T.; Dohnal, P.; Novotny, O.; Varju, J.; Roučka, Š.; Greene, C. H.; Kokoouline, V. Binary and Ternary Recombination of D_3^+ Ions with Electrons in He-D_2 plasma. *Phys. Rev. A: At., Mol., Opt. Phys.* **2009**, *80*, 042706-1−9.

(20) Varju, J.; Roučka, Š.; Kotrík, T.; Plašil, R.; Glosík, J. Application of NIR − CRDS for State Selective Study of Recombination of Para and Ortho H_3^+ Ions with Electrons in Low Temperature Plasma. *J. Phys.: Conf. Ser.* **2010**, *227*, 012026 (4 pages).

(21) Kotrík, T.; Dohnal, P.; Korolov, I.; Plašil, R.; Roučka, S.; Glosík, J.; Greene, C. H.; Kokoouline, V. Temperature Dependence of Binary and Ternary Recombination of D_3^+ Ions with Electrons. *J. Chem. Phys.* **2010**, *133*, 034305−034313.

(22) Glosík, J.; Plašil, R.; Kotrík, T.; Dohnal, P.; Varju, J.; Hejduk, M.; Korolov, I.; Roučka, Š.; Kokoouline, V. Temperature Dependence of

C.2

Binary and Ternary Recombination of D_3^+ ions with Electrons. *Mol. Phys.* **2010**, *108*, 2253−2264.
(23) Varju, J.; Hejduk, M.; Dohnal, P.; Jílek, M.; Kotrík, T.; Plašil, R.; Gerlich, D.; Glosík, J. Nuclear Spin Effect on Recombination of H_3^+ Ions with Electrons at 77 K. *Phys. Rev. Lett.* **2011**, *106*, 203201−203205.
(24) Rubovič, P.; Dohnal, P.; Hejduk, M.; Plašil, R.; Glosík, J. Binary Recombination of H_3^+ and D_3^+ Ions with Electrons in Plasmas at 50 − 230 K. *J. Phys. Chem. A* **2013**, DOI: 10.1021/jp3123192.
(25) Dohnal, P.; Hejduk, M.; Varju, J.; Rubovič, P.; Roučka, Š; Kotrík, T.; Plašil, R.; Glosík, J.; Johnsen, R. Binary and Ternary Recombination of Para-H_3^+ and Ortho-H_3^+ with Electrons: State Selective Study at 77−200 K. *J. Chem. Phys.* **2012**, *136*, 244304-1−14.
(26) Dohnal, P.; Hejduk, M.; Rubovič, P.; Varju, J.; Roučka, Š.; Plašil, R.; Glosík, J. Binary and Ternary Recombination of D_3^+ Ions at 80−130 K: Application of Laser Absorption Spectroscopy. *J. Chem. Phys.* **2012**, *137*, 194320-1−8.
(27) Dohnal, P.; Hejduk, M.; Varju, J.; Rubovič, P.; Roučka, S.; Kotrík, T.; Plašil, R.; Johnsen, R.; Glosík, J. Binary Recombination of Para- and Ortho-H3+ with Electrons at Low Temperatures. *Philos. Trans. R. Soc. A* **2012**, *370*, 5101−5108.
(28) Glosík, J.; Plašil, R.; Poterya, V.; Tichy, M.; Pysanenko, A. Experimental Study of Recombination of H_3^+ Ions with Electrons Relevant for Interstellar and Planetary Plasmas. *J. Phys. B: At. Mol. Opt. Phys.* **2001**, *34*, L458−L494.
(29) Plašil, R.; Varju, J.; Hejduk, M.; Dohnal, P.; Kotrík, T.; Glosík, J. Experimental Study of Para- and Ortho-H_3^+ Recombination. *J. Phys Conf. Ser* **2011**, *300*, 012023 (8 pages).
(30) Amano, T. Is the Dissociative Recombination of H_3^+ Really Slow? A New Spectroscopic Measurement of the Rate Constant. *Astrophys. J., Lett.* **1988**, *329*, L121−L124.
(31) Gougousi, T.; Johnsen, R.; Golde, M. F. Recombination of H_3^+ and D_3^+ Ions in a Flowing Afterglow Plasma. *Int. J. Mass Spectrom.* **1995**, *149−150*, 131−151.
(32) Amano, T. The Dissociative Recombination Rate Coefficients of H_3^+, HN_2^+, and HCO. *J. Chem. Phys.* **1990**, *92*, 6492−6501.
(33) Johnsen, R. Kinetic Processes in Recombining H_3^+ Plasmas. *Philos. Trans. R. Soc. A* **2012**, *370*, 5109−5117.
(34) Smith, D.; Španěl, P. Dissociative Recombination of H_3^+. Experiment and Theory reconciled. *Chem. Phys. Lett.* **1993**, *211*, 454−460.
(35) Inglis, D. R.; Teller, E. Ionic Depression of Series Limits in One-Electron Spectra. *Astrophys. J.* **1939**, *90*, 439−448.
(36) Mitrafanov, A. V. On a Revised Version of the Inglis-Teller Formula. *Soviet Astronomy-AJ* **1973**, *16*, 867−869.
(37) Kotrík, T.; Dohnal, P.; Rubovič, P.; Plašil, R.; Roučka, S.; Opanasiuk, S. Glosík. Cryo-FALP Study of Collisional-Radiative Recombination of Ar+ Ions at 40−200 K. *Eur. Phys. J.: Appl. Phys.* **2011**, *56*, 24011−24016.
(38) Dohnal, P.; Rubovič, P.; Kotrík, T.; Hejduk, M.; Plašil, R.; Johnsen, R.; Glosík, J. Ternary Recombination of Ar^+ with Electrons in He at Temperatures 50−100 K. To be published.
(39) Hejduk, M.; Dohnal, P.; Varju, J.; Rubovič, P.; Plašil, R.; Glosík, J. Nuclear Spin State-Resolved Cavity Ring-Down Spectroscopy Diagnostics of a Low-Temperature H_3+−Dominated Plasma. *Plasma Sources Sci. Technol.* **2012**, *21*, 024002−024011.
(40) Cao, Y. S.; Johnsen, R. Neutral Stabilized Electron-ion Recombination in Ambient Helium Gas. *J. Chem. Phys.* **1991**, *94*, 5443−5446.
(41) Stevefelt, J.; Boulmer, J.; Delpech, J. Collisional-Radiative Recombination in Cold Plasmas. *Phys. Rev. A: At., Mol., Opt. Phys.* **1975**, *12*, 1246−1251.
(42) Kotrík, T.; Dohnal, P.; Roučka, S.; Jusko, P.; Plašil, R.; Glosík, J.; Johnsen, R. Collisional Radiative Recombination $Ar^+ + e + e$; Experimental Study at 77−180 K. *Phys. Rev. A: At., Mol., Opt. Phys.* **2011**, *83*, 032720-1−032720-8.
(43) Vriens, L.; Smeets, H. M. Cross-section and Rate Formulas for Electron Impact Ionization, Excitation, and Total Population of Excited Atoms. *Phys. Rev. A: At., Mol., Opt. Phys.* **1980**, *22*, 940−951.
(44) Pohl, T.; Vrinceanu, D.; Sadeghepour, H. R. Rydberg Atom Formation in Ultracold Plasmas: Small Energy Transfer with Large Consequences. *Phys. Rev. Lett.* **2008**, *100*, 223201-1−3.
(45) Vrinceanu, D. Electron Impact Ionization of Rydberg Atoms. . *Phys. Rev. A: At., Mol., Opt. Phys* **2005**, *72*, 022722-1− 8.
(46) Collins, C. B. Collisional-Dissociative Recombination of Electrons with Molecules. *Phys. Rev. A: At., Mol., Opt. Phys.* **1965**, *140*, 1850−1857.
(47) Chupka, W. A. Factors Affecting Lifetimes and Resolution of Rydberg States Observed in Zero-Electron-Kinetic-Energy Spectroscopy. *J. Chem. Phys.* **1993**, *98*, 4520−4530.
(48) Dutta, S. K.; Feldbaum, D.; Walz-Flannigan, A.; Guest, J. R.; Raithel, G. High-Angular-Momentum States in Cold Rydberg Gases. *Phys. Rev. Lett.* **2001**, *86*, 3993−3996.
(49) Lebedev, V. S. Ionization of Rydberg atoms by neutral particles. I. Mechanism of the Perturber-Quasifree-Electron Scattering. *J. Phys. B: At. Mol. Opt. Phys.* **1991**, *24*, 1977−1991.
(50) Flannery, M. R. Transportcollisional Master Equations for Termolecular Recombination as a Function of Gas Density. *J. Chem. Phys.* **1991**, *95*, 8205−8226.
(51) Pitaevskii, L. P. Electron Recombination in an Atomic Gas. *Sov. Phys. JETP* **1962**, *15*, 919−921.
(52) Hickman, A. P. Theory of Angular Momentum Mixing in Rydberg-Atom-Rare-Gas Collisions. *Phys. Rev. A: At., Mol., Opt. Phys.* **1978**, *18*, 1339−1342.
(53) Petrignani, A. Private communication. 2012.
(54) Kreckel, H.; Novotny, O.; Crabtree, K. N.; Buhr, H.; Petrignani, A.; Tom, B. A.; Thomas, R. D.; Berg, M. H.; Bing, D.; Grieser, M.; et al. High-Resolution Storage-Ring Measurements of the Dissociative Recombination of H_3^+ Using a Supersonic Expansion Ion Source. *Phys. Rev. A: At., Mol., Opt. Phys.* **2010**, *82*, 042715-1−11.
(55) Jungen, Ch.; Pratt, S. T. Low-Energy Dissociative Recombination in Small Polyatomic Molecules. *J. Chem. Phys.* **2010**, *133*, 214303-1−9.
(56) Macdonald, J. A.; Biondi, M. A.; Johnsen, R. Recombination of Electrons with H_3^+ and H_5^+ Ions. *Planet. Space Sci.* **1984**, *32*, 651−654.

C.2

D. Para-hydrogen generator

D.1 Ladder diagram of electronic security system

The ↑ symbol indicates the rising edge, "/" indicates the negation. S stands for "set", R for "reset". Internal binary value container are marked as Mn (n is a number). Xn are input hardware signals, Yn are output signals to the relays. Rn are internal registers that can hold decimal values. Big square elements are built-in software modules. The module Tn is a timer, CMP is a comparator (Sa $\stackrel{?}{=}$ Sb), TOGG toggles the binary value written in the square, RST resets the register.

The first sequence of the program serves to interpret the signal from the hardware button. If it is pressed two times, the override value M3 is set to 1. This signal serves to override the decision whether the compressor should be running or not based on the pressure in the isolation vacuum X1, a condition of the turbine X3, the pressure above the rotary pump X and on the fact, whether the time-scheduler was set (see section Compressor switch-on sequence at line N0015). Positive value of M3 also keeps the valve above the rotary pump open even if the pressure is high. This is useful when we pump out the hydrogen from the catalyst container.

The water supply is controlled by a sequence N0016–N0020. The flow of water is monitored by a flow meter (a simple floating contact) X2. In case of instability of the water supply the compressor is switched off and if the X2 is switched on it waits 2 minutes to be sure that the flow is stable. This sequence also serves to switch on the compressor when the water valve is scheduled to be switched on.

The sequence starting from N0021 deals with the switch-on time-schedule. The start time (hh:mm:ss) is put to registers 1003 (hh), 1002 (mm) and 1001 (ss) and compared with the machine time.

The relays Yn control the following: ($n = 0$) – power source of the compressor, (1) – power switch of the turbine, (2) – the valve above the rotary pump, (3) – the valve for water cooling the compressor and the turbine.

Printed Item: Ladder Diagram - Main_unit1

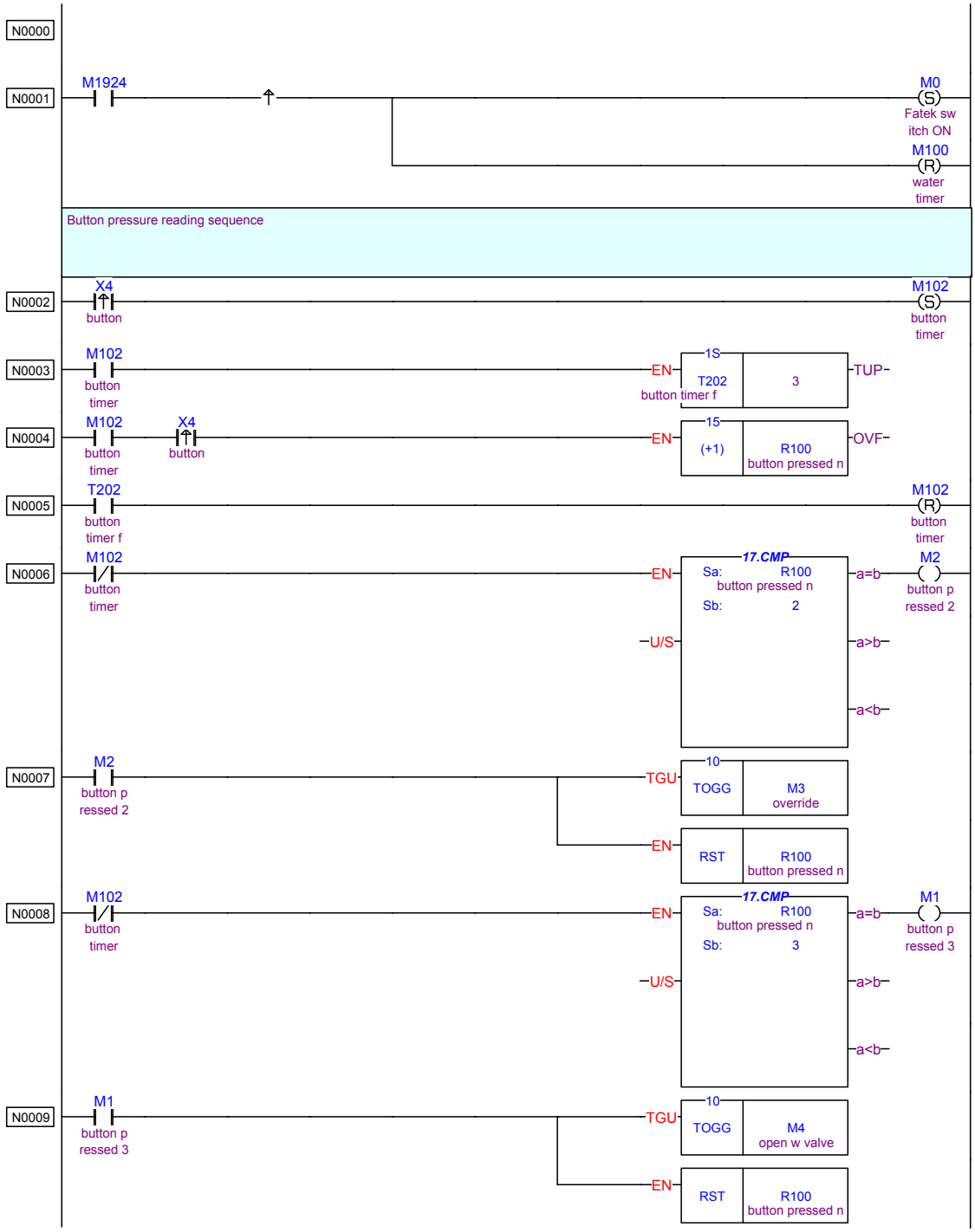

Printed Item: Ladder Diagram - Main_unit1

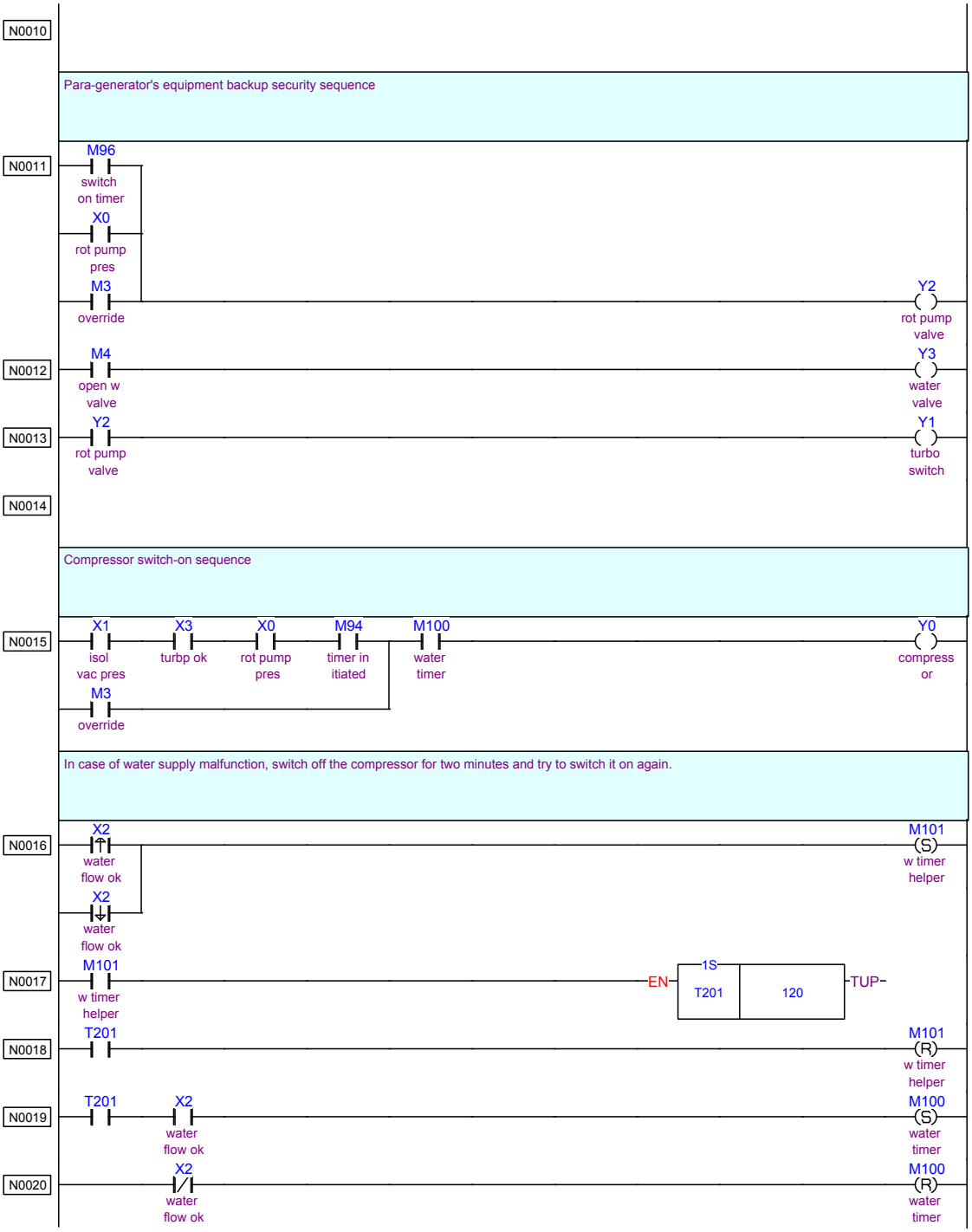

Printed Item: Ladder Diagram - Main_unit1

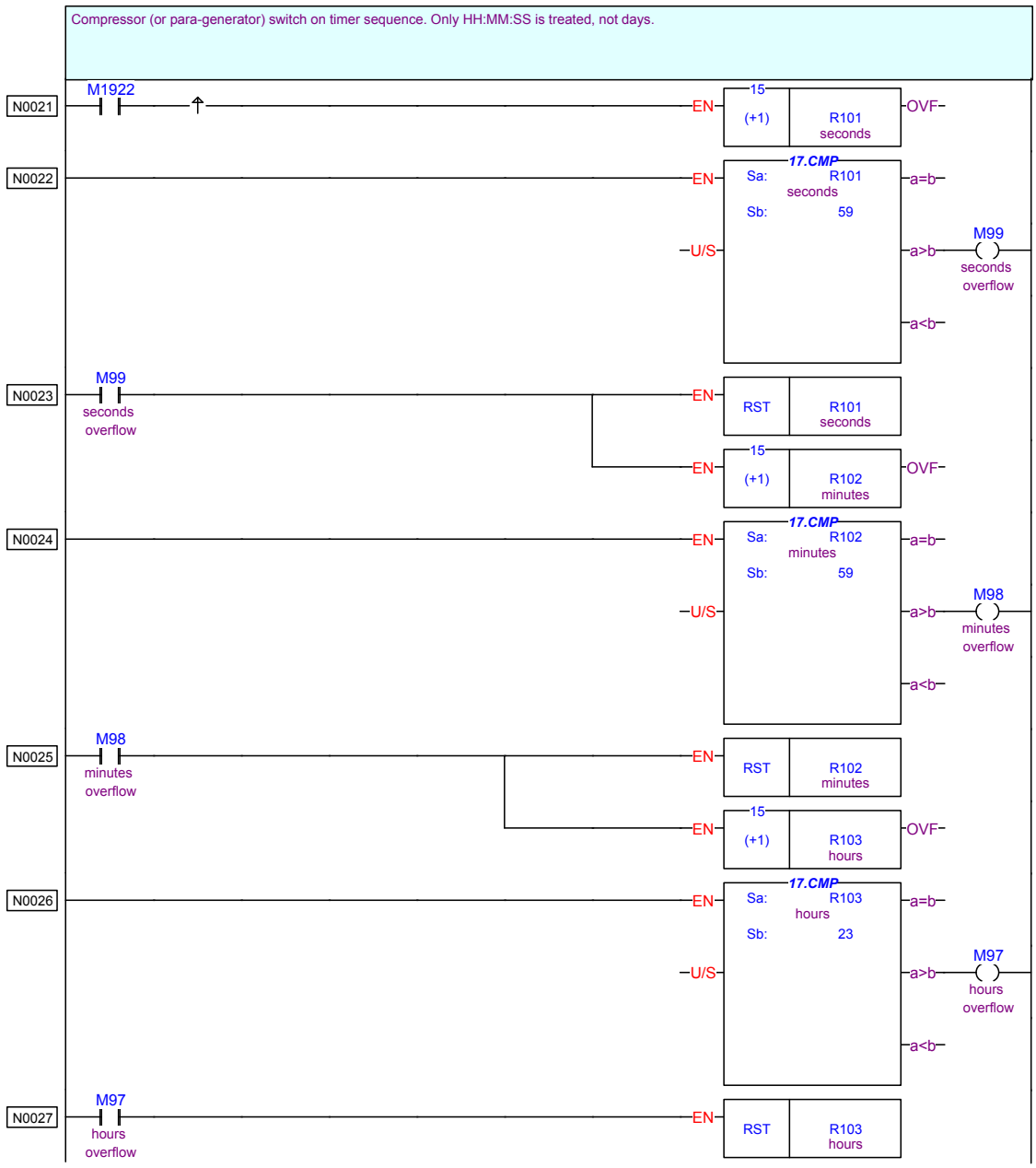

Printed Item: Ladder Diagram - Main_unit1

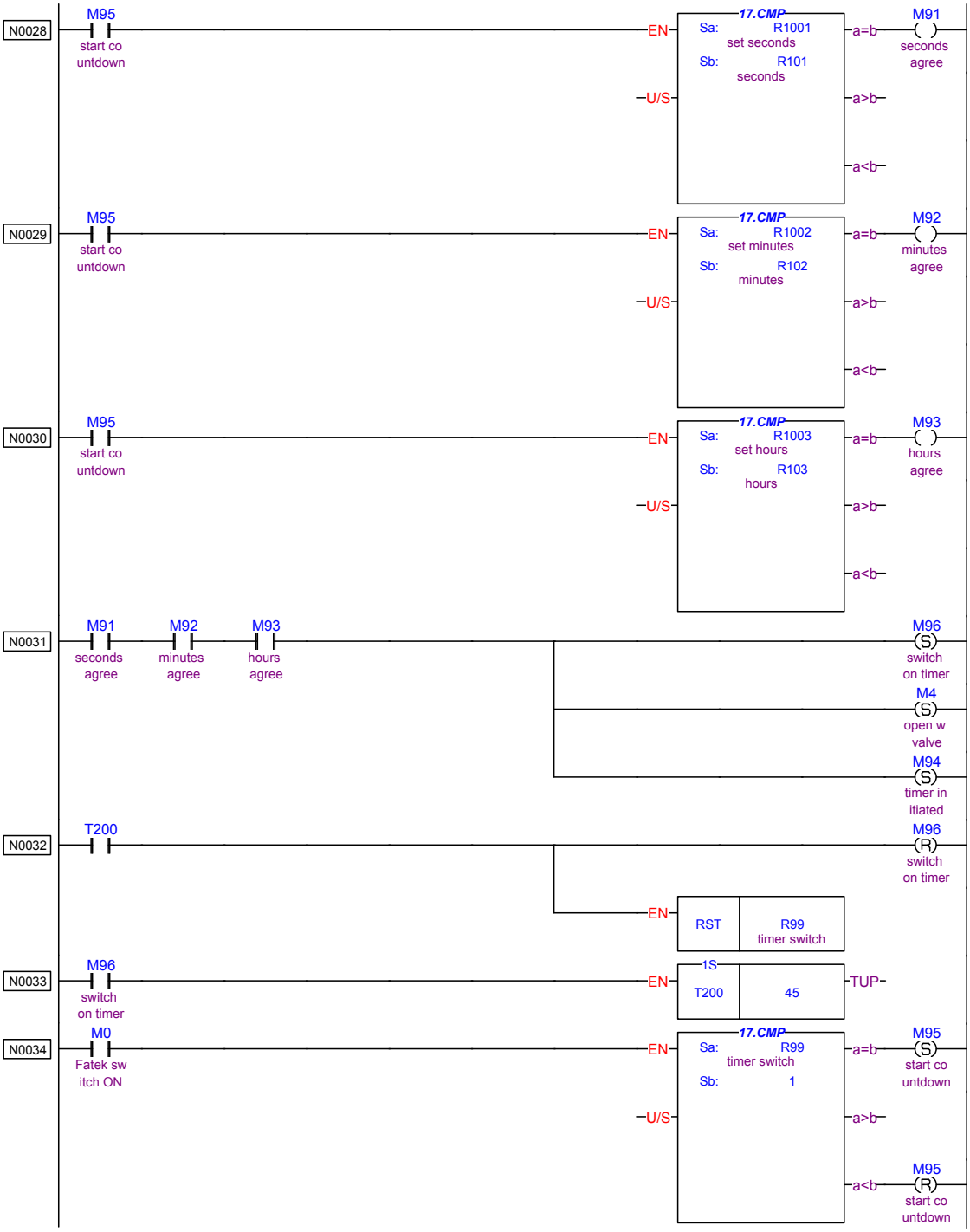

Printed Item: Ladder Diagram - Main_unit1